technische universität
dortmund

Arbeit zur Erlangung des akademischen Grades
eines Doktors der Naturwissenschaften
(Dr. rer. nat.)

Systematic Uncertainties of High Energy Muon Propagation using the Leptonpropagator PROPOSAL

Jan Benjamin Soedingrekso
geboren in Wuppertal

2021

Lehrstuhl für Experimentelle Physik V
Fakultät Physik
Technische Universität Dortmund

Erstgutachter:	Prof. Dr. Dr. Wolfgang Rhode
Zweitgutachter:	Prof. Dr. Bernhard Spaan
Abgabedatum:	01. Juli 2021

Abstract

Muons are the dominant particle type measured in almost every underground experiment mainly driven by the high production rate of muons in cosmic-ray induced air showers as well as the long muon range. Due to their stochastic propagation behavior, they can remain undetected with minimal energy losses in veto regions while producing a signal-like signature with a large stochastic energy loss inside a detector. Therefore, accurate description of theoretical models and precise treatment in simulations as well as a validation of the cross-section with measurements are required.

In this thesis, systematic uncertainties in simulations of high-energy muons were analyzed and improved, which can be divided into three parts. The theoretical models of the cross-sections were revised and radiative corrections for the pair production interaction were calculated. In a next step, the Monte-Carlo simulation library PROPOSAL was completely restructured in a modular design to include more accurate models and corrections. Due to its improved usability through the modular design and its accessibility as free open-source software, PROPOSAL is now used in many applications, from large simulation frameworks, such as the CORSIKA air shower simulation, to small simulation studies. The third part consisted of a feasibility study using PROPOSAL to measure the bremsstrahlung cross-section from the energy loss distribution, which can be measured in cubic kilometer-sized detectors. For a detector resolution similar to that of the IceCube neutrino telescope, the bremsstrahlung normalization was estimated with an uncertainty of $\pm 4\,\%$.

Kurzfassung

Myonen sind der dominierende Teilchentyp, der in fast allen Untergrundexperimenten gemessen wird, hauptsächlich bedingt durch die hohe Produktionsrate von Myonen in durch kosmische Strahlung induzierten Luftschauern sowie die große Myonenreichweite. Aufgrund ihres stochastischen Propagationsverhaltens können sie mit minimalen Energieverlusten unentdeckt durch Vetoregionen propagieren und innerhalb des Detektors mit einem großen stochastischen Energieverlust eine signalartige Signatur erzeugen. Daher sind eine genaue Beschreibung der theoretischen Modelle und eine präzise Behandlung in Simulationen sowie eine Validierung des Wirkungsquerschnitts mit Messungen erforderlich.

In dieser Arbeit wurden systematische Unsicherheiten in Simulationen hochenergetischer Myonen analysiert und verbessert, was in drei Teile unterteilt werden kann. Die theoretischen Modelle der Wirkungsquerschnitte wurden überarbeitet und

Strahlungskorrekturen für die Paarproduktionswechselwirkung wurden berechnet. In einem nächsten Schritt wurde die Monte-Carlo-Simulationsbibliothek PROPOSAL in einem modularen Design komplett umstrukturiert, um genauere Modelle und Korrekturen einbeziehen zu können. Aufgrund der verbesserten Nutzbarkeit durch den modularen Aufbau und der Zugänglichkeit als freie Open-Source-Software wird PROPOSAL inzwischen in vielen Anwendungen eingesetzt, von großen Simulations-Frameworks, wie der Luftschauer-Simulation CORSIKA, bis hin zu kleinen Simulationsstudien. Der dritte Teil bestand aus einer Machbarkeitsstudie unter Verwendung von PROPOSAL zur Messung des Bremsstrahlungsquerschnitts aus der Energieverlustverteilung, die in kubikkilometergroßen Detektoren gemessen werden kann. Für eine Detektorauflösung, welcher der des IceCube-Neutrinoteleskops ähnelt, wurde die Bremsstrahlungsnormalisierung mit einer Unsicherheit von $\pm 4\,\%$ abgeschätzt.

Contents

1 Introduction

Muons have been first discovered in cloud chamber observations in 1936 [AN36]. Due to their propagated range, energy loss profile and deflection, their signature in the detector didn't match the behavior of an electron or a proton. In particular, it's the range of muons, that they can propagate through large volumes of media before they lost all of their energy, which makes them special and interesting for nearly all particle detectors on earth. Muons are the only particle type from cosmic-ray induced air showers that can reach detectors located deep underground. Therefore, they are the dominant measured event signature for underground experiments and often seen as an unwanted background. With the high rate of cosmic-rays hitting the atmosphere, their secondary muons contribute to a third of the natural radiation consumption for humans on earth.

But these muons can also be used for indirect measurements of cosmic-rays. In the context of astroparticle physics or multi-messenger astronomy, cosmic-rays are just one type of messenger discovered in 1914 [Hes12]. Electromagnetic waves are by far the oldest approach to observe the sky, mainly at optical frequencies. In the 20th century also other wavelengths of the electromagnetic spectrum from radio frequencies to γ-rays were used to further understand astrophysical processes in Multi-Wavelength studies. The 21st century, especially the last decade revealed two further messengers, "neutrinos" and "gravitational waves" making the 2010s a golden decade for astronomy. And maybe in this century, another type of messenger can be unveiled, the Dark Matter.

All of these messengers need to get combined to extract the full picture and get a deeper understandings of astrophysical processes. One example of how the advantages and disadvantages can get combined is the observable horizon. While the neutrinos only lose their energy due to the expanding universe, resulting in the horizon of $^{c}/_{H_0} \approx 4\,\mathrm{GPc}$, the observable distance for gravitational waves depends on the total mass of the binary system [Abb+20b]. However, protons and photons interact with the diffuse electromagnetic *cosmic background* [HMS18], limiting their horizon depending on their energy [Des06]. The strongest attenuation is driven by the Cosmic Microwave Background (CMB) limiting the distance of PeV photons to 10 kPc, which is barely the distance to our galactic center, and ZeV protons to 10 MPc, which just includes the nearest galaxies [DGR13]. The CMB is considered

to be a left-over from the big bang when the temperature drops below the critical value to perform electromagnetic pair production and annihilation. Due to the expanding universe, the temperature of the CMB is today at 2.7 K [Zyl+20].

Besides these fixed limitations for the incoming messenger flux, the detection and analysis methods have been steadily developed to gather more information and increase the sensitivities leading to the current knowledge on particle physics and astronomy. Although many new astroparticle experiments or enhancements are planned, the size of most particle detectors converge to their possible limits. Further large increases of detection volumes depend on large increases of investments, which are challenging and are often not in relation to the gain of sensitivity. Therefore the software improvements including the simulation and reconstruction methods become more important to keep up with the new detectors and to improve the sensitivity for the existing ones.

One part of these soft-improvements consists of modern methods of computer science and statistics to analyze the data using e.g. machine learning approaches to extract and reconstruct the measured events. The other part consists of more accurate theoretical calculations and more flexible simulations including these accurate models and being adaptive to the different demands of the experiments to reduce the systematic uncertainty.

This work focuses on the latter part to reduce the systematic uncertainty for the muon simulation and provide this to diverse types of experiments. Since, there is no astrophysical source, sending a test beam of messengers to calibrate the detection, simulations are necessary to understand the measured data. A precise description of the stochastic behavior of muons is therefore crucial for cosmic-ray and neutrino detectors as muons are the dominating event signature.

In Chapter 2 the generation and in 3 the detection processes of muons measured on Earth is presented introducing the demands for muon simulations. In chapter 4 the muon interactions and their uncertainties are discussed and in 5 the developments of the revised simulation library PROPOSAL is described. In chapter 6 a simulation study to measure the muon bremsstrahlung is presented before giving an outlook in chapter 7 enrolling the possibilities for further analysis based on this work.

2 Muon Generation

Regarding the natural generation processes, muons with energies above a GeV detected at the surface are produced by cosmic-ray or neutrino interactions. While muons with these energies can still be produced at particle physic experiments, at energies above several TeV, even the strongest accelerator experiment, the LHC, is not powerful enough to create such energetic muons. Those high energetic muons can only be created by cosmic-rays or neutrinos.

At the Earth's surface, most of the muons are going downward, originating from interactions of cosmic-ray in the atmosphere. After $\mathcal{O}(10^4)$ meter-water-equivalent (mwe) even the highest energetic muons lost all of their energy and stop before they decay [Zyl+20]. Therefore all muons propagating longer distances through the Earth will get absorbed. Only neutrinos can travel through the Earth without any interaction and can convert to their charged leptonic counterpart just before the surface. Therefore muons seen in a detector going downward most-often originate from cosmic-rays while upward-going muons originate from neutrino interactions.

2.1 Cosmic-Ray induced Muons

Cosmic-rays hit the atmosphere with a rate of $1\,\mathrm{kHz/m^2}$ and consist mainly of Protons (75 %), Helium (17 %) and heavier nuclei [GER16]. Depending on the energy range these ratios are shifted towards the heavier nuclei, mainly iron, dominating at higher energies. The cosmic-ray spectrum is shown in Figure 2.1 together with models describing the composition of the nuclei.

2.1.1 Cosmic-Ray Energy Spectrum

The energy spectrum of incoming cosmic-rays, shown in Figure 2.1b, is focusing above the GeV energy range where most of the particles are produced outside of our solar system. Until energies of roughly a GeV the main source of measured cosmic-ray events originates from our sun with a variable event rate depending on the sun's activity. Cosmic-rays from outside of our solar system are screened by the Heliosphere.

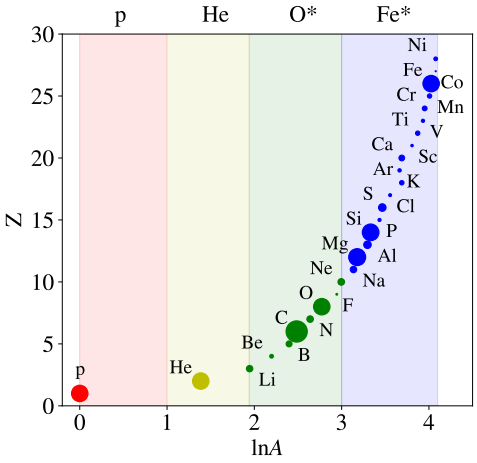

(a) Composition of the cosmic-rays grouped nearly equally in their logarithmic mass between proton and nickel. The size of the circles denotes the flux ratio compared to the leading element in each group. [Dem+18]

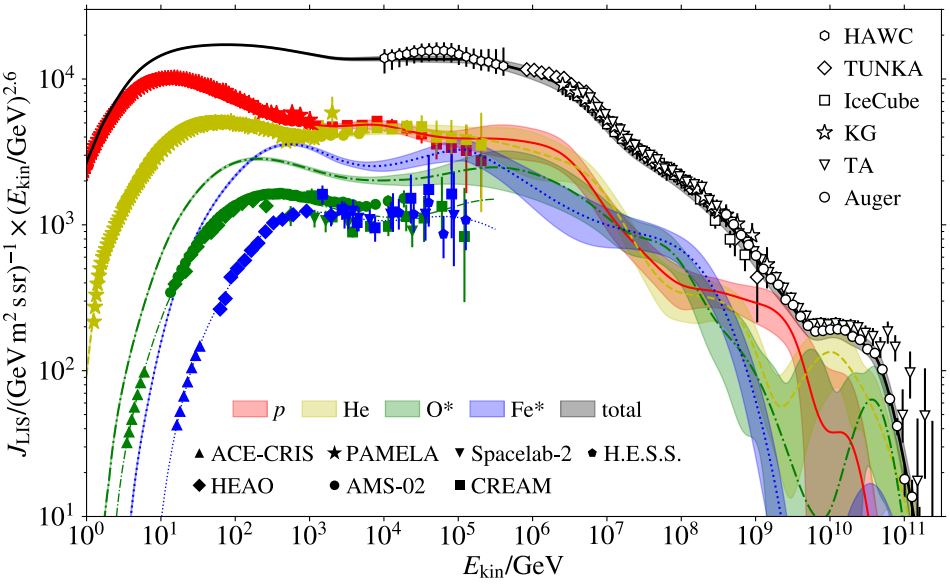

(b) Global Spline Fit of the measured all-particle cosmic-ray energy spectrum. For Oxygen and Iron the data points represent the measured elemental flux and the model lines are shown without error bars for the elemental flux and with error bars for the group flux. [Dem+19]

Figure 2.1: The energy spectrum of the cosmic-rays from the GeV range to the GZK-cutoff. Up to a PeV, space-based detectors measure the cosmic-rays directly being able to differentiate between the compositions. Above a PeV, ground-based detectors measure the cosmic-rays indirectly via air showers.

Above a GeV, the magnetic fields of the sun are not powerful enough to accelerate particles to such high energies and galactic sources are the main source of cosmic rays. The main type of cosmic accelerators is considered supernova remnants (SNRs). Supernovæ occur on average once in a century in our galaxy, while their shock waves propagate hundreds of years into the interstellar medium. The particles with these energies are considered to undergo the so-called Fermi acceleration, a shock acceleration resulting in a power-law spectrum $E^{-\gamma}$ with an index of $\gamma = 2$. Due to interaction losses and the probability to escape the galactic magnetic field the spectrum gets steeper and results in a measured spectral index of 2.7 on Earth. SNRs can accelerate particles up to a PeV, a region called the *knee* of the spectrum.

Above the *knee* and until the so-called *ankle* at an EeV yet unknown galactic sources, probably Pulsars or Quasars become dominant resulting in an increased measured spectral index of 3.1. Above the *ankle* sources inside our galaxy are not powerful enough to accelerate such high energetic particles and extragalactic sources, e.g. Active Galactic Nuclei, become the main contributor. The resulting spectral shape flattens again to an index of 2.6. At around 1×10^{20} eV the protons interact with the photons of the CMB to a Delta resonance, resulting in the GZK-cutoff of the energy spectrum, predicted by Greisen, Zatsepin and Kuz'man [Gre66; ZK66].

2.1.2 Cosmic-Ray induced Air Shower

When cosmic-rays reach the Earth they interact with the dense medium of the atmosphere. Depending on the energy and the composition of the particle, the height of the first interaction is at 10 km to 15 km. The secondary particles of this interaction again interact with the atmosphere resulting in a particle cascade or air shower that consists of thousands or even billions of particles. These showers can be categorized into hadronic, muonic and electromagnetic shower components, which are illustrated in Figure 2.2a.

The electromagnetic shower component consists of electrons, positrons and photons. Starting e.g. with a high energy photon the two main gamma interactions are the production of an electron-positron pair, also called the Bethe-Heitler process, and Compton Scattering. While the latter is just important for the deflection, the pair production is the important process for the shower development. The produced electrons and positrons dominantly lose their energy via bremsstrahlung, creating again a high energy photon. The Positron can also annihilate with the atomic electrons creating a photon pair, which is a sub-dominant process.

The cycle of photon pair production and electron/positron bremsstrahlung continues until the bremsstrahlung photons are below an MeV and therefore not energetic

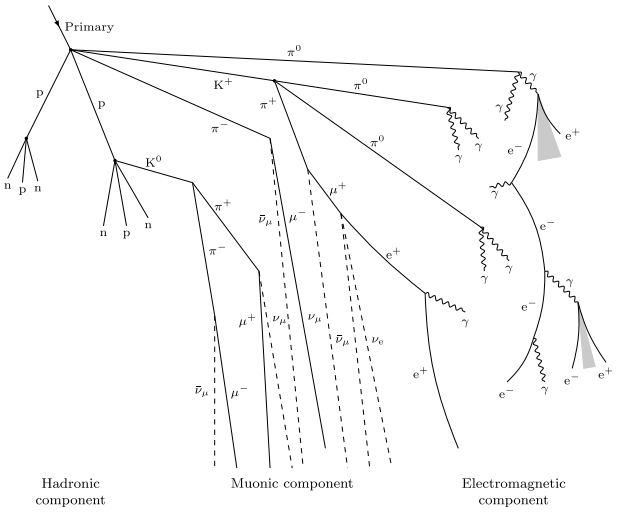

(a) Basic scheme of the interactions and particles for the shower components of an air shower. Adapted from [Kra15]

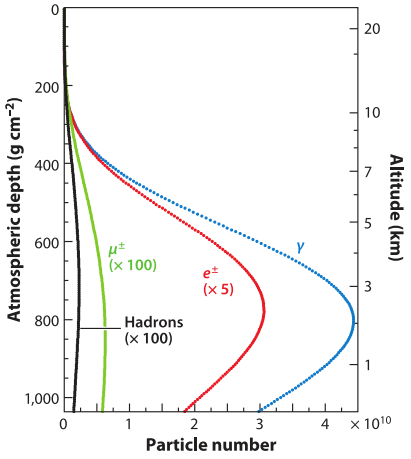

(b) Development of the number of produced shower particles for a 10^{19} eV proton induced vertical air shower. [EHP11]

Figure 2.2: Development of a cosmic-ray induced air shower. To the left the different sub-showers divided into an electromagnetic, a muonic and a hadronic component is shown. To the right the contribution of these sub-showers and particles during the shower development is shown.

enough to create an electron/positron pair. Due to the high number of charged particles (c.f. Figure 2.2b) that are created, this shower component produces the dominant amount of the Cherenkov light and is also important for the radio signal of a shower. The production of a muon pair is a sub-dominant process as the muon mass is 200 times higher than the electron mass decreasing the phase space and is therefore not important for the electromagnetic shower development. However, it is a non-negligible process regarding the number of produced muons inside the shower, while the main production originates from the hadronic shower.

The hadronic shower component mainly consists of the lightest mesons, charged Pions and Kaons ($m_{\pi^\pm} \approx 140\,\mathrm{MeV}, m_{K^\pm} \approx 494\,\mathrm{MeV}$ [Zyl+20]). Due to their relatively long lifetimes of $\tau_{\pi^\pm} = 26\,\mathrm{ns}$ and $\tau_{K^\pm} = 12\,\mathrm{ns}$, they propagate and lose a significant amount of their energy through interactions before they decay. Pions decay mainly into muons, as their rest mass is just slightly higher. Kaons either directly decay into muons (or electrons) or first decay into Pions, which then decay to muons and neutrinos. The energy losses during the propagation of the Pions and Kaons lead to a steepening of the resulting muon and neutrino energy spectrum to a spectral index of 3.7. The muons or neutrinos originating from these processes are called *conventional atmospheric* muons or neutrinos.

In addition to Pions and Kaons also short-lived mesons and baryons are produced in hadronic showers. They consist mainly of mesons with a charm quark, like the D-Meson, of Λ-Baryons and unflavored mesons, while the latter do not often decay into muons and muon neutrinos. Due to their short lifetime ($\tau \leq 1\,\mathrm{ps}$), they do not lose energy during their short propagation and directly decay. The resulting energy spectrum of the decay products is therefore similar to the primary spectrum as the spectral index does not change. Although these processes are sub-dominant, the flatter spectral index of the resulting muons and neutrinos makes them relevant at higher energies. Due to the direct decay of the hadrons, which mainly consist of charmed mesons, the resulting muons or neutrinos are called *charmed* or *prompt atmospheric* muons or neutrinos.

The muonic shower component mainly originates from the hadronic shower component and produces just a few secondaries compared to the other shower particles. The high muon mass ratio compared to the electron also decreases the interaction probability as the bremsstrahlung cross section is proportional to $1/m^2$. Combined with the relatively high lifetime, the muon range through dense media is the highest, neglecting neutrinos, making them the biggest background for all particle detectors even if they are located deep underground. Except for detectors placed at high altitudes, they are the only shower component for inclined showers measured on the Earth's surface, neglecting the electromagnetic radiation like Cherenkov light,

Fluorescence light or the radio signal. The resulting muon and neutrino energy flux from cosmic-ray induced air showers is shown in Figure 2.3.

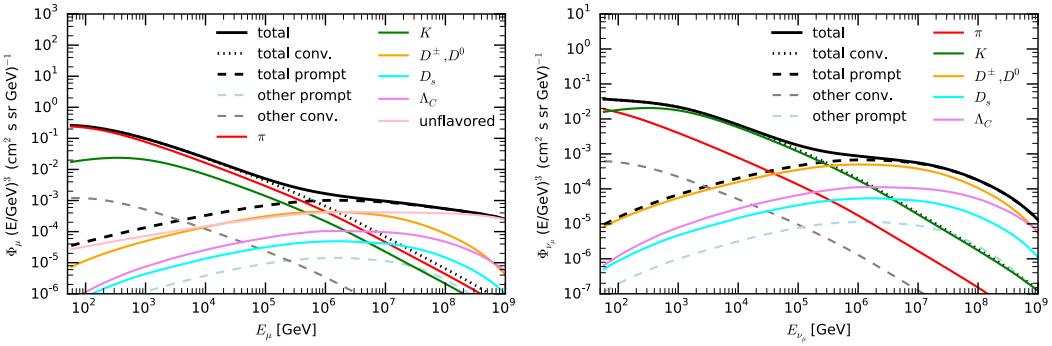

Figure 2.3: Predictions of the atmospheric muon and neutrino flux at the surface using matrix cascade equations. [Fed+15]

A longitudinal shower profile and the contribution of the different sub-shower types is shown in Figure 2.2b. An increasing number of particles at the beginning of the shower development can be seen as well as a decreasing part when more and more bremsstrahlung photons are too low energetic to produce an electron-positron pair. The resulting maximum of the longitudinal shower profile $X_{\max}$ at roughly 5 km for vertical showers varies for the different primary particle types and energies making it an important feature to classify the primary particle.

Another important feature to estimate the energy of the primary particle is the number of muons detected at the Earth's surface. Unfortunately, there is a discrepancy between the number of muons measured in air shower detectors, which exceeds the number of muons produced in air shower simulations starting at primary energies of 10^{16} eV [Dem+19]. That is seen across multiple experiments with a significance of 8 , known as the *Muon Puzzle* [Alb+21].

It is considered, that most of the discrepancy arises from the uncertainties of the hadronic interaction models. While most of the models are influenced by accelerator measurements from e.g. the LHC, these models provide good agreements for high transversal momentums. In the forward direction, the beam pipe and not a detector is located, which is fine for those experiments as most differential cross sections diverge in the forward direction. However, astroparticle physics experiments most often measure the shower in the forward direction leading to fewer cross-checks with the accelerator measurements. This type of challenge to evaluate cross section also in the forward direction does not just occur for the hadronic models, but for all types of particle interaction including the muon cross sections.

A precise description of the muon bundles is also crucial for underground detectors to separate these background events from their signal. While there are also muons with a high transversal momentum compared to the shower axis resulting in a lateral distribution [EHP11] most of the high energetic muons propagate close to the primary direction making a separation between them challenging. An extraction of muon physics parameters out of these muon bundles is therefore limited and single muons are required to provide a deeper understanding.

2.2 Neutrino induced Muons

Compared to the cosmic-ray induced muons that occur only in bundles, neutrinos produce single muons. Further muons are produced in the hadronic cascade at the neutrino vertex or as muon pair production. But these muons have much less energy and stop far before the main muon produced by the neutrino, so they can be neglected regarding muon energies of GeV or above.

2.2.1 Neutrino Energy Spectrum

The neutrino energy spectrum shown in Figure 2.4 is assumed to starts with a high number of cosmological neutrinos or the cosmic neutrino background (CνB). Like the CMB they are left-overs from the big bang when the temperature drops below the critical value of weak lepton production and annihilation. It consists of all neutrino flavors but the energies are far too low to be measurable with current technology.

Until keV-energies, thermal neutrinos from the sun are predicted [VTR20] before at neutrino energies of keV and MeV solar neutrinos from fusion processes dominate the neutrino flux on Earth with additional contributions of terrestrial anti-neutrinos from naturally decaying radioactive nuclide. Additional anti-neutrinos from nuclear reactors also contribute to the neutrino flux depending on the location on Earth [Usm+15]. Although only electron neutrinos are produced in radioactive decays or fusion processes, solar neutrinos are measured in all three flavors through the neutrino oscillation further described in section 2.2.2.

Furthermore in the MeV range neutrinos from supernova remnants also contribute to the neutrino flux. For the last supernova, SN1987A, where the neutrino contribution was first measured, the neutrino flux was orders of magnitudes higher than the SNR flux, dominating the spectrum at MeVs during that burst.

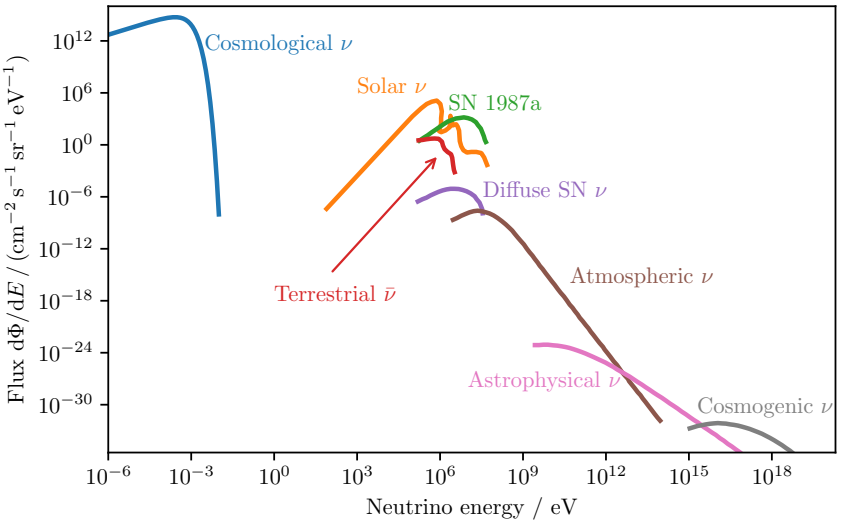

Figure 2.4: The diffuse neutrino energy spectrum at the Earth from the cosmological neutrino background $C\nu B$ to cosmogenic neutrinos. The gap between the $C\nu B$ and the solar neutrinos from nuclear processes is filled by thermal solar neutrinos, not included here (c.f. [VTR20]). Adapted from [KS12].

For neutrino energies starting around a GeV cosmic-ray induced atmospheric neutrinos are the main contributors. Their flux can be approximated by a broken power-law of *conventional* and *prompt* atmospheric neutrinos as described in section 2.1.2. At around 100 TeV both the prompt atmospheric and astrophysical neutrinos (probably from AGNs) starts dominating the flux both due to their flatter spectrum. While the astrophysical flux has already been measured by IceCube, the prompt component has always been fitted to zero and its contribution remains hidden.

The neutrino creation process for the cosmic accelerators (possibly Active Galactic Nuclei) is similar to the atmospheric neutrinos. Accelerated protons interact near the source and through the Pion and muon secondaries, neutrinos are produced. In contrast to the atmospheric neutrinos, the medium at astrophysical sources is not as dense as the atmosphere and the Pions and muons do not lose much of their energy before they decay. Therefore the energy spectrum does not get steeper and the spectral index remains on the level of the Fermi acceleration near 2.

The two main processes of the accelerated protons for the neutrino production are

the pp-channel and the $p\gamma$-channel.

$$pp \rightarrow \pi^+\pi^- ... \tag{2.1}$$

$$p\gamma \rightarrow \Delta^+ \rightarrow \begin{cases} \pi^+ n \\ \pi^0 p \end{cases} \tag{2.2}$$

In the pp-channel, a proton interacts with another proton in the surrounding matter near the source producing an equal amount of π^+ and π^-. In the $p\gamma$-channel, a proton interacts with a photon producing a Delta-resonance resulting in the production of only positively charged Pions. A way to distinguish between neutrinos and anti-neutrinos at these energies could therefore give further insights into the production processes [Bie+17].

Starting at 10 PeV the so-called *cosmogenic neutrinos* are predicted to be the main contributors. They are produced from decaying Delta-resonances induced by cosmic-ray protons interacting with the CMB at the GZK-limit. Unfortunately, they have not been measured yet, as the detectors to measure them with radio techniques are currently in the phase of planning and fund raising.

2.2.2 Neutrino Flavors at Earth

As already mentioned for solar neutrinos, the primary electron neutrino flux on Earth is measured in all three neutrino flavors due to neutrino oscillation [Ahm+01]. The distance between the Earth and the sun is greater than the oscillation length for neutrinos at these energies. For an initial electron neutrino flux, the oscillations lengths for the lepton flavors are shown in Figure 2.5a. Also for terrestrial distances neutrino oscillation is measurable e.g. for atmospheric neutrinos, where the flavor composition depends on the zenith angle [Fuk+98]. The neutrino propagating through the Earth further changes due to the different oscillation behavior between the propagation through matter compared to vacuum (MSW effect) [MS85; Wol78].

For astrophysical sources like SNRs or AGNs, the propagation distances are much larger than the oscillation length and the mean probability averaged over the oscillation is used to describe the neutrino flux composition depending on the initial production composition. There are three mainly discussed production scenarios describing one likely and two extreme scenarios of neutrino production.

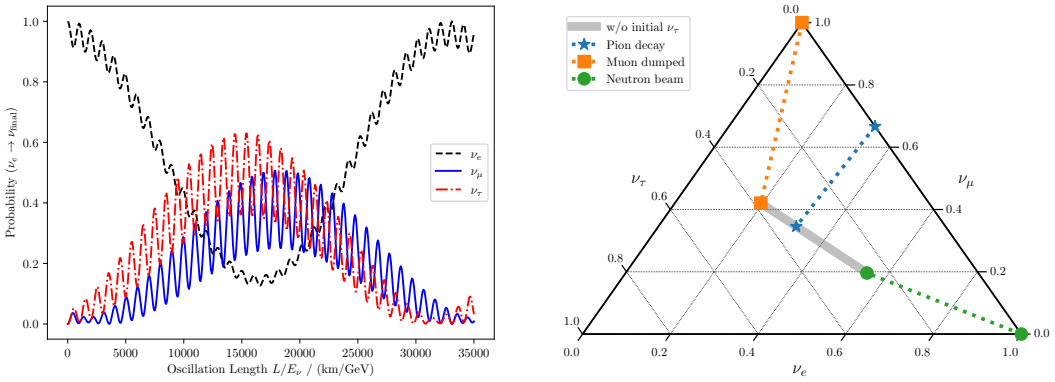

(a) Oscillation length for an initial electron neutrino flux into the three neutrino flavor.

(b) Neutrino flavor triangle for different source scenarios.

Figure 2.5: Neutrino flavor ratios for different observation distances to the source. To the left one full oscillation length is shown and on the right the average of the oscillation periods is shown. The currently measured oscillation parameters [Zyl+20] and an inverted mass hierarchy as this is slightly favored is used.

Assuming pure **pion decay** processes, the flavor ratio $\nu_e : \nu_\mu : \nu_\tau$ is $1 : 2 : 0$

$$\pi^+ \to \mu^+ \nu_\mu \tag{2.3}$$

$$\mu^+ \to e^+ \nu_e \bar{\nu}_\mu, \tag{2.4}$$

Equivalent processes happen for the π^- decay.

In the **muon damping** model, also assuming pure pion decays, the produced muons interact near the production region and lose most of their energy before they decay assuming a more dense medium around the source. The outgoing neutrinos of the muon decay are therefore in the range of a few MeV which is not measurable for astroparticle detectors. The resulting flavor ratio of $0 : 1 : 0$ then does not contain electron neutrinos. Atmospheric electron neutrinos are mainly produced in Kaon decay as Kaons decay equally into muons and electrons.

In the other extreme scenario, a high energy **neutron beam** is assumed at the source. In the decay of the neutrons, a pure electron neutrino flux with a flavor ratio of $1 : 0 : 0$ is produced.

For all three neutrino production scenarios, the flavor ratio that would be measured on earth after averaging over the neutrino oscillation is shown in Figure 2.5b. Independent of the neutrino creation model at the astrophysical source, neutrinos of all three flavors will arrive at the earth through neutrino oscillation, including tau

neutrinos. The most discussed scenario of the dominating pion production without muon damping produces a nearly equal amount of $1 : 1 : 1$.

Tau neutrinos are of special interest since the rate for direct production of the tau lepton with its high mass of 1.7 GeV is highly suppressed; both in air showers and at extragalactic sources. They are only measurable through neutrino oscillation and have therefore high confidence being of astrophysical origin.

Due to the negligible initial tau neutrino flux, the currently measured oscillation parameters assuming the standard model allows the neutrino flavor arriving on earth just to be in a distinct region of the flavor ratio, shown in Figure 2.5b. A precise measurement of the neutrino flavors could limit the allowed source scenarios.

The tau lepton, produced during the neutrino interaction as described in the following section, also decays into muons making them a non-negligible source of neutrino-induced muons.

2.2.3 Neutrino Interactions

There are three different interaction modes, illustrated in Figure 2.6, on how neutrinos can interact with matter.

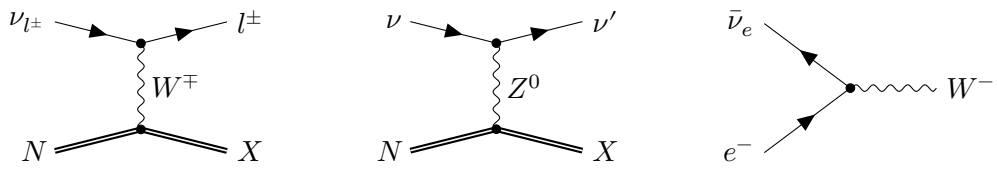

(a) Charged Current (CC) **(b)** Neutral Current (NC) **(c)** Glashow Resonance

Figure 2.6: The feynman diagrams of the most dominant neutrino interactions at high energies.

The **Charged Current** (CC) interaction, with a W-boson as the exchange particle between the nucleon and the neutrino, is the main producer of high energy muons. While the neutrino converts into its charged counterpart-lepton the other outgoing product is the hadronic cascade. The **Neutral Current** (NC) Interaction, with a Z-boson as the exchange particle, just produces an energy loss of the neutrino without converting it. Therefore only the hadronic cascade is the visible outcome of this interaction. For both the CC and NC interactions on average a third of the neutrino energy is stored as hadronic cascade and two-thirds in the outgoing lepton, shown in Figure 2.7b.

The CC interaction is the dominant interaction contributing two-thirds to the total cross section, while the NC just contribute a third, as shown in Figure 2.7a. For lower energies, the anti-neutrino cross section is smaller as the valence quarks are the main interaction partners. The sea quarks and thereby an equal treatment of neutrino and anti-neutrino become more important at higher energies.

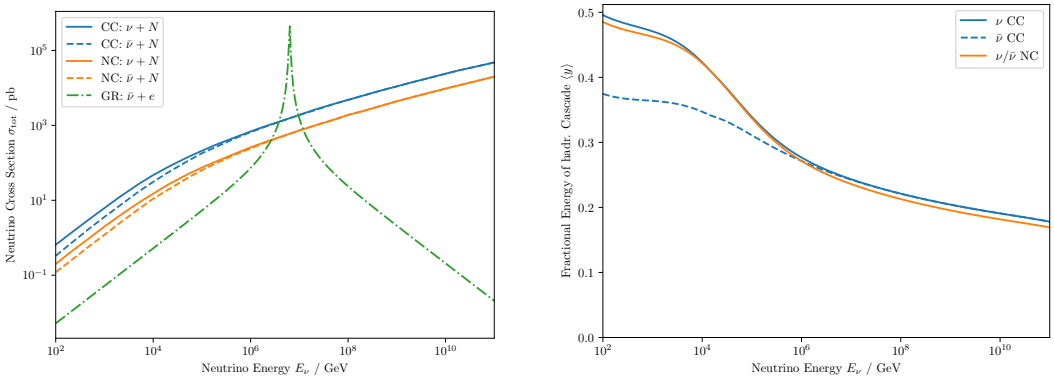

(a) Total neutrino cross section

(b) Average energy loss to the hadronic cascade relative to the neutrino energy.

Figure 2.7: Neutrino cross section for the Charged Current (CC) the Neutral Current(NC) and the Glashow Resonance(GR). For the CC and NC interaction, the calculation from [CMS11] and for the Glashow resonance, the parametrization of [Bar+14] are used.

At an energy of 6.3 PeV, the peak of the **Glashow Resonance** (GR) dominates the cross section [Gla60]. At this energy, the anti-electron neutrino interacts resonantly with an atomic electron producing a W^--boson. The result is a huge hadronic cascade, as the W-Boson decays with the hole energy, producing also multiple higher energetic muon tracks characteristic for this interaction. Next to the hadronic decay mode in $^2/_3$ of the cases, the remaining third is equally distributed on the three leptonic decay modes. Although the resulting muons are challenging to identify, a first candidate of a high energetic muon originating from a Glashow resonance has been found [Aar+16].

The energy distribution of muons propagating out of a hadronic cascade is described in [Pan+09].Compared to the directly produced muon of the CC interaction, the secondary muons of the hadronic cascade are much less energy while still producing a non-negligible signature. Especially, as the hadronic interactions not only occur at the neutrino vertex but also at each inelastic nuclear interaction along a muon track.

3 Muon Detection

Muons can be measured by the energy losses along their propagated track, each producing a particle cascade. While the bare muon also produces a signal, the main signature is produced by the secondaries of the energy losses. Here the main detection techniques of muons for cosmic-ray detectors and neutrino telescopes are presented.

3.1 Detection principles

The **Cherenkov Effect** [Che34] describes the optical light produced by a charged particles propagating faster than the speed of light through a medium. Due to the through-going charged particle, the medium gets polarized and creates a signal. These signals are emitted coherently when the charged particle propagates faster than the speed of light in this medium, creating a Cherenkov cone with an opening angle of $\cos\theta = 1/\beta n$ similar to a hypersonic cone of an Airforce jet. n is the refraction index that also depends on the wavelength. The Frank-Tamm formula [FT37] describing the spectrum of the emitted Cherenkov photons has a $1/\lambda^2$ dependency, with the wavelength λ, and is therefore UV-divergent (neglecting the suppressing contribution of the refraction index). Focusing on the optical wavelength and the medium ice, around 400 Cherenkov photons are emitted per centimeter with the main contribution of around 400 nm (blue light). The energy loss caused by the Cherenkov effect is around 170 eV/cm which is four orders of magnitudes below the minimum Ionization loss of 2 MeV / cm and is therefore negligible for the energy loss during the propagation. The Cherenkov light can be measured with Photomultiplier Tubes (PMTs) with the advantage of a wide collection area useful in water tanks but with the disadvantage of demanding high voltages. Alternatively, the light can be measured with Silicon Photo Multiplier (SiPM) being able to operate without high voltages but only having a small collection area and therefore only applicable when the light is guided to them.

The **Askaryan Effect** [Ask62] describes the radio signal caused by the relativistic propagation of a particle cascade. In principle, the radio signal is produced by the geomagnetic and the Askaryan effect, but it is commonly known as the Askaryan effect. The geomagnetic effect describes the separation of positrons and electrons

during an electromagnetic cascade due to the geomagnetic field. Due to the high number of shower particles, this creates a dipole perpendicular to the shower axis changing over time as the shower increases to its $X_{\max}$ and then decreases. Since there are only atomic electrons and no positrons, these electrons of a medium get knocked-out by the shower particles and the shower front gets charged negatively leaving the positively charged ions behind. This charge imbalance along the shower axis is also changing over time as the shower develops which is considered as the Askaryan effect. Both effects are just measurable because the particle cascade propagates faster than the speed of light in the medium thus producing a coherent radio signal at the Cherenkov angle. For air showers, the radio signal is mainly produced by the geomagnetic effect while for more dense media, like ice, the Askaryan effect produces the dominant radio signal. Only the highest energetic particle showers ($>$ EeV) produce a sufficient amount of electrons and positrons and thereby a detectable radio signal. The energy loss of 18 MeV for an EeV shower due to this effect is even more negligible compared to the Cherenkov radiation. The radio signal with wavelengths of a meter has a much higher attenuation length of about a kilometer in ice compared to 100 m for optical light.

Even before the radio signal, Askaryan predicted an **acoustic signal** produced by high energetic cascades [Ask57]. The huge amount of high energy charged particles inside the small shower region increases the energy and thereby the temperature of the medium in this area. The heated region expands and creates an acoustic wave with a maximum frequency at 10 kHz. Through the coherent superposition of the sound waves, an acoustic signal perpendicular to the particle shower is produced that can be measured [Lah17]. Similar to the radio signal the attenuation length is on the order of a kilometer making both techniques interesting for rare events requiring huge detection volumes.

The **fluorescence effect** in general describes atoms or molecules that get excited and thus emitting optical light. In the context of particle detectors, this is mainly used in scintillator detectors where the charged particle excites the scintillator material when passing through which emits light. While the scintillation area can have a size of $\mathcal{O}(m^2)$, the emitted light can then be guided to a detector that just needs a small collection area, like an SiPM. Besides this use of the fluorescence effect, the fluorescence light is used in the detection of the excited nitrogen molecules in the atmosphere caused by the huge number of high energetic particles in the shower [Kei+13]. The emitted fluorescence light at each shower depth is equivalent to the energy loss per distance making the energy of the shower extractable via the integral of the longitudinal shower profile. Another type is the luminescence light which is used in searches of magnetic monopoles with neutrino telescopes, where the radio-luminescence induced by these highly ionizing particles has become a field of research [PP19].

3.2 Air Shower Detectors

The different signals an air shower produces are measured with multiple approaches, from the direct detection of the different shower particles at high altitudes over the muon detection at the surface to the fluorescence or radio signal besides the shower axis.

3.2.1 Gamma-Ray induced Air Shower Detectors

Extended air shower Arrays (EAS-Arrays) are placed at high altitudes, ideally near the typical maximum of the shower profile $X_{\max}$ to measure most of the produced particles inside the detector. One approach is using a dense array of closed tanks filled with purified water. Through-going charged particles of the shower produce Cherenkov light inside the water, which can be detected with optical sensors mainly PMTs. Currently, the most sensitive observatory is the HAWC detector [Abe+17] operating at an altitude of 4.1 km above sea level (asl) in the Sierra Negra, Mexico. Inside an area of 22 000 m^2, 300 cylindric tanks are placed each containing around 200 m^3 of water with 4 PMTs at the bottom measuring the Cherenkov light. The upcoming LHAASO experiment in Tibet [Bai+19] will increase the sensitivity for air showers due to the higher altitude at 4400 m asl. Although EAS-Arrays are mainly designed to measure γ-ray induced air showers, one can also use them to analyze cosmic-ray induced showers in the PeV range around the *knee* [Alf+17]. Muons can be identified as they reach the ground of the detector producing light along their full track, while electrons will lose nearly all of their energy during their propagation through around 4 m of water from the top of a tank to the bottom creating a uniform light pool.

Another type of telescope that was mainly developed for gamma astronomy but is also used to study cosmic-ray physics are imaging air Cherenkov telescopes (IACTs). The detection techniques of both types of gamma telescope designs are illustrated in Figure 3.1a. Hereby, the relativistic particles of an air shower are not measured directly, but indirectly via the Cherenkov light, they produce in the atmosphere, which can be also measured at moderate altitudes. The current most sensitive telescopes are the HESS [Ash+20], MAGIC [Ale+16] and VERITAS [Sta+16] telescopes operating at 1800 m 2200 m, 1300 m asl. respectively. Electromagnetic or hadronic showers produce elliptical camera pictures with an additional spread-out for hadronic showers due to the higher transverse momentum of the hadronic interaction products. Compared to that, muons produce a ring-like signature when propagating to the ground near the telescope. Using this unique signature, IACT arrays measuring the same hadronic shower in multiple telescopes as well as the

muons can give further insights into the muon flux produced in air showers [MDP19]. However, this approach will only work with an array of many telescopes as will be built in the upcoming CTA observatory [Ach+19]. Compared to the closed tanks of EAS-Arrays with a duty cycle of nearly 100 %, IACTs can only operate at clear, moonless nights limiting their duty cycle to 20 %.

3.2.2 Cosmic-Ray induced Air Shower Detectors

Also at these moderate altitudes, it is possible to measure the fluorescence light produced mainly by the electromagnetic component of an air shower. As these fluorescence detectors can cover a large effective area, rare events like the cosmic-rays at the GZK cut-off can be measured. Currently, the most sensitive experiments for this type of detection are the Telescope Array [Tok+12; Abu+13] in Utah observing the northern hemisphere and the Pierre Auger Observatory [Aab+15] in Argentina for the southern hemisphere both operating at around 1400 m asl. The Pierre Auger Observatory, shown in Figure 3.1b consists of 24 fluorescence telescopes and 1500 Water Cherenkov Tanks on an area of 300 km^2 each containing 12 m^3 water and 3 PMTs.

Combining the fluorescence detection with an array of surface detectors sparsely placed on a large area to measure the particles reaching the ground has become a successful approach to measure the highest cosmic-rays. In this hybrid method, the fluorescence detectors measure the longitudinal profile of the shower and thereby the energy of the shower. The surface detectors measure the electromagnetic component only for vertical showers or just the muonic component for inclined showers being sensitive to the mass composition of the cosmic-ray. While the surface detectors have a full duty cycle, the fluorescence detectors can only operate at clear nights, similar to the IACTS and EAS-Arrays and their duty cycles. In combination with the lateral shower profile and its arrival times measured by the surface detectors, the main information of the primary particle, composition, energy and direction can be reconstructed. Unfortunately, discrepancies in the number of muons between the measurement and the prediction of the simulation limit the use of Monte-Carlo based analysis and therefore the sensitivity on the mass composition.

Recent developments for the Pierre Auger Observatory [Aab+16; Cas19] also include the usage of scintillator detectors at the surface, which are more sensitive to the electromagnetic component while being less sensitive to the nearly horizontal propagating muons of inclined showers. Also part of this upgrade is placing radio antennas at each station to detect the radio signal thus measuring more components of the shower to better reconstruct the particle shower.

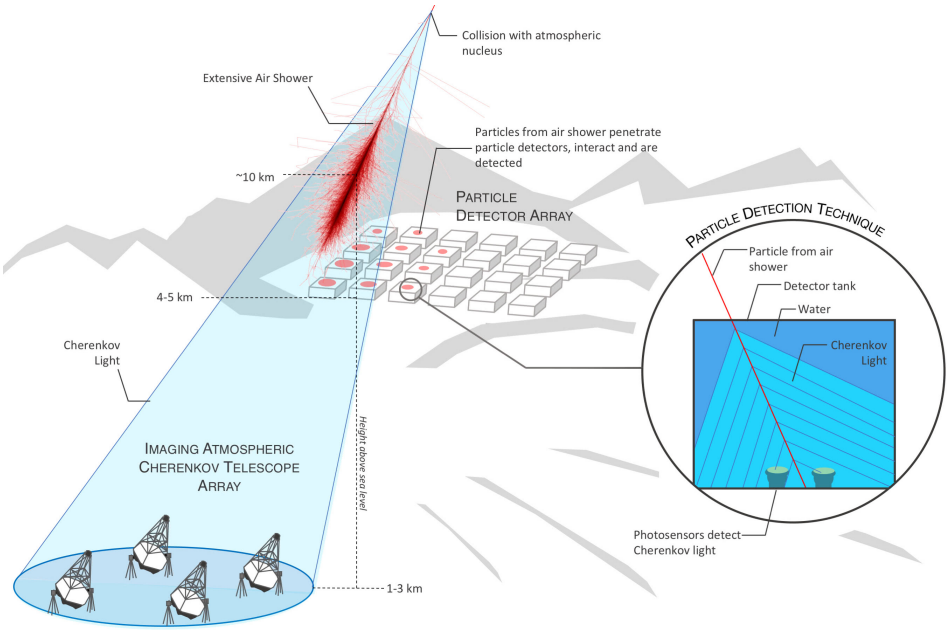

(a) Direct particle detection at high altitudes with an extended air shower array and Imaging Air Cherenkov Telescopes at lower altitudes detecting the produced Cherenkov light in the atmosphere. [Sch19]

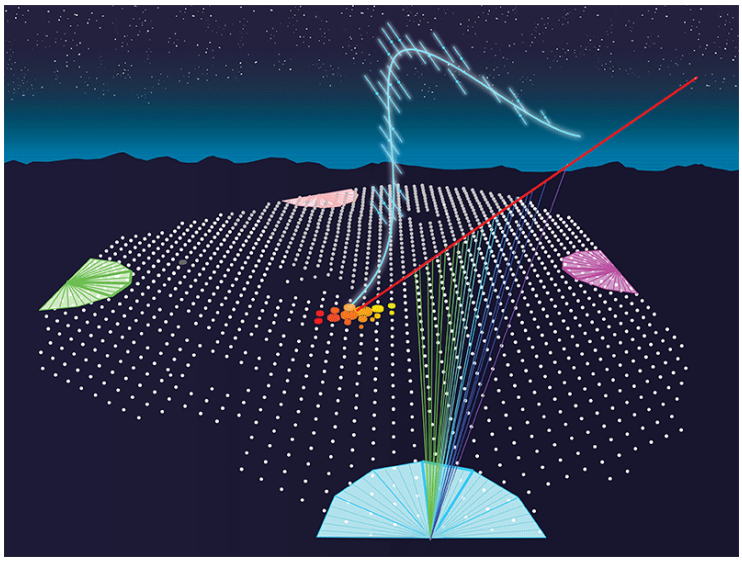

(b) Air shower measurement techniques of the Pierre-Auger Observatory using surface detectors and Fluorescence detectors. [Gai16]

Figure 3.1: Air shower measurement techniques using direct particle detection at high altitudes with an extended air shower array and the produced Cherenkov light in the atmosphere using Imaging Air Cherenkov Telescopes.

3.2.3 Further Detectors measuring Atmospheric Muons

A transit between a cosmic-ray induced muon detector and a neutrino detector is the NEjtrinnyj VOdnyj (Water) Detektor, NEVOD [Pet15] located inside a building at the MePhI in Moscow. The detector, shown in Figure 3.2, consists of a water-filled chamber with a size of $9\,\mathrm{m} \times 9\,\mathrm{m} \times 26\,\mathrm{m}$. Inside this indoor pool, 25 Strings each containing three or four Quasi-Spherical-Modules which themselves consist of six PMTs looking in all three orthogonal directions, forward and backward and measure the light of the muons propagating through the chamber. Due to the three-dimensional detector structure, the muons are not just registered, but also their energy loss behavior can be measured. To increase the angular resolution for horizontal events, the DECOR enhancement was built consisting of streamer tube chambers at the sidewalls of the detector. The high sensitivity on horizontal air showers and muon bundles makes this detector unique to analyze atmospheric muons and the Muon-Puzzle. Next to the measurement of atmospheric air showers, NEVOD can detect neutrinos selecting upward-going events.

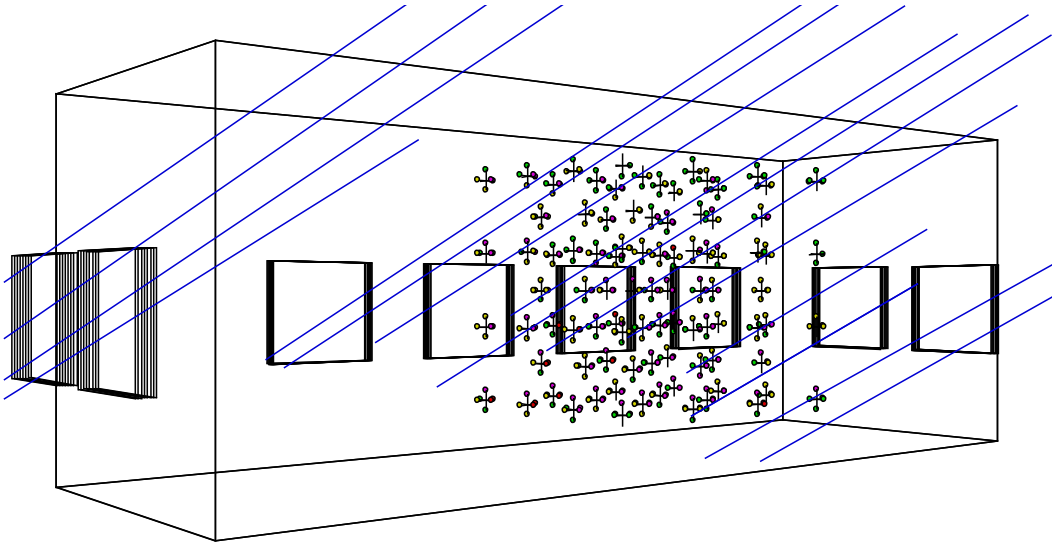

Figure 3.2: Sketch of the NEVOD-DECOR detector consisting Quasi-Spherical-Modules. [Bog18]

Another field of research detecting atmospheric muons with applications outside of the particle physics is the muon tomography. Using the attenuation of the muon flux that varies between different materials, larger volumes of unknown material can be detected. Application areas are the detection of varying magma chambers leading to a prediction of an eruption sequence of a volcano [Tan+09] or the detection of an

unknown chamber in the Cheops pyramid [Mor+17]. Further applications are the measurement of large-angle Coulomb scattering to detect materials with high atomic numbers [Bor+03]. Those detectors consist of several layers of plastic scintillators with the size of some m^2 each passing the light to an SiPMs to track the number of muons and their direction. An overview of the current muon imaging tools is reviewed in [BDG20].

So far, only experiments at the surface have been discussed measuring the muonic shower component as part of the signal or the main signal. For most experiments located deep underground atmospheric muons are considered as background and not used to study cosmic ray physics, but to search for rare events like proton decays or Dark Matter interactions. An exemplary detector for Dark Matter is the PICO detector [Amo+19] in the Sudbury mine in Canada 2 km below the surface, which equals 6 kmwe. Inside a pressure vessel with a diameter of 60 cm and a height of 167 cm superheated liquid C_3F_8 is used to measure small recoil energies (1 keV to 100 keV) induced by elastic scattering of Weakly Interacting Massive Particles (WIMPs), a candidate for Dark Matter. The main background limiting the sensitivity is not the atmospheric muons themselves, but the neutrons produced in interactions near the detector after propagating all the way down. For these types of experiments, a precise description of the angular and energy distribution of the muon flux is crucial, especially the probability to reach those depths for inclined muons traveling even greater distances through the rock. Therefore, the physical models need to be calculated and simulated with high precision, even for the edge cases of the stochastic propagation. An exemplary detector for proton decay was the Fréjus-Detector [Dau+95] located 4800 mwe under the Col du Fréjus. The calorimetric detector of the size () used iron to track particle interactions inside the detector. Although a proton decay had not been measured, atmospheric muons had been used to create a depth curve and also the energy spectrum of atmospheric neutrinos had been unfolded.

3.3 Neutrino Detectors

Besides the NEVOD Detector, most neutrino detectors are located deep underground to exclude the dominating background of atmospheric muons. The low interaction rate of neutrinos is on the one side an advantage as it increases the observable horizon and let them propagate even through dense media like the core of the earth. On the other side, this makes them challenging to detect and a large volume of detector material is required. Due to the steep power-law dependence of the energy flux the energy range of the neutrinos scales with the size of the detection volume. Four main types of neutrino telescopes have been established so far.

3.3.1 Types of Neutrino Telescopes

An exemplary detector in the neutrino energy range from MeV to 10 GeV is the Super-Kamioka Neutrino Detection Experiment [Abe+18] located in a former mine 1 km deep underground in Japan. It consists of a cylindrical tank with 40 m in diameter and height filled with 50 kt of purified water. The Cherenkov light produced by particles interacting inside this tank is measured with 13 000 PMTs positioned at the walls. This peripheral detector type is used, since the absorption length of the Cherenkov radiation is larger than the detector size. Similar structures for this energy range are SNO [And+21], BOREXINO [Ali+09] and JUNO [Cao+19], all located deep underground with several kt of liquid and transparent detector material, water or liquid scintillator and the PMTs at the walls.

To detect neutrinos with energies above 10 GeV larger detector volumes with an effective radius of $\mathcal{O}(100\,\mathrm{m})$ are required. These volumes can just be reached by using natural resources and placing the detectors inside the water, i.e. glacial ice, deep lakes or the sea. Those distances exceed the absorption lengths of the Cherenkov light for water and a lattice structure of the detector is used. Currently, the largest and most sensitive detector is the IceCube Neutrino Observatory at the South Pole with a detection volume of a cubic kilometer, which is further described in section 3.3.2. Inside a detection volume of a cubic kilometer, the Cherenkov light produced by neutrinos or atmospheric muons is measured with around 5000 PMTs. Therefore this type of telescope is labeled *Cherenkov Neutrino Telescope*. Further neutrino telescopes using the detection principle like IceCube are the ANTARES/Km3Net [Age+11; Adr+16] experiment in the Mediterranean sea, the Baikal/GVD in Lake Baikal [Bel+97; Avr+19] and the P-ONE experiment in the Cascadia Bassin in front of Vancouver [Ago+20]. Compared to IceCube these telescopes are all upgrading to a volume of a cubic kilometer, are all located in the northern hemisphere and all use liquid water as detection volume. Although the detection media is always water-based, the propagation of the Cherenkov light mainly described by the scattering and absorption differs significantly, as shown in Table 3.1. While a strong absorption leads to the loss of photons and worse energy measurements, a strong scattering delays the photons and leads to a loss of directional information.

With this type of neutrino telescopes neutrinos with energies up to 10 PeV can be measured. Also with the planned IceCube-Gen2 detector increasing the size by a factor of ten [Aar+21] the expected flux of the highest energetic neutrinos is too low to be detectable. However, similar to the Pierre-Auger Observatory a maximum size of this type of detector is reached with Gen2. To detect even higher energetic neutrinos and analyze the predicted cosmogenic neutrinos, detectors measuring the radio signal are under development. Because of the long wavelength, these radio

Table 3.1: Characteristic lengths of absorption λ_{abs} and scattering λ_{scat} for selected locations with a Cherenkov-based neutrino detector. For detectors in liquid water, the range indicates the seasonal variation. The scattering lengths are corrected for the average Mie-Angle of the medium $\lambda_{\text{eff}} = \lambda_{\text{scat}}/(1 - \langle\cos\theta\rangle)$. [Bot16]

Location	Depth / km	λ_a / m	λ_{eff} / m
Lake Baikal	~ 1	22	150-400
Mediterranean Sea	> 1.5	40-70	200-400
South Pole	$1.5 - 2$	110	25
South Pole	$2 - 2.5$	220	47

pulses can propagate several kilometers through the ice. Therefore these detectors can be placed sparsely and cover a cubic kilometer with just a single station. There are currently two attempts to build a Radio-Neutrino Detector; one as part of IeCube-Gen2 in the Antarctic Ice and another one on Greenland [Agu+20].

Another approach to measure neutrinos is looking for showers coming from Earth as just neutrinos can propagate through the Earth. The ANITA experiment consists of radio antennas on a balloon. During the flights around the Antarctic circle, it measures the radio signals coming from the Earth. Pierre Auger is looking for showers going upward for extremely inclined showers. If they measure not just the muon component but also the electromagnetic shower inside their surface detectors, the shower must have started deep inside the atmosphere, which only neutrinos can create. HAWC looks at showers coming from neighboring mountains and MAGIC looks at the Atlantic if the view to the stars is not clear but the view to the sea. Both again looking for a hadronic shower, only Tau Neutrinos can produce. For all these experiments again atmospheric muons are the dominant background by orders of magnitudes. Therefore an accurate description for all energies and energy losses is crucial to cover also the edge cases in the simulations.

3.3.2 IceCube Neutrino Observatory

The biggest neutrino telescope is the IceCube detector located at the geographic south pole, shown in Figure 3.3a. On a hexagonal grid of a square kilometer, 78 Strings are drilled into the glacial ice with a string distance of 125 m. Each string contains 60 Digital Optical Modules (DOMs) equally placed between a depth of 1500 m and 2500 m. Each DOM contains a Photomultiplier looking downward and

measuring the emitted Cherenkov light of muons and neutrino interactions. The surrounded detection volume contains a cubic kilometer of ice measuring neutrino energies between 100 GeV and 10 PeV. For higher energies, the event rate is too small and for lower energies, the string spacing is too large.

In the middle of IceCube 8 Strings, each with 60 DOMs of higher quantum efficiency are placed more densely together. This extension called "DeepCore" decreases the lower threshold for neutrino energies to 10 GeV and uses the rest of IceCube as a veto region. Another extension is "IceTop" where a water Cherenkov tank is placed at the surface of each string. This can either be used as an air shower detector at an altitude of 3 km with the benefit of IceCube as a further muon detector to deeper analyze the atmospheric muons. On the other side, it works as a veto for IceCube to distinguish down-going neutrinos from atmospheric muon events as the neutrinos should not be seen in IceTop.

There are currently plans for an extension of IceCube named IceCube-Gen2 [Aar+21]. The planned detector is shown in Figure 3.4. An extension called "IceCube-Upgrade" has already been funded to test new types of DOMs for Gen2. Gen2 will enlarge the detected volume to 8 km^3 and will be placed around IceCube. In contrast to IceCube, the Strings in Gen2 will be organized on a sunflower structure avoiding corridors where muons can sneak inside the inner volume and mimic a starting event. Besides, a radio detector is planned, placing the antennas on a grid with an inner distance of a kilometer covering an area of 100 km^3 to analyze the cosmogenic neutrinos.

A distinct astrophysical neutrino source has also not been measured yet as well as a class of sources in a stacked search [Aar+20b; Aar+17]. However, a coincidence of a high energy neutrino event originating from the same direction as an AGN flaring at the same time in the gamma energy region is the first hint of a possible neutrino source [Aar+18a; Aar+18b].

Event Signatures

The measured event signatures are mainly divided into tracks and cascades. A long track signature of an atmospheric muon bundle is shown in Figure 3.3b. Tracks are long, nearly straight lines along the muon path with the energy losses along the track producing the track signature. Due to their long range, they can be further classified into starting, stopping, through-going and corner clippers. Only neutrinos can produce starting events and stopping events can only be produced by a huge stochastic loss, which happens rarely or by low energetic muons. Most-often, muons propagate through the detector producing a long path along their track. There is

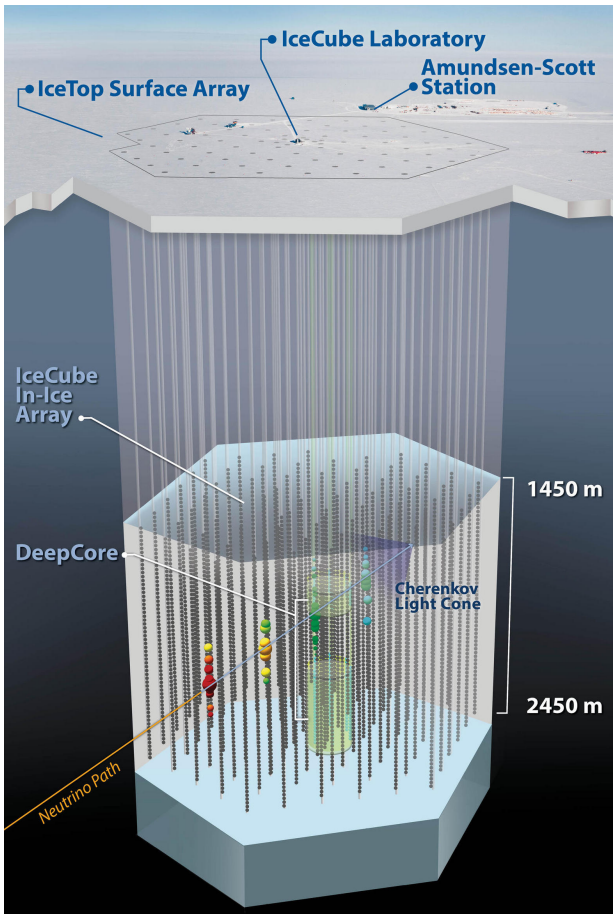

(a) Sketch of the IceCube facilities at the South Pole and how an event view of a muon neutrino could look like. [Ice20]

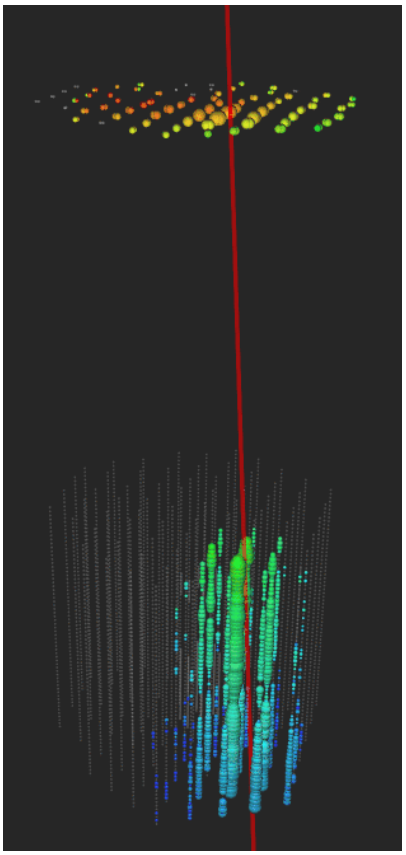

(b) Event view of a measured cosmic ray event in IceTop and IceCube on 02.07.2010 with a reconstructed primary particle energy of 300 PeV. [Ice20]

Figure 3.3: The IceCube Neutrino Observatory including the IceTop Array at the surface, the main in-ice detector and the DeepCore extension. For the event views, each colored circle indicates a DOM that measured light. The color ranges represents the time from red, early to blue, late. The size of the DOMs scales with the amount of detected light.

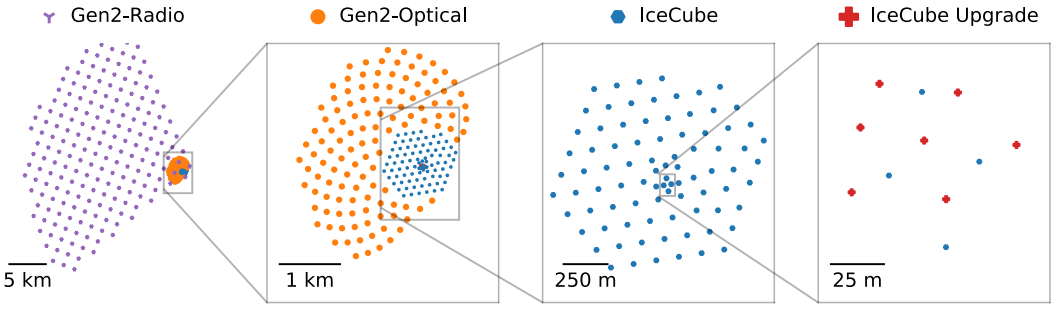

Figure 3.4: Schematic top view of the IceCube detector compared to the enhancements for Gen2. [Aar+21]

however the special case of a corner clipper, that can mimic a cascade-like event at the edge of the detector.

A particle shower created by a single particle interaction (or multiple interactions inside a small range of less than 10 m, which is pint-like for IceCube), produces a rather spherical spread of the produced Cherenkov light. Although the particle cascade is boosted in the forward direction with just small transversal momentum and a Molière radius in the ice of 10 cm [Zyl+20], the small scattering length creates a spherical propagation of the produced Cherenkov light.

NC-interactions of all neutrino flavors have just a visible hadronic shower, as the incoming and outgoing neutrino doesn't produce a signal, thus producing a single cascade. Regarding CC interactions and starting with the electron neutrino, the additional electron loses most of its energy in less than 10 m in the ice. As this distance is point-like for IceCube, the resulting cascade also has a spherical structure. Although there are differences in the shower developments of electromagnetic and hadronic cascades, especially through the later decays of neutral hadrons, it was not possible yet to distinguish between electromagnetic and hadronic cascades [Ste17].

The greater mass of muons compared to electrons makes them lose their energy much slower and let them travel several kilometers through the ice. From the hadronic cascade at the neutrino interaction vertex, a long track is going out. Therefore muon neutrinos do not have to interact inside the detection volume and can also interact far before the detector with the muons traveling inside, increasing the effective detector volume.

Tau leptons have an even higher mass compared to the muons and have therefore a smaller energy loss resulting in a thin propagation track. But the small lifetime of 290 fs makes them decay directly or for higher energies let them just travel 50 m per PeV. The event signature depends on the decay channel; two-thirds are the

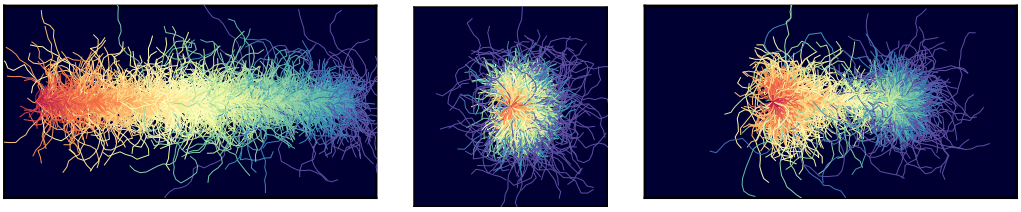

Figure 3.5: Simulated paths of the produced Cherenkov photons for the three major event signatures of a through-going muon (left) an electron neutrino (middle) and a tau neutrino (right). The color represents the time from red (early) to blue (late). [Aar+18c]

hadronic decay channel and the last third is equally distributed between the muonic and the electronic channel. Until energies of around 10 TeV the second hadronic or em-cascade can not be distinguished from the first hadronic cascade at the neutrino vertex. For higher energies first, a double pulse waveform at a single DOM can be registered and later these two cascades get separated more clearly and a double cascade or double bang signature is created. These three major event signatures are shown in Figure 3.5.

The muonic tau decay also contributes to the amount of incoming muons starting before the detector. For events starting inside the detector, the outgoing track is smaller compared to the hadronic cascade as the additional neutrinos from the tau decay take away some energy. For higher energies, the thin tau track goes over to a brighter muon track. But these differences in the track signature can just be separated statistically for many events and not on an event level due to the stochasticity of the propagation. Due to the limited resolution, there has been just one promising tau neutrino event seen with IceCube after 10 years of measurement [MS19; Abb+20a].

Event selections

The main interesting features to be reconstructed are the primary particle type, its energy and the direction. To extract the primary particle type a classification of the different event signatures is required. For these selections, multivariate methods are required since the atmospheric muon rate of 1 kHz, is many orders above the atmospheric neutrino rate of 1 mHz or the astrophysical neutrino rate of 1 µHz.

A pure **cascade sample** contains mostly CC interacting electron neutrinos, fewer NC events and a few tau neutrinos. Cascade searches [Aar+20a] uses the outer DOM layers as veto region against through-going muons, which have a detection rate

that is multiple orders of magnitudes higher. But even in DeepCore, muon tracks are contaminating the cascaded selections when traveling in the middle between the strings due to the lattice structure. Also, the stochasticity of the propagation processes, allowing muons to travel without visible losses and then deposit all of their energy in a catastrophic loss inside the detector limits the selection efficiency. As these processes are rare, an accurate description of the muon physics even at the tails or edges of the total and differential cross section is needed. These selection methods are not just valid for cascades, but all kind of starting events.

The tracks are further separated between up-going and down-going tracks. Down-going events are most-often atmospheric muons reaching the detector as bundles with a lateral distance of some meter between them. Those events are seen as one thick, bright track due to the limited resolution preventing a separation of the single muons from a bundle. Therefore those muon bundles are in principle of limited usefulness since the number of muons and their energy is not reconstructible. An approach to analyzing atmospheric muon bundles is the search for a **leading muon** containing most of the bundle energy [Fuc16a; Fuc16b; Wer17]. A bundle of many low energetic muons creates a bright track with a continuous energy loss. Leading or single muons have higher stochasticity, e.g. with a huge bremsstrahlung loss resulting in a thinner track with brighter cascades along it. As these muons are produced in one of the first interactions of the air shower they can provide further insights into the particle processes in the atmosphere.

Another approach to use atmospheric muons is using **stopping muons** [Hoi17; Nin19]. They are most-often single muons and have energies of just several 100 GeV when entering the detector. At these energies, they are in the regime of the minimal Ionization and can be used to calibrate the detector and measure systematic parameters. For stopping muons, also the range they have traveled through the ice is known which is an approximation of their energy at the surface. Therefore they can also be used to study cosmic ray and air shower physics, but in comparison to the leading muons for higher energies, stopping muons provide insights at lower energies.

Up-going muon tracks can only be neutrino-induced muons as muons cannot propagate large distances through the earth. Unfortunately, a simple extraction of these muons with a zenith cut is not satisfying as the resulting sample is still dominated by mis-reconstructed muons. Although the directional resolution is high for tracks, sometimes it can exceed 5° and contaminate the sample. Therefore advanced machine learning algorithms are used to extract a purified sample [Ste19]. The filtered track events are an ideal single muons sample at all energies; good to analyze the muon physics, e.g. the energy loss profile. Just for the starting events, the hadronic cascade of the neutrino interaction contaminates a little bit.

Event Reconstruction

After the selection, the energy and directional reconstruction is the remaining step before analyzing the desired event sample. An overview of the standard reconstruction methods is given in [Ahr+04; Aar+14]. In recent years also modern, machine-learning-based methods using e.g. Deep Neural Networks have been developed increasing the accuracy of the reconstruction [Hue17a; Hue17b; Hue18; Abb+21a]. A comparison of the standard and neural network approaches for the reconstructions is shown in Figure 3.6 as well as their energy dependence.

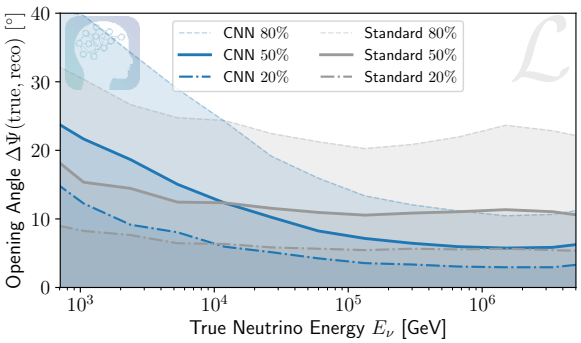

(a) Resolution of the angular reconstruction for cascades comparing the standard likelihood approach with a Neural Network (CNN). [Abb+21a]

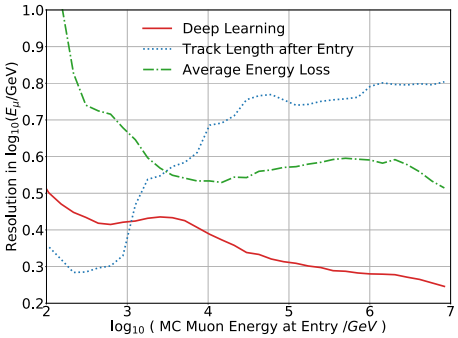

(b) Resolution of the energy reconstruction for tracks comparing the standard $\mathrm{d}E/\mathrm{d}X$ and track length approach with a Deep Neural Network. [Hue17b]

Figure 3.6: Energy dependence of the resolution of the challenging reconstruction parameters in IceCube. On the left the angular reconstruction for cascades and on the right the energy reconstruction for tracks is compared between modern neural network approaches and the default likelihood approaches.

The directional resolution for tracks is comparably high (0.5°) while being low for cascade events (15°). Regarding the energy reconstruction, it's the other way round. When a cascade is contained inside the detector the energy resolution is high due to the calorimetric measurement resulting in an uncertainty of 10 %. For through-going tracks, just a portion of the muon energy loss is deposited inside the detector For muons above a TeV the energy is reconstructed using the average energy loss per distance $\mathrm{d}E/\mathrm{d}X$, which increases nearly linear with the muon energy (c.f. section 4.1). Therefore, the track inside the detector is split into multiple segments and the high energetic, stochastic losses are cut away to extract the continuous energy loss. Since the linear dependency of the average energy loss on the muon energy starts at around a TeV, while being independent for lower energies, this can only be applied at energies above a TeV. For starting tracks, the energy resolution of the muons and

neutrinos improves, due to the additional information of the hadronic cascade at the vertex. For low energy muons, the average energy loss is not proportional to the muon energy. As these muons are most-often stopping inside the detector, the track length can be used to reconstruct the energy.

Next to the energy and direction, also the energy losses along a muon track can be reconstructed, which is important for analyses depending on the stochasticity, e.g. when creating a leading muon sample. Since IceCube cannot distinguish between single energy losses, the track inside the detector is split into multiple segments as for the $\mathrm{d}E/\mathrm{d}X$ energy reconstruction and the energy loss in each segment unfolded. This is just sensitive to high stochastic energy losses and can be used to study the energy loss profile of the muons.

Systematic Uncertainties

The remaining task, an analysis has to consider, are systematic uncertainties. In every experiment, some remaining parameters are challenging to calibrate or measure and have uncertainties that are non-negligible for analyses. For the IceCube detector, one main systematic parameter is the quantum efficiency of the DOMs, short DOM efficiency. This varies the amount of detected light and has an uncertainty of $\pm 5\,\%$. However, in this factor multiple uncertainties are combined, all scaling the amount of detected photons and which cannot be distinguished from each other. Also cross-section uncertainties may be an origin, why this factor is not equal to 1.

The other main uncertainties are the ice properties, mainly the absorption and scattering lengths, which are depth-dependent. The depth dependence does not originate due to the different levels of pressure and thus temperature, but due to several layers of dust [Ack+06; Aar+13]. Especially in the middle of the detector at a depth around 2 km the absorption length is significantly decreased and nearly all photons get absorbed before reaching a DOM. This blind layer is slightly indicated in Figure 3.3b. Further systematics of the glacial ice like the anisotropy are discussed in detail in [Ron19].

Next to these detector and ice properties, further sub-dominant systematics arise due to the theoretical uncertainties of the physical processes. Regarding the muon physics, the uncertainties of the cross sections needs to be differentiated between the processes dominant for the low energy losses and processes dominating the high, stochastic energy losses. While an increase of the low energy losses can already be compensated by an increase in the DOM efficiency, the uncertainties of the stochastic energy losses have not been considered, yet. Since the stochasticity of the

muon affects the performances of separating leading muon, cascade or tau samples, an approach to include them is analyzed in this work.

One of the largest systematic uncertainties is the flux of atmospheric neutrinos, which is often the limiting factor for the sensitivity of analysis. This can be avoided using e.g. an unfolding approach, which is independent of the flux model used in the simulations. However, if this is not feasible, the uncertainty of the flux needs to be taken into account, e.g. by using the so-called Barr parameters [Bar+06].

To take into account all of these systematics, simulation sets each varying one or two systematic parameters on a grid and interpolations between these grid points were used in analyses. However, this grid approach increases the number of required simulation sets for every further systematic parameter resulting in the curse of dimensionality. There is now a new approach [Aar+19] where for each simulation run a new set of all systematic parameters is sampled from their uncertainty distribution, including correlation. With this Monte-Carlo approach, the phase space can be filled also when including further systematics.

4 Muon Interaction

The muon cross-sections described in this chapter focus on muons above a GeV and the relevant processes for the simulation of astroparticle experiments. These processes are all included in the simulation library PROPOSAL or are intended to be included in the future. In principle, they are also valid for the other charged leptons, electrons, and taus, if not stated differently.

All cross-sections σ are differential in the energy loss v relative to the energy of the primary particle E, given as $\mathrm{d}\sigma/\mathrm{d}v$ or as the average energy loss over distance X

$$\left\langle -\frac{\mathrm{d}E}{\mathrm{d}X} \right\rangle = \frac{N_A}{A} E \int v \frac{\mathrm{d}\sigma}{\mathrm{d}v} \mathrm{d}v. \tag{4.1}$$

The cross-sections are also given in a generalized form for particles with mass M and charge z. Mainly the natural unit system is used with the symbolic definitions listed in Table 4.1.

Table 4.1: Definitions of the symbols used in this thesis, unless stated otherwise or mentioned explicitly.

Symbol	Definition
c_0	Speed of light in vacuum ($= 1$ in n.u. and $\approx 3 \times 10^8\,\mathrm{m\,/\,s}$ in SI units)
N_A	Avogadro constant ($\approx 6 \times 10^{23}\,/\,\mathrm{mol}$)
α	Fine structure constant ($\approx 1/137$)
$m_{e,\mu,\ldots}$	Mass of a particle with the lower index defining the particle type
$r_{e(\mu)}$	Classical electron (muon) radius ($r_e \approx 2.8\,\mathrm{fm}, r_\mu = r_e {}^{m_e}\!/_{m_\mu}$)
E, p	Energy and momentum of a particle with $E^2 = p^2 + m^2$
β, γ	Lorentz factors in relativistic approximation, $\beta = p/E$ and $\gamma = E/m$
M, z	Mass and charge of the primary particle to propagate
Z, A	Number of protons (nucleons) in the target nucleus
K	Ionization constant $4\pi N_A r_e^2 m_e \approx 0.3\,\mathrm{MeV\,cm^2/mol}$
X_0	Radiation length of a medium (c.f. 5.2.2)
q, Q^2	4-momentum of the virtual photon exchanged with a nucleus
$B_{(\mathrm{in})\mathrm{el}}$	(in)elastic radiation logarithm constant of the screening (section 5.2.2)

An overview of the energy loss of muons is shown in Figure 4.1 which is divided into four areas in energy. At the lowest energies ($\beta < \alpha$) the velocity of the muons is smaller than the velocity of the valence electrons. Non-ionizing losses mainly driven by nuclear recoil are the main process for $\beta \ll \alpha$ before ionizing energy losses increase proportionally to the velocity of the muon [GMS01]. The energy region between $\alpha < \beta < 0.1$ is not yet theoretically well understood and only empirical models are used to describe these energy losses [GMS01]. For both low energy regions, the data in Figure 4.1 are taken from pion and proton tables in [Ber+93] and scaled according to the mass ratios to the muon. Both regions also differ between μ^+ and μ^- since the latter is likely to get captured into atomic orbitals, quickly cascading down into the 1s orbital and then decay or weakly interact with the nucleus (c.f. [Mea01]).

For $\beta > 0.1$, the ionization and excitation losses are well described by the Bethe-Bloch theory. The energy loss decreases to a minimum ionization point, a characteristic energy for a medium at around a GeV before it starts increasing logarithmically with the energy. The radiative losses, i.e. bremsstrahlung, pair production, and inelastic nuclear interaction, increase linearly with the energy surpassing the ionization losses at a TeV and dominating the energy loss at high energies. Initially, the inelastic nuclear interaction is just a 10 % correction compared to the other two processes, but increases slightly quicker and surpassing the other two even before the LPM-effect limits them, which occur between PeV and ZeV energies and is therefore not included in Figure 4.1.

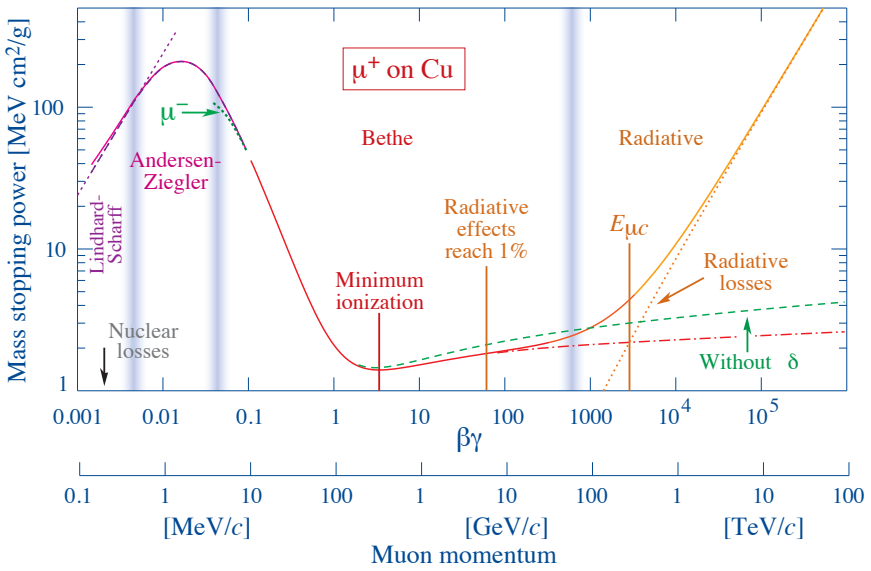

Figure 4.1: Average energy loss of muons in copper. [Zyl+20]

4.1 The average Energy Loss

At energies above a GeV, muons lose their energy via four main interaction types, ionization, e^+e^- pair production, bremsstrahlung, and inelastic nuclear interactions, which is often referred to as photonuclear interaction. While the ionization is nearly constant and just increases logarithmically with the energy, the other three processes increase linearly with the energy surpassing the Ionization at around a TeV, depending on the medium. This behavior can be visualized in the average energy loss in Figure 4.1. Besides the four main interactions, there are further processes with just minor influence on the energy loss, but also important for the muon propagation, the $\mu^+\mu^-$ pair production, and the weak interaction. Regarding the decay, the muons have a relatively long lifetime of around 2.2 µs [Zyl+20]. They usually lose nearly all of their energy, slow down that the μ^- even get absorbed by an atom and decay with a total energy of almost their rest mass. Therefore, the decay process does also not contribute to the energy loss as indicated in Figure 4.2a.

As the weak interaction and the decay are purely stochastic processes and have no continuous energy loss, their contribution in Figure 4.2a is adapted. For both the decay and the weak interaction, the average energy loss is indicated by multiplying the energy times the total cross-section. Using the mean lifetime τ, the cross-section for the decay is defined by

$$\sigma_{\text{decay}} = \frac{1}{\beta\gamma\tau c_0}. \tag{4.2}$$

The sum of the energy loss can be parameterized using a quasi-linear approximation

$$\left\langle -\frac{\mathrm{d}E}{\mathrm{d}X} \right\rangle = a(E) + b(E) \cdot E. \tag{4.3}$$

Thereby, the functions a and b only depend logarithmically on the energy, while a is mainly defined by the Ionization and b by the three radiative processes.

Assuming a and b as constant values, the average range of the muons can be approximated by

$$R_{\langle -\frac{\mathrm{d}E}{\mathrm{d}X} \rangle} = \frac{1}{b} \ln\left(1 + \frac{b}{a}E\right). \tag{4.4}$$

This simple linear model, shown in Figure 4.2b, already provides a rough description of the muon energy loss and range and is used in many applications as a first estimation of the muon contribution. A comparison with more precise calculations of the range using Monte-Carlo techniques is shown in Figure 5.9.

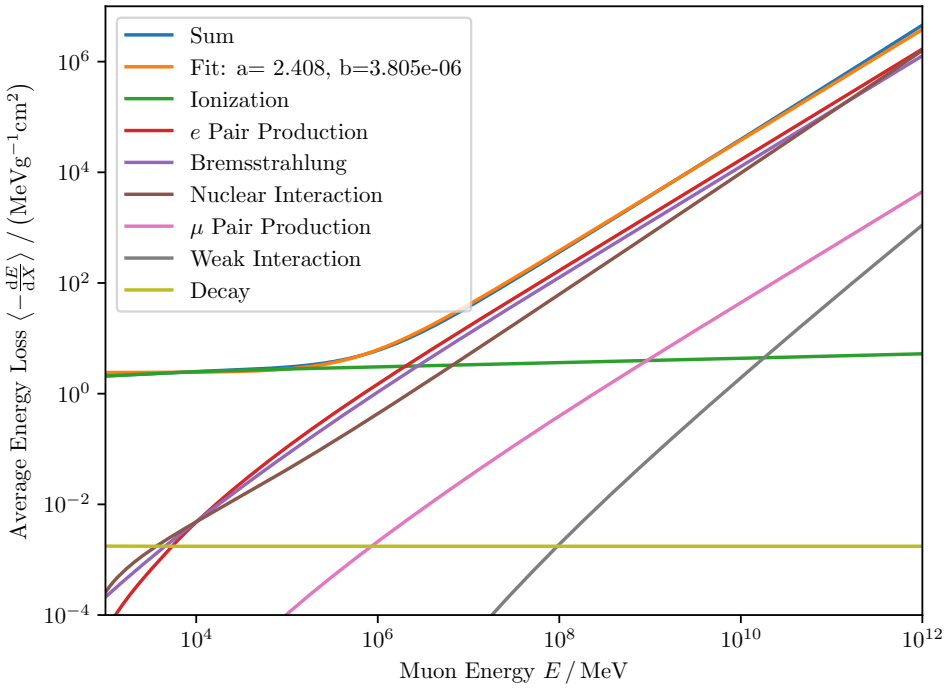

(a) The average energy loss of muons.

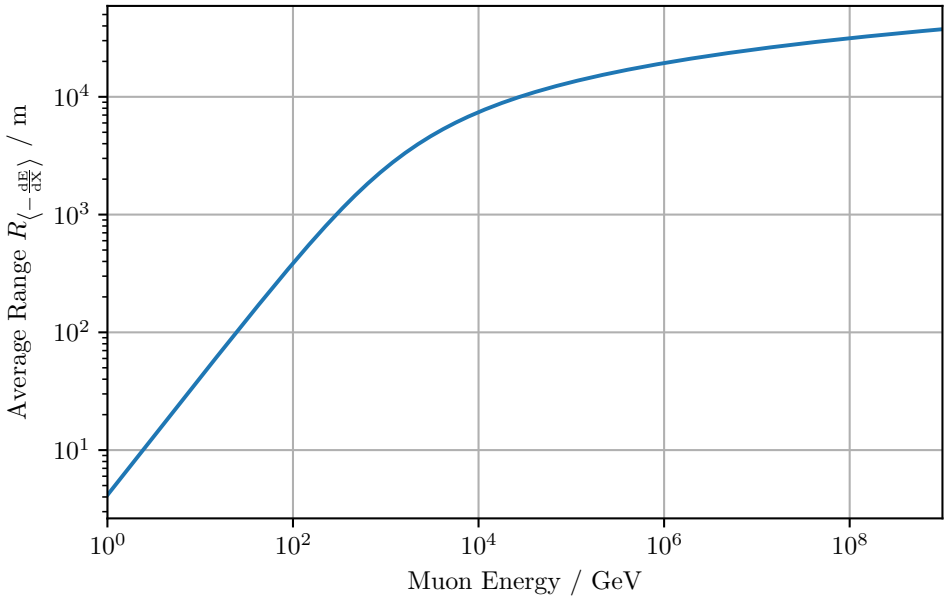

(b) The average range of muons using the $\langle -\frac{dE}{dX} \rangle$ fit.

Figure 4.2: The average energy loss and range of muons in Standard Rock ($Z = 11, A = 22$) using the linear approximation in 4.3. The fitted values are then used to calculate the average range given by 4.4. The contribution of the decay and the weak interaction to the "continuous energy loss" is described in the text.

4.2 Ionization

The ionization describes the release of an electron from the atomic shell, producing an ion. Regarding the muon cross-sections, the excitation of an atom and the scattering at atomic electrons are included in the wider meaning of Ionization. In contrast to all other interactions, the ionization is given as differential cross-section, but also in the average energy loss, since the density effect can only be included in the average energy loss.

The differential cross-section describing the knock-on electrons was mainly derived by Bethe [Bet30] and combined with further corrections into an expression by Rossi [Ros52].

$$\frac{\mathrm{d}\sigma}{\mathrm{d}v} = \frac{1}{2} K z^2 \frac{Z}{A} \frac{1}{(\beta E v)^2} \left[1 - \beta^2 \frac{v}{v_{\max}} + \frac{1}{2} \left(\frac{v}{1 + 1/\gamma} \right)^2 \right] \tag{4.5}$$

The $1/v^2$ dependency already indicates that this cross-section is responsible for the lower energy losses. The maximum energy transferred to the electrons is given by [Zyl+20]

$$E v_{\max} = \frac{2 m_e \beta^2 \gamma^2}{1 + 2\gamma \frac{m_e}{M} + \left(\frac{m_e}{M}\right)^2}, \tag{4.6}$$

which is an analytic interpolation between the approximations of the extreme scenarios at low and high energies

$$E v_{\max} = \begin{cases} 2 m_e \beta^2 \gamma^2, & \text{for } 2\gamma m_e \ll M \\ M \beta^2 \gamma & \text{for } 2\gamma m_e \gg M. \end{cases} \tag{4.7}$$

According to (4.1) the average energy loss is obtained by integrating (4.5) between

$$v_{\min} = \frac{1}{2 m_e E} \left(\frac{I_{\text{excit.}}}{\beta\gamma} \right)^2, \tag{4.8}$$

and a v_{up} located between the limits. Including the correction of the density effect δ, this results in

$$\frac{\mathrm{d}E}{\mathrm{d}X} = z^2 \frac{Z}{A} \frac{K}{2\beta^2} \left[\ln \frac{2 m_e \beta^2 \gamma^2 E v_{\text{up}}}{I_{\text{excit.}}^2} - \beta^2 \left(1 + \frac{v_{\text{up}}}{v_{\max}} \right) + \left(\frac{v_{\text{up}}}{2(1 + 1/\gamma)} \right)^2 - \delta \right] \tag{4.9}$$

with $I_{\text{excit.}}$ the mean excitation energy of the medium. The reason for integrating to v_{up} instead of $v_{\max}$ is due to the energy loss cut, described in section 5.2.6, that is necessary for the simulations.

The density effect describes the reduction of the ionization due to the polarisation of the medium, which has an increasing effect at higher energies, indicated in Figure 4.1. This is not included in the differential cross-section as it is a purely continuous energy loss process and not a stochastic interaction. Depending on the energy parameter $x = \log_{10}(\beta\gamma)$, it is parameterized in [Ste52]

$$\delta = \begin{cases} \delta_0 10^{2(x-x_0)}, & \text{for } x < x_0 \\ 2\ln 10x + c + a(x_1 - x)^b, & \text{for } x_0 \leq x \leq x_1 \\ 2\ln 10x + c & \text{for } x_1 \leq x \end{cases} \tag{4.10}$$

The density constants $\delta_0, x_0, x_1, a, b, c$ as well as the excitation energy $I_{\text{excit.}}$ are specific constants for each medium and defined in [GMS01]. For selected media that are implemented in PROPOSAl, these constants are listed in Table 4.2.

Table 4.2: The excitation energy and further density correction parameters for selected media mainly used in PROPOSAL. [GMS01]

Medium	$I_{\text{excit.}}$	x_0	x_1	a	b	$-c$	δ_0
Air	85.7	1.7418	4.2759	0.109 14	3.3994	10.5961	0
Water	79.7	0.2400	2.9004	0.091 16	3.4773	3.5017	0
Ice	79.7	0.2586	2.8190	0.091 16	3.4773	3.5873	0
Standard Rock	136.4	0.0492	3.0549	0.083 01	3.4120	3.7738	0
Iron	286.0	−0.0012	3.1531	0.146 80	2.9632	4.2911	0.12
Uranium	890.0	0.2260	3.3721	0.196 77	2.8171	5.8694	0.14

The inelastic bremsstrahlung on atomic electrons when the atomic electron emits the bremsstrahlung, described in section 4.3.3, is most often considered as an ionization loss since the atom also gets ionized. While the main bremsstrahlung cross-section has an energy loss behavior of $1/v$ the so-called e-diagrams (see the Feynman diagram in Figure 4.6b) have a sharp energy loss spectrum of $1/v^2$, shown in (4.25), similar to ionization.

The differential cross section of the ionization processes is shown in Figure 4.3a mainly showing the $1/v^2$ dependency and a flattening of the e-diagram bremsstrahlung to small energy losses due to the parametrization. In Figure 4.3b the average energy loss of the two contributions and the additional density correction are shown.

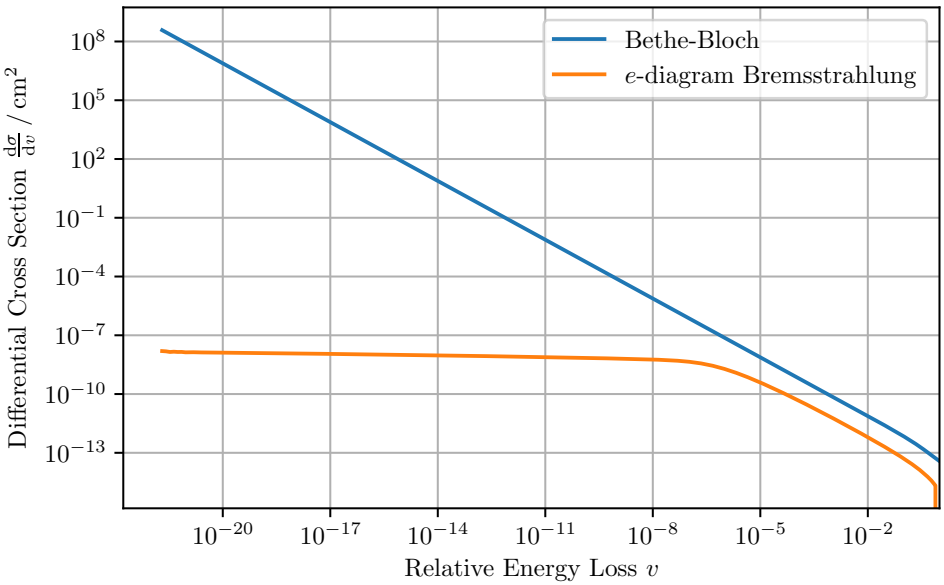

(a) The differential cross section of the ionization processes at 1 TeV.

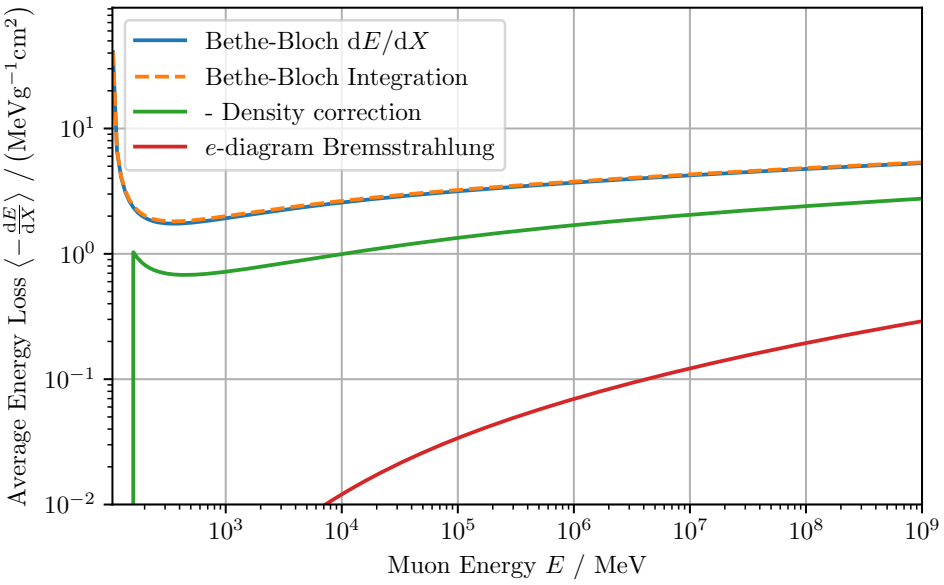

(b) The average energy loss of the ionization processes.

Figure 4.3: The Ionization cross-section of muons in Standard Rock ($Z = 11, A = 22$). The Bethe-Bloch term is compared to the inelastic interaction on atomic electrons with the electrons emitting a bremsstrahlung photon (e-diagram) and the negative contribution of the density correction.

4.3 Bremsstrahlung

The Bremsstrahlung process, where the muon emits a photon and exchanges the remaining momentum with a nucleus in an elastic process, can be visualized in the Feynman diagrams in Figure 4.4.

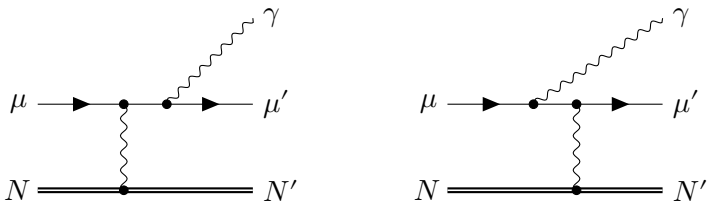

Figure 4.4: The two Feynman diagrams of a muon emitting a Bremsstrahlung photon and exchange a momentum with a nucleus are shown, differing in the order when the photon to the nucleus and the bremsstrahlung photon couples to the muon line.

A general expression of the cross-section was first derived in [BH34a]

$$\frac{\mathrm{d}\sigma}{\mathrm{d}v} = \frac{\alpha}{v}\left(2z^2 Z r_e \frac{m_e}{M}\right)^2 \left[(2-2v+v^2)\Phi_1 - \frac{2}{3}(1-v)\Phi_2\right], \tag{4.11}$$

with the screening functions Φ_1 and Φ_2 described later. The two main behaviors of the cross-section can already be seen here. First, the mass ratio m_e/M explains, why bremsstrahlung is the dominating process of high energetic electrons, that it is still significant for muons and negligible for heavier particles like taus. Second, the flat $1/v$ dependency is responsible for the large stochasticity of the bremsstrahlung interaction since on a logarithmic scale the probability for a small continuous loss is equal to that of a large stochastic loss.

Due to the $1/v$ dependence of the differential cross-section, there is a divergence for small energy losses due to the massless photon, which can be interpreted as an infinite probability to emit a photon with no energy. Although the average energy loss is finite, this is a problem for numerical simulations. In Monte-Carlo simulations, this issue is solved by splitting the calculation of the interaction probabilities into a continuous and stochastic propagation, described in section 5.

The limits on the energy loss for the bremsstrahlung cross-section are

$$v_{\min} = 0 \quad \text{and} \quad v_{\max} = 1 - \frac{3}{4}\frac{M}{E}\sqrt{e}Z^{1/3}. \tag{4.12}$$

While the lower bound for the energy loss is set by the massless photon, the upper bound is in principle just limited by the particle mass $1 - M/E$. However, the part of the Feynman diagram describing the nuclear interaction is just described effectively using approximations. The upper bound is defined by the logarithms in the screening functions, described in section 4.3.1, so the resulting cross-section does not become negative, which would be unphysical. Therefore, the edge of the phase space where the muon loses all its energy to the photon is not described properly, yet. For all calculations described in this section, the assumption of only relativistic particles is used i.e. $M \ll E$.

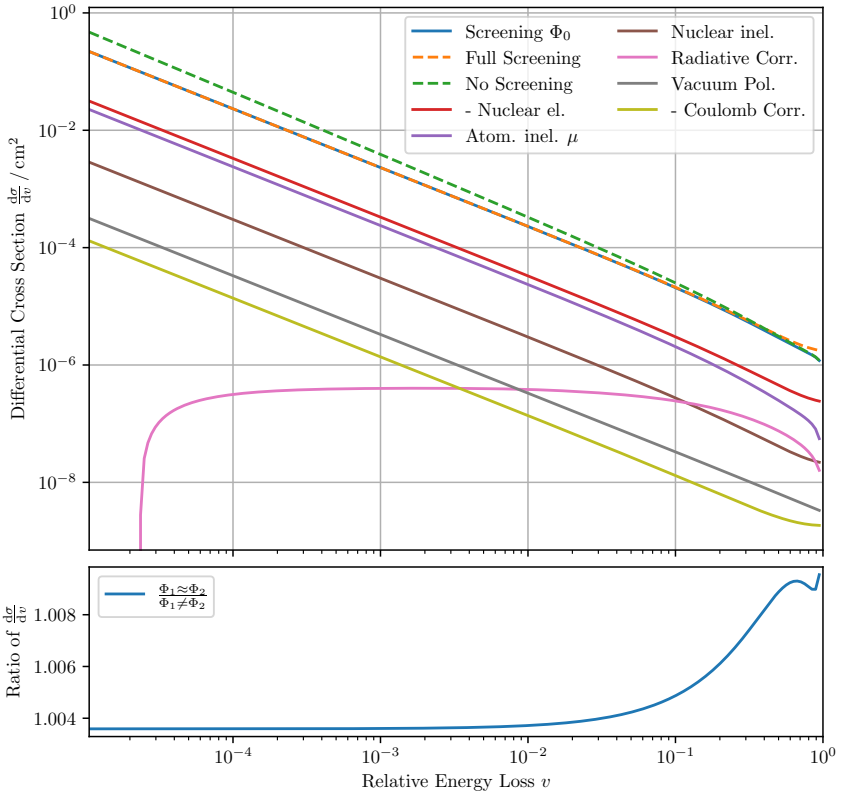

Figure 4.5: Differential cross-section of the muon bremsstrahlung at an energy of 1 TeV in Standard Rock ($Z = 11, A = 22$).

The differential cross-section is shown in Figure 4.5 mainly illustrating the $1/v$ dependency and the relevant processes influencing the cross-section. The following subsections describe these effects contributing including the elastic and inelastic nuclear and atomic form factor as well as the coulomb and radiation correction and finally the matter effects. All these processes do also appear for the pair production

processes. To not duplicate the passages, these effects are mainly described in this section.

4.3.1 Screening Functions for elastic Interactions

The simplest way to describe the nuclear interaction is using a coulomb field of a point-like particle with the charge Z. However, a more advanced approach describes the nucleus of a finite size which is surrounded and screened by atomic electrons. The Fourier transform of the radial charge distribution of the nucleus, called the *nuclear form factor*, is used to include these effects in the screening functions. For the atomic electrons, the corresponding Fourier transform is called the *atomic form factor*. These functions only depend on the minimum momentum transfer to the nucleus given by

$$\delta = \frac{M^2 v}{2E(1-v)}. \tag{4.13}$$

Since the form factors effect different regions of Q^2, the screening functions can be separated into a part Φ^0 at low Q^2 where the atomic form factor dominates and a part Δ at high Q^2 where the nuclear form factor dominates

$$\Phi = \begin{cases} \Phi^0 - \Delta, & Z = 1 \\ \Phi^0 - \Delta(1 - \frac{1}{Z}) & Z > 1. \end{cases} \tag{4.14}$$

Assuming a point-like nucleus the screening functions can be described in the extreme cases of no screening (ns) and full screening (fs) by

$$\Phi^0_{1,\mathrm{ns}} = \ln \frac{M}{\delta} - \frac{1}{2} \qquad \Phi^0_{2,\mathrm{ns}} = \Phi^0_1 \tag{4.15a}$$

$$\Phi^0_{1,\mathrm{fs}} = \ln \left(\frac{M}{m_e} B_{\mathrm{el}} Z^{-1/3} \right) \qquad \Phi^0_{2,\mathrm{fs}} = \Phi^0_1 - \frac{1}{6} \tag{4.15b}$$

An analytical interpolation between these extreme scenarios have been calculated in [San18] using the techniques of [PS68] resulting in

$$\Phi^0_1 = \ln \frac{\frac{M}{m_e} B_{\mathrm{el}} Z^{-1/3}}{1 + \frac{\delta}{m_e} \sqrt{e} B_{\mathrm{el}} Z^{-1/3}} \quad \text{and} \quad \Phi^0_2 = \ln \frac{\frac{M}{m_e} e^{-1/6} B_{\mathrm{el}} Z^{-1/3}}{1 + \frac{\delta}{m_e} e^{1/3} B_{\mathrm{el}} Z^{-1/3}}. \tag{4.16}$$

The interpolated screening together with the extreme scenarios are shown in Figure 4.5 illustrating the relevance of the full screening for small energy losses and the transition to no screening at high energy losses.

For the nuclear form factor a step function can be used according to [Bug77], or more accurate parametrizations like a Fermi distribution, with the step at the critical momentum [KKP95]

$$q_c = \frac{m_\mu e}{D_n} \qquad \text{with} \qquad D_n = 1.54A^{0.27}. \tag{4.17}$$

The correction due to the finite size of the nucleus, decreasing the screening by around 10 %, can be parametrized independent of δ by [ABB94]

$$\Delta_1 = \ln\frac{M}{q_c} + \frac{\rho}{2}\ln\frac{\rho+1}{\rho-1} \quad \text{and} \quad \Delta_2 = \ln\frac{M}{q_c} + \frac{3\rho-\rho^3}{4}\ln\frac{\rho+1}{\rho-1} + \frac{2M^2}{q_c^2} \tag{4.18}$$

with $\rho = \sqrt{1+\frac{4M^2}{q_c^2}}$. This description of the nuclear form factor was calculated regarding muons, especially the fit for D_n. In q_c the muon mass is used explicitly, since $\hbar c_0/m_\mu \approx 2\,\text{fm}$ is an axcellent scaling for nuclear sizes. However, since the influence of the mass of the primary particle is just a small correction to an overall percent contribution, this is also applicable to particles with different mass, like electrons or taus.

The independence of the minimum momentum transfer only breaks at high values of δ near the muon mass. Differences to calculations including this dependency [KKP95] therefore only occur at high energy losses of $v \sim 1$ where the cross-section is already relatively small. Since the general approximation of relativistic incoming and outgoing particles is assumed for all calculations presented here, the δ dependence is negligible. In future parametrizations aiming to describe also the highest energy losses properly, this needs to be taken into account.

4.3.2 Approximated Screening

Due to the small difference between the screening functions Φ_1 and Φ_2, which even vanishes in the no screening case, this difference is often neglected and the approximation

$$\Phi = \Phi_1 \approx \Phi_2 \tag{4.19}$$

is used. Thereby, the differential cross-section of (4.11) simplifies to

$$\frac{\mathrm{d}\sigma}{\mathrm{d}v} = \frac{\alpha}{v} Z \left(2zr_e\frac{m_e}{M}\right)^2 \left(\frac{4}{3}(1-v)+v^2\right)\Phi. \tag{4.20}$$

Following the parametrization of [KKP95], the “interpolation” between the extreme scenarios of the screening in (4.15) can be described with the no screening case

corrected by the screening of to the atomic form factor Δ_a and the nuclear form factor Δ_n.

$$\Phi = \ln \frac{M}{\delta} - \frac{1}{2} - \Delta_a - \Delta_n. \tag{4.21}$$

Here, the correction due to the nuclear form factor was calculated including the dependency of δ.

$$\Delta_a = \ln \left(1 + \frac{1}{\delta \sqrt{e} B_{\text{el}} Z^{-1/3} / m_e} \right) \quad \text{and} \quad \Delta_n = \ln \frac{D_n}{1 + \delta (D_n \sqrt{e} - 2)/M}. \tag{4.22}$$

The difference between the approximated screening of [KKP95] and without the approximation [San18] in the differential cross-section is shown in Figure 4.5. The maximum error of this approximation is less than a percent.

This parametrization is widely used in the literature and the default in PROPOSAL under the name *KelnerKokoulinPetrukhin*.

4.3.3 Inelastic Corrections

So far only the elastic interactions with the target atom have been discussed. The inelastic nuclear form factor, describing the excitation of the nucleus, is already included in (4.14) and differs compared to the elastic nuclear form factor only by a factor of $1/Z$ [ABB94]. This is not the case for Hydrogen since there are no nuclear excitations.

The inelastic atomic form factor describes the interaction with atomic electrons as the target particle that is screened by the field of the nucleus. As shown in Figure 4.6 it consists of two types of diagrams depending on whether the muon or the electron emits the bremsstrahlung photon.

The cross-section for the μ-diagrams calculated in [KKP95] is similar to (4.20) also using the approximation $\Phi_1 \approx \Phi_2$. The error due to this approximation does not increase the overall uncertainty since this contribution is already a correction to the main bremsstrahlung cross-section. The screening function changes to $\Phi \to \Phi^{\text{inel}}$ with

$$\Phi^{\text{inel}} = \ln \frac{M/\delta}{M\delta/m_e^2 + \sqrt{e}} - \ln \left(1 + \frac{m_e}{\delta B_{\text{inel}} Z^{-2/3} \sqrt{e}} \right). \tag{4.23}$$

Due to the different target, the maximum energy loss, which is, in fact, the maximum energy that is transferred to the bremsstrahlung photon neglecting the energy

(a) μ-diagram. **(b)** e-diagram.

Figure 4.6: The Feynman diagrams of the inelastic atomic form factors with the atomic electron as target. In the μ-diagram the bremsstrahlung is emitted by the muon, in the e-diagram it is emitted by the electron. The patterned circles replace the two diagrams shown in Figure 4.4 differing in the order of the photons coupling to the fermion line.

transferred to the electron, changes to

$$v_{\max} = \frac{m_e(E-M)}{E(E-p+m_e)}. \tag{4.24}$$

As already mentioned in section 4.2 the e-diagrams are considered with the ionization or knock-on electron process since the cross-section has a $1/v^2$ dependency and the average energy loss increases logarithmically with the energy. The cross-section can be parametrized [KKP97] as a correction factor to the ionization cross-section from (4.5).

$$\frac{\mathrm{d}\sigma}{\mathrm{d}v} = \frac{\mathrm{d}\sigma}{\mathrm{d}v}_{\text{ioniz}} \cdot \frac{\alpha}{2\pi}[a(2b+c)-b^2] \tag{4.25}$$

with the logarithmic functions

$$a = \ln\left(1+\frac{2Ev}{m_e}\right), \quad b = \ln\frac{1-v/v_{\max}}{1-v} \quad \text{and} \quad c = \ln\frac{2m_e\gamma(1-v)}{Mv}. \tag{4.26}$$

The maximum energy loss here refers to the $v_{\max}$ for the ionization in (4.6). The term b is divergent for $v \to v_{\max}$ which is an integrable singularity at the edge of the phase space but can causes issues in numerical calculations. However, this is a minor correction to the main ionization term and only occurs at the highest energy losses where all other interactions dominate the ionization and can be neglected. But it can still cause issues in numerical simulations and requires further investigations in upcoming works.

4.3.4 Radiative Corrections

Reducing the uncertainty of the cross-section below the percent level also requires the inclusion of next-to-leading order (NLO) processes that are suppressed by a factor of α due to the additional vertex. The diagrams for all NLO processes comprising vacuum polarization, self-energy, vertex correction, box diagram, and double bremsstrahlung are shown in Figure 4.7.

These diagrams have been calculated in [San18] and the relative difference to the tree-level contribution has been parametrized using the approximation of (4.19).

The vacuum polarization can be estimated independent of the other diagrams. Since it only affects the four-momentum of the virtual photon exchanged with the nucleus, it can be included as a correction to the screening function.

$$\frac{\mathrm{d}\sigma}{\mathrm{d}v} = \left(2\alpha z Z r_e \frac{m_e}{M}\right)^2 \frac{1}{v}\left(\frac{4}{3}(1-v)+v^2\right)\Phi_1(\delta)s_{\mathrm{vac}}(\delta, Z) \tag{4.27}$$

Like the screening function, the correction factor only depends on the minimal momentum transfer to the nucleus and has been parameterized to

$$s_{\mathrm{vac}}(\delta, Z) = \frac{b}{\pi}\ln[a^{1/b} + e^{c/b}\delta], \qquad a, b, c \in f(Z) = f_1 + f_2 Z^{1/3}.$$

	f_1	$f_2/10^3$
a	2.603	−64.68
b	0.2672	9.791
c	2.055	−86.08

(4.28)

Since this is a correction of $\mathcal{O}(10^{-4})$ compared to the main contribution, it is not included in the PROPOSAL simulation, yet.

All other NLO diagrams cannot be estimated independent of each other, since the *photon mass* that is temporarily introduced to deal with divergences in the loop integrals only cancels out in the sum of all diagrams. To simplify the calculation, the Weizsäcker-Williams method has been used to describe the Coulomb field of the nucleus with a real photon stream and using the NLO-corrections of the Compton process calculated in [BF52]. The calculation assumes that all out-going particles are boosted in the forward direction. The relative deviation in the differential cross-section of the sum of the radiative corrections to the main bremsstrahlung contribution has been parameterized to

$$\frac{\mathrm{d}\sigma}{\mathrm{d}v} = \left(\alpha z^2 Z r_e \frac{m_e}{M}\right)^2 \frac{1}{v}\Phi_1(\delta)s_{\mathrm{rad}}(v). \tag{4.29}$$

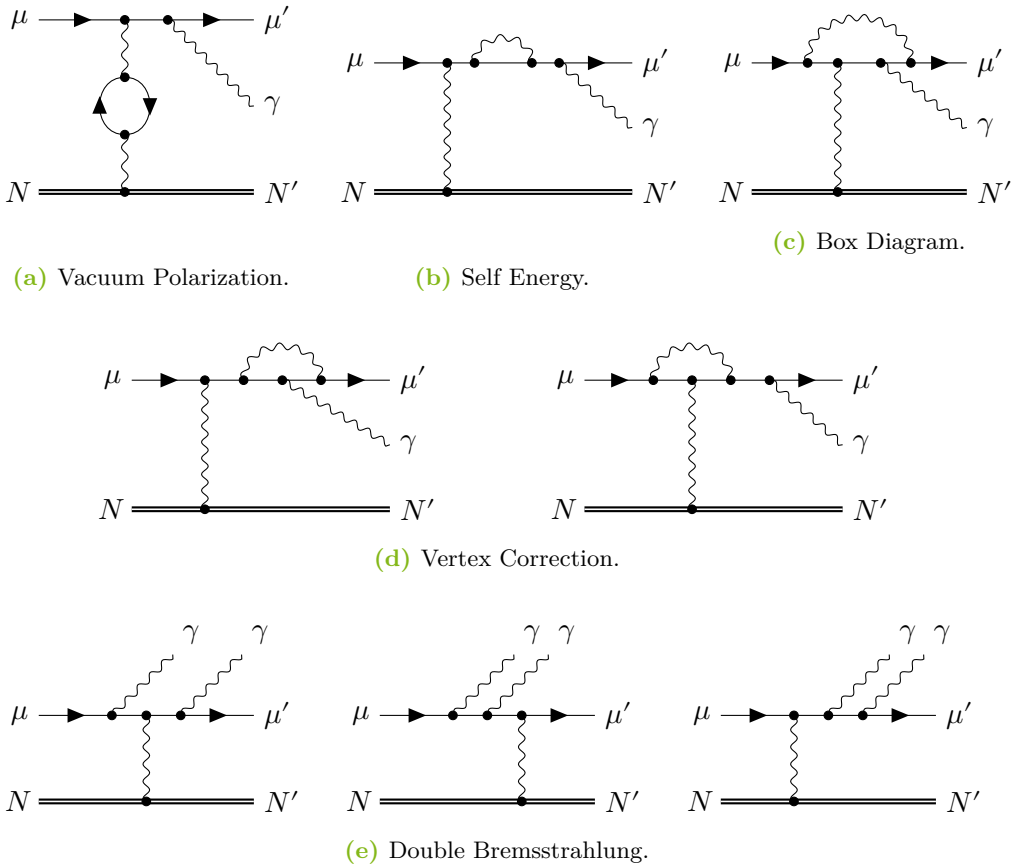

(a) Vacuum Polarization.

(b) Self Energy.

(c) Box Diagram.

(d) Vertex Correction.

(e) Double Bremsstrahlung.

Figure 4.7: The NLO Feynman diagrams for the bremsstrahlung interaction. For the vacuum polarization, fermion self-energy, box diagram, and the vertex correction, only the NLO processes to the first diagram in Figure 4.4 are shown where photon to the nucleus couples first to the muon line and after that the bremsstrahlung photon gets emitted. The diagrams with the reverse order are constructed in the same way. For the double bremsstrahlung, all occurring diagrams are shown since the second bremsstrahlung photon cannot be distinguished from the first one.

The correction factor only depends on the relative energy loss with the coefficients listed in Table 4.3

$$s_{\text{rad}}(v) = \begin{cases} \sum_{n=0}^{2} a_n v^n & v < 0.02 \\ \sum_{n=0}^{3} b_n v^n & 0.02 \leq v < 0.1 \\ \sum_{n=0}^{2} c_n v^n + c_3 v \ln v + c_4 \ln(1-v) + c_5 \ln^2(1-v) & 0.1 \leq v < 0.9 \\ \sum_{n=0}^{2} d_n v^n + d_3 v \ln v + d_4 \ln(1-v) + d_5 \ln^2(1-v). & 0.9 \leq v \end{cases} \tag{4.30}$$

Table 4.3: Coefficients of the parametrization of the radiative corrections to the bremsstrahlung on a nucleus.

n	0	1	2	3	4	5
a_n	−0.003 49	148.84	−987.531			
b_n	0.1642	132.573	−585.361	1407.77		
c_n	−2.8922	−19.0156	57.698	−63.418	14.1166	1.842 06
d_n	2134.19	581.823	−2708.85	4767.05	1.529 18	0.361 933

The contribution of the vacuum polarization and the other radiative corrections are shown in Figure 4.5. While all other contributions have a $1/v$ dependency, the parametrization of the radiative corrections behaves differently, since the correction become negative for small v.

4.3.5 Coulomb Corrections

The exchange of a single photon with the nucleus is called Born-approximation. Multiple exchanges with the nucleus, which are described with a Coulomb field are called Coulomb corrections. While, the radiative corrections describe the higher-order processes along the muon line, scaling with α, higher-order corrections with the nucleus scale with $Z\alpha$. For heavy atoms like gold or uranium, this correction is close to 1. Therefore, not just the NLO contribution is relevant but also all higher-order processes, as indicated in the Feynman diagram in Figure 4.8. The sum of all these diagrams can be calculated using recursive relations, leading to the

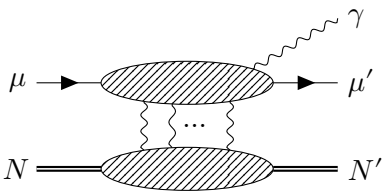

Figure 4.8: The Feynman diagram for Coulomb corrections to the bremsstrahlung process.

power series series

$$f(x) = x^2 \sum_{n=1}^{\infty} \frac{1}{n(n^2 + x^2)}. \tag{4.31}$$

For a point-like nucleus, the cross-section was already calculated in [BM54; DBM54]. Including the negative corrections of an extended nucleus, this results into the overall negative contribution described by [AB97]

$$\frac{\mathrm{d}\sigma}{\mathrm{d}v} = -\frac{\alpha}{v} \left(2zZr_e \frac{m_e}{M}\right)^2 \left(1 - \frac{2}{3}v + v^2\right) f(Z\alpha). \tag{4.32}$$

Further investigations on Coulomb corrections on extended nuclei are have been made in [SR18]. This correction was recently included in the simulation of PROPOSAL.

4.3.6 Bremsstrahlung in a Medium

So far only the interaction on a single, isolated atomic target has been considered. Inside a medium, further atoms influence the interaction leading to the interference of multiple targets. Since the interaction length, the part on the muon track on which the photon is emitted, increases with the muon energy, this length can reach the macroscopic scale and include multiple atoms thus interfering and reducing the cross-section. Here the parametrizations collected in [Kle99; Pol+01; Pol+02] is used.

LPM Effect

The suppression of the exchange of the virtual photon between the muon and the nucleus is named after Landau, Pomeranchuk, and Migdal (LPM effect) [LP53b; LP53a; Mig56; Mig57].

The effect can be included by multiplying a correction factor to the main cross-section (4.11)

$$\frac{\mathrm{d}\sigma}{\mathrm{d}v} = \frac{\mathrm{d}\sigma}{\mathrm{d}v}\Big|_{\mathrm{Brems}} \cdot \frac{\frac{\xi(s)}{3}(v^2 G(s) + 2[1 + (1-v)^2]\phi(s))}{\frac{4}{3}(1-v) + v^2}, \tag{4.33}$$

which in principle is a substitution of the v dependence term of the approximated bremsstrahlung (4.20). The so-called Migdal functions can be parameterized by [Sta+82]

$$G(s) = \begin{cases} 3\psi(s) - 2\phi(s), & s < 0.710390 \\ \frac{36s^2}{36s^2+1}, & 0.710390 \leq s < 0.904912 \\ 1 - 0.022/s^4 & s \geq 0.904912 \end{cases} \tag{4.34a}$$

$$\phi(s) = \begin{cases} 1 - \exp\left(-6s[1 + (3-\pi)s] + \frac{s^3}{0.623 + 0.796s + 0.658s^2}\right) & s < 1.54954 \\ 1 - 0.012/s^4 & s \geq 1.54954 \end{cases} \tag{4.34b}$$

$$\xi(s) \approx \xi(s') = \begin{cases} 2 & s' < s_1 \\ 1 + h - \frac{0.08(1-h)[1-(1-h)^2]}{\ln s_1} & s_1 \leq s' < 1 \\ 1 & s' \geq 1 \end{cases} \tag{4.34c}$$

using

$$\psi(s) = 1 - \exp\left(-4s - \frac{8s^2}{1 + 3.936s + 4.97s^2 - 0.05s^3 + 7.50s^4}\right), \tag{4.35}$$

$$s = \frac{s'}{\sqrt{\xi(s')}}, s_1 = \sqrt{2}\left(\frac{m_e}{M}\frac{D_n Z^{1/3}}{B_{el}}\right)^2, s' = \frac{1}{8}\sqrt{\frac{E_{\mathrm{LPM}}}{E}\frac{v}{1-v}}, h = \frac{\ln s'}{\ln s_1}. \tag{4.36}$$

The characteristic energy above which the LPM effect becomes significant is given by

$$E_{\mathrm{LPM}} = \frac{\alpha^2 M^2 X_0}{4\pi m_e r_e}. \tag{4.37}$$

A strong suppression corresponds to $s \to 0$ leading to $G(s), \phi(s) \to 0$ and low suppression corresponds to $s \to \infty$ resulting in $G(s), \phi(s) \to 1$ where the LPM correction factor (4.33) becomes 1.

The LPM suppression on the average energy loss, which is also relevant for the pair production process but at higher energies, is shown in Figure 4.9.

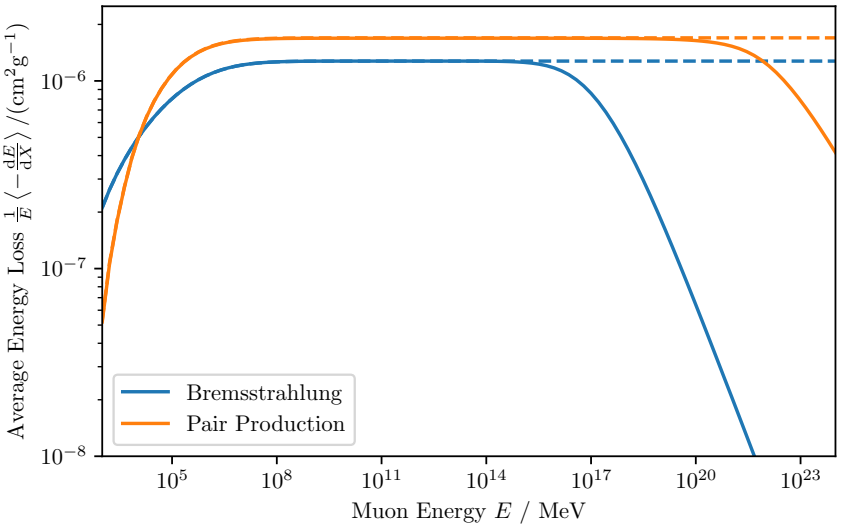

Figure 4.9: Effects of the LPM correction on the average energy loss of the bremsstrahlung and pair production processes for muons in ice. At high energies, the dashed line indicates the absence of the LPM effect and the straight line includes the LPM suppression.

Dielectric Effect

Next to the nuclear interaction, also the emission of the bremsstrahlung photon gets suppressed, which is called Ter-Mikaelean or Dielectric effect [Ter54]. The TM-effect can be included in the LPM correction by substituting

$$\xi(s) \to \xi(\Gamma s), \quad \phi(s) \to \frac{\phi(\Gamma s)}{\Gamma}, \quad G(s) \to \frac{G(\Gamma s)}{\Gamma^2} \tag{4.38}$$

with

$$\Gamma = 1 + 4\pi \frac{m_e^2}{M^2} \frac{r_e^3}{\alpha^2 v^2} N_A \rho \frac{\sum Z}{\sum A} \tag{4.39}$$

Hereby, ρ is the density of the medium and in the last fraction the sum over all atoms of the molecule or medium is done.

This effect limits the number of low-energy photons as can be seen in Figure 4.10 and thereby vanishes the $1/v$ divergence of the bremsstrahlung cross-section for $v \to 0$.

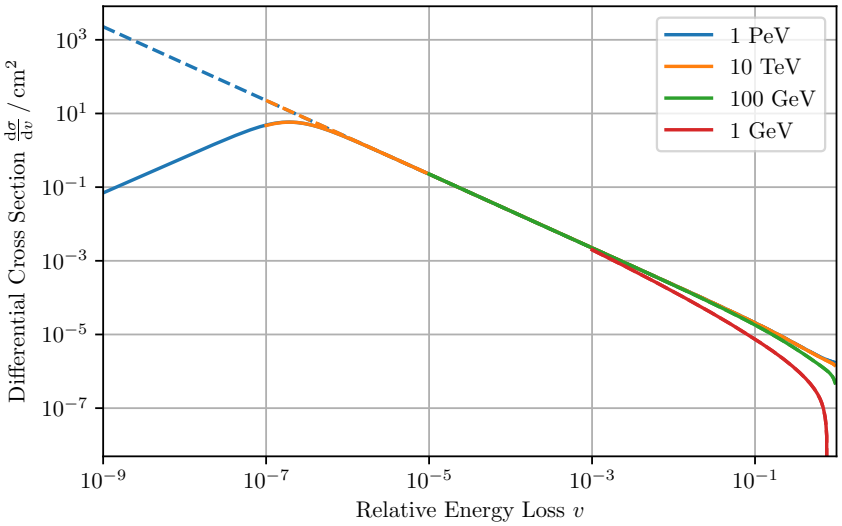

Figure 4.10: Effects of the dielectric correction on the differential bremsstrahlung cross-section for muons in Standard Rock ($Z = 11, A = 22$). The dashed line for low energy losses indicates the absence of the dielectric effect and the straight line includes the dielectric suppression.

4.3.7 Diffractive Corrections

Up to this point only the muon, or atomic electron, emit the bremsstrahlung photon. In [KF99] the diffraction of the bremsstrahlung on a nucleus was calculated also being a correction on the percent level. This correction is in particular of interest, since it differs between a μ^- and a μ^+, while all other processes contributing to the cross-section that have been considered so far do not depend on the charge of the primary particle. In fact, it is not the diffractive process, which depends on the charge, but the interference term. Since the cross-section for the μ^- decreases while for the μ^+ it increases, the deviation between both processes can be as large as 10 % at 10 TeV. Unfortunately, the interference term, which is the interesting part of this correction has not yet been parameterized and can therefore not be included in simulations.

4.3.8 Remaining Uncertainties

Compared to the last review of the uncertainties of the muon cross-sections [Kok99], now the remaining uncertainties are of the order of 1e-3 and are thereby comparable with numerical uncertainties due to interpolations of the cross-sections and averaged energy losses. However, especially the edge case of an extremely high energy loss

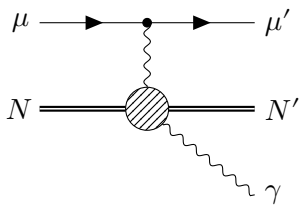

Figure 4.11: The Feynman diagram of the diffractive bremsstrahlung. The pattern blob indicates both orderings when both photon couple to the nucleus.

has become a topic of interest, since the searches for Glashow resonances and tau neutrinos reveal the first promising results and the hunt for neutrinos or rare events, in general, goes on. Therefore, the rejection of the dominating muon background has to become increasingly precise and even the rate of the largest energy losses needs to be described with high accuracy. This is the task for the upcoming works to satisfy the requirements on simulations of future neutrino telescopes.

4.4 e^+e^- Pair Production

The creation of an electron-positron pair can be described by two types of Feynman diagrams on tree-level shown in Figure 4.12. In the first one, the electron-positron pair couples to the atom which is called e-diagram, and the second one with the muon coupling to the atom is called μ-diagram. The latter has a similar structure compared to the bremsstrahlung diagram except for the emitted photon producing an e^+e^--pair. Due to the additional Vertex, the μ-diagram cross-section is suppressed by a factor of α compared to the bremsstrahlung.

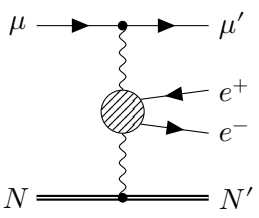

(a) e-diagram.

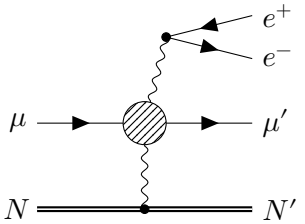

(b) μ-diagram.

Figure 4.12: The Feynman diagrams of the e^+e^- pair production for the e-diagram, where the electron couples to the nucleus and the μ-diagram, where the muon couples to the nucleus. The patterned blob stands for both scenarios where one of the virtual photons couples first or last are included.

In general, the pair production and the bremsstrahlung interaction are closely related and share many effects contributing to the cross-section. As already mentioned in the bremsstrahlung section, these effects are mainly described in that section giving room to focus here on the calculation of radiative corrections. Similar to the calculations for the bremsstrahlung, all calculations in this section assume that all incoming and outgoing particles are high energetic enough that they can be treated in the relativistic approximation.

Since two secondaries are produced in this interaction, the cross-section is not just differential in the energy loss but also in the asymmetry parameter

$$\rho = \frac{\varepsilon_+ - \varepsilon_-}{\varepsilon_+ + \varepsilon_-} \tag{4.40}$$

defining how much energy is transferred to the electron ε_- compared to the positron ε_+. The sign of ρ is not relevant, as it just appears as ρ^2. Regarding the interference between the $e-$ and $\mu-$diagram, there are terms with a linear dependency to ρ. However, these terms vanish when integrating over ρ due to the different charge parity of these diagrams.

The differential cross-section can be written in the form

$$\frac{\mathrm{d}^2\sigma}{\mathrm{d}v\mathrm{d}\rho} = \frac{2}{3\pi}(zZ\alpha r_e)^2 \frac{1-v}{v}\left(\Phi_e + z^2\frac{m_e^2}{M^2}\Phi_\mu\right) \tag{4.41}$$

where Φ_e and Φ_μ denote the contribution of the two types of diagram. Since the μ-diagram is suppressed by m_e^2/M^2 similar to the bremsstrahlung cross-section, the e-diagram is the dominating contributor to this interaction.

The allowed kinematic region of the cross-section is in principle defined by the masses, i.e. for the energy loss $v_{\min} = 2m_e/E$ and $v_{\max} = 1 - M/E$. Similar to the bremsstrahlung, due to relativistic approximations, the limits further shrink down to only obtain a positive cross-section

$$v_{\min} = \frac{4m_e}{E}, \qquad v_{\max} = 1 - \frac{M}{E}\frac{3\sqrt{e}}{4}Z^{1/3}, \tag{4.42}$$

$$\rho_{\min} = 0, \qquad \rho_{\max} = \sqrt{1 - \frac{v_{\min}}{v}}\left(1 - \frac{6M^2}{E^2(1-v)}\right). \tag{4.43}$$

These limits as well as the main calculations of the individual contributions $\Phi_{e,\mu}$ to the cross-section were estimated in [KP69; KP71] using the dimensionless parameters

$$\beta = \frac{v^2}{2(1-v)} \qquad \text{and} \qquad \xi = \left(\frac{vM}{2m_e}\right)^2 \frac{1-\rho^2}{1-v}. \tag{4.44}$$

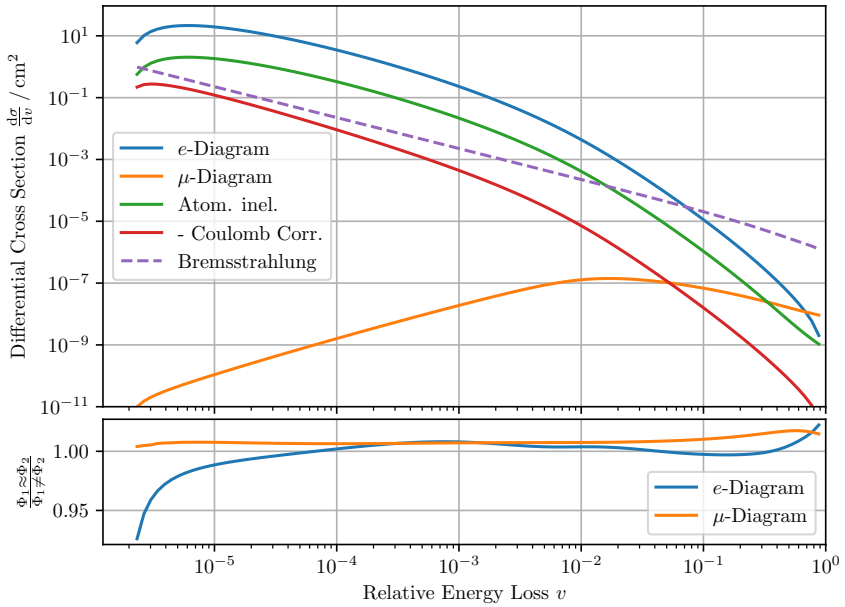

Figure 4.13: Differential cross-section of the two pair production diagrams.

Therefore β does not denote the Lorentz variable in all subsections to be consistent with the naming in the literature.

The differential cross-sections of the two pair production diagram types integrated over ρ are shown in figure 4.13, where the dominance of the e-diagram over a wide range of the energy loss distribution can be seen. Just at high energy losses the μ-diagram surpasses the e-diagram and contributes significantly. The main contribution of the average energy loss originates from the many small losses of the e-diagram due to its sharp energy loss spectrum of $1/v^3$ to $1/v^4$. Therefore, pair production is sometimes called a flaring torch for neutrino telescopes; the more energy the muon has, the more electrons that can emit Cherenkov light are produced, and the brighter track becomes.

The contributions $\Phi_{e,\mu}$ can further be split into

$$\Phi_{e,\mu} = C_1^{e,\mu} L_1^{e,\mu} + C_2^{e,\mu} L_2^{e,\mu} \tag{4.45}$$

where $L_{1,2}$ are similar to the screening functions of the bremsstrahlung cross-section in section 4.3.1.

4.4.1 Approximated Screening

Analogous to (4.19), the screening functions can be approximated with $L_1 \approx L_2$ as introduced in [KK68], which simplifies the individual contributions to $\Phi_{e,\mu} = C_{e,\mu} L_{e,\mu}$ using the expressions

$$C_e = [(2+\rho^2)(1+\beta) + \xi(3+\rho^2)] \ln(1+1/\xi) + \frac{1-\beta-\rho^2}{1+\xi} - (3+\rho^2), \quad (4.46a)$$

$$C_\mu = [(1+\rho^2)(1+3/2\beta) + (1+2\beta)(1-\rho^2)/\xi] \ln(1+\xi) + \xi\frac{1-\beta-\rho^2}{1+\xi} + (1+2\beta)(1-\rho^2). \quad (4.46b)$$

presented in [KP69]. In this proceeding, also the screening functions again with an analytical interpolation between full- and no screening including the Thomas Fermi model for the atomic form factor is derived. The correction of the finite size of the nucleus in the nuclear form factor using a Fermi distribution was derived in [KP71] resulting in

$$L_e = \ln \frac{B_{\text{el}} Z^{-1/3} \sqrt{(1+\xi)(1+Y_e)}}{1 + \frac{2m_e\sqrt{e}B_{\text{el}}Z^{-1/3}(1+\xi)(1+Y_e)}{Ev(1-\rho^2)}} - \frac{1}{2}\ln\left[1 + \left(\frac{3}{2}\frac{m_e}{M}Z^{1/3}\right)^2 (1+\xi)(1+Y_e)\right], \quad (4.47a)$$

$$L_\mu = \ln \frac{\frac{2}{3}\frac{M}{m_e} B_{\text{el}} Z^{-2/3}}{1 + \frac{2m_e\sqrt{e}B_{\text{el}}Z^{-1/3}(1+\xi)(1+Y_\mu)}{Ev(1-\rho^2)}} \quad (4.47b)$$

with

$$Y_e = \frac{5 - \rho^2 + 4\beta(1+\rho^2)}{2(1+3\beta)\ln(3+1/\xi) - \rho^2 - 2\beta(2-\rho^2)}, \quad (4.48a)$$

$$Y_\mu = \frac{4 + \rho^2 + 3\beta(1+\rho^2)}{(1+\rho^2)(3/2+2\beta)\ln(3+\xi) + 1 - 3/2\rho^2}. \quad (4.48b)$$

This parametrization is widely used in the literature and the default in PROPOSAL under the name *KelnerKokoulinPetrukhin*.

4.4.2 Advanced Screening

Using the same procedure as mentioned above but without the approximation $L_1 \approx L_2$ the expressions were calculated in [San18] leading to

$$C_1^{e,\mu} = C_{e,\mu} - C_2^{e,\mu} \quad (4.49)$$

using the expressions of (4.46) and

$$C_2^e = [(1-\rho^2)(1+\beta) + \xi(3-\rho^2)]\ln(1+1/\xi) + 2\frac{1-\beta-\rho^2}{1+\xi} - (3-\rho^2) \quad (4.50a)$$

$$C_2^\mu = [(1-\rho^2)(1-\beta) + \xi(1+\rho^2)]\frac{\ln(1+\xi)}{\xi} + 2\frac{1-\beta-\rho^2}{1+\xi} - +1-\beta-(1+\beta)\rho^2. \quad (4.50b)$$

For numerical stability the screening functions $L_{1,2}$ are expressed in two regions of

$$X_{e,\mu} = \exp\left(-\frac{\Delta_{e,\mu}}{C_{e,\mu}}\right) \quad (4.51)$$

using the relative correction

$$\Delta_e = [(2+\rho^2)(1+\beta) + \xi(3+\rho^2)]\,\mathrm{Li}_2\,\frac{1}{1+\xi} - (2+\rho^2)\xi\ln(1+1/\xi) - \frac{\xi+\beta+\rho^2}{1+\xi} \quad (4.52a)$$

$$\Delta_\mu = \left[(1+\rho^2)(1+{}^3\!/_2\beta) - (1+2\beta)(1-\rho^2)/\xi\right]\mathrm{Li}_2\,\frac{\xi}{1+\xi} \quad (4.52b)$$
$$+ (1+{}^3\!/_2\beta)\frac{1-\rho^2}{\xi}\ln(1+\xi) + \left[1-\rho^2-\frac{\beta}{2}(1+\rho^2)+\frac{1-\rho^2}{2\xi}\beta\right]\frac{\xi}{1+\xi}.$$

Hereby the dilogarithm as defined in (A.1) is used. For small X_e or ${}^{\Delta_e}\!/_{C_e} \geq 0$ the screening functions can be expressed in the form

$$L_1^e = \ln\frac{B_{\mathrm{el}}Z^{-1/3}\sqrt{1+\xi}}{X_e + \frac{2m_e\sqrt{e}B_{\mathrm{el}}Z^{-1/3}(1+\xi)}{Ev(1-\rho^2)}} - \frac{\Delta_e}{C_e} - \frac{1}{2}\ln\left[X_e + \left(\frac{m_e}{M}D_n\right)^2(1+\xi)\right] \quad (4.53a)$$

$$L_2^e = \ln\frac{B_{\mathrm{el}}Z^{-1/3}e^{-1/6}\sqrt{1+\xi}}{X_e + \frac{2m_e e^{1/3}B_{\mathrm{el}}Z^{-1/3}(1+\xi)}{Ev(1-\rho^2)}} - \frac{\Delta_e}{C_e} - \frac{1}{2}\ln\left[X_e + \left(\frac{m_e}{M}D_n\right)^2 e^{1/3}(1+\xi)\right] \quad (4.53b)$$

and for large X_e or ${}^{\Delta_e}\!/_{C_e} < 0$ the equivalent expressions are

$$L_1^e = \ln\frac{B_{\mathrm{el}}Z^{-1/3}\sqrt{1+\xi}}{1 + \frac{2m_e\sqrt{e}B_{\mathrm{el}}Z^{-1/3}(1+\xi)}{Ev(1-\rho^2)}X_e^{-1}} - \frac{\Delta_e}{2C_e} - \frac{1}{2}\ln\left[1 + \left(\frac{m_e}{M}D_n\right)^2(1+\xi)X_e^{-1}\right] \quad (4.54a)$$

$$L_2^e = \ln\frac{B_{\mathrm{el}}Z^{-1/3}e^{-1/6}\sqrt{1+\xi}}{1 + \frac{2m_e e^{1/3}B_{\mathrm{el}}Z^{-1/3}(1+\xi)}{Ev(1-\rho^2)}X_e^{-1}} - \frac{\Delta_e}{2C_e} - \frac{1}{2}\ln\left[1 + \left(\frac{m_e}{M}D_n\right)^2 e^{1/3}(1+\xi)X_e^{-1}\right] \quad (4.54b)$$

Using the same procedure for the μ diagram, the resulting expressions for small X_μ ($\Delta_\mu/C_\mu \geq 0$) are

$$L_1^\mu = \ln \frac{X_\mu \frac{M}{m_e} B_{\text{el}} Z^{-1/3} D_n}{X_\mu + \frac{2m_e\sqrt{e}B_{\text{el}}Z^{-1/3}(1+\xi)}{Ev(1-\rho^2)}}, \quad L_2^\mu = \ln \frac{X_\mu \frac{M}{m_e} B_{\text{el}} Z^{-1/3} D_n}{X_\mu + \frac{2m_e e^{1/3}B_{\text{el}}Z^{-1/3}(1+\xi)}{Ev(1-\rho^2)}} \tag{4.55}$$

and for large X_μ ($\Delta_\mu/C_\mu < 0$) the equivalent expressions are

$$L_1^\mu = \ln \frac{\frac{M}{m_e} B_{\text{el}} Z^{-1/3} D_n}{1 + \frac{2m_e\sqrt{e}B_{\text{el}}Z^{-1/3}(1+\xi)}{Ev(1-\rho^2)} X_\mu^{-1}}, \quad L_2^\mu = \ln \frac{\frac{M}{m_e} B_{\text{el}} Z^{-1/3} D_n}{1 + \frac{2m_e e^{1/3}B_{\text{el}}Z^{-1/3}(1+\xi)}{Ev(1-\rho^2)} X_\mu^{-1}}. \tag{4.56}$$

The effect of the different approaches including the screening on the differential cross-section is shown in Figure 4.13 with a maximum deviation of half a percent.

4.4.3 Inelastic interaction on Atomic Electrons

When the muon interacts with the nucleus, the atomic electrons screen the electromagnetic field of the nucleus. But the muon can also interact with the atomic electrons screened by the nuclear field. This interaction on atomic electrons can be included effectively by replacing Z^2 in the differential cross-section (4.41) with $Z(Z+1)$ or more precisely with $Z(Z+\zeta)$ using

$$\zeta = \frac{0.073 \ln \frac{E/M}{1+\gamma_1 Z^{2/3} E/M} - 0.26}{0.058 \ln \frac{E/M}{1+\gamma_2 Z^{1/3} E/M} - 0.14}, \qquad \begin{array}{c|cc} & Z=1 & Z\neq 1 \\ \hline \gamma_1/10^{-5} & 4.4 & 1.95 \\ \gamma_2/10^{-5} & 4.8 & 5.3 \end{array} \tag{4.57}$$

as derived in [Kel98]. The dependence of ζ on the energy and the atomic number is shown in Figure 4.14.

4.4.4 Coulomb Correction

Multiple interactions or exchanging photons between the electron line and the nucleus become significant for nuclei with high atomic numbers as already described in section 4.3.5 for bremsstrahlung. These Coulomb corrections shown in the Feynman diagram in Figure 4.15 are only calculated for the e-diagram since this is the main contribution.

The corresponding cross-section has been calculated in [Iva+98a; Iva+98b]

$$\frac{\mathrm{d}^2\sigma}{\mathrm{d}v\mathrm{d}\rho} = -\frac{4}{3\pi}\frac{Z^2\alpha^4}{m_e}\frac{1-v}{v} C_e f(Z\alpha) \tag{4.58}$$

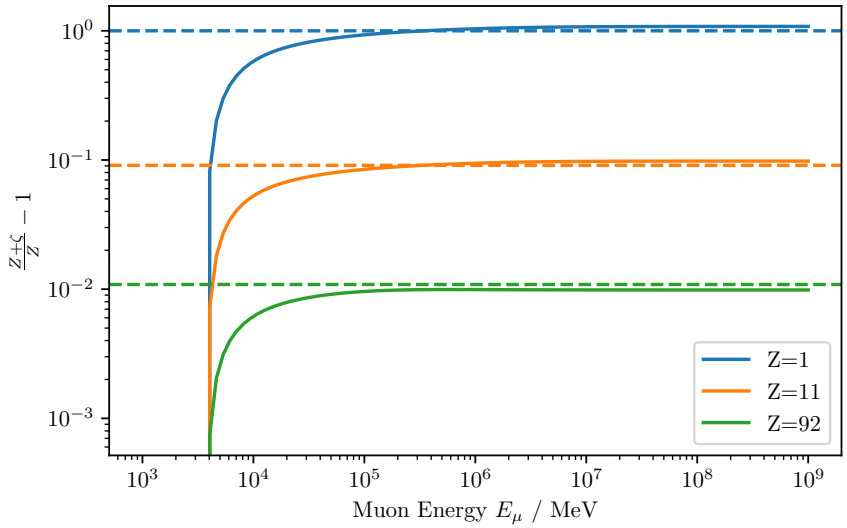

Figure 4.14: Energy dependence of the interaction on atomic electrons using the advanced description of $\zeta(E)$ (straight lines) and the approximation $\zeta = 1$ (dashed lines) for three different nuclei.

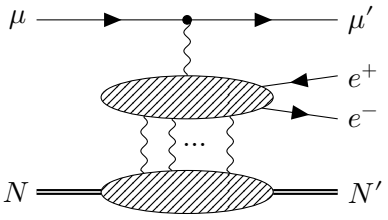

Figure 4.15: The Feynman diagram for Coulomb corrections to the e-diagram of the pair production process.

using the series for the recursive relation f of (4.31). This correction to the differential cross-section is on the order of $\mathcal{O}(10^{-3} - 10^{-4})$ as shown in Figure 4.13 and recently included in the PROPOSAL simulation.

4.4.5 LPM Effect

So far only the cross-sections for the interaction at an isolated atom have been considered. Similar to the bremsstrahlung, the coherence length of the pair production interaction at higher muon energies also increases to macroscopic scales of the distance between two molecules in the medium. This effect of scattering on multiple atoms called LPM effect can be included by replacing the contribution C_e with [Pol+02]

$$C_e \to (1+\beta)[A + (1+\rho^2)B] + \beta[C + (1+\rho^2)D] + (1-\rho^2)E \tag{4.59}$$

The so-called Ternovskii functions introduced in [Ter60] are defined as

$$A = \frac{G}{2}(1+2G\xi)\ln\frac{s^2(1+\xi)^2+1}{s^2\xi^2} - G + Gs\left(1+\frac{s^2-1}{s^2+1}\xi\right)\Psi \tag{4.60a}$$

$$B = \Phi(1+\Phi\xi)\ln\frac{s(1+\xi)+1}{s\xi} - \Phi \tag{4.60b}$$

$$C = -G^2\xi\ln\frac{s^2(1+\xi)^2+1}{s^2\xi^2} + G - G^2\frac{s^2-1}{s}\xi\Psi \tag{4.60c}$$

$$D = \Phi - \Phi^2\xi\ln\frac{s(1+\xi)+1}{s\xi} \tag{4.60d}$$

$$E = -s\Psi \tag{4.60e}$$

using the abbreviations

$$\Phi(s) = \frac{s}{s+1}, \qquad G(s) = \frac{s^2}{s^2+1}, \qquad \Psi = \arctan[s(\xi+1)] - \frac{\pi}{2} \tag{4.61}$$

and

$$s = \frac{3}{2}\sqrt{\frac{E_{\mathrm{LPM}}}{E}\frac{1}{v(1-\rho^2)}}, \qquad E_{\mathrm{LPM}} = \frac{M^4}{2\pi\alpha^2 n\sum_i Z^2} \tag{4.62}$$

The effect is already shown in Figure 4.9 and compared to the LPM effect of the bremsstrahlung, the decreasing effect on the pair production cross section starts at even higher energies, even above the GZK-cutoff. However, neutrino searches are looking for energies up to 10^{30} eV and therefore it is necessary to include even these effects.

4.4.6 Radiative Correction

Radiative Corrections or NLO processes, already described in section 4.3.4, are suppressed by α and are necessary to reduce the uncertainty to a permille level. Only the NLO processes for the e-diagrams are considered, as the μ-diagrams are already a correction to this process. For a first estimation of the effect of radiative corrections, only the NLO processes on the muon line are calculated. This includes the vacuum polarization, the vertex correction, and the emit of a bremsstrahlung photon illustrated in Figure 4.16.

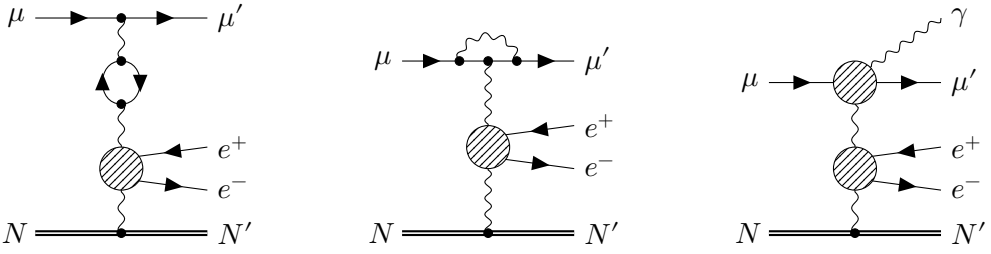

(a) Vacuum Polarization. **(b)** Vertex Correction. **(c)** Bremsstrahlung.

Figure 4.16: The NLO Feynman diagrams for the e-diagram of the pair production at the muon line including the vacuum polarization, vertex correction, and additional bremsstrahlung. The patterned circle indicates that both scenarios when the photon couples to the fermion line are included.

Like the NLO corrections to the bremsstrahlung process, the vertex correction and the additional bremsstrahlung can just be calculated together. Due to the infrared divergence arising in the loop integrals, a photon mass is introduced in both terms which just cancels out in the summation of both. The vacuum polarization can be calculated independently of the other two processes.

For the calculations, the tree-level cross-sections of the pair production of [Bug77] are used, where also the bremsstrahlung is calculated. Next to the energy loss and the asymmetry, they are differential in the 4-momentum squared of the exchanging photons K^2, Q^2 where the first describes the photon between the muon and the electron line. This parametrization is used, since it provides all tensors of the individual fermion lines, making them easy to replace and extend. The cross-sections are in good agreement with the parametrizations described previously, shown in Figure A.1.

To enhance the tree-level cross-sections with the loop contributions, the expressions of vacuum polarization and soft bremsstrahlung calculated in [MO65] and the vertex correction from [AB81] are used. Technical details to the numerical calculations

are described in section A.2. The resulting contribution of about a percent of these NLO diagrams are shown in Figure 4.13.

4.4.7 Remaining Uncertainties

Similar to the bremsstrahlung, the main uncertainties arise due to the effective description of the nuclear interaction on how the screening functions are a proper approximation for the atomic and nuclear form factors. Regarding the radiative corrections, the NLO processes along the electron line have not been calculated, yet. Both, the description of the nuclear interaction and the NLO processes result in uncertainties on the percent level. [SKP20]

Interference terms between the e-diagram and the μ-diagram vanish after integrating over ρ as described in [Kel67]. However, regarding the doubly differential cross-section the interference term differs between the μ^+ and the μ^- that are not included, yet. Compared to the bremsstrahlung, diffractive corrections and their interference terms, which would also differ between the muon charge, are therefore less important.

4.5 Inelastic Nuclear Interaction

The inelastic nuclear interaction describes the inelastic exchange of a photon between the muon and a nucleus by creating a hadronic cascade or at least a pion (the lightest hadron). It is also often called the Photonuclear Interaction, which however commonly refers to a real photon interacting with the nucleus and getting absorbed. In contrast to the previously described interactions, producing an electromagnetic cascade, hadronic interactions are part of the QCD. Due to the complex calculation of hadronic cascades, there are dedicated tools like Sibyll [Rie+20] to calculate or sample the individual secondary particles. For the simulation in PROPOSAL, only the calculation of the energy loss and the deflection is relevant.

The main part of this interaction originates from interactions with low Q^2 which is not well described by perturbative QCD and therefore phenomenological models are used. Here, the Vectormeson Dominance (VMD) and the Regge Model are described, both implemented in PROPOSAL.

For both approaches, the integration limits for the energy loss are defined by the Pion mass m_π and the average nucleon mass of the nucleus $\bar{m}_N$ is given by

$$v_{\min}E = m_\pi + \frac{m_\pi^2}{2\bar{m}_N} \qquad \text{and} \qquad v_{\max}E = 1 - \frac{\bar{m}_N}{2}\left(1 + \frac{M^2}{\bar{m}_N^2}\right). \tag{4.63}$$

While the VMD parametrizations are already integrated over Q^2, the Regge models are still differential in the momentum. The integration limits of Q^2 are

$$Q^2_{\min} = \frac{M^2 v^2}{1-v} \qquad \text{and} \qquad Q^2_{\max} = 2\bar{m}_N(Ev - m_\pi) - m_\pi^2. \tag{4.64}$$

As can be seen in the differential cross sections in (4.65) or (4.65) the dependence on the energy loss is $1/v$. Therefore, the inelastic nuclear interaction is also flat in the energy loss distribution as shown in Figure 4.17a and is next to the bremsstrahlung responsible for large stochastic losses. For muons, this process is only a 10 % correction to the average energy loss. But for taus or particles with higher mass, this interaction is the main energy loss process at high energies.

4.5.1 Vector Meson Dominance

In the VMD model, the interaction of the photon with the nucleus is described via hadrons. Thereby the photon virtually fluctuates into vector mesons like the ρ or ω meson and their excited states. A widely used parametrization for the VMD model was introduced in [BB80; BB81] and was later improved for taus or heavier particle in general in [BS03] with the parameterized hard component in [Bug+04]. The hard component in this context means the perturbative part of the process. The differential cross-section is given by

$$\begin{aligned}\frac{\mathrm{d}\sigma}{\mathrm{d}v} = \frac{\alpha}{2\pi} z^2 A \sigma_{\gamma N} v \Bigg\{ & \frac{1}{4}\left[\left(\kappa + \frac{2M^2}{m_2^2}\ln\left(1+\frac{m_2^2}{t}\right) - \frac{2M^2}{t}\right)\right] \\ & + \frac{3}{4}G\left[\kappa\ln\left(1+\frac{m_1^2}{t}\right) - \frac{\kappa m_1^2}{m_1^2+t} - \frac{2M^2}{t} + \frac{4M^2}{m_1^2}\ln\left(1+\frac{m_1^2}{t}\right)\right] \\ & + \frac{M^2}{2t}\left[\frac{3}{4}G\frac{m_1^2-4t}{m_1^2+t} + \frac{m_2^2}{4t}\ln\left(1+\frac{t}{m_2^2}\right)\right]\Bigg\} + \left.\frac{\mathrm{d}\sigma}{\mathrm{d}v}\right|_{\text{hard}}\end{aligned} \tag{4.65}$$

with

$$t = Q^2_{\min}, \quad \kappa = 1 - \frac{2}{v} + \frac{2}{v^2}, \quad m_1^2 = 0.54\,\mathrm{GeV}^2, \quad m_2^2 = 1.8\,\mathrm{GeV}^2 \tag{4.66}$$

The shadowing or screening function G of the nucleons here denotes the fact, that the probability of a photon interacting with multiple nucleons is significant. Therefore

the cross-section of the hole nucleus is smaller than the cross-section with a single nucleon times the atomic number since these cross-sections interfere destructively. The shadowing can be described by [BB81]

$$G(x) = \begin{cases} 1, & Z = 1, \\ \frac{3}{x^3}\left(\frac{x^2}{2} - 1 + e^{-x}(1+x)\right) & Z \neq 1 \end{cases} \quad \text{with} \quad x = 0.00282 A^{1/3} \sigma_{\gamma N}(\nu). \tag{4.67}$$

The most uncertain parameter in this calculation is the cross-section of the photon nucleon absorption $\sigma_{\gamma N}$. For the energy loss dependency in the following equations, the dimensionless parameter $\nu = v * E/GeV$ is used to be consistent with the literature. In [BB81] the process was approximated to

$$\sigma_{\gamma N} = 114.3 + 1.647 \ln^2(0.0213\nu). \tag{4.68}$$

However, there are multiple approaches to describe this cross-section, also implemented in PROPOSAL. One of the earliest, and still used approach, was calculated in [Cal+79] using also a semi-analytical parametrization

$$\sigma_{\gamma N} = 49.2 + 11.1 \ln \nu + 151.8/\sqrt{\nu}. \tag{4.69}$$

Also, combinations of these parametrizations have been used, each in the energy region, where it best describes the cross-section. Following [KP97], for energy losses ν below 17 GeV the parametrization of [BP75]

$$\sigma_{\gamma N} = 96.1 + 82/\sqrt{\nu} \tag{4.70}$$

is used. For energy losses between 17 and 200 GeV formula (4.68) is used and above 200 GeV (4.69).

Another approach is by using electron-proton scattering data of the HERA experiment and extrapolate into the region $Q^2 \to 0$ [Bre+99]

$$\sigma_{\gamma N} = 63.5 s^{0.0097} + 145/\sqrt{s} \qquad \text{with} \qquad s = 2\bar{m}_N \nu \tag{4.71}$$

Following [Rho93], the HERA data (listed in Table A.1) can also be interpolated directly to properly include resonances occurring at lower energies. For high energies above 200 GeV also the parametrization of (4.69) is used.

For muons and taus, perturbative corrections or the hard component has been parameterized in [Bug+04] using the polynomial function

$$\left.\frac{\mathrm{d}\sigma}{\mathrm{d}v}\right|_{\text{hard}} = \frac{A}{v} \sum_{k=0}^{7} a_k \log_{10}^k v \tag{4.72}$$

with the coefficients a_k listed in Tab. 2 of [Bug+04]. Unfortunately, these perturbative corrections can just be included for muons and taus and no other particles. Moreover, in [Bug+04] the coefficients have just been tabulated for energies between 100 GeV to 10^9 GeV and energy losses above 10^{-7}. This causes a kink in the cross-section or energy loss at these thresholds and needs to be extended in the future. This kink, as well as the growing influence of the perturbative contribution, is shown in Figure 4.17b. The effect of the different parametrizations of $\sigma_{\gamma N}$ on the differential cross-section is shown in Figure 4.17a.

4.5.2 Regge Model

In the Regge model, the interaction of the photon with the nucleus is described with the so-called quasi-particles *Pomeron* and *Reggeon* as exchange particles. At smaller energies, the Reggeon dominates corresponding to the limiting case of photoabsorption, while at higher energies, the Pomeron is used for the slowly increasing cross-section and an improved description in the diffractive region.

The differential cross-section can be described by [Abr+91]

$$\frac{\mathrm{d}^2\sigma}{\mathrm{d}v\mathrm{d}Q^2} = \frac{4\pi\alpha^2 z^2}{Q^4}\frac{F_2}{v}\left[1 - v - \frac{\bar{m}_N x v}{2E} + \left(1 - \frac{2M^2}{Q^2}\right)\frac{v^2(1 + 4\bar{m}_N^2 x^2/Q^2)}{1 + R_{12}}\right] \quad (4.73)$$

with the structure function of the nucleus F_2, the ratio R_{12} between the longitudinal and transversal part of the cross-section and the Bjorken x

$$x = \frac{Q^2}{2\bar{m}_N E v}. \quad (4.74)$$

There are multiple approaches [Abr+91; BM02] to approximate the structure-functions using a combination of the individual structure functions of the quasi-particles Reggeon and Pomeron. Here, the ansatz following [Abr+91] is described. Regarding the lowest order, $R_{12} \approx 0$ for this approach while recent measurements indicate that $R_{12} \neq 0$. In other parametrizations of the photonuclear interaction, R_{12} is a function of Q^2 and the Bjorken x. In [BM02], the ratio R_{12} is described by SLAC measurements [Abe+99] for large Bjorken $x > 10^{-3}$ and with an effective VMD model [MRS99] for $x \to 0$.

The structure-function is described by

$$F_2 = F_{2,p} G(x)(Z + (A - Z)R_{pn}) \quad (4.75)$$

with the shadowing $G(x)$ and the relation between structure-function of the proton and neutron

$$R_{pn} = 1 - 1.85x + 2.45x^2 - 2.35x^3 + x^4 \tag{4.76}$$

The structure-function of the proton can be described with an effective photon mass m_γ by

$$F_{2,p} = \frac{Q^2}{Q^2 + m_\gamma^2}(F_2^P + F_2^R) \tag{4.77}$$

where the last term in brackets denotes the structure-function of the Pomeron and Reggeon according to the index. For the following expressions, the index i is a placeholder for either Pomerons (P) or Reggeons R, Their individual structure-functions can be described by

$$F_2^i = c_i x_i^{a_i}(1-x)^{b_i} \tag{4.78}$$

Of these six parameters, the Reggeon parameters a_R, b_R, c_R as well as b_P increase with Q^2, while the other two Pomeron parameters a_P, c_P decrease with Q^2. The Reggeon and Pomeron parameters are approximated with the functions respectively for the increasing and decreasing Q^2 dependency

$$f_i(t) = f_{1,i} + f_{2,i}t^{f_{3,i}} \qquad \text{and} \qquad f_i'(t) = f_{1,i} + (f_{1,i} - f_{2,i})\left(\frac{1}{1+t^{f_{3,i}}} - 1\right), \tag{4.79}$$

where t is defined by

$$t = \ln \frac{\ln \frac{Q^2+Q_0^2}{\Lambda^2}}{\ln \frac{Q_0^2}{\Lambda^2}}, \tag{4.80}$$

using a scale parameter Λ and a further free parameter Q_0^2. The x_i in the structure-function of the Pomeron and Reggeon correspond to the Bjorken x for these quasi-particles

$$x_i = \frac{Q^2 + m_i^2}{Q^2 + m_i^2 + W^2 - \bar{m}_N^2} \tag{4.81}$$

with W describing the invariant mass of the photon

$$W^2 = \bar{m}_N^2 + 2\bar{m}_N Ev - Q^2 \tag{4.82}$$

This results in 18 coefficients for the Reggeon and Pomeron parameters in (4.79) and 5 further fit parameters, $m_\gamma^2, m_P^2, m_R^2, \Lambda^2, Q_0^2$, which are fitted to the electron-proton

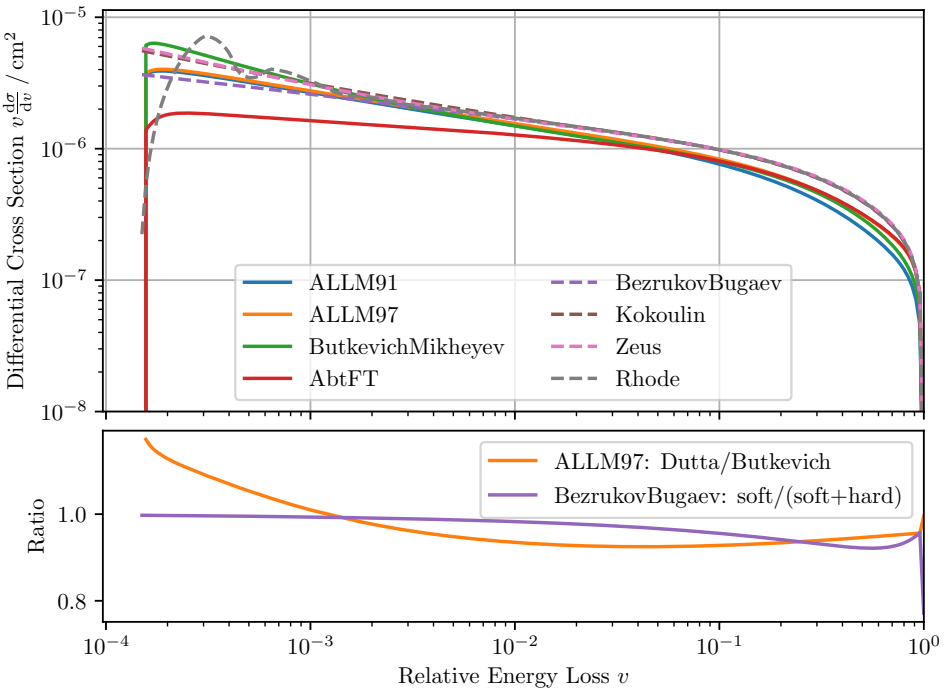

(a) Differential cross-section.

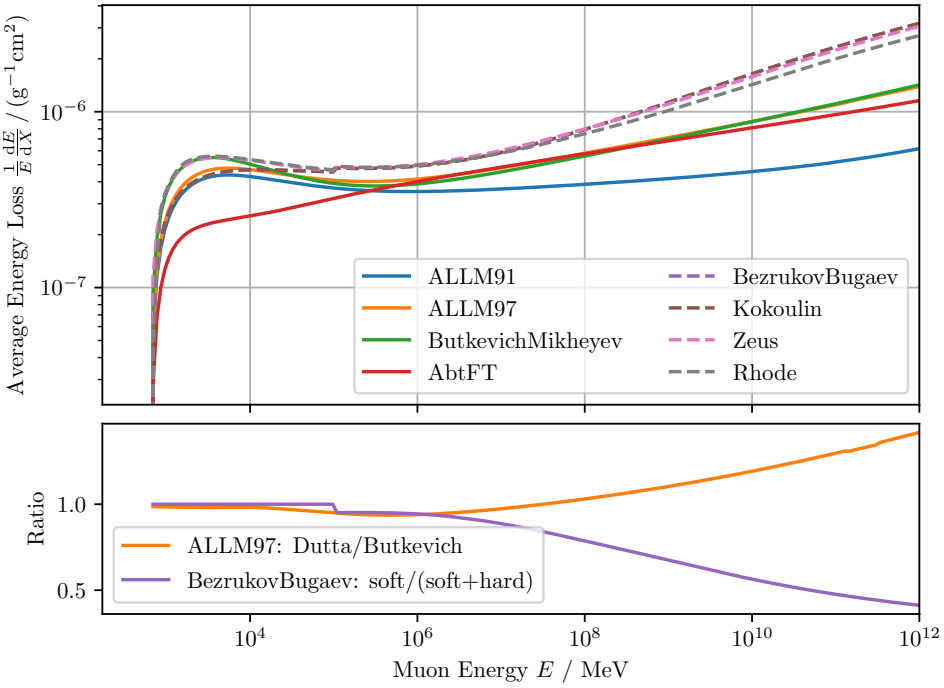

(b) The average energy loss.

Figure 4.17: The cross-section of the inelastic nuclear interaction for muons in Standard Rock using different parametrizations. Straight lines correspond to Regge Models and dashed lines to VMD models. The influence of the hard, perturbative contribution for the VMD model and a different shadowing parametrization for the Regge model is shown in the lower plots.

scattering data of the HERA experiment. There have been multiple revisions [AL97; Abt+17] to the original fit parameters using more recent and accurate measurements. The parameters for multiple revisions are listed in Table A.2.

The shadowing can be described independently of the structure-function calculation. Compared to (4.67), it depends on the Bjorken x. For $Z = 1$ there is no shadowing effect, as described earlier, but for $Z > 1$ other nucleons can interfere with the interacting nucleon. Following the parametrization of [Dut+01], the shadowing can be described by

$$G(x) = \begin{cases} A^{-0.1} & x < 0.0014 \\ A^{0.069 \log_1 0x + 0.097} & 0.0014 \geq x < 0.04 \\ 1 & 0.04 \geq x \end{cases} \tag{4.83}$$

Further shadowing expressions exist e.g. in [BM02]. The effect of choosing between these two shadowing parametrizations is shown in Figure 4.17. Also, the difference in the differential cross-section, as well as the average energy loss, between the mentioned Regge models and the VMD models are shown in Figure 4.17.

4.5.3 Uncertainties

The inelastic nuclear interaction is still the process with the largest uncertainties of $\mathcal{O}(10\%)$ of the four main interactions. These uncertainties mainly arise due to the lack of information in the region of low Q^2 and how precise the extrapolations in the region are. An accurate description also for the limits of $Q^2 \to 0$ and high Q^2 is still a widely discussed topic of research. Regarding the average energy loss in Figure 4.17b, the VMD models are close together as well as the Regge models, neglecting the old ALLM91 parametrization. However, there is a clear separation between these two approaches, that needs to get resolved. Furthermore, it is still unclear how the cross-section increases for higher energies. There is the Froissart bound, that the cross-section can not increase faster than $\ln^2 E$, but the energy dependence could also increase with $\ln E$. Next to the perturbative corrections, which need improvements, at least for the hard component of the VMD model, there are also higher-order radiative corrections, contributing to the cross-section in the percent level. Numerical calculations have been performed in [San18] but these corrections have not been parameterized, yet.

4.6 Rare but Relevant Interactions

There are two further processes, the muon pair production and the weak interaction, which are suppressed by at least 10^{-4} and do not contribute to the energy loss calculation significantly, as already shown in Figure 4.2a. They are therefore smaller than systematic uncertainties of the theoretical models or the interpolation error. However, the following processes are mentioned in this section, and also implemented in PROPOSAL, since they produce unique event signatures inside detectors. Although these processes are rare, they are relevant for astroparticle experiments, which constantly improve their sensitivity and are in particular interested in rare events and processes beyond the standard model.

4.6.1 Muon Pair Production

The production of a $\mu^+\mu^-$-pair is an interesting process since it produces a muon bundle out of a single muon, sometimes called muon trident. The production of a muon bundle by a primary muon is also possible in inelastic nuclear interactions, however, these muons are usually much less energetic compared to a muon trident process.

It is closely related to the e^+e^--pair production and similar Feynman diagrams describe the interaction, just replacing the electron secondaries of Figure 4.12 with muons. In contrast to the electron pair production, two particles of the same kind occur in the final state with the out-going primary and one of the secondaries, and the interference becomes important.

Due to the two secondary particles, the cross-section is, next to the energy loss, also differential in an asymmetry parameter, similar to (4.40). Following the calculation of [KKP00] the cross-section has a similar form compared to the electron pair production (since they are the same authors)

$$\frac{\mathrm{d}\sigma}{\mathrm{d}v\mathrm{d}\rho} = \frac{2}{3\pi}(Z\alpha r_\mu)^2 \frac{1-v}{v} C \ln X. \tag{4.84}$$

Compared to (4.41), r_e is replaced by r_μ, reducing the cross-section by $\mathcal{O}(10^{-4})$. Also for this process, no possibility to change the charge of the primary particle is made as this cross-section is specified only for muons producing muons. However, the mass of the primary particle is not set to m_μ to indicate which term derives from a secondary particle and where the primary mass is used.

A combined expression for the two kinds of diagrams (i.e. e and μ diagrams for the electron pair production) is used

$$C = [(2+\rho^2)(1+\beta) + \xi(3+\rho^2)]\ln(1+1/\xi) \tag{4.85}$$
$$+ [(1+\rho^2)(1+{}^3\!/_2\beta) - (1+2\beta)(1-\rho^2)/\xi]\ln(1+\xi) \tag{4.86}$$
$$- 1 - 3\rho^2 + \beta(1-2\rho^2), \tag{4.87}$$

which is the sum of (4.46) They can be combined, since there is no mass difference between the secondary and the primary particle and therefore also the radiation logarithm approximating the screening is the same. This can be parameterized similar to (4.47) with

$$X = 1 + U_\rho - U_{\rho_{\max}} \tag{4.88}$$

and

$$U_\rho = \frac{0.65A^{-0.27}B_{\text{el}}Z^{-1/3}\frac{M}{m_e}}{1 + \frac{2\sqrt{e}M^2B_{\text{el}}Z^{-1/3}(1+\xi)(1+Y)}{m_eEv(1-\rho^2)}} \qquad \text{with} \qquad Y = 12\sqrt{M/E} \tag{4.89}$$

The dimensionless parameters β and ξ are defined similarly to (4.44) but without the mass terms in ξ as they cancel out.

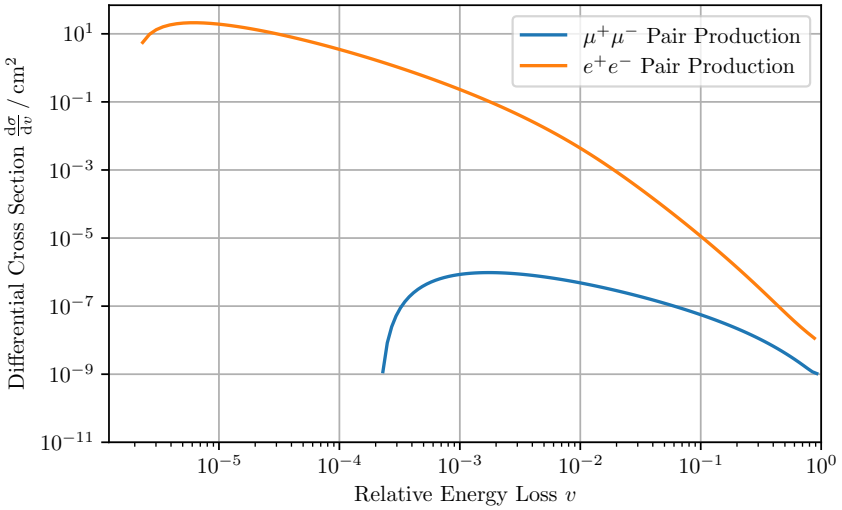

Figure 4.18: Differential cross-section of the muon pair production compared to the two main diagrams of the electron pair production at 1 TeV in Standard Rock.

In contrast to (4.42) there are no relativistic approximation for the kinematic limits

of the asymmetry and the energy loss which are given by

$$v_{\min} = 2m_\mu/E, \qquad v_{\max} = 1 - M/E, \tag{4.90}$$

$$\rho_{\min} = 0, \qquad \rho_{\max} = 1 - \frac{2m_\mu}{vE}. \tag{4.91}$$

After the integration over the asymmetry, the differential cross-section is shown in Figure 4.18 and compared to the other interactions. Due to the similar energy loss dependency, the close relation to the electron pair production can also be seen, here.

The uncertainties of this event are mainly driven by the effective description of the nuclear interaction as well as by the interference terms. However, knowing this process with uncertainties in the percent level, which this cross-section fulfills, is sufficient as this is only a minor correction.

4.6.2 Weak Interaction

The weak interaction, here, describes the exchange of a weak boson with the nucleus. This process is even more suppressed than the muon pair production as shown in Figure 4.2a due to the high mass of the weak bosons, which are created virtually. Regarding the exchange of a $W^\pm$ boson, the muon converts to a neutrino, while producing a large hadronic cascade in the DIS of the weak boson with the nucleus. This is the reverted process of the neutrino interaction described in the Feynman diagrams in Figure 2.6a. Since the neutrino is not visible in a detector, the muon signal disappears. For detectors like the IceCube experiment, searching for rare neutrino events and trying to identify tau neutrinos or Glashow resonances, this rare process needs to be taken into account as a muon background event.

A back of the envelope estimation of the contamination of these muon events compared to an expected tau neutrino flux assuming a $1 : 1 : 1$ neutrino flavor ratio results in a contribution of 10 %. Regarding the exchange of a Z^0 boson, the muon is not converted to a neutrino thus only losing some amount of its energy. This process is just a rare process, which cannot be distinguished from an inelastic nuclear interaction. Therefore only the charge current interaction is relevant and also implemented in PROPOSAL.

The same cross-section used for the neutrino interaction can also be used for this process, due to crossing symmetry. For the used neutrino cross-section calculated by [CMS11], data of the HERA experiment[1] were interpolated for an energy range

[1] For the parton distribution functions, HERAPDF1.5 [Aar+10; Coo10] was used.

of 10 GeV to 10^{12} GeV. The differential cross sections were tabulated for the proton and neutron cross-section. The resulting cross-section for PROPOSAL is the mean cross-section according to the number of the individual nucleons in the nucleus

$$\frac{\mathrm{d}\sigma}{\mathrm{d}y} = \frac{Z}{A}\frac{\mathrm{d}\sigma_p}{\mathrm{d}y} + \left(1 - \frac{Z}{A}\right)\frac{\mathrm{d}\sigma_n}{\mathrm{d}y}. \tag{4.92}$$

The cross-section is also just valid for charged leptons converting into neutrinos in this flavor-changing charged current and not valid for any other particle type. A differential cross-section in the energy loss v would be a delta function at 1 since the muon does not exist afterward. Therefore it has no contribution to the continuous energy loss and is purely stochastic. Instead of the energy loss, it is differential in the Bjorken y describing the relative energy transferred to the nucleus. The limits for the Bjorken y in this parametrization are

$$y_{\mathrm{min}} = \frac{Q^2_{\mathrm{min}}}{E(m_p + m_n) + \left(\frac{m_p + m_n}{2}\right)^2} \qquad \text{and} \qquad y_{\mathrm{max}} = 1, \tag{4.93}$$

where the neutrino mass is neglected for the upper limit and Q^2_{min} is set to $1\,\mathrm{GeV}^2$.

The uncertainty of this interaction is mainly driven by the Parton distribution function and the limitations of perturbative QCD below Q^2_{min}, as already discussed in section 4.5 about the inelastic nuclear interaction. However, due to the rareness of this process, the order of magnitude is sufficient for background rate estimations.

4.7 Scattering and Deflection

In the context of astroparticle physics, the energy loss and the scattering angle are typically calculated independent of each other and not through a two-dimensional differential cross-section, like in particle physics experiments using earth-bound accelerators. The reason for this is again the difference in the detection angle; in astroparticle physics, mainly the particles scattered in the forward direction are measured, where the differential cross-section diverges, while in accelerator experiments the beam pipe excludes the extreme forward region.

Similar to the energy loss processes, also the scattering and deflection of the muons are relevant, although at energies above a TeV the out-going muon direction is highly boosted in the forward direction. Therefore it is mainly relevant for lower energies or for large stochastic interactions, where the muon loses most of its energy, which is mainly driven by bremsstrahlung and inelastic nuclear interactions. However, due to the long ranges muons can propagate, many small deflections can sum up in

measurable deviations from the initial shower axis. Besides, the deflection processes are especially relevant for electron and high energy photons regarding the lateral shower profile of electromagnetic air showers.

4.7.1 Multiple Scattering

Similar to the average energy loss, many small elastic deflections can be averaged and combined for a certain distance X in the so-called *Multiple Scattering*. This is also named after Moliere, who introduced the theory and calculation formalism for this process [Mol47; Mol48]. To increase the performance of the complex calculation, the distribution of the scattering angle can be approximated with a Gaussian distribution introduced in [Hig75] and later improved by [LD91]. The scale of the normal distribution is thereby given as

$$\theta_0 = \frac{13.6\,\mathrm{MeV}}{\beta c_0 p}|z|\sqrt{\frac{X}{X_0}}\left(1 + 0.088\log_{10}\frac{X}{X_0}\right), \tag{4.94}$$

with the radiation length X_0 described in section 5.2.2. The difference between the more accurate description by Moliere and the Gaussian approximation by Highland, Lynch, and Dahl (HLD) is shown in Figure 4.19. Although the Gaussian approximation underestimates the tail of the distribution for large scattering angles, the main part around the peak is accurately described. Therefore it is widely used in simulation algorithms.

4.7.2 Stochastic Deflection

The stochastic scattering process, here, focuses on the deflection of the muons. Although the secondary particles were also emitted not exactly in the forward direction, they are not long-ranged and therefore their direction is not relevant for muon simulations in neutrino telescopes.

For each of the four main muon energy loss processes, a parametrization of the stochastic deflection is implemented in PROPOSAL. Except for the Ionization, where a deterministic deflection is used, the formalism to sample the deflection angle of the muon is described using a random number ξ that is uniformly distributed between zero and one. All of them are independent of the medium and are described in detail in [Gut21].

A comparison between the distribution of sampled deflection angles for the four main processes, described below, is shown in Figure 4.20.

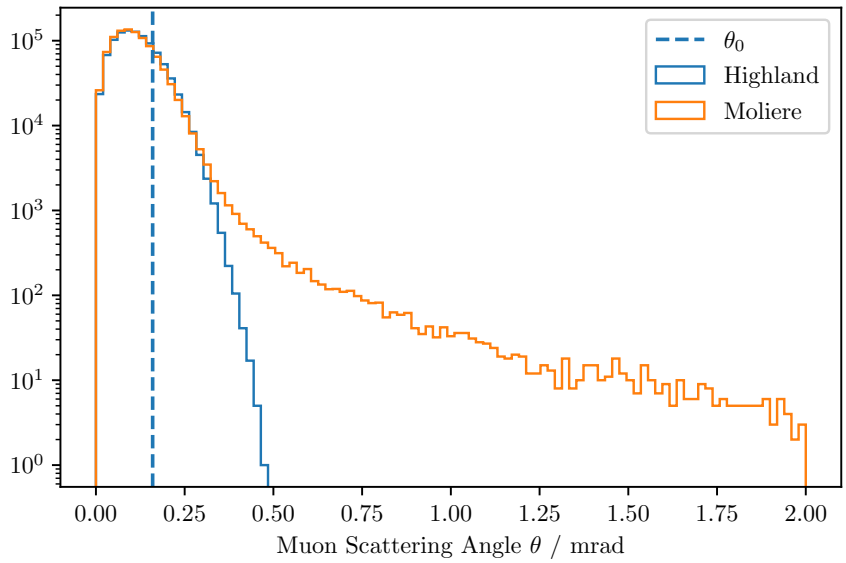

Figure 4.19: Distribution of 10^5 sampled scattering angles of Multiple Scattering comparing the Highland and the Moliere parametrization. The deviation of muons after 10 m in Standard Rock is shown with a fixed initial energy of 1 TeV and final energy of approximated 982 567 MeV according to the average energy loss.

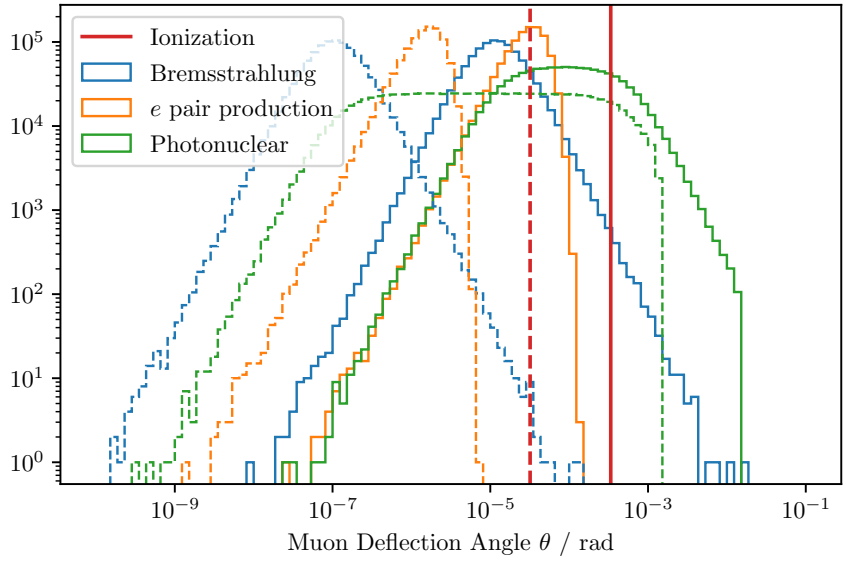

Figure 4.20: Distribution of 10^5 sampled scattering angles comparing the main energy loss processes. The deflection is calculated according to muons with an initial energy of 1 TeV losing 10 % (straight) and 0.1 % (dashed) of their energy in the stochastic process.

The Ionization deflection is calculated using four-momentum conservation and assuming that the atomic electron is at rest before the interaction. Then, the deflection of the muon is defined by [Gut21]

$$\cos\theta = \frac{(E_i + m_e)E_f - E_i m_e - m_\mu^2}{p_i p_f} \tag{4.95}$$

where the indices i, f respectively represent the initial and final energy and momentum of the muon.

For the Bremsstrahlung deflection, the parametrization described in [GEA19] is used, following a distribution proportional to $x/(1+x^2)^2$. A small momentum transfer to the nucleus is assumed and therefore both the photon and the muon have equal transverse momenta resulting in the relation

$$\theta_\gamma = \frac{M}{E} r \qquad \text{and} \qquad \theta_\mu = \frac{v}{1-v}\theta_\gamma \tag{4.96}$$

with

$$r = \sqrt{\frac{a}{1-a}}, \qquad a = \xi \frac{r_{\max}^2}{1+r_{\max}^2}, \qquad r_{\max} = \min\left(1, \frac{1-v}{v}\right)\frac{E}{M}\theta^\star$$

The accuracy for this calculation is around 20 % for deflection angles below $\theta^\star \approx 1°$.

The Pair Production deflection can be expressed following [Van86], assuming an exponential distribution around the mean squared of the deflection angle

$$\theta_\mu = \sqrt{-\ln(1-\xi)\theta_{\text{rms}}^2}, \tag{4.97}$$

which is given by

$$\theta_{\text{rms}} = \frac{2.3 + \ln\frac{E}{\text{GeV}}}{(1-\nu)\frac{E}{\text{GeV}}}\left(1 - \frac{2m_e}{\nu E}\right)^2 \min\left[a\nu^{0.25}\left(1 + \frac{bE}{GeV}\right) + \frac{c\nu}{\nu+1}, e\right] \tag{4.98}$$

with the scaled energy loss parameter $\nu = \frac{v}{1-M/E}$. For muons the constants a to e are given by $a = 8.9 \times 10^{-4}, b = 1.5 \times 10^{-5}, c = 0.032, d = 1, e = 0.1$.

The Photonucular Deflection is again parameterized following the description of [GEA19]. Based on [BP75], the cross section differential in Q^2 (which is called t) is used to estimate the deflection angle resulting in

$$\sin^2 \theta/2 = \frac{t_\xi - t_{\min}}{4E^2(1-v) - M^2 - 2t_{\min}}. \tag{4.99}$$

The limits for the momentum are given by

$$t_{\min} = \frac{M^2 v^2}{1-v} \qquad \text{and} \qquad t_{\max} = 2\bar{M}_N E v \tag{4.100}$$

and the sampled momentum by

$$t_\xi = \frac{t_1}{(1 + {}^{t_1}/_{t_{\max}}) \left[\frac{1+{}^{t_1}/_{t_{\min}}}{1+{}^{t_1}/_{t_{\max}}}\right]^\xi - 1}, \qquad \text{with} \qquad t_1 = \min((Ev)^2, 0.4\,\text{GeV}^2).$$

A simple approximation for the deflection angle, which can be applied to each interaction type is the inverse Lorentz Gamma M/E. This is often used when propagating particles, if no other physical model is available, to include some sort of deflection in the simulation.

4.8 Decay

The discussed decay widths are applicable for any leptonic decay of an initial lepton, which is either a muon or a tau. The muons only have a single decay channel, i.e. $\mu^- \to e^- \nu_\mu \bar{\nu}_e$, while taus have the electronic and the muonic tau component as leptonic channels and further hadronic channels, which are not considered here. Averaging over the polarization, the differential decay width of the electron energy in the rest frame of the muon is given by [Zyl+20]

$$\frac{\mathrm{d}\Gamma}{\mathrm{d}x} = \frac{G_F^2 M^5}{192\pi^3}(3-2x)x^2, \qquad \text{with} \qquad x = \frac{E_l}{E_{l,\max}} \tag{4.101}$$

in the limits

$$E_{l,\min} = m_l, \qquad \text{with} \qquad E_{l,\max} = \frac{M^2 + m_l^2}{2M} \tag{4.102}$$

The index l denotes the produced lepton. In (4.101) the neutrino masses as well as $x_{\min}^2 \sim ({}^{m_l^2}/_{M^2})$ are neglected. This is working for muon decays where the muon mass is 200 times higher than the electron mass. But for muonic tau decays, where the tau is only 17 times heavier than the muon, this approximation can not be

applied anymore. Without this approximation, the differential decay width is given by [LP04]

$$\frac{\mathrm{d}\Gamma}{\mathrm{d}x} = \frac{G_F^2 M^3}{24\pi^3} E_{\max} \sqrt{E_l^2 - m_l^2} \left[3\frac{E_l}{M} - 4\frac{E_l^2}{M^2} + \frac{m_l^2}{M^2} \left(3\frac{E_l}{M} - 2 \right) \right]. \tag{4.103}$$

The difference between these two decay widths can already be seen in the muon decay and is mainly obtained at lower energies of the produced lepton, which is in the tail of the distributions, as shown in Figure 4.21.

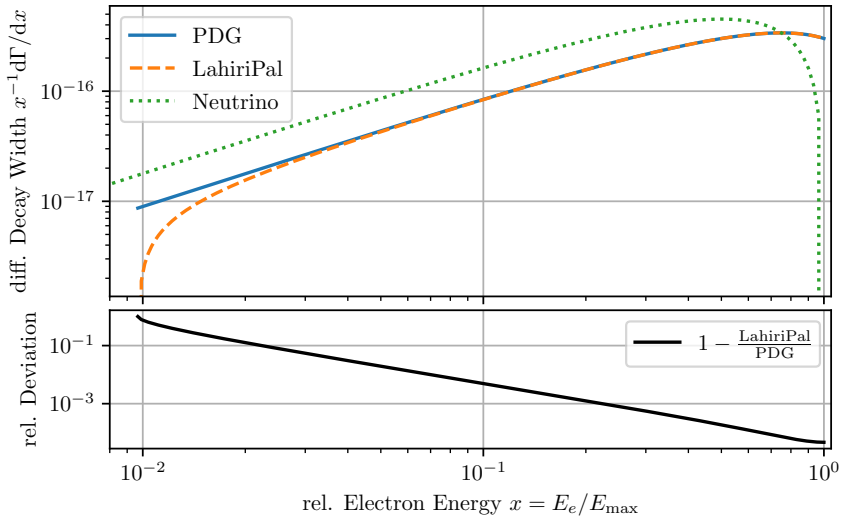

Figure 4.21: The differential decay width of the relative electron energy in muon decays weighted to X^{-1}. The deviation using the approximation $(m_l/M)^2 \approx 0$ (PDG) compared to a more accurate parametrization is shown in the lower plot. For comparisons, the differential decay width of the electron neutrino is also included.

The energy of the produced left-handed electron neutrino can be obtained by the decay rate [Zyl+20]

$$\frac{\mathrm{d}\Gamma}{\mathrm{d}y} = \frac{G_F^2 M^5}{32\pi^3}(1-y)y^2, \qquad \text{with} \qquad y = 2E_{\nu_e}/M. \tag{4.104}$$

In contrast to the electron distribution, the neutrino distribution has its maximum at lower energies as shown in Figure 4.21.

5 Muon Simulation

Each analysis lacking in calibration measurements to perform a data-driven approach to analyze the experimental data requires simulations. These simulations can be deterministic after a given initial condition, e.g. by solving the differential equations describing the processes iteratively, which is used in fluid dynamics. However, high-energy particles behave stochastically during their propagation, choosing from different interactions and producing further stochastic particles. A deterministic approach for particle simulations would mean to average out the stochastic nature of the particle behaviors. This can be used to produce distributions of the incoming particle flux. But also at the edges of the kinematic regions or in the far tail of a distribution, this approach is limited to bin widths introduced when discretizing the differential equations. Besides, experiments in particle or astroparticle physics need to simulate individual event signatures they measure in their detector and therefore Monte-Carlo techniques are used. Thereby, each propagation step is randomly sampled according to the physical distribution.

The name Monte-Carlo is named after the capital of Monaco which is known for its casinos and gambling, where the decision of winning or losing is random and determined e.g. by rolling dice. Transfered to particle physics, the full event simulation consists of the combination of these single random decisions for each propagation step. This allows to fill out the high dimensional phase space of possible event signatures by simulating a huge amount of Monte-Carlo events, which can result in billions of simulated events.

The benefit of Monte-Carlo simulations representing the whole phase space of possible event signatures can be explained by Monte-Carlo integration. For high dimensional integration problems, deterministic approaches, using for example grid-based approaches, get outperformed by Monte-Carlo techniques, which are independent of the dimensions and the accuracy scale only with the square root of the sampling points. While introducing an additional parameter into a high dimensional Monte-Carlo simulation, the number of simulated events required for an accurate description of the allowed phase space, does not increase. Even the edge cases of the phase space are therefore included, which is important in particular as the amount of the interesting signal events in particle physic experiments are typically many orders of magnitude below the number of background events.

In many particle and astroparticle physics experiments, atmospheric muons are the dominant type of background although the detectors are most often located underground to reduce already a huge amount of these disturbing events. For an accurate description of muon events that can, due to their stochastic behavior, mime signal-like events, even the rarest interactions need to be simulated with a decent amount of statistics. A large amount of Monte-Carlo simulations is therefore required to achieve this accuracy and a trade-off between the performance of the simulation and its precision has to be made, adapted to each detector resolution. Also, tools have to be developed to match both requirements with the specialty for muons to propagate through large volumes.

5.1 Muon Simulation Tools

There are multiple simulation tools that can propagate muons. Most of them are based on the methods for the interactions and the average energy loss developed in *MUDEDX* [LKV85] and for the energy thresholds dividing continuous and stochastic energy losses, introduced in *PROPMU* [LS91]. A similar version of the latter is used in KM3Net, called *PropaMuon* [Aie+20]. Due to the deviations observed between these two frameworks [DR01], mainly driven by the difference in their algorithmic approach, further advanced tools were developed. Two examples of these frameworks, that are still maintained and further developed is *MUM* [SBK01; BSK00], used in the Baikal experiment [Bel+97], and the most widely used muon propagator *MUSIC* [Ant+97; KKS99; Kud09], which is used in most underground experiments like Kamiokande [Abe+18].

These simulation tools are mainly used to propagate atmospheric muons from the surface to the underground detector. The muon generation in the air shower and their propagation in the atmosphere to the surface are performed by air shower frameworks like CORSIKA [Hec+98; Eng+19], AIRES [Sci19], or ZHS [ZHS92] for homogeneous media. To generate a muon flux near the detector region and skip the runtime consuming part of the air shower simulation, tools like MUPAGE [CMS09] and MuonGun (based on [Bec+06]) used in the neutrino telescopes KM3NeT and IceCube respectively were developed, parameterizing the energy and zenith dependent flux of the muon bundles in certain depths.

An alternative approach to estimate the atmospheric muon flux near the detector is by using the Matrix cascade equation and solve the differential equation of the shower development, like in CONEX [Ber+07], MCEq [Fed+15], or EMCa [MFH19; ML19], where the latter is specialized in the calculation of electromagnetic component. Out of the estimated flux distribution, individual muons can be sampled to be propagate

inside the detector. However, since the differential equations have to get discretized, the resolution of the simulated muon flux depends on the binning, and muons in the far tails of the flux distribution can not be described accurately.

An alternative approach to overcome the runtime intensive production of large air shower simulation datasets to describe the event signature, but still using Monte-Carlo methods is the backward Monte-Carlo approach by PUMA [Nie+18]. Instead of forward propagating the muons from the air shower to the detector, they get propagated backward from the detector to their initial state in the air shower. This is mainly used when the forward propagation becomes extremely inefficient, e.g. if the detection area is small, while the muons can originate from a wide field of the sky, like in the muon tomography of pyramids.

The simulation of particles inside the detector is nearly always performed by the simulation framework GEANT4 [Ago+03; All+06; All+16; GEA19]. There, the most accurate description of physical models and materials is given. However, the design of the simulation architecture and algorithm is optimized for detectors of the size of $\mathcal{O}(10\,\mathrm{m})$ and already the propagation over distances of 100 m becomes extremely inefficient. For larger detectors, like neutrino telescopes, dedicated tools to propagate particles through large volumes, as described before, are required.

In this work, an alternative to the previously mentioned muon simulation tools, the simulation library *PROPOSAL*, propagating leptons and high energy photons, has been further developed.

5.2 The Leptonpropagator PROPOSAL

PROPOSAL stands for ***PR**opagator with **O**ptimal **P**recision and **O**ptimized **S**peed for **A**ll **L**eptons* and is a C++ and python library for the Monte-Carlo simulation of high energy particles [Köh+13]. Focusing on the electroweak interactions of leptons and high energy photons, PROPOSAL is a simulation library for Monte-Carlo propagation providing multiple selectable interaction and scattering models. It was initially designed to propagate muons through large volumes of media and calculate the tau decay for the IceCube Neutrino Observatory. After a couple of restructuring cycles and further enhancements and improvements PROPOSAL is now a modular simulation library used in several simulation frameworks of astroparticle physics experiments. For the final calculations and plots of this work, version 7.1.0 was used.

PROPOSAL is a free open-source software with an LGPL License and is being developed on GitHub[1]. It can be installed as a classic `cmake` project, using the package manager conan[2] for the C++ library, or pip[3] for the python library. It provides the full track of a propagated particle, single propagation steps or just the theoretical description provided by the cross-sections for fine-tunable settings. These settings are mainly defined by the input particle, the cross-sections and their parametrizations, the medium, and the cuts of the energy loss from which the integrals for the individual propagation steps can be calculated, which is described in the following sections.

5.2.1 Historical Overview

PROPOSAL is the successor of MMC (Muon Monte-Carlo) [Chi03; CR04], written in Java, which was designed to propagate muons efficiently through large volumes of ice for the AMANDA and IceCube detector. There were two different requirements for the muon simulations of neutrino telescopes. First, a highly performant muon propagation through tens of kilometers of ice to the detector to obtain a sufficiently accurate muon spectrum at the detector. Second, a precise muon simulation inside the detector region providing the energy losses for further steps of the simulation chain. Due to the limited detector resolution, these experiments just differentiate between an electromagnetic or hadronic cascade going out of the interaction and are not interested in an accurate sampling of the secondary particles. The propagation of taus was also included while not being the focus in the development. At the energies relevant for IceCube, taus almost immediately decay, which is trivial to calculate when approximating any hadronic decay channel as two-body decay. The electron propagation was not included, since this is equivalent to an electromagnetic cascade.

Next to the efficient propagation of muons, the possibility to perform simulation studies analyzing the effects of systematic uncertainties of the cross-sections was also a key target of this simulation tool. Therefore multiple parametrizations for the bremsstrahlung and photonuclear interactions were implemented. For pair production, there was a lack of comprehensible alternatives and for ionization, which is only dominant for lower energies where these losses can also be measured, the cross-section was already accurate enough.

During the transition of the IceCube software from Java to C++, also the muon and tau simulation chain was rewritten in C++ and renamed to PROPOSAL. This com-

[1] see `https://github.com/tudo-astroparticlephysics/PROPOSAL/`
[2] `https://conan.io/center/proposal`
[3] `https://pypi.org/project/proposal/`

plete revision of the simulation code was done in numerous works at TU Dortmund University. In [Fra11; Sch11] the focus was on the accurate interpolation of the cross-sections while also studying the deviations between the multiple parametrizations for the interactions. Possible calculations on GPUs were tested in [Fuc12] and found to be only relevant for the interpolation methods. In [Gei13] multiple parametrizations for the Molière Scattering were implemented. All of these works were developed under the supervision of [Köh13] and resulted in a publication [Köh+13] summarizing these works and describing the new simulation tool.

For the next years, PROPOSAL was maintained by [Fuc16a] and in close collaboration with the IceCube collaboration. Meanwhile, theoretical calculations on new parametrizations of the bremsstrahlung and pair production cross-sections were developed in [Men14; San14; Soe16]. This was further developed in [San18] leading to the publication [SKR18] of higher-order corrections of the bremsstrahlung cross-section in collaboration with the MEPhI who already developed the commonly used cross-section parametrizations. These new cross-sections for bremsstrahlung and pair production were implemented in PROPOSAL and presented in [SSR19].

In this work, further enhancements and improvements were implemented within multiple restructuring cycles. The first cycle of restructuring together with [Dun18] introduced a more modular and polymorph structure and established PROPOSAL as a software library. Unit tests were introduced to test each part individually and verify the reproducibility of the simulation. Initially intended for easier testing, the so-called propagation utility was introduced collecting the integrals required during the propagation (described in section 5.2.7) and separate them from the main propagation routine. Also, pybindings were introduced so PROPOSAL can be used as a C++ or python library, two of the most common programming languages in the scientific community by now. Furthermore, the decay process was completely revised introducing a new phase space calculation for many-body decays. The whole improvements are described in the publication [Dun+19]. With this new structure, new experiments became interests in using this simulation software, e.g. for radio neutrino astronomy [Gla+20]. A first attempt to introduce neutrino propagation to be able to simulate tau regeneration was done in [Fra20].

The interest in using PROPOSAL for the air shower simulation framework CORSIKA (c.f. section 5.3.2) to calculate the electromagnetic shower component introduced the second round of restructuring to meet these requirements. New cross-sections for electrons, positrons, and high energy photons were implemented in [Ala20] and presented in [Ala+20]. CORSIKA introduced a new kind of use case of PROPOSAL as it wants to get the physics, e.g. the cross-sections or mean free path so that PROPOSAL is proposing an interaction step while CORSIKA is propagating the particles. For this purpose, the propagation utilities became important and the new

level of modularity was introduced. This is mainly described in [Sac21], implementing also new interpolation techniques.

Regarding the most recent developments, in [Gut21] the deflections at stochastic processes were introduced and in [Bol21] the produced electromagnetic air showers in the new CORSIKA framework using PROPOSAL are compared to previous versions of CORSIKA. Jean-Marco Alameddine is the next main developer after this work and was already doing key developments in the second round of restructuring. In the following sections, the current status of PROPOSAL is described.

5.2.2 Medium and Component

In PROPOSAL, the targets, where the particles interact, are either the medium or single components, i.e. the atoms, of the medium. These components are defined by

- the name of the component.
- the charge Z of the component
- the average mass A of an atom

Next to the components defined in the periodic table, there are also effective elements, like the *StandardRock* with $Z = 11, A = 22$, which is an effective description of $CaCO_3$ and a widely used material describing rock. Out of these adjustable parameters, the following parameters are calculated during initialization:

- the average mass of a nucleon $\bar{m}_N$
- the elastic and inelastic constant of the radiation logarithm $B_{\text{(in)el}}$
- the Woods-Saxon potential (up to now, only used in the *ButkevichMikheyev* parametrization)

There are several values given for the constant of the radiation logarithm which is required to describe the elastic atomic form factor (see section 4.3.1). In the Thomas-Fermi model for the electron distribution, $B_{\text{el}} \approx 183$, independent of the nuclear charge but only applicable for elements with high Z [BH34b; Bet34]. However, B_{el} in principle depends on the nuclear charge. A more accurate description using the Hartree-Fock model [KKP99] results in the values listed in Table 5.1. For the constant of the inelastic radiation logarithm, PROPOSAL only differentiates between Hydrogen with $B_{\text{inel}} = 1429$ and all other elements with $B_{\text{inel}} = 1194$ [Tsa74].

Table 5.1: The Z dependence of the elastic radiation logarithm constants in the Hartree-Fock model, calculated in [KKP99]. This parameter was originally introduced as a constant in the logarithm of the screening function Φ_1 in the complete screening approximation.

Z	B_{el}	Z	B_{el}	Z	B_{el}	Z	B_{el}	Z	B_{el}
1	202.4	8	173.4	15	172.2	22	176.8	53	178.6
2	151.9	9	170.0	16	173.4	26	175.8	74	177.6
3	159.9	10	165.8	17	174.3	29	173.1	82	178.0
4	172.3	11	165.8	18	174.8	32	173.0	92	179.8
5	177.9	12	167.1	19	175.1	35	173.5		
6	178.3	13	169.1	20	175.6	42	175.9	others	182.7
7	176.6	14	170.8	21	176.2	50	177.4		

The Wood-Saxon potential is defined by [BM02]

$$N_S(A) = 4\pi\rho_0 \int_{r_0}^{\infty} \frac{r^2}{1+\exp((r-r_0)/a)} \mathrm{d}r \quad \text{with} \quad r_0 = 1.12A^{1/3} - 0.86A^{-1/3}. \tag{5.1}$$

For a constant $a = 0.54\,\text{fm}$ and $\rho_0 = 0.17\,\text{fm}^{-3}$, it can analytically be integrated to

$$N_S(A) = 4\pi\rho_0[ar_0^2\log(2) + a^2 r_0\pi^2/6 + 3/2 a^3\zeta(3)], \tag{5.2}$$

where $\zeta(x)$ is the Riemann zeta function.

There are also processes, where the interaction is a continuous process and does not occur at a single atom, like the density correction for ionization or the LPM and dielectric effect. The medium constants for the ionization and density correction were already given in section 4.2. Besides, the medium is defined by its density, which can be varied according to a given density distribution, described in section 5.2.3.

From the list of components and the density, the following parameters are calculated during the initialization:

- the number of protons, i.e. the charge Z
- the number of nucleons
- the mol density

- the radiation length, which is required for the LPM effect and the description of multiple scattering

The radiation length describes the distance when the electron has on average lost $1/e$ of its energy. Since bremsstrahlung is the dominating process, the total cross-section of the electron bremsstrahlung in the complete screening case is used to calculate the radiation length

$$X_0 = \frac{\sum A}{\sum \sigma_{e,\text{brems.}} A}, \tag{5.3}$$

where the sum is over each component.

The densities for a medium are mainly taken from [Zyl+20]. However, there are processes, like the LPM effect, depending on the density of the medium in a more complex way than just a linear factor in the cross-section. In principle, the change of the density can therefore not be treated independently of the cross-section. Since the cross-sections are interpolated before the propagation to increase the performance, approximations are required, like assuming a locally homogeneous medium. This issue is also faced by other simulation frameworks and finding a decent approximation or alternative treatment is still an ongoing topic of research.

5.2.3 Geometries and Density Profiles

A particle can be propagated through different sectors of media, each defined by a geometry and a density distribution.

There are three geometries available in PROPOSAL.

- A `sphere` is defined by the coordinate of its origin and its `radius`. The sphere can also be a spherical shell by setting an `inner_radius`, which is e.g. used to describe the different layers of the earth.
- A `cylinder` is defined by the same parameters of a `radius` and an `inner_radius` as the spherical shell and the `height`. In contrast to the radius, there is no inner height of the cylindric shell.
- A `box` is defined by the center coordinate and the `length`, `width`, and `height`. Compared to the sphere or the cylinder, no inner lengths can be defined.

With these geometries, the environment of the simulation can be created. Each geometry also consists of a `hierarchy` parameter, that in the case of overlapping geometries, the one with a higher hierarchy is chosen. If both hierarchies are equal, the geometry with a higher density is used.

The density inside a geometry can also be varied along an axis using the following density profiles

- A homogeneous density
- An exponential decreasing or increasing density
- A polynomial density distribution
- A distribution defined by interpolating splines.

Not for all interactions, the density can be treated separately. The LPM effect has larger effects if the medium is denser and the distance to the next atom is smaller resulting in stronger influences of their wave functions with the interaction. However, the cross-section integrals, described in section 5.2.6, as well as the propagation integrals, described in section 5.2.7, are interpolated before the propagation. Therefore density effects in inhomogeneous media can only be taken into account for a reference point assuming no major changes of the density inside the geometry. Since the density effects are mainly minor corrections or have significant effects only at higher energies, this is still applicable for most experiments. Nevertheless, this is an important issue, which needs to get solved in the future, especially for the electron, positron, and photon propagation in the atmosphere.

5.2.4 Particles and Secondaries

As the name of PROPOSAL suggests, all leptons, meaning charged leptons of all three flavors (electrons, muons, and taus) including their anti-particles and their corresponding neutrinos can be propagated. In addition, high-energy photons can also be propagated due to similar propagation behaviors. Also, exotic particles beyond the Standard Model of particle physics like magnetic monopoles and supersymmetric staus are implemented and can be propagated using the same propagation techniques. Since all cross-sections are implemented adapting to the mass and charge of the primary particle, as described in chapter 4, the same cross-sections as for the muon propagation can be used for custom particles, e.g. a muon with a mass of 500 GeV or a milicharged particle with a charge of 10^{-3} [Ple+20; AKM21]. The simple adaption of the particle definition is limited to the cross-sections for charged and massive particles; cross-sections for neutrinos or high energy photons can not be used for this.

In principle, every kind of particle can be propagated by changing the particle properties and using a set of suitable cross-sections given to the propagation. For the above-mentioned particles, the relevant cross-sections or decay channels are

implemented. Further cross-sections can simply be added. The particle properties called `ParticleDef` consist of the following parameters.

- The `name` of the particle.
- The `mass` of the particle.
- The parameter `low` defining the lower limit of the particle energy to calculate the propagation integrals for the interpolation tables, thereby defining the lower limit until the particle can be propagated. This is usually set to the mass of the particle except for the massless particles, where it is a small value, which is necessary due to the logarithmic energy scale of the interpolation. For photons, the value is two times the electron mass.
- The `lifetime` of the particle. Stable or exotic particles have an infinite lifetime.
- The `charge` of the particle.
- The `hard_component_table` containing the parameters for the optional nuclear inelastic interaction. These tables are only provided for muons and taus (c.f. section 4.5.1).
- The `decay_table` listing the possible decay channels for the particle. This is only provided for muons and taus.
- The `particle_type` is the PDG code the particle.
- The `weak_partner` is the PDG code of the weak partner particle produced in a charged current weak interaction. This is only defined for leptons.

To propagate these particles, the dynamic properties are collected in the so-called `ParticleState` storing the following parameters.

- The `position` of the particle.
- The `direction` of the particle.
- The `energy` of the particle. This directly also sets the `momentum` for massive particles.
- The simulation `time` of the particle.
- The `propagated_distance` storing the distance the particle has been propagated.
- The `type` of the particle, i.e. an identifier using the PDG codes.

Next to the particles that can be propagated, the secondary particles of the decays or interactions, abbreviated as secondaries, are implemented. They can either be extracted as pseudo particles just referring to the type of the interaction and its dynamic properties similar to the `ParticleState`. Adaptations are made for continuous energy losses, which have an initial and final time or direction. On the other side, also real particles can be sampled out of these pseudo decay or energy loss objects.

For the bremsstrahlung or the ionization, where just a photon or an electron is produced, this conversion is trivial. For the electron or muon pair production, the asymmetry parameter ρ, see (4.41) or (4.84) of the electron or muon pair can be sampled to distribute the energy loss among the individual particles. For the photonuclear interaction, it is not possible in PROPOSAL to sample individual particles, since the complex calculation to simulate particles of a hadronic shower is a research topic on its own, still facing the problem of the *muon puzzle* (see section 2.1.2). Existing tools are dealing specifically with hadronic cascades, like Sibyll [Rie+20] or QGSJet [Ost11], which an applicant can use if this is required. The direction of these secondaries of energy losses, either they are pseudo or real particles, are set to the direction of the primary particle before the stochastic process. Although, there are deflection calculations for the primary particle, as described in section 4.7.2, but no deflection for the secondaries, yet.

For the decay, there is also the possibility to sample the individual product particles out of a pseudo decay object. However, the decay process differs compared to the energy loss processes, as not all of the decay energy is stored in an electromagnetic or hadronic cascade as some amount of the energy is taken away by the neutrinos. Therefore, it is also possible to sample just the energy that is stored in a hadronic or electromagnetic cascade and therefore visible to the detector. For the leptonic decays, only the produced electron or muon can be sampled. For hadronic decays, only the neutrino energy needs to get sampled.

5.2.5 Cross Sections

Next to the cross-sections relevant for the muon propagation described in section 4 there are further parametrizations available for most interactions to perform systematic studies on the effect of different cross-sections on the propagation. The additional interactions and parametrizations for electrons, positrons, and high energy photons to produce an electromagnetic shower are based on the simulation software EGS [Hir+05] and are described in [Ala20]. For the neutrino propagation, the cross-sections of [CMS11] are used which are already introduced for the weak interaction. Additional effects like the Glashow resonance or neutrino oscillations are

not implemented, yet. For each of the main particle types that can be propagated, there is a default cross-section set available to reduce the complexity of the usage. A complete description of the available processes and their parametrizations are listed in Table 5.2. Their names are most often the authors of the corresponding publication, or with a descriptive naming of their purpose.

Table 5.2: List of implemented cross-section parametrizations in PROPOSAL.

Ionization	**Photonuclear**	**Annihilation**
BetheBlochRossi	VMD	Heitler
BergerSeltzerBhabha	Zeus	
BergerSeltzerMoller	BezrukovBugaev	**Compton**
	Kokoulin	KleinNishina
Bremsstrahlung	Rhode	
KelnerKokoulinPetrukhin	Regge	**Photo Pair Production**
PetrukhinShestakov	ALLM91[4]	Tsai
CompleteScreening	ALLM97[5]	
AndreevBezrukovBugaev	ButkevichMikheyev	μ **Pair Production**
SandrockSoedingreksoRhode	RenoSarcevicSu	KelnerKokoulinPetrukhin
ElectronScreening	AbtFT	
	BlockDurandHa	**Weak Interaction**
e **Pair Production**		CooperSarkarMertsch
KelnerKokoulinPetrukhin	Shadowing	
SandrockSoedingreksoRhode	DRSS[6]	
ForElectronPositron	ButkevichMikheyev	

For **Ionization** the default cross-section for massive particles is the parametrization called *BetheBlochRossi*, i.e. the parametrization described in section 4.2. Due to the additional Feynman diagrams for electrons with Bhabha scattering and positrons with Møller scattering, the default cross-section are slightly different and are labeled *BergerSeltzerBhabha* and *BergerSeltzerMoller* [Bha36; Møl32; BS64].

For the **Bremsstrahlung**, the default cross-section is the widely used *KelnerKokoulinPetrukhin* parametrization, described in section 4.3.2. A parametrization using the analytical interpolation of the screening as described in (4.16) and another approach for the nuclear form factor is given by the *PetrukhinShestakov* parametrization [PS68]. In the *AndreevBezrukovBugaev* parametrization [ABB94], no approximation of the screening ($\Phi_1 \neq \Phi_2$) was made. The calculation combining the benefits of these three parametrizations with additional radiative corrections is the *SandrockSoedingreksoRhode* parametrization, which is described in section 4.3. There is also a parametrization approximated for high energies, called *CompleteScreening*. Since

bremsstrahlung is the dominant energy loss process for electrons and positrons, there is a dedicated parametrization for them, called *ElectronScreening*.

For the e **pair production**, the widely used default is the *KelnerKokoulinPetrukhin* parametrization [KP71; Kel98], described in section 4.4.1. A parametrization without the screening approximation ($\Phi_1 \neq \Phi_2$) is *SandrockSoedingreksoRhode* [SSR19]. There is a dedicated parametrization, *ForElectronPositron*, again for electrons and positrons, due to the interference terms of the same particles in the final state. This is similar to the **muon pair production** (c.f. section 4.6.1), where the parametrization is called *KelnerKokoulinPetrukhin* [KKP00].

The **inelastic nuclear interaction** is the relevant processes with the highest theoretical uncertainties. Hence the one with the most parametrizations that can be divided into the approach of a Vector Meson Dominance and the Regge models as described in section 4.5. For the VMD model, there are the parametrizations of *BezrukovBugaev* [BB80], *Kokoulin* [KP97], *Rhode* [Rho93], and *Zeus* [Bre+99], already described in section 4.5.1. For the Regge models, there is the initial *AbramowiczLevinLevyMaor* parametrization published in the year 1991 [Abr+91] and the parametrization from 1997 using updated fit parameters [AL97], where the latter is the default photonuclear parametrization. This fit was redone on more recent HERA measurements in 2017 which can be used with *AbtFT* [Abt+17]. Two alternative approaches can be used with the parametrization *ButkevichMikheyev* [BM02] and with *BlockDurandHa* [BDH14]. Dedicated for supersymmetric staus, a calculation for spin 0 particles is available under the name *RenoSarcevicSu*. For the Regge models also the parametrization of the shadowing effect can be selected. There is the *ButkevichMikheyev* parametrization, corresponding to the same-named cross-section and alternatively the *DuttaRenoSarcevicSeckel* [Dut+01] parametrization of the shadowing effect.

For the dedicated interactions of recently added particles to propagate, i.e. electrons, positrons, high energy photons, and neutrinos, there is up to now, only one parametrization per interaction available. The **Weak Interaction** either for neutrino propagation or for charged leptons is described by the parametrization of *CooperSarkarMertsch* [CMS11]. For the **Annihilation** of a positron interacting with an atomic electron, the parametrization of *Heitler* [Hei54] is used. For high energy photons, the processes of **Pair Production** and **Compton Scattering** are included described by the parametrization names *Tsai* and *KleinNishina* respectively.

All cross-sections are implemented differential in the relative energy loss v as $\mathrm{d}\sigma/\mathrm{d}v$, except for the purely stochastic processes, from now on called catastrophic interactions, where the primary particle does not exist anymore, i.e. Annihilation, weak interaction, and pair production by photons. For cross-sections that are also

differential in a second parameter, i.e. the asymmetry ρ in the electron and muon pair production or the momentum Q^2 for the Regge approach of the photonuclear interaction, this second dimension is integrated numerically for a consistent treatment of the cross-sections.

To create a cross-section in PROPOSAL, one has to define at least a `ParticleDef` and a `Medium` or `Component` object, where the interaction takes place. It is also possible to scale a cross section using a `Multiplier`, which can be adapted for each interaction individually. Besides the implementation of different parametrizations for an interaction, this scaling can be used to analyze uncertainties of the cross section (c.f. section 6.2). For the total cross-section or the average energy loss, also the energy loss cut, described in the next section needs to be defined in case of non-catastrophic interactions.

5.2.6 Energy Loss Cuts Separating Continuous and Stochastic Losses

Before describing the propagation principles the energy loss cuts, as an important mechanism to simulate muons, needs to be introduced. As outlined in chapter 4.3 the bremsstrahlung cross-section on an isolated atom diverges for small energy losses, meaning that there is an infinite possibility to create a photon with no energy. Compared to the other interactions, where the lower limit is defined by the masses of the produced particles, the lower limit for bremsstrahlung is 0 due to the massless photon. Although the bremsstrahlung cross-section does not diverge when propagating through media due to the dielectric effect, calculating this interaction is still numerically unstable and should be avoided.

Even when neglecting bremsstrahlung, it is also highly inefficient to simulate a huge amount of low energetic electrons produced in small energy losses regarding pair production or ionization with lower thresholds for the energy loss of $\approx 1\,\mathrm{MeV}$ and $\mathcal{O}(100\,\mathrm{eV})$ respectively. It would cost more runtime during the simulation and more resources to store all the energy losses, which might not even get measured by the detector.

Therefore all small energy losses up to a certain threshold are combined and averaged out into a continuous loss. In PROPOSAL, this threshold can be set as an absolute energy, called e_{cut} or relative to the energy of the primary particle, called v_{cut}. The threshold is then chosen as the minimum between both,

$$e_{\mathrm{cut}} = \min(e'_{\mathrm{cut}}, v_{\mathrm{cut}} \cdot E_{\mathrm{particle}}) \quad \text{with } e_{\mathrm{cut}} \in (0, \infty) \text{ and } v_{\mathrm{cut}} \in (0, 1]. \tag{5.4}$$

A purely continuous simulation can be achieved with $e_{\mathrm{cut}} = \infty$ and $v_{\mathrm{cut}} = 1$. This would be without any stochasticity and therefore deterministic.

First introduced in [LS91], the energy loss cut represents the threshold between an average energy loss

$$f(E) := -\frac{\mathrm{d}E}{\mathrm{d}X} = E \cdot \sum_{\text{processes}} \sum_{\substack{\text{atom} \\ \text{in medium}}} \frac{N_A}{A} \int_{v_{\min}}^{v_{\text{cut}}} v \frac{\mathrm{d}\sigma}{\mathrm{d}v} \mathrm{d}v \tag{5.5}$$

and the number of stochastic losses per distance

$$\frac{\mathrm{d}N}{\mathrm{d}X} = \sum_{\text{processes}} \sum_{\substack{\text{atom} \\ \text{in medium}}} \frac{N_A}{A} \sigma(E), \qquad \text{with} \qquad \sigma(E) := \int_{v_{\text{cut}}}^{v_{\max}} \frac{\mathrm{d}\sigma}{\mathrm{d}v} \mathrm{d}v. \tag{5.6}$$

The abbreviations $f(E)$ and $\sigma(E)$ are defined to be consistent with the literature. With this approach, all small energy losses with an energy $E_{\text{Loss}} < e_{\text{cut}}$ are combined to a continuous loss and averaged out, while all energy losses above the cut are treated stochastically. The energy loss cut is therefore an important parameter to adjust both the performance and precision of the propagation focusing on the former by using high cuts, or on the latter by using small cuts.

In Figure 5.1 the effect of different energy loss cuts on the average energy loss and the stochastic interaction probability is shown. Compared to the average energy loss without an energy loss cut (see Figure 4.2a), the ionization dominates the small energy losses, also at higher muon energies. The huge amount of low energetic ionization losses is also seen in the stochastic interaction probability and the rise of the number of secondaries between the already low cut of 500 MeV and the cut at 1 MeV.

The integrals presented in (5.5) and (5.6) are interpolated and can then be used for the propagation integrals described in the next section. Next to these two integrals of the cross-sections, a third integral is created when using the option `continuous_randomization`, described in section 5.2.8. Hereby, the second momentum of the cross-section

$$\left\langle \frac{\mathrm{d}E^2}{\mathrm{d}X} \right\rangle = E^2 \int_{v_{\min}}^{v_{\text{cut}}} v^2 \frac{\mathrm{d}\sigma}{\mathrm{d}v} \mathrm{d}v \tag{5.7}$$

is calculated and used to smear out the continuous energy loss and slightly randomize the deterministic calculation.

5.2.7 *One propagation step for PROPOSAL*

Out of the cross-sections and the energy loss cuts, the propagation integrals, collected in the so-called `propagation_utilities` can be calculated. These integrals or utilities are required to perform a single propagation step.

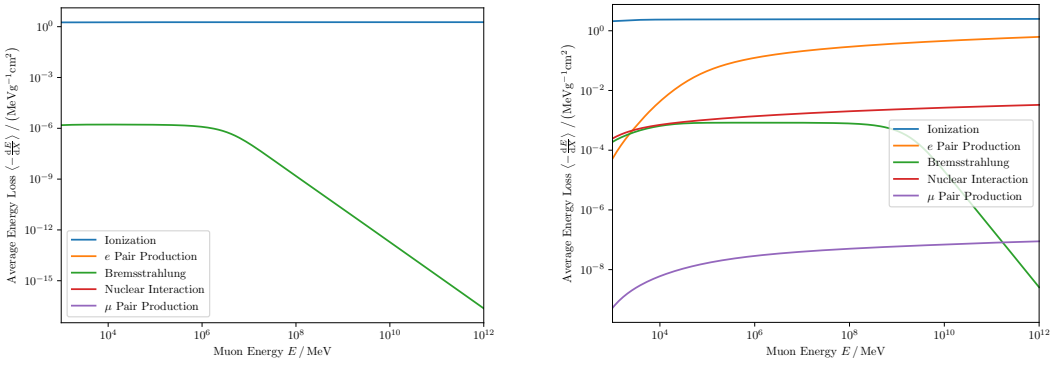

(a) $\left\langle \frac{\mathrm{d}E}{\mathrm{d}X} \right\rangle$ with $e_{\mathrm{cut}} = 1\,\mathrm{MeV}$.

(b) $\left\langle \frac{\mathrm{d}E}{\mathrm{d}X} \right\rangle$ with $e_{\mathrm{cut}} = 500\,\mathrm{MeV}$.

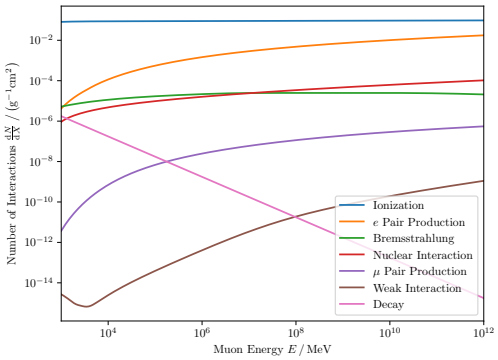

(c) $\frac{\mathrm{d}N}{\mathrm{d}X}$ with $e_{\mathrm{cut}} = 1\,\mathrm{MeV}$.

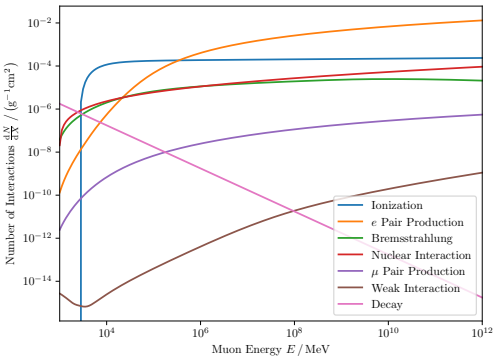

(d) $\frac{\mathrm{d}N}{\mathrm{d}X}$ with $e_{\mathrm{cut}} = 500\,\mathrm{MeV}$.

Figure 5.1: Continuous energy loss and stochastic interaction probability of muons in Ice for an energy loss cut of 1 MeV and 500 MeV.

There are two approaches on how PROPOSAL can estimate or sample from an initial state i the next interaction point with the final state f;

- by solving the energy integral taking into account the continuous losses,
- and by using the mean free path length assuming no continuous losses.

If the particle propagation includes also continuous energy losses, which is the case for charged leptons, the default approach to sample the next interaction is by solving the so-called **Energy Integral**

$$P(E_i \leq E \leq E_f) = -\int_{E_i}^{E_f} p(E)\mathrm{d}E, \tag{5.8}$$

with the probability distribution $p(E)$ for an interaction and the cumulative distribution $P(E)$. The general idea was developed in [SBK01] and [CR04]. Instead of sampling a distance or length, the calculation is performed in energies, which is more accurate and numerically stable and e.g. independent of the density (when neglecting effect such as the LPM dependence). The goal is to sample the energy E_f the muon has, right before it has the next stochastic interaction while the difference between the initial energy E_i and E_f is lost due to continuous losses. In a second step, the distance is calculated according to the sampled E_f, see (5.19).

To derive the energy integral to calculate the next stochastic point, the track between the initial and final state is divided into infinitesimal small track sections Δx. The probability of having no stochastic loss in each of these track sections but one stochastic interaction at the state f can be written as

$$\Delta P_f = \prod_{j=i}^{f-1}(1-\sigma_j\Delta x_j)\sigma_f\Delta x_f \tag{5.9}$$

$$\approx \exp\left(-\sum_{j=i}^{f-1}\sigma_j\Delta x_j\right)\sigma_f\Delta x_f \tag{5.10}$$

$$\xrightarrow{\Delta x\to 0} \mathrm{d}P_f = \exp\left(-\int_{x_i}^{x_f}\sigma(E(x))\mathrm{d}x\right)\sigma_f\mathrm{d}x_f \tag{5.11}$$

where the approximation of $\Delta x \ll 1$ is used in the second line and $\sigma_j = \sigma(E(x_j))$ is the probability for a stochastic loss at state j as defined in (5.6). For the transformation to an energy integral, (5.5) is used, resulting in

$$\mathrm{d}P_f = \exp\left(\int_{E_i}^{E_f}\frac{\sigma(E)}{f(E)}\right)\frac{\sigma(E_f)}{-f(E_f)}\mathrm{d}E_f. \tag{5.12}$$

When integrating over the probabilities the cumulative distribution of (5.8) is obtained

$$P(E_f \leq E \leq E_i) = \int_{P_i=0}^{P_f} \mathrm{d}P_f. \tag{5.13}$$

This can be integrated using the substitution

$$u(E) = \int_{E_i}^{E} \frac{\sigma(E')}{f(E')}\mathrm{d}E' \qquad \text{and} \qquad \mathrm{d}u = \frac{\sigma(E)}{f(E)}\mathrm{d}E, \tag{5.14}$$

resulting in

$$P(E_f \leq E \leq E_i) = \exp\left(\int_{E_i}^{E_f} \frac{\sigma(E)}{f(E)}\mathrm{d}E\right). \tag{5.15}$$

Finally, the energy E_f can be sampled using a random number $\xi \in (0, 1]$ with

$$\ln \xi = \int_{E_i}^{E_f} \frac{\sigma(E)}{f(E)}\mathrm{d}E, \tag{5.16}$$

which has a solution if

$$\xi < \exp\left(\int_{E_i}^{E_{\text{low}}} \frac{\sigma(E)}{f(E)}\mathrm{d}E\right), \tag{5.17}$$

where E_{low} is the `low` parameter of the particle definition, described in section 5.2.4, and therefore always smaller than E_i. If the random number is greater than the integral, there is no stochastic loss.

If the particle can decay, the energy $E_{f,\text{decay}}$, where the next decay would occur, can be sampled similarly to solving the energy integral for interactions. By replacing the interaction probability in (5.16) with the decay cross-section defined in (4.2), the **Decay Integral** is defined by

$$\rho \ln \xi = \int_{E_i}^{E_{f,\text{decay}}} \frac{\mathrm{d}E}{f(E)\gamma\beta\tau c_0}. \tag{5.18}$$

In contrast to the interaction cross-sections, the decay cross-section is independent of the medium and the density does not cancel out with the continuous losses. Therefore, the density must be taken into account.

Out of the sampled energy E_f, the distance where the next stochastic loss would occur can be calculated using the so-called **Tracking Integral**, defined by

$$-\int_{E_i}^{E_f} \frac{\mathrm{d}E}{f(E)} = \int_{x_f}^{x_i} \rho(x)\mathrm{d}x \xrightarrow{\rho=const.} x_i - x_f. \tag{5.19}$$

For inhomogeneous media, the density profile needs to be considered for the tracking integral. Alternatively, the distance can be calculated in units of grammage instead of distances, separating the density distribution from the tracking integral.

Regarding purely stochastic propagations, e.g. for neutrinos, there is no energy loss between two stochastic interactions. Therefore the calculations are not in energies, but in distances, and the interaction and tracking integrals (5.11) and (5.19) reduce to

$$x_f - x_i = \frac{-\ln \xi}{\sigma(E)}. \tag{5.20}$$

This equation can also be derived by sampling from an exponential distribution with the mean free path length of the interactions, which is proportional to the inverse cross-section. It is also applicable for scenarios where continuous energy losses are present, but where the step length between two stochastic losses is small. In Figure 5.2, a comparison between the two approaches of calculating the next interaction point is shown. Only for the rare scenarios, in which most of the energy is lost, there are larger deviations.

Next to the sampled decay or interaction energy, also energy thresholds can be set optionally limiting estimation of the next track point or energy. This can either be a limitation in the maximum energy the particle can lose continuously between two stochastic interactions. Another limitation of the energy is that the particle energy threshold has been reached, i.e. the minimal energy, until the particle should get propagated. The final energy of a single propagation step is therefore defined by

$$E_f = \max(E_{\text{interaction}}, E_{\text{decay}}, E_i - E_{\text{max continuous loss}}, E_{\text{min particle}}) \tag{5.21}$$

The next track point is finally chosen between the sampled interaction point, calculated either via the estimated energy with (5.21) or directly via (5.20), the

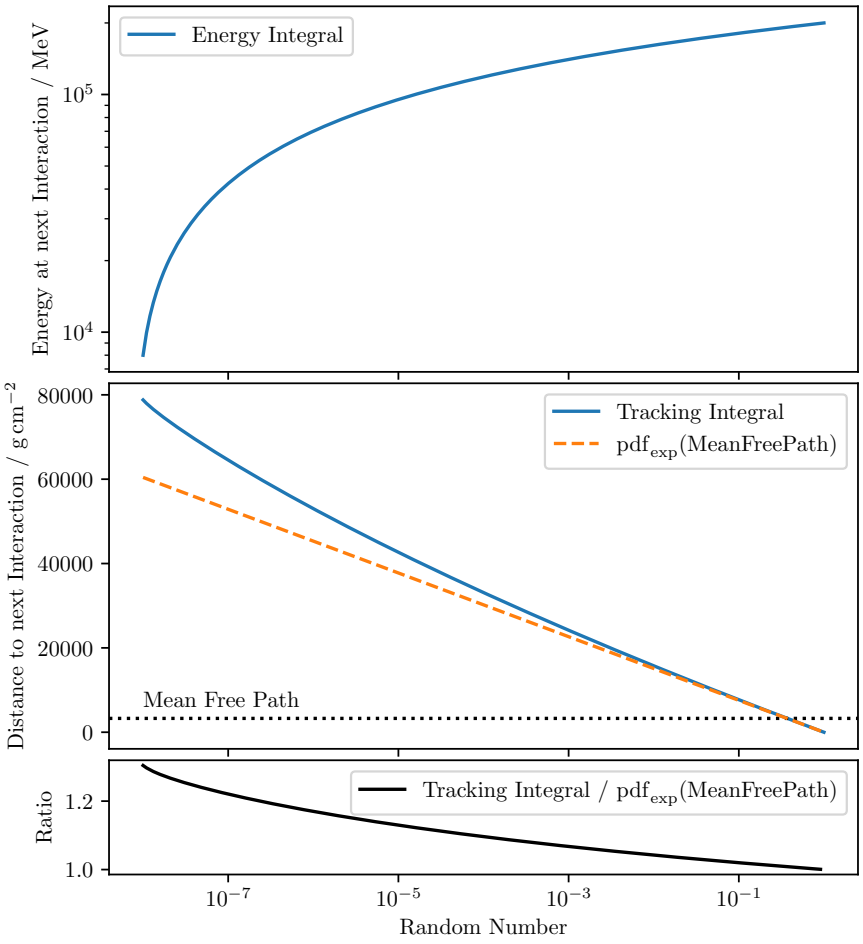

Figure 5.2: Calculation of the distance to the next interaction point for a muon with an initial energy of 2×10^5 MeV in ice using an energy loss cut of 500 MeV. The approach using the tracking integral via the sampled energy integral is compared to a sampling of an exponential probability distribution function (pdf) with the mean free path length as the scale parameter.

step limitation, and the edge of the current geometry, the particle is propagated through

$$x_f = \min(x_{\text{interaction}}, x_{\text{max step}}, x_{\text{border}}). \tag{5.22}$$

The limitation of the step length, in the energy or the distance, is important for processes assuming a constant particle energy between two stochastic interactions, especially when calculating the magnetic pulse of an air shower. However, when forcing maximum continuous losses of e.g. 1 % of the initial energy, this can results in many small propagation steps without a stochastic loss for lower energies and thereby an inefficient performance.

The **Time Integral** calculating the time until the particle reached a certain energy loss can either be calculated in a similar way as the tracking integral including the continuous losses resulting in

$$t_i - t_f = \int_{E_i}^{E_f} \frac{\mathrm{d}E}{f(E)} \frac{1}{\underbrace{c_0 p/E}_{v(E)}}. \tag{5.23}$$

For only stochastic propagations of massless particles like photons or neutrinos, the time can be calculated with

$$t_i - t_f = \frac{x_f - x_i}{c_0}. \tag{5.24}$$

At high energies, this is also an accurate approximation if the particles are massive and lose energy along the track since the assumption of propagating with the speed of light is a good approximation, as shown in Figure 5.3.

In case a non-catastrophic interaction is chosen, the relative energy loss of the stochastic interaction is sampled with the so-called **Stochastic Integral**

$$\xi = \frac{1}{\sigma(E)} \int_{v_{\text{cut}}}^{v_{\text{Loss}}} \frac{\mathrm{d}\sigma}{\mathrm{d}v} \mathrm{d}v. \tag{5.25}$$

The estimation of the stochastic interaction can be divided into three parts; the interaction type, the target with which it interacts, i.e. the atom or in case of ionization the medium, and the relative energy loss. By stacking these probabilities, the interaction can be sampled with a single inverted cumulative probability distribution, shown in Figure 5.4.

After calculating the stochastic energy loss, the stochastic deflection can optionally be sampled, as described in section 4.7.2. Finally, the remaining dynamic properties

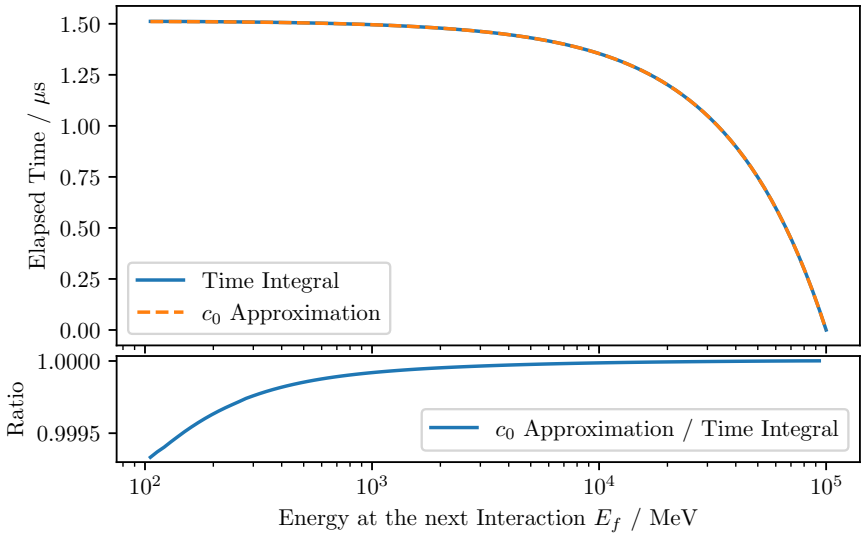

Figure 5.3: Calculation of the time at the next interaction point for a muon with an initial energy of 10^5 MeV in ice using an energy loss cut of 500 MeV. The approach of the time integral is compared to the approximation that the particle propagates with c_0.

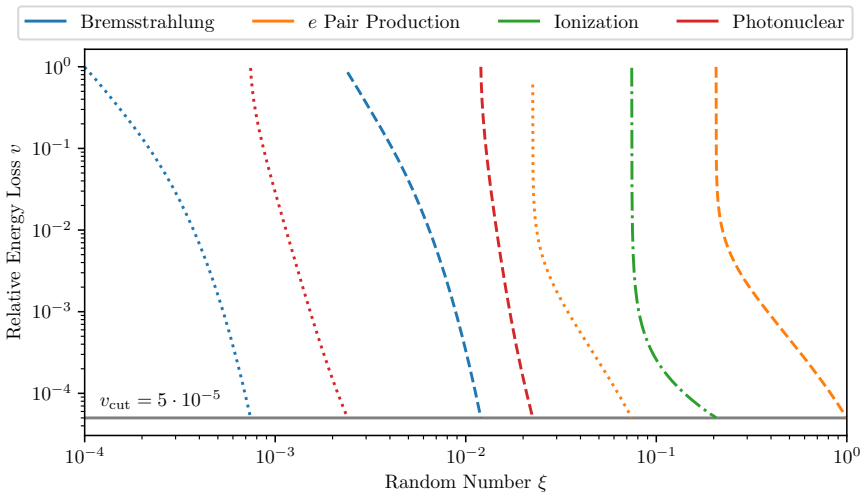

Figure 5.4: The stacked and inverted cumulative distribution of a stochastic loss for a muon with an initial energy of 10^5 MeV in ice using an energy loss cut of 500 MeV. The interaction is split between the probabilities for the different targets; Hydrogen (dotted), Oxygen (dashed), and Ice (dash-dotted).

(see section 5.2.4) of the particle like the propagated distance are updated. If the particle didn't lose too much energy that its remaining energy is still above the threshold, the cycle starts again and the next interaction point is sampled.

These are the main calculations, which are performed in each step of the particle propagation. They can optionally further be improved via the two processes described in the following section; the so-called *Continuous randomization* and *Multiple Scattering*.

5.2.8 Continuous Randomization

As already described in section 5.2.6, the choice of the energy loss cut mainly influences the performance of the simulation. Smaller cuts are more accurate, thus slower and higher cuts are more performant, thus less precise. In any case, this is an unphysical cut producing an artifact in the simulation. Therefore the cut has to be chosen, that these artifacts are not visible in the simulation of the experiment, or at least they should be reduced as much as possible.

There are two main scenarios with different requirements for muon simulations. Calorimetric measurements are often more sensitive to the energy losses than to the bare muon track. An absolute value of the energy loss cut is then often used according to the detection sensitivity. The other scenario is propagating muons through large distances to the detector, where the track of the muon with its energy losses is not visible to the detector. This is often the case for experiments located deep underground. Here, only an accurate description of the incoming muon flux at the detector is required and not a precise calculation of the energy losses. Therefore, a relative energy loss cut is often used in these cases. Regarding the IceCube detector, both scenarios are required.

When setting the absolute energy of the cut below the detection sensitivity of the calorimeter, the artifacts of the energy loss cut are not visible to the detector. However, for the second scenario with the performant muon simulation and a relative cut, detectable artifacts may remain in the muon flux.

The main artifact can be seen in the energy spectrum of the muons after propagating a certain distance, as shown in Figure 5.5b. Each muon propagating the distance without any stochastic interaction arrives with the same energy, resulting in a peak in the distribution. The position of the peak is determined by the continuous losses of the muon according to the cut. After the peak, there is a gap in the spectrum of the size of the energy loss cut, since a single stochastic loss requires at least the amount of the energy loss cut.

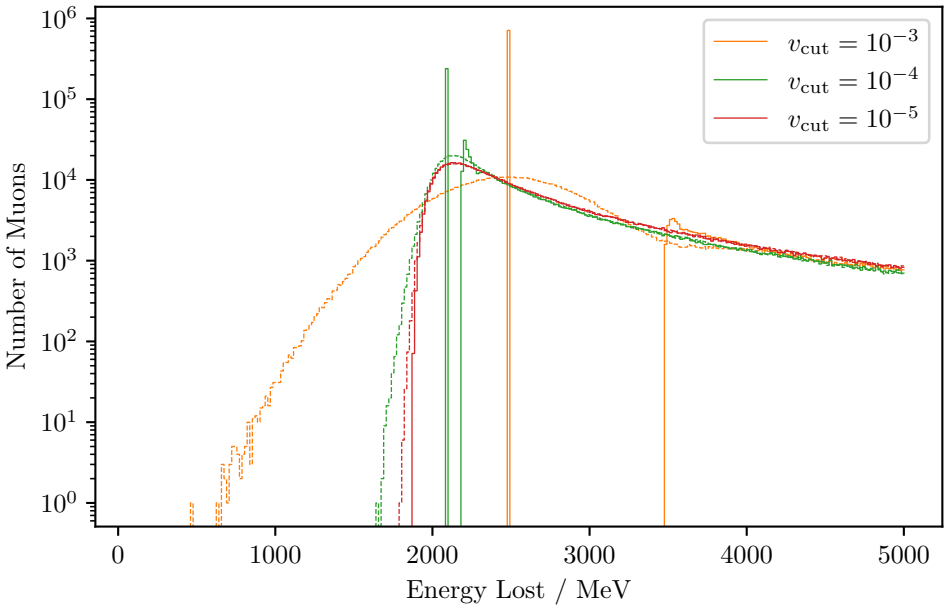

(a) The spectrum of the lost energy.

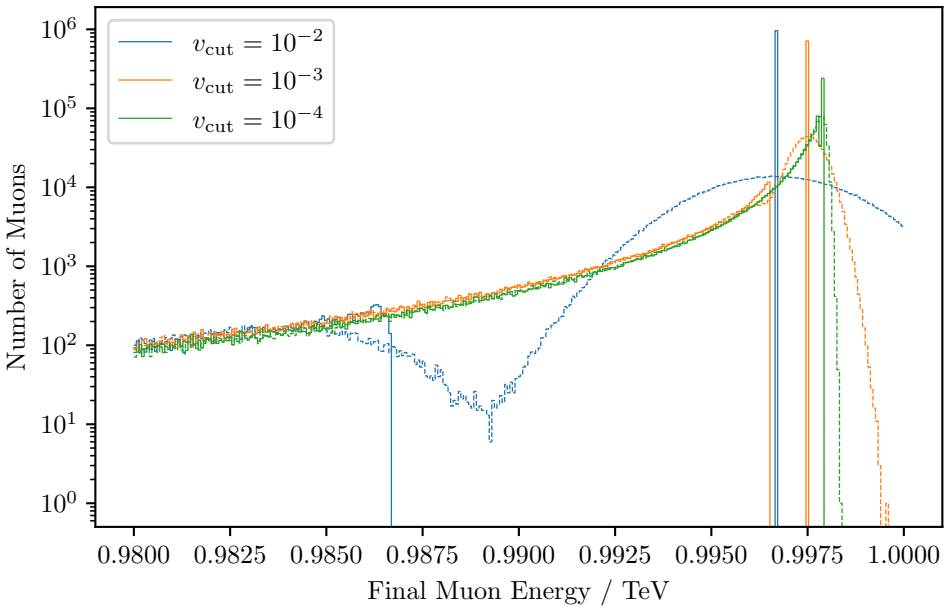

(b) The muon energy spectrum after propagation.

Figure 5.5: The energy spectrum of the muon energy and the summed energy lost after propagating 10^6 muons through 1 m of ice. For different energy loss cuts v_{cut} the energy spectra are compared including continuous randomization (dashed) and without this smearing (solid).

Table 5.3: Comparison of the runtime performance of 10^6 muons propagated with different energy loss cuts through 1 m of ice.

Continuous Randomization	Energy Loss Cut v_{cut} 10^{-2}	10^{-3}	10^{-4}	10^{-5}
True	9 s	12 s	21 s	93 s
False	9 s	12 s	20 s	89 s

The main idea is now to smear out the sampled energy E_f of the muon, after the calculation of the tracking and the time integral to randomize the continuous propagation step. The randomization is performed using a Gaussian distribution with the mean E_f. The variance of the distribution is calculated using the second momentum of the energy loss, as already indicated in (5.7). The variance, defined by

$$\left\langle \frac{\Delta(\Delta E)^2}{\Delta x} \right\rangle = \left\langle \frac{\Delta E^2}{\Delta x} \right\rangle - \left\langle \frac{\Delta E}{\Delta x} \right\rangle^2 \tag{5.26}$$

can be calculated similar to the derivation of the energy integral, dividing the track between two stochastic losses in many small track segments and summing up their contribution

$$\langle \Delta(\Delta E)^2 \rangle = \sum_{j=i}^{f} \left[\left\langle \frac{\Delta E^2}{\Delta x} \right\rangle_j \Delta x_j - \left\langle \frac{\Delta E}{\Delta x} \right\rangle_j^2 \underbrace{(\Delta x_j)^2}_{\approx 0} \right] \tag{5.27}$$

$$\xrightarrow{\Delta x \to 0} \approx \int_{x_i}^{x_f} \left\langle \frac{\mathrm{d}E^2}{\mathrm{d}x} \right\rangle \mathrm{d}x. \tag{5.28}$$

In the second line, the limit of infinitesimally small track lengths is used neglecting the terms of $(\Delta x)^2$. The integral over the track segments can again be written as an integral over the energies, similar to the energy integral for the interaction or decay, resulting in the **Continuous Randomization Integral**

$$\langle \Delta(\Delta E)^2 \rangle = \int_{E_i}^{E_f} \frac{E^2}{-f(E)} \left\langle \frac{\mathrm{d}E^2}{\mathrm{d}x} \right\rangle. \tag{5.29}$$

The effect of the runtime for the 10^6 muons propagated for Figure 5.5 is listed in Table 5.3. A reduction in runtime performance is visible if the continuous

randomization is included. However, while for high energy cuts, other processes are more dominant and the different cuts do not influence significantly the runtime, this changes drastically for smaller cuts increasing the runtime by nearly an order of magnitude due to the additional propagation steps.

5.2.9 Multiple Scattering

The theory of multiple scattering of a muon between two stochastic losses has already been described in section 4.7.1. There are several options available to calculate the multiple scattering:

- It is possible to propagate without scattering to increase the performance if the deflections are not relevant.
- The other extreme is a precise calculation of `Moliere`'s theory on multiple scattering, described in detail in [Gei13]. This however can increases the runtime performance by orders of magnitude depending on the energy, as presented in [Dun+19].
- The `Highland` approximation to Molière's theory using a Gaussian distribution, as described in (4.94).
- The Highland approximation, as described before, but considering also the continuous energy losses, is called `HighlandIntegral`.

Only the latter includes the continuous energy loss during the propagation step, while the others assume a constant particle energy of E_i. Including the continuous loss, the calculation of the scattering angle in the Highland approximation given by (4.94) changes to the **Scattering Integral**

$$\theta_0 = 13.6\,\mathrm{MeV}\left(1 + 0.088\log_{10}\frac{X}{X_0}\right)\sqrt{\int_{E_f}^{E_i}\mathrm{d}E\frac{E^2}{p^4}\frac{1}{-f(E)X_0}}. \tag{5.30}$$

In Figure 5.6 the effect of the different parametrizations for multiple scattering on the muon simulation is shown and compared also to the effect of stochastic deflections. As already discussed in section 4.7.1, the Highland parametrization is an accurate approximation for small angles but does not accurately describe the tail in the distribution of the Molière scattering at high scattering angles. Including the continuous energy losses for the scattering angle has only an influence when using higher energy loss cuts and larger steps. Thereby, the runtime increased by a couple of percents when including a scattering calculation, as shown in Table 5.4.

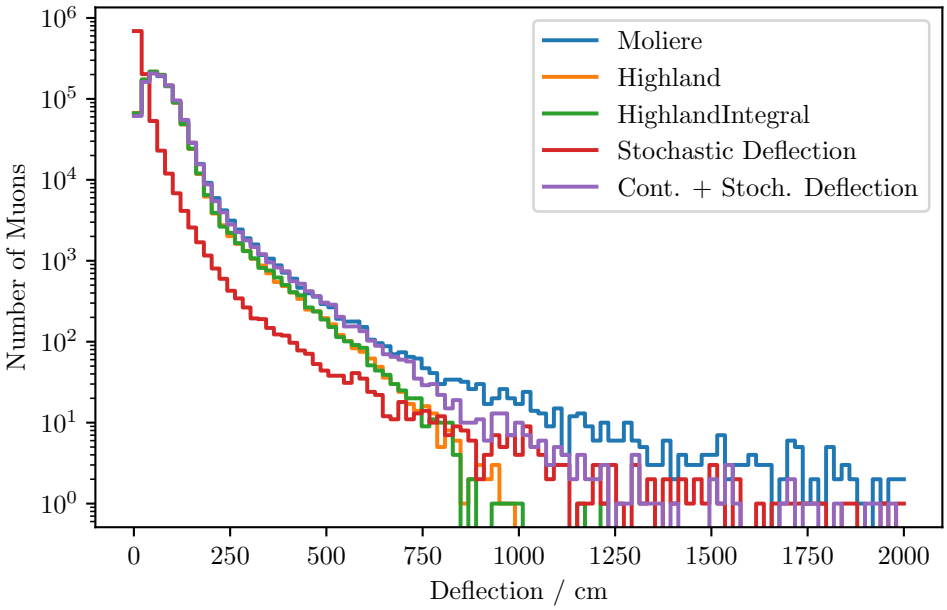

Figure 5.6: Comparison of different deflection calculations for 10^6 muons propagating 1 km through ice with an energy loss cut of 500 MeV. Either only multiple scattering according to the parametrization is used, or only stochastic deflections for the scattering, or both processes. In the latter case, the HighlandIntegral parametrization for multiple scattering is used.

Table 5.4: Comparison of runtime performance of 10^6 muons propagated with different Scattering calculations through 1 km of ice with an energy loss cut of 500 MeV.

Scattering Mode	Runtime / s
No Scattering	404
Moliere	894
Highland	416
HighlandIntegral	463
Stochastic Deflection	428
Cont. and Stochastic Deflection	439

Only the calculation of the Molière scattering drastically increases the performance by more than a factor of 2, which is even larger for higher energetic particles.

For the stochastic deflection, there are also multiple parametrizations available in PROPOSAL. The standard parametrizations for the muon deflection are described in section 4.7.2 and discussed in detail in [Gut21]. They only have minor influences on most interactions with small deflection angles. However, for larger deviations of the muon axis, they contribute significantly to the distribution, and in the tail, their influence is comparable to the effects of the Molière scattering.

5.2.10 The Propagator

The modules described above are combined to finally create the so-called Propagator, which propagates the particle until a certain condition and returns the track. The propagator can be initialized using the following steps:

1. Define a particle definition, a medium, a selection of cross-section parametrizations, and the energy loss cuts, if necessary, to create the cross-section integrals.
2. Out of the cross-section integrals, the propagation utilities can be defined. The utilities consist of the following modules:
    - An interaction module providing the energy integral and the stochastic integral.
    - A displacement module providing the tracking integral and the calculator of the mean free path length.
    - A time module, calculating the time either with the time integral or with the approximation assuming a velocity of c_0.
    - An optional decay module providing the energy integral for the decay process.
    - An optional continuous randomization module.
    - An optional scattering module containing the multiple scattering and the stochastic deflections.
3. The propagation utilities, together with a geometry and a density profile, define a sector, where a particle can propagate through.
4. With a list of sectors, e.g. differing in the energy loss cuts before and inside the detector, the propagator can be initialized.

These objects can either be defined explicitly in a script using the PROPOSAL library, or these settings can be defined inside a `json` configuration file.

After the initialization of the settings, the propagator can propagate a particle. The propagation loop starts with the sampling of the next interaction point or energy. After that, further parameters of the final particle state like the time are estimated including optional corrections due to scattering or the energy randomization. Then, the stochastic loss is sampled and the cycle of propagation starts again until it terminates. There are the following termination conditions for the propagation:

- The particle decays.
- The particle has a catastrophic interaction, e.g. weak interaction or annihilation, and ceases to exist after the interaction.
- The particle has reached the end of the defined environment and there is no further sector geometry in the direction of the particle.
- An optionally set maximum propagation length has been reached.
- An optional minimum of the particle energy has been reached.
- The particle leaves the detection region.

Regarding the latter case, it is of interest for experiments on how the muons propagate before they reach the detector and in particular how they behave inside the detector. But when leaving the detection volume, muons do not need to get propagated further. They might still be highly energetic and propagate large distances e.g. a neutrino-induced, up-going muon in IceCube can propagate to the stratosphere and beyond. Therefore a threshold of the hierarchy in the geometries is implemented. Each sector defining the detection area contains a hierarchy above this threshold. If the particle enters a sector above this hierarchy threshold, it propagates until it reaches the border of all sectors above the threshold. If the next sector has a hierarchy below the threshold, the propagation stops.

After the propagation, the track of the particle is returned consisting of the interaction points and the entry and exit points of geometries. Out of this track, the continuous or the stochastic losses can be extracted and filtered for a specific interaction type. Also, the secondary particles of the interactions or the decay can be produced as described in section 5.2.4.

Using the interaction points in the track, also the particle state at each point of the continuous step can be extracted using re-simulations. For a given energy, the tracking integral (5.19) and the time integral (5.23) are used to determine the particle state. Alternatively, a propagated distance can be given to determine the particle state at this distance. This deterministic approach of re-propagating one step is

not useful when including continuous randomization, and will produce inconsistent results due to the shift of the final energy. Also, the multiple scattering is just approximated with a straight line between the initial and the final state. In principle, the particle would scatter less at high energies in the beginning and deviate more in the latter part of the track at lower energies. However, since the random state is not stored for each step, a straight line is the most generic approximation. The particle track of a single muon including its energy losses is shown in Figure 5.7.

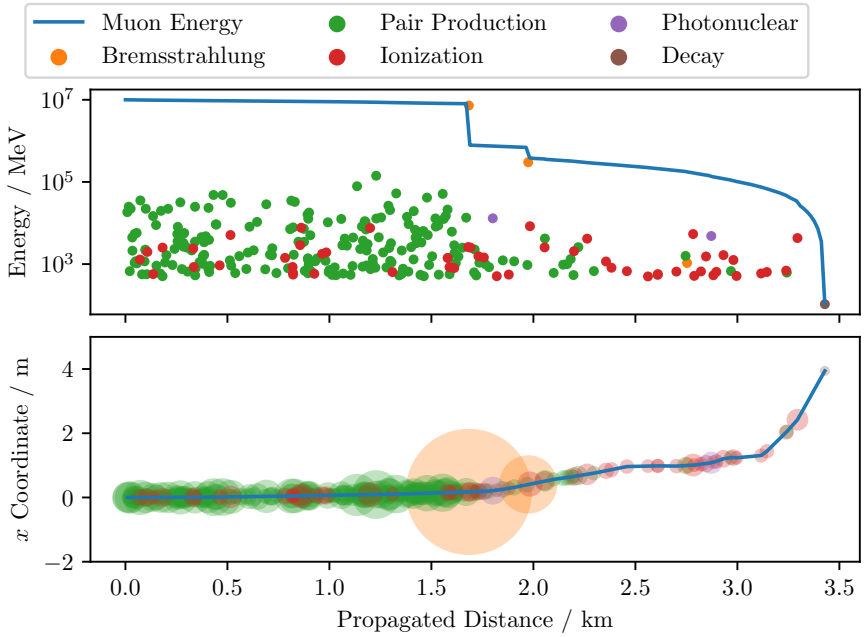

Figure 5.7: The energy loss of a 10 TeV muon during its propagation through ice with an energy loss cut of 500 MeV until it decays is shown in the upper plot. The deflection of the above-mentioned muon projected on the x axis, while initially propagated along the z-axis, including the energy losses on the track is shown in the lower plot. The radius of the energy loss circles is scaled with the square root of the energy loss.

.

5.2.11 Decay

For the different decay channels of muons and taus, multiple decay sampling methods are implemented in PROPOSAL. The two leptonic decay methods with an approximated production of the electronic decay channel and the more accurate approach for the muonic decay channel are already described in section 4.8.

Regarding the hadronic decay modes of the tau, there are two methods available, both only considering the phase space sampling, not the matrix element. In the first versions of PROPOSAL, there was only the phase space sampling for a two-body decay implemented. This is exact for the decay into a Pion and a neutrino. The decay channels where more decay products are produced were described effectively with a two-body decay into an intermediate particle, a resonance, that predominantly decays into the desired products. For example, the decay channel $\tau^- \to \pi^-\pi^0\nu_\tau$, which is the largest decay channel of a tau, was described as a two-body decay into the neutrino and $\rho(770)^-$, which decays with more than 99 % in the channel $\rho(770)^- \to \pi^-\pi^0$. Therefore, it is a reasonable approximation for a simple description of the tau decay. However, without further dynamics of a matrix element, a pure phase space consideration of a two-body decay results in a constant, deterministic value of the produced particle energies in the rest frame of the tau. This can be explained since for the two particles in the rest frame of the primary, there is only one possible configuration of one particle going in one direction and the other particle in the opposite direction. In the resulting energy distribution of the hadronic particles in the rest frame, four peaks occurred for the four implemented decay channels. In the boosted frame of the primary particle, this resulted in step functions in the energy distribution of the hadronic products, with a step at the mass of a hadronic product. This is further explained in [Dun+19] visualizing also the artifacts in the energy spectra.

Since these step functions were observed in IceCube simulations, a many-body phase space sampling was introduced in [Dun18]. Thereby, the Raubold-Lynch algorithm is used, recursively factorizing an n-body decay into n two-body decays, which can be calculated. Since this algorithm generates decay events, which are not equally distributed in the phase space, a rejection sampling can be applied to extract a uniformly distributed phase space. However, since the generation of a single decay product configuration already requires $3n - 4$ random numbers, the rejection sampling can increase the amount of required random numbers by an order of magnitude depending on the configuration. If the requirement on the decay simulation is only a continuous spectrum without steps, this uniform sampling is not necessary. Regarding the runtime, the decay calculation is not critical compared to the propagation and a more accurate sampling of the phase space doesn't change this relation. But the huge number of random numbers, which can be in the order of $\mathcal{O}(10^2)$ for a single decay calculation due to the simple rejection sampling, needs to be considered if an efficient usage of random numbers is necessary. This could be improved in future works by introducing more efficient methods like importance sampling.

Yet, there is no matrix element implemented for any decay channel and a constant matrix element of 1 is used. However, it is possible to include an external function

calculating the matrix element. Thereby, the aforementioned rejection sampling for a uniform phase space gets weighted according to the matrix element. This is also applicable and can be tested for the muon decay, where the matrix element is defined by

$$\mathcal{M} = 64 G_F^2 p_1 p_2, \tag{5.31}$$

with

$$p_1 = E_\mu E_{\bar{\nu}_e} - \vec{p}_\mu \cdot \vec{p}_{\bar{\nu}_e} \qquad \text{and} \qquad p_2 = E_e E_{\nu_\mu} - \vec{p}_e \cdot \vec{p}_{\nu_\mu}. \tag{5.32}$$

Comparing the sampled electron spectra in Figure 5.8b with the two leptonic decay sampling methods shows, that the many-body phase space sampling including the matrix element is as accurate as the improved leptonic decay sampling. However, regarding also the sampled energies of the two neutrinos in Figure 5.8a, different shapes of the spectra are observed. In the two leptonic decay sampling approaches only for the charged, massive leptonic product, the energy, and the direction get sampled. For the neutrino states, only the direction for one neutrino gets sampled while the other neutrino gets the opposite direction, in the rest frame. The energy for both neutrinos is also not sampled and each neutrino receives the energy

$$E_\nu = \frac{1}{2}\sqrt{(m_\mu^2 - E_e)^2 - p_e^2}. \tag{5.33}$$

On the other side, the many-body phase space calculation with the matrix element is assumed to produced the more accurate result. Comparing the neutrino spectra in Figure 5.8a with Figure 4.21 indicates that the many-body decay calculation produces a more plausible spectrum of neutrino energies. Since the neutrino spectra have not been validated, yet, further investigations are necessary, especially in the light of a growing interest in simulating tau regeneration through the earth. Therefore, also a more accurate description of the hadronic decay products is necessary. But as already mentioned, the processes of hadronic interactions are a research topic on its own with dedicated tools for each problem. For the hadronic tau decay, the default simulation framework is TAUOLA [JKW91; Jad+93; Dav+12; Chr+18], used in nearly every experiment requiring an accurate description of the tau decay. In a future extension of PROPOSAL, an interface to this framework can be implemented.

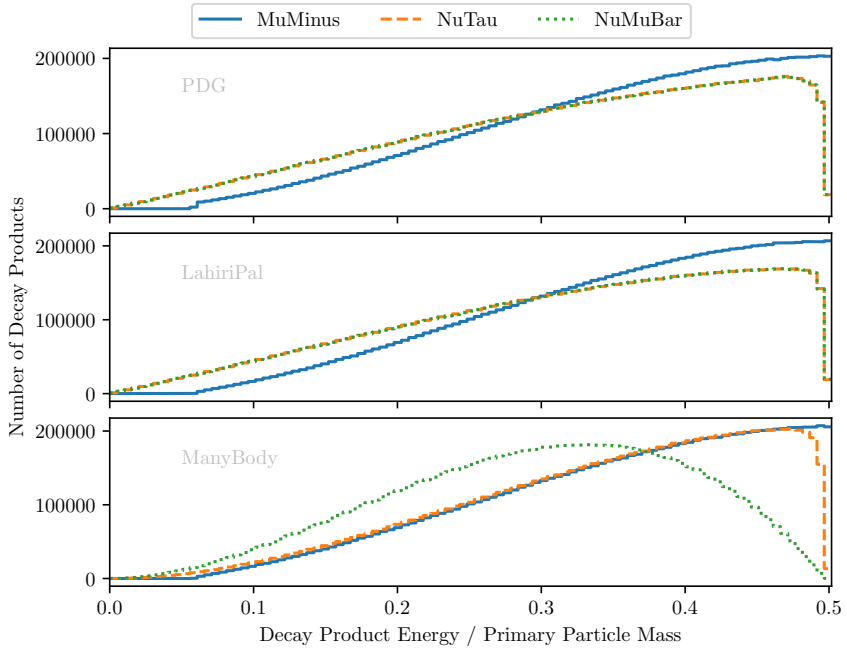

(a) Energy spectra of all decay products.

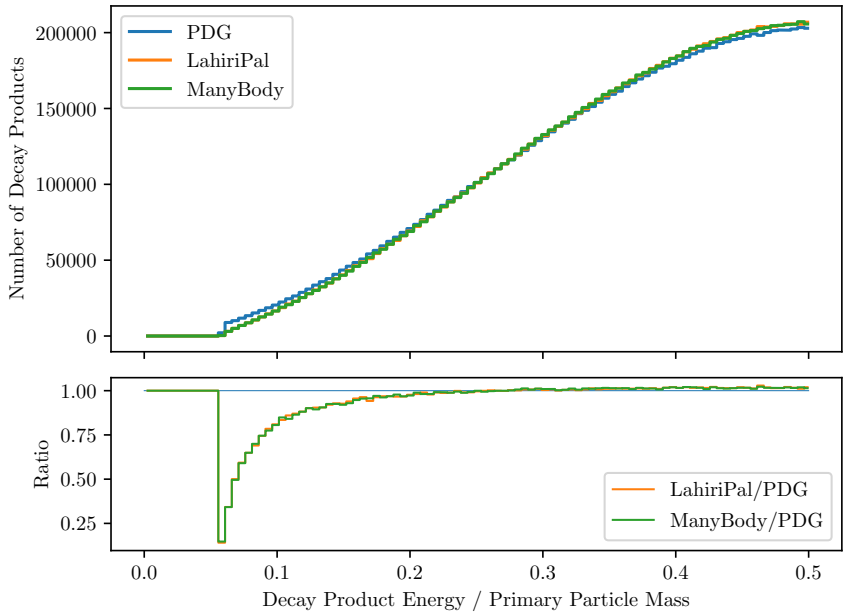

(b) Energy spectrum of the produced muons.

Figure 5.8: The Energy Spectra of the decay product of 10^7 taus decaying at rest. The approximated (PDG) and the more accurate (LahiriPal) leptonic decay calculations are compared to the many-body decay calculation.

5.3 Usage of PROPOSAL in Simulation frameworks

Initially intended as a muon propagator, PROPOSAL evolves to an electroweak interaction module. PROPOSAL is currently used in many different applications, from large simulation frameworks to small case studies. Since it is written in C++ and also callable in python, it is easily adaptable in new applications. It has common installation approaches as a classic `cmake` project, which is used in most scientific software frameworks, or using the conan package manager. The dependencies of `boost` and `eigen`, which are already available in most scientific frameworks as well as the widely used `spdlog` are also `cmake` projects. To build the python interface, the widely used library connecting C++ and python `pybind11` is used. With the simple installation via pip (`pip install proposal`), PROPOSAL is now also used in many small-scaled simulation studies.

5.3.1 High Energy Neutrino Telescopes

High energy neutrino telescopes, especially the IceCube experiment, were the initial purpose and are still the main users of PROPOSAL. For the IceCube simulation, PROPOSAL propagates high energy muons and taus as e.g. described in [Aar+16]. The IceCube collaboration is also providing significant contributions to the development. Also in the simulation chains of other neutrino telescopes PROPOSAL is available for their muon propagation, like in the Baikal experiment [Pas19] or KM3NeT [Aie+20].

Inside the IceCube simulation, PROPOSAL is used with two configurations. The generated muon events from atmospheric air showers, which CORSIKA can propagate to the surface of the ice, get further propagated through the ice to the detector region with PROPOSAL. The neutrino-induced muons are generated inside the ice (not necessarily directly at the detector) or the bedrock below the detector, using e.g. GENIE [And+10] or ANIS [GK05] or the recently developed LeptonInjector [Abb+21b], and then get further propagated with PROPOSAL. Since these muons can have high energies propagating tens of kilometers through the ice, as shown in Figure 5.9, a relatively high energy loss cut of $v_{\text{cut}} = 10^{-2}$ is used with the continuous randomization option. Thereby, only the final muon state at the detector entrance is of interest, as well as stochastic interactions, where again long-ranged muons are produced, that can reach the detector. These interactions are photonuclear interactions, $\mu^+\mu^-$ pair production, and weak interactions.

The second configuration is the propagation inside the detector with an energy loss cut of 500 MeV, since the detector is not sensitive to smaller energy losses. An energy distribution of the produced secondaries inside the detector is shown in Figure 5.10.

After the propagation with PROPOSAL, the next module in the simulation chain, the Cascade Monte-Carlo (CMC),uses the the stochastic interactions along the muon track and samples the Cherenkov photons according to the energy and differentiating between electromagnetic and hadronic cascades. Also, the Cherenkov photons along the continuous energy loss step of the muon is simulated according to an energy loss cut of 500 MeV.

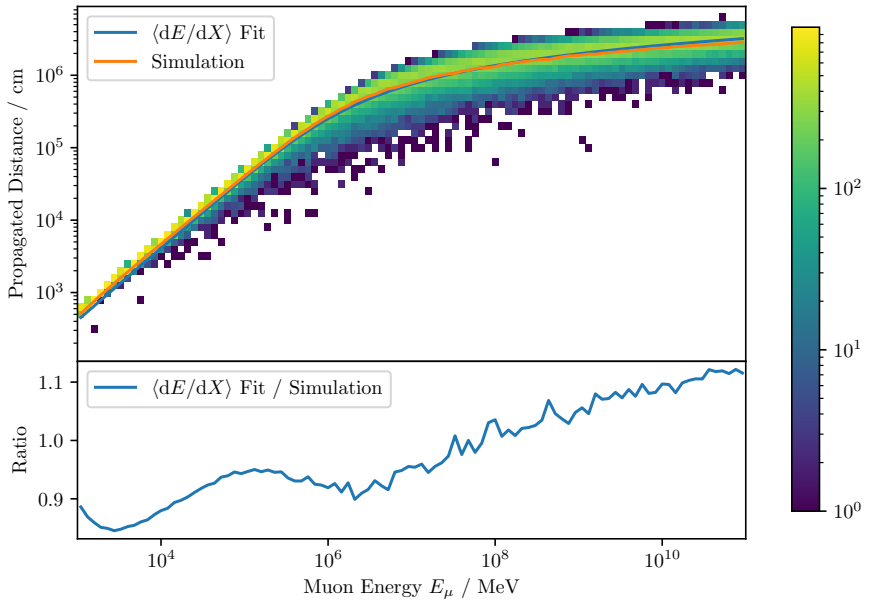

Figure 5.9: The energy dependent range distribution of muons in ice. For each energy bin, 10^3 muons are propagated with a relative energy cut $v_{\text{cut}} = 10^{-2}$. The median in each energy bin is compared to the Fit of the average energy loss, described in section 4.1.

.

Next to the muon, also tau events in IceCube are simulated with PROPOSAL using the same energy loss cuts as for muons. An important difference compared to muons is, that for the propagation before the detector also the decay products which can consist of long-ranged muons, need to get stored. Regarding searches for physics beyond the Standard Model in IceCube, PROPOSAL was used to propagate stable massive particles, like staus, with an implemented behavior similar to muons but with a mass of 500 MeV.

Besides the neutrino telescopes detecting Cherenkov light, also the experiments of radio neutrino astronomy are using PROPOSAL for the muon and tau propagation [Gla+20]. Since these detectors are searching for the highest energies and are

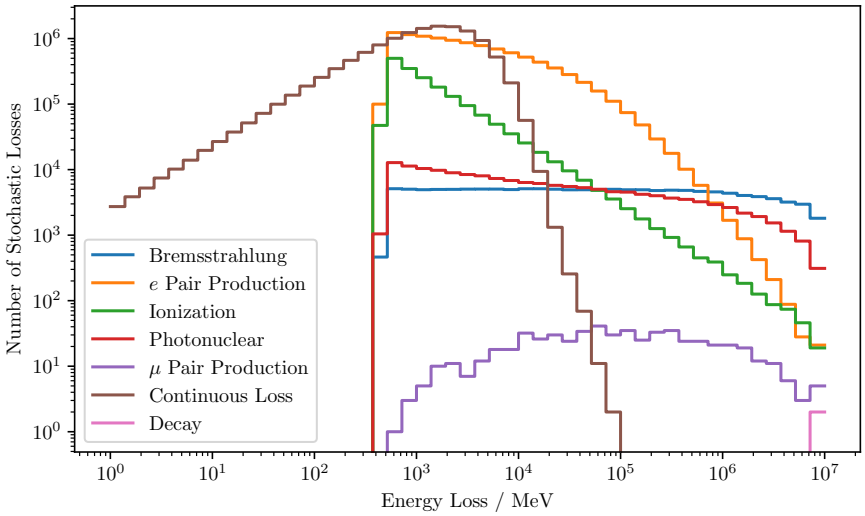

Figure 5.10: The energy distribution of the secondaries produced when propagating 10^6 muons through 1 km of ice using an energy loss cut of 500 MeV.

.

sensitive to electromagnetic cascades above a PeV, an energy loss cut of 100 TeV is used. A peculiarity for the simulations of these experiments are the extremely high energies and their sensitivity calculations ranging until 10^{30} eV, where also the tau leptons propagate significant ranges. In simulation studies [GNG20] the effect of large stochastic energy losses of muons miming neutrino events was analyzed using PROPOSAL. Hereby, it doesn't have to be a single stochastic loss, but also the sum of several smaller energy losses inside a track segment of $\mathcal{O}(10\,\mathrm{m})$ have significant contributions.

5.3.2 Air Shower Simulation

In recent years, the air shower simulation framework CORSIKA [Hec+98; Eng+19] with its monolithic structure written in Fortran has been restructured and rewritten into a modular structure, written in C++. For this new CORSIKA 8 version, also the electromagnetic shower calculation needed a restructuring. In the old version of CORSIKA 7, a modified version of EGS4 [Bie+94; Nel+94; Hir+05] was used with additional corrections for the LPM effect. Since EGS4 is also based on a monolithic structure, written in Fortran, PROPOSAL is used as a physics module providing the electromagnetic interaction processes. Although PROPOSAL was more designed as a muon and tau propagator, similar cross-sections and propagation algorithms are

used for the propagation of electrons, positrons, and high energy photons. These enhancements of PROPOSAL were presented in [Ala+20].

Also, the energy region is different for some application with lower energy cuts of around 1 MeV. In particular, these low energetic particles are important, since the charge excess of electrons compared to positrons for the Askaryan effect is mainly driven by low energetic electrons produced in Compton scattering or ionization processes. Furthermore, CORSIKA uses PROPOSAL in a new way. Instead of propagating the particles for CORSIKA, PROPOSAL is proposing an interaction step along with further modules like the decay module. Then CORSIKA determines the next step and propagates the particle itself. Therefore the individual modules from the `propagation_utilities` are used.

Many different modules providing physical input are required in air shower simulations, which are mainly calculating their processes independent of each other. On the one hand, this is a necessary to keep a modular design. On the other hand, multiple processes can affect each other, which requires approximations to be made. This can exemplarily be described regarding the multiple scattering. Multiple scattering is one of the main processes in electromagnetic showers responsible for the deviation of the particles from the shower axis, affecting lateral profiles significantly. In principle, the scattering consists of a positional deviation and a change in direction. However, due to the additional deflection induced by the magnetic field, these two deviation processes interfere with each other. Therefore, the multiple scattering currently only changes the direction, neglecting the positional shift.

Another approximation regarding the electromagnetic propagation with PROPOSAL is the continuous energy loss, which is not calculated using the energy integral (c.f. section 5.2.7). Instead, the interaction point is sampled with the mean-free path length, thereby assuming no continuous energy losses. A correction for the continuous losses is calculated in a second, independent step.

Although not all effects and corrections for the electromagnetic shower propagation are implemented yet in PROPOSAL compared to EGS4, shower distributions like the longitudinal or lateral profile were in good agreement with the old version CORSIKA 7 or other air shower frameworks, like AIRES and ZHS as presented in [Ala+21a]. However, this is an ongoing field of research where PROPOSAL will play a key role in electromagnetic shower simulations for air shower experiments like Pierre Auger, HAWC, and CTA. Thereby, PROPOSAL can for example also provide the electromagnetic processes for hadronic particles and calculate the ionization losses.

5.3.3 Underground Experiments and Further Application Areas

Next to the application in new physical areas, the main usage of PROPOSAL is still the propagation of muons through large volumes. Thereby the underground experiments with small detection volumes also start using PROPOSAL for calculating the incoming muon flux. Since these detectors are sensitive to low energy processes, not implemented in PROPOSAL, GEANT4 is used for the propagation inside the detector. This was exemplarily done in a simulation study for the DUNE experiment [Sch+21].

In an ongoing analysis for the PICO detector calculating the atmospheric muon flux deep underground at the detector, MCEq is used to estimate the main parts of the incoming muon distribution. However, since the analysis with PICO is also sensitive to the rare muons in the tail of the energy distribution, a combination of MCEq and PROPOSAL as a Monte-Carlo propagator is used [FWP21].

Due to its simple installation and usage, PROPOSAL is not limited to being used in large simulation frameworks running on high-performance clusters. It can also be used to produce lightweight simulation studies when only limited resources are available, like on a notebook. For example, in [GNG20] the effect of large stochastic energy losses of muons producing a neutrino-like radio signal is estimated.

Another advantage for BSM studies is the modular structure of the particle definition and the cross-section in PROPOSAL. The custom particle properties can be defined and a BSM particle can be propagated with these properties, according to selected interaction processes. For example, this has been used to calculate the sensitivity of neutrino telescopes for milicharged particles [AKM21].

6 Analyzing Muon Properties

Providing the ability to perform studies on the systematic uncertainties of muon cross-sections is one of the main goals and advantages of the simulation library PROPOSAL. The main questions for improved cross-sections in simulations are, what effects do these improvements have on simulated events and their agreement with measured data. Thereby, the effects can either be analyzed in simulated event distributions regarding only the particle physics properties independent of the detector. In air shower simulations, the longitudinal and lateral distribution of the occurring particle types are that kind of relevant parameters, that can be compared. Regarding muons in deep underground experiments, the energy and zenith distribution of the incoming muon flux as well as the energy loss behavior are the most important parameters.

The effects can also be analyzed after the full simulation chain including detector-specific thresholds or resolutions of the reconstruction. After the question, if the effect is still visible on the detector level, the step is to find out how much it can affect further analysis and if it needs to be taken into account in the calculation of systematic uncertainties. If this is the case, one can finally try to measure these effects.

In this chapter, these three approaches of detector independent and detector specific simulation studies as well as an outlook on potential measurements of the muon cross-sections are discussed, focusing on large volume neutrino detectors.

6.1 Propagation Effects of Improved Muon Cross Sections

For muon energies above a TeV, the energy loss is dominated by pair production for small energy losses and bremsstrahlung for large energy losses. Both interactions contribute nearly equally to the average energy loss as shown in Figure 4.2a. Next to the widely used standard cross-sections, which for both interactions the parametrizations were calculated by the group labeled *KelnerKokoulinPetrukhin* (KKP95), also improved bremsstrahlung and pair production cross-sections labeled *SandrockSoedingreksoRhode* (SSR19) are implemented in PROPOSAL. The differences between these parametrizations are an improved treatment of the screening

effect for both processes and radiative corrections for bremsstrahlung, which is described in section 4. As shown in Figure 6.1, the average energy loss of the bremsstrahlung increases by around 2 %, mainly driven by the additional radiative corrections. The improved screening for pair production decreases the average energy loss by half a percent.

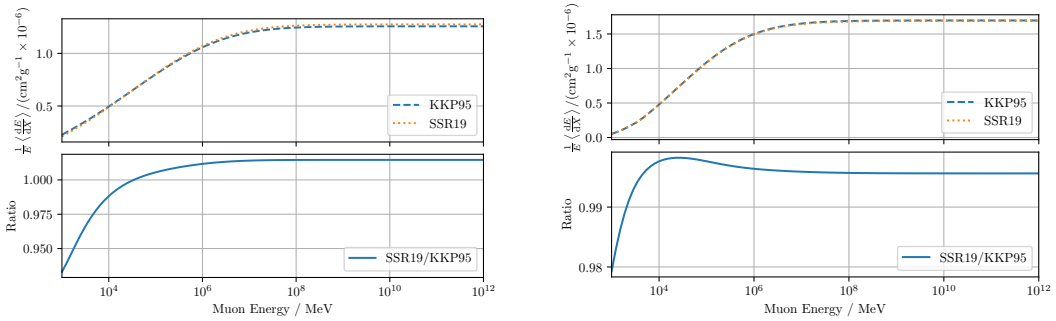

(a) Average energy loss of bremsstrahlung.

(b) Average energy loss of pair production.

Figure 6.1: The average energy loss of muons in ice comparing the *KelnerKokoulin-Petrukhin* (KKP95) parametrization and the *SandrockSoedingreksoRhode* (SSR19) parametrization.

The overall increase of the average energy loss further affects the survival probability and the distribution of incoming muons for underground detectors. This slightly changes the range distribution to smaller propagated lengths as shown in Figure 6.2a. The expected change in the energy distribution at a certain distance towards smaller muon energies due to the increased loss is also observed, shown in Figure 6.2b. However, the number of muons losing just a small amount of their energy is increased, which can be explained due to the higher stochasticity. But these are rather small effects compared to the introduced error of an energy loss cut, shown in Figure 5.5b.

For large volume detectors like neutrino telescopes, also the energy loss behavior inside the detector is relevant, especially for the energy reconstruction or event selection. Thereby, the combined effect of increased bremsstrahlung and decreased pair production cross-section is even more significant and can directly be seen, as shown in Figure 6.3a. Also, the effect of including the muon pair production is compared, shown in Figure 6.3b, slightly indicating more low energy losses driven by the additional low energy muons. But this is less significant compared to the clear deviation due to the bremsstrahlung and pair production cross-sections. The next step is now to analyze if this deviation is still visible on detector level, described in the next section. The results of this section were also presented in [SSR19].

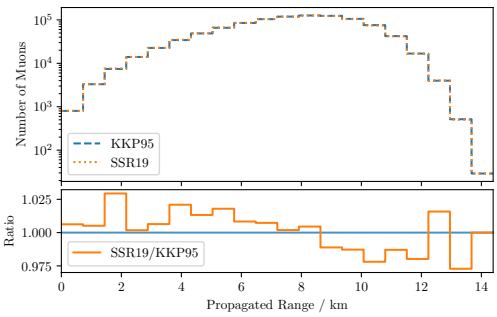

(a) The range distribution of 10^6 muons propagated until they decay.

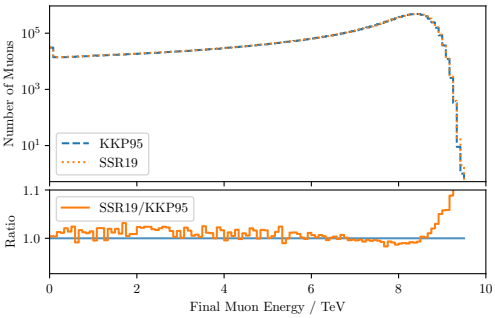

(b) The muon energy distribution of 10^7 muons after propagating 1 km.

Figure 6.2: Comparison of propagating muons through ice with an initial energy of 10 TeV and an energy loss cut of 500 MeV. The propagation with the default cross-sections for bremsstrahlung, i.e. the *KelnerKokoulinPetrukhin* (KKP95) parametrization, is compared with the *SandrockSoedingreksoRhode* (SSR19) parametrization.

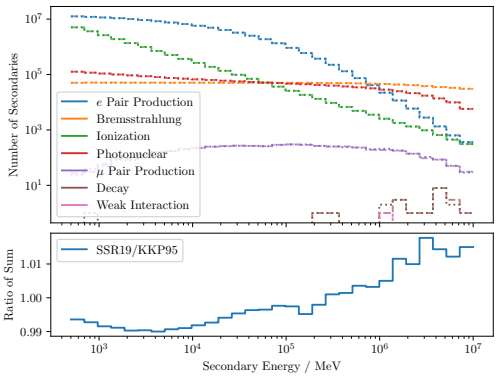

(a) Comparing the bremsstrahlung and pair production parametrization of *KelnerKokoulinPetrukhin* (KKP95) with the *SandrockSoedingreksoRhode* (SSR19) parametrization.

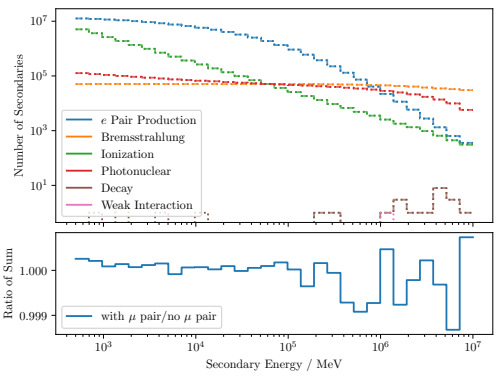

(b) Comparing the effect of including the muon pair production, where the muons are further propagated taking into account also their energy losses.

Figure 6.3: Comparison of the secondary energy distribution of 10^7 muons propagated with an initial energy of 10 TeV through 100 m of ice with an energy loss cut of 500 MeV.

6.2 Feasibility study to measure the Bremsstrahlung Cross Section

The significant effects of the improved muon cross-section on the energy loss distribution in Figure 6.3 raise the question of how much this affects the energy reconstruction for neutrino telescopes which rely on an accurate description of the continuous and stochastic losses. This would then also affect e.g. the energy flux measurements of astrophysical neutrinos. A further question is, whether the energy loss distribution can even be measured. This would validate the theory of both pair production and bremsstrahlung calculations, which dominate in different parts of the energy loss spectrum.

There have been measurements of the muon cross-section with the ATLAS detector below 100 GeV [Ama+01] and less precise measurements using cosmic-ray induced muons up to 1 TeV [Sak+92], where the ionization is still dominating the energy loss. Since the stochastic processes start to dominate at energies around a TeV, such a measurement is still required. Hereby, large volume neutrino telescopes like IceCube, measuring muons with energies from below a TeV up to the PeV region, provide the unique opportunity to perform such a measurement, which would be the first in this energy region.

In this section, a feasibility study is described to measure the cross-section using the energy loss profile along the produced tracks inside a cubic kilometer scale detector. Regarding the reconstruction of single energy losses along the muon track, small energy losses can not be distinguished and rather measured as continuous loss, especially for a sparsely instrumented detector, like neutrino telescopes, while large stochastic losses can be identified and reconstructed as a single high energy loss or cascade. Since bremsstrahlung interactions are dominating those high energy losses, this study focuses on measuring the bremsstrahlung cross-section.

Also, the efficiency of the photomultipliers and the spectral index of the muon flux are included as further systematic parameters to analyze their correlation with this study. Although both systematic parameters will have larger impacts on the energy loss distribution, this will affect the whole secondary distribution, while bremsstrahlung only affects the largest losses.

The created toy Monte-Carlo simulation and reconstruction is adapted to imitate the simulation and reconstruction methods used in the IceCube experiment. Also, the statistic of the used event sample and energy spectrum are based on public IceCube analysis. However, they can be applied to any neutrino telescope configuration. A generic framework is created, where the configuration of the detector scale or

the reconstruction performance can be adjusted to perform the study for another dedicated detector.

One has to point out that the scope of this study is not to fine-tune the analysis on the simulation model or a specific detector configuration and produce as many simulations to extract the best achievable results out of this toy Monte-Carlo. This is a feasibility study if a measurement of the Bremsstrahlung is possible for neutrino telescopes and tries to be as simple and resource efficient as it can.

This study was developed in collaboration with Mirco Hünnefeld, Maximilian Meier, and Alexander Sandrock and the results were presented in [Soe+20].

6.2.1 Event Sample

For the dataset of this study, a single muon sample with a decent statistic of muon energies above a TeV and a good measurement of the energy loss profile is required. This is currently only achievable using cubic kilometer sized neutrino telescopes. Although atmospheric muons are abundant for neutrino telescopes, they are of limited use regarding a measurement with the energy loss distribution. Most cosmic-ray induced muons arrive as low energy stopping muons, which are not in the relevant energy region, or they arrive in bundles, where the separation of single muons and the reconstruction of their energy losses is not feasible. Therefore, neutrino-induced muons are used in this analysis, since they don't arrive as bundles and they are in the relevant energy region.

Neutrino-induced muons are produced with a hadronic cascade at the neutrino vertex, containing on average $1/3$ of the neutrino energy (see Figure 2.7b), which cannot be distinguished from an energy loss. This disturbs especially the large stochastic losses, which are the focus of this study. However, most of the muons are produced outside of the detector propagating inside without any detectable light of the vertex. This can for example be indicated by the difference of two orders of magnitude in the number of neutrino events between a track sample [Aar+16] and cascade sample [Aar+20a]. Therefore this effect can be neglected for this study. Trident processes, here the muon pair production, can also create a bundle out of a single muon. But these muons are usually comparably low energetic and do not propagate large distances or change the energy loss profile significantly, shown in Figure 6.3b.

A comparable dataset is the sample of up-going, thereby neutrino-induced, muon tracks measured in ten years by the IceCube Collaboration [Ste19], further described in [Aar+16]. As shown in Figure 6.4, the event distribution of the neutrino sample consists of roughly 245 000 events between 1 TeV and 100 TeV and approximately

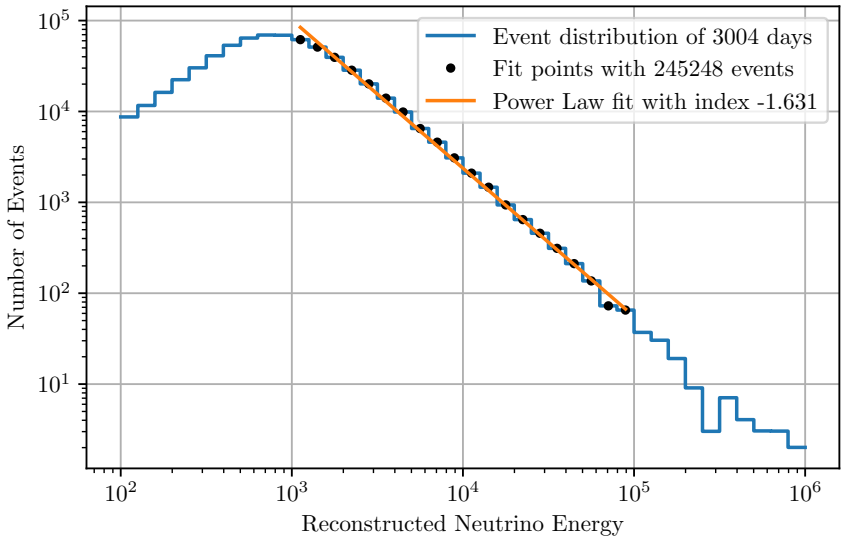

Figure 6.4: Event spectrum of selecting up-going muon events using ten years of IceCube data. [Ste19]. A power law is fitted for events with a reconstructed muon energy between 1 TeV and 100 TeV.

follows a power-law spectrum with a spectral index of 1.6. This is a relatively flat spectrum compared to the steeper spectral index of the atmospheric or astrophysical flux, which are approximately 3.7 and 2.3 respectively. However, this can be explained with the detector acceptance and the higher probability of higher energetic muons to get detected and included in the dataset [Aar+16].

6.2.2 The Toy Monte-Carlo

The simulation uses the PROPOSAL library for the Monte-Carlo propagation of the muons. The default cross-section for ionization, e^+e^- pair production, bremsstrahlung, and inelastic nuclear interaction are used including the LPM effect, while the bremsstrahlung can be scaled according to a given multiplier. To save computation time, all further corrections are turned off, i.e. the μ pair production and the weak interaction, scattering and deflection calculations as well as exact time calculations. The medium is set to ice and an energy loss cut of 500 MeV between stochastic and continuous losses is used, which is also used in the IceCube simulation chain.

The initial energy of the propagated muons is sampled from a power-law $\propto E^{-\gamma}$ with a spectral index of $\gamma = 1$ in the energy range between 100 GeV and 1 PeV. With this flat spectrum also high energy muons get simulated with a decent statistic

to estimate their contribution to this study. The transformation to a more realistic energy spectrum of the muons can be considered by re-weighting the events.

The maximum distance muons are allowed to propagate is varied between 100 m and 1 km and is randomly chosen from a uniform distribution to take into account the different propagation lengths inside the detector. Although a description of the length distribution for the used muon sample is not publicly available, a uniform distribution is a conservative assumption, since the selection of muons favors long tracks. Especially as the propagation lengths inside the detector can also reach 1.5 km.

A smearing of the energy loss profile, compared to the differential cross section is included intrinsically in the simulation setup as just the starting muon energy (that is the energy when the muon enters the detector) for all the energy losses of the track is used and not the muon energy at each energy loss. However, on average, a TeV muon is not losing much of its energy within a kilometer, as shown in Figure 6.2b. Regarding initial energies around 10 TeV and a propagated distance of 100 m, energy losses of more than 10 % of the muon energy occur less than once per muon, which can be seen in Figure 6.3a. Since this study is focused on high energy losses, this does not affect the analysis significantly. Besides, this effect is included in all energy loss distributions and here, just the differences between these distributions are of interest.

For real simulation of the detector, further processes and acceptance corrections are considered in the simulation chain, like noise, triggers, and the generation and propagation of Cherenkov photons. Out of the measured time series of the pulses by the photodetectors, further reconstruction methods are applied to parametrize. These simulations are specific for each detector and most often produced by closed source software. Furthermore, these steps are computationally expensive compared to the fast muon simulation. To create a toy Monte Carlo including semi-realistic detector effects, the following smearing and cutoff steps are performed to extract the measured energy losses of a muon.

1. The position or vertex of each stochastic loss is smeared out. Thereby, the energy loss is not deposited at a single point, but along the track according to a Gaussian distribution with the width σ_V.

2. Each muon track is divided into equidistant track segments of a certain length ΔX.

3. The expected energy loss in each segment is accumulated from the smeared out stochastic losses distributed on the track segments and the number of continuous losses according to their fraction in each segment.

4. To model hits in the photo multipliers of the detector, the expected energy losses per track segment in MeV are sampled using a Poisson distribution.

5. Due to the finite energy resolution, these hits, representing the energy, are further smeared out using a Gaussian distribution. The width of the Gaussian distribution $\sigma_E = \sigma_{\text{base}} \cdot f_E$ consists of a scaling parameter f_E and an energy-dependent resolution σ_{base} similar to the energy resolution of IceCube [Aar+14] shown in Figure 6.5.

6. The energy measured in each track segment can be scaled according to a given efficiency of the photomultipliers, taking into account a further systematic uncertainty parameter.

7. Finally, a threshold E_{cut} is applied and segments with an energy below this threshold are discarded, taking into account the limited detector sensitivity.

Independent of the simulation of the measured energy loss of the segments, the measured length the muons are propagated inside the detector is simulated by smearing out the true length using a Gaussian distribution with the width σ_L.

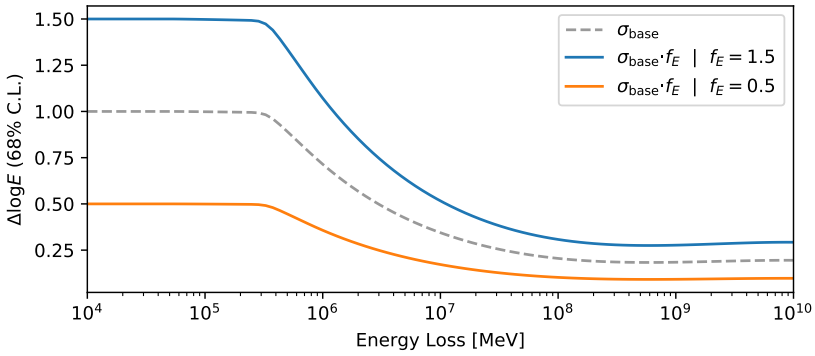

Figure 6.5: The energy-dependency of the resolution of the energy reconstruction σ_E for the three resolution settings listed in Table 6.1. The shape of the curve is taken from [Aar+14].

This study is performed using three different settings for the detector resolution, listed in Table 6.1; one considered as baseline setting, one with a low resolution, and one with high resolution. These three settings are comparable to the main IceCube array, the DeepCore, and the IceCube-Gen2 expansions respectively. For an example muon track, Figure 6.6 shows the energy loss profile reconstructed with the three resolution settings compared to the true energy loss profile.

Table 6.1: For this study, three different sets of resolution settings were chosen: low, medium, and high resolution.

Resolution Parameter	High	Medium	Low
Vertex resolution σ_V / m	2	5	10
Track segment length ΔX / m	5	15	30
Energy resolution factor f_E	0.5	1.0	1.5
Energy cutoff E_{cut} / MeV	10	50	100
Length resolution σ_L / m	10	50	100
Energy Uncertainty Cut	0.2	0.4	0.6
Coefficient of Determination R^2	0.9	0.95	0.995

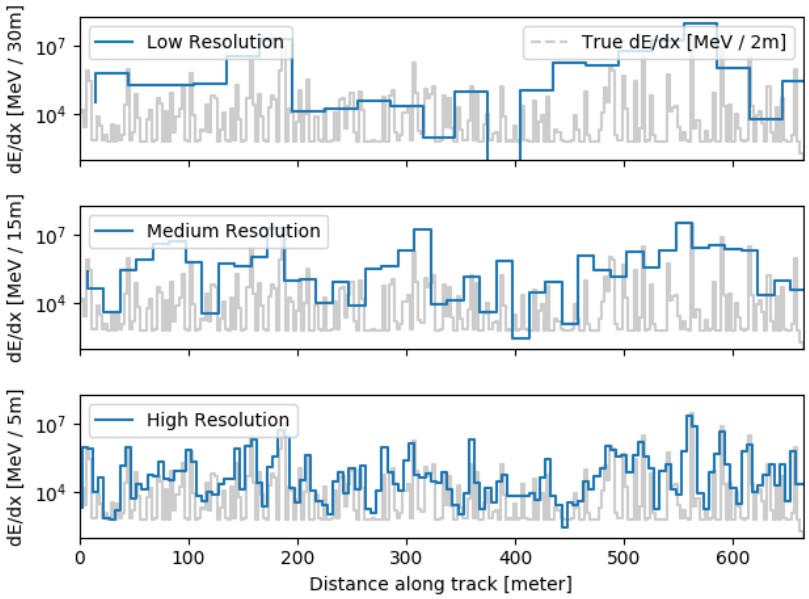

Figure 6.6: The final energy loss profile for an example muon track reconstructed with the three resolution settings according to Table 6.1. The true energy losses use a track segment length of 2 m to compare the results.

6.2.3 Energy Reconstruction

Next to the two "measured" parameters, the length and the energy losses, also the reconstructed energy is required for this study, which is estimated using the energy losses per track segment. The energy of the muon when it enters the detector is reconstructed using two independent reconstruction methods to validate their results.

To calibrate both energy reconstruction methods a dataset with 10^6 muons and a spectral index of $\gamma = 1$ is created. A larger energy range from 1 GeV to 100 PeV is used to avoid boundary effects and also correctly reconstruct the edge cases. To use just events with enough information, only events with a track length $l > 100\,\mathrm{m}$ are selected for the calibration.

In the so-called "truncated energy" method the linear behavior of the overall continuous energy loss to the muon energy (c.f. Figure 4.2a) is used. It is similar to the method described in [Aar+14], which is the default energy reconstruction for high energy muons in IceCube. This dependency is mainly driven by the pair production interaction, where the amount of low energy losses just increases linearly with the muon energy. On the other side, the bremsstrahlung-driven energy losses are equally distributed in the log space of the muon energy. This results in mainly stochastic losses that are uncorrelated with the muon energy. Therefore the stochastic losses are cut out for this method and the "truncated" energy loss segments are used. Here, the 10 % of the track segments with the highest losses are ignored. The dependency of the remaining energy losses and the muon energy is calibrated using a spline-fit. For the baseline resolution, the calibration and the performance of this method are shown in Figure 6.7. For the other two resolutions, this is shown in section B.1.1

Below a TeV, the Ionization is dominating the muon energy loss and there is no correlation between the continuous energy loss and the muon energy due to the nearly flat dependency (c.f. section Figure 4.2a). This limits the resolution at lower energies for this method and in general. Another approach at these energies is the track length, but even at several 100 GeV the average propagated distance of muons in ice exceeds a kilometer. As this analysis is more focused on muons above a TeV, more advanced methods improving the truncated energy reconstruction are not considered here.

Varying the cross-sections and changing the relation between small continuous losses and large stochastic losses might affect the energy reconstruction. However, the analysis should be sensitive to changes in the energy loss distribution, while other parameters should remain stable. A shift also in the energy reconstruction would

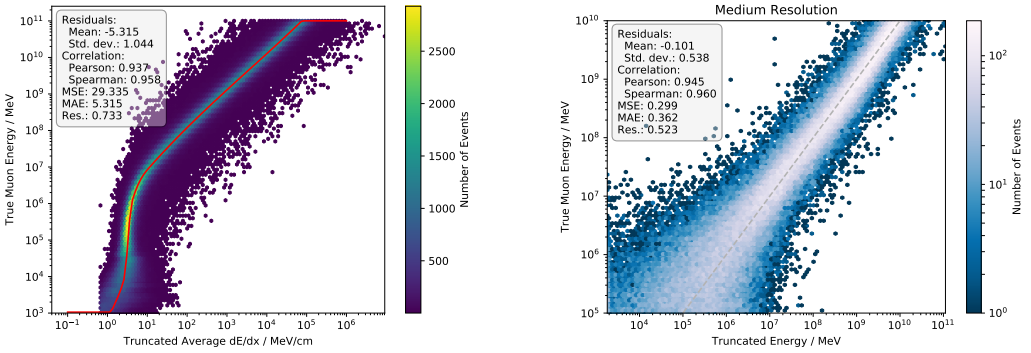

(a) The calibration curve, shown in red.

(b) The performance of the reconstruction.

Figure 6.7: The truncated energy reconstruction for the baseline resolution setting. On the left side, the correlation between the average energy loss of the truncated track segments and the true muon energy is calibrated, using a spline fit. On the right side, the performance using this calibration is evaluated on an independent dataset.

mean, that muons of different energy regions would get compared, directly lead to a different energy loss profile, disturbing the cross-section measurement.

Therefore, a second and independent method to reconstruct the energy using a neural network is implemented, also as a cross-check to the truncated energy method. This machine learning method has shown comparable or even improved performances in IceCube compared to the best likelihood-based energy proxies like truncated energy [Hue17a; Hue18]. In principle, the network can learn the same truncated energy method described above, while using the available information to learn also the other reconstruction methods, e.g. the track length correlation or using the stochastic losses as a lower limit. Here, a combination of convolutional layers, to learn the correlation between the neighboring segments, and dense layers, combining the elements, is used to estimate the energy. The rather small network architecture for this light-weighted study is listed in Table 6.2.

Comparing the performance of these two energy reconstruction methods, regarding Figure 6.7b and 6.8a, the truncated energy method performs slightly better at the relevant energies above a TeV. The neural network provides stable performances also at lower energies, probably using the track length dependency for these events. But in general, both methods provide similar results, shown in detail in section B.1.2, and can be used as realistic energy reconstruction methods.

To discard the muons with large mis-reconstructed energies, disturbing the energy loss spectrum and reducing the sensitivity of this study, an estimation of the

Table 6.2: The convolutional neural network architecture used for the energy reconstruction.

Layer Name	Details			
	Kernel size	Filters	Activation	Units
Batch Normalization	Normalization of reconstructed energy loss input			
Convolution 1D	7	15	relu	
Convolution 1D	7	15	relu	
Max Pooling 1D	2			
Convolution 1D	7	15	relu	
Convolution 1D	7	15	relu	
Max Pooling 1D	2			
Convolution 1D	7	15	relu	
Convolution 1D	7	5	relu	
Flatten	Flatten layer			
Dense			relu	32
Dense			relu	16
Dense			None	1

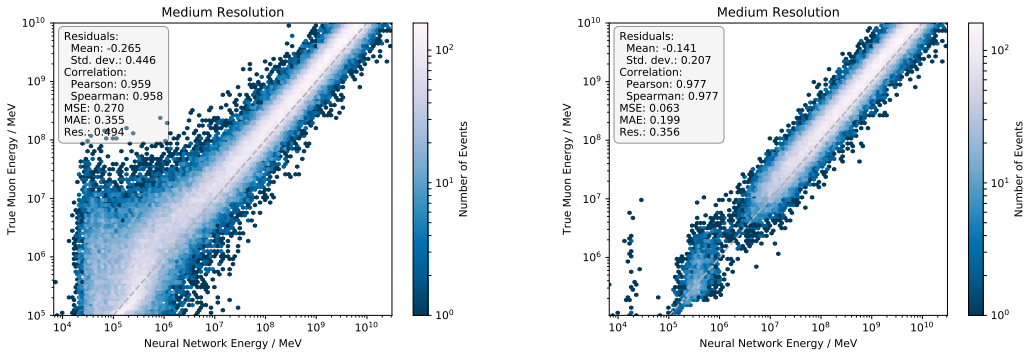

(a) All events. **(b)** 50 % of the events.

Figure 6.8: The performance of the neural network reconstruction of the muon energy for the baseline resolution. On the right side, an uncertainty cut is applied filtering 50 % of the best reconstructed events compared to the full event sample on the left side.

uncertainty of the energy reconstruction is required. Recent developments show, that such uncertainty estimators provide accurate and robust estimations of the real deviation, useful in IceCube analysis [Hue17a]. Again a neural network is used with nearly the same network architecture as for the energy reconstruction but using the absolute function for the activation. The network then returns the absolute value of the estimated deviation of the reconstructed energy in the log space. The increase in the performance of the energy reconstruction using a cut of the energy uncertainty estimator is indicated in Figure 6.8b. However, this uncertainty cut reduces also the size of the data sample and for each resolution setting a trade-off between a high sample statistic and good reconstructed events is made for the selection.

For a final check of the energy reconstruction, its correlation to the scaling of the bremsstrahlung cross-section has to be analyzed. As already mentioned, a correlation between these parameters would be a circle conclusion, since the energy loss distributions are created according to the reconstructed energy. If this also changes, the effect of a changing energy loss profile is a circle. Therefore, both parameters have to be uncorrelated, at least inside the parameter space this study is focused on. In principle, the energy reconstruction of course depends also on the bremsstrahlung cross-section as described above. A higher bremsstrahlung cross-section results in more high energy losses and fewer lower energetic losses. This changes the ratio between small continuous losses and high stochastic losses the reconstruction methods are tuned on. But the energy reconstruction should be robust against small changes in the bremsstrahlung cross-section, as the same amount of stochastic losses should get truncated.

Regarding changes of $\pm 10\,\%$ in the bremsstrahlung cross-section, no changes of the energy reconstruction are observed, as shown in Figure 6.9. Just for large scalings of the bremsstrahlung by orders of magnitudes, the relation between continuous and stochastic losses changes significantly and the correlation gets visible, shown in Figure B.8. This independence of the energy reconstruction from small bremsstrahlung changes is observed for each resolution setting and both reconstruction approaches (see section B.1.3). In general, the cross-check of the energy reconstruction was successful, since both approaches produce similar and robust results.

6.2.4 Parameterizing the Energy Loss Distribution

Before creating the energy loss distributions, an event selection consisting of two pre-cuts is performed discarding mis-reconstructed events. First, only events propagating at least 100 m through the detector are selected to avoid corner clippers and make sure, that a sufficient part of the track is visible to reconstruct the relevant information. The second cut is performed on the energy uncertainty parameter and

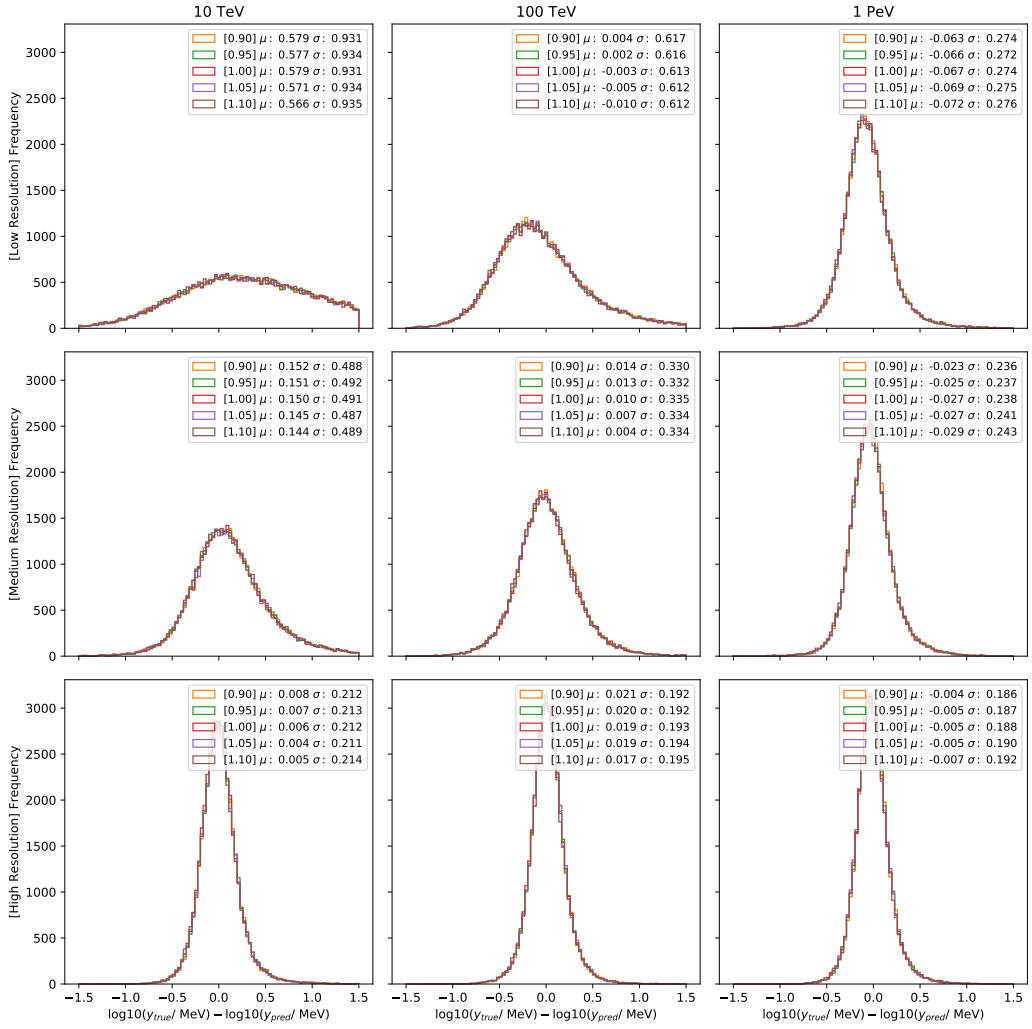

Figure 6.9: The pull distribution of reconstructed energies using the truncated energy method for the three resolution settings and muon energies. The multiplier, scaling the bremsstrahlung cross-section is varied between 0.9 and 1.1, and the mean and standard deviation for each multiplier dataset is estimated.

can be adapted for each resolution setting. For this study, the energy loss cut for the three resolution settings is listed in Table 6.1.

Furthermore, only muon energies between 1 TeV and 100 TeV are selected, since lower energetic muons are dominated by ionization losses and higher energies are lacking of statistics. The selected muon range is divided into three equally sized bins in $\log_{10}$-space between 1 TeV and 10 TeV and two bins also equally distributed in $\log_{10}$-space between 10 TeV and 100 TeV. This corresponds approximately to the energy ranges listed in Table 6.3.

Table 6.3: Energy ranges of reconstructed muon energies selected for this study.

Energy Range / TeV	
Lower Bound	Upper Bound
1	2.15
2.15	4.64
4.64	10
10	31.6
31.6	100

Using the reconstructed energy losses per track segment, an energy loss histogram is created for each muon energy bin according to the weight of the given energy spectrum. Assuming a Poisson distribution for the content of each energy loss bin, the normalized energy loss distribution H and its error E can be expressed by

$$H = \frac{\sum L_i w_i}{\sum w_i d_i} \qquad \text{and} \qquad E = \frac{\sum L_i w_i^2}{\sum w_i d_i}. \tag{6.1}$$

with the energy loss histograms L the energy weight w and the propagated distances d per event i. Since the energy losses histogram is just comparable with the same propagated distance, they are normalized by the weighted propagation length. Using the produced energy loss distributions, the main task is to parameterize and fit the differences between these energy loss histograms according to the fit parameters. The variations of the three fit parameters are listed in Table 6.4.

For each scaling of the bremsstrahlung cross-section (Multiplier) 1×10^7 muons are simulated between 100 GeV and 1 PeV with a spectral index of 1. Then, each bremsstrahlung multiplier dataset is reconstructed with the different efficiency of the photomultipliers (DOM efficiency). Therefore the different DOM efficiency data points are correlated and not created using independent Monte-Carlo simulations. However, this approximation was made to reduce the runtime of the simulation. This gets even more relevant for the spectral index (Gamma) as these datasets are

Table 6.4: Interpolation settings for the three fit parameters.

Fit Parameter	Bremsstrahlung	DOM Efficiency	Spectral Index
Interpolation Points	9	9	9
Interpolation Range	[0.9, 1.1]	[0.9, 1.1]	[1.5, 1.9]
Fit Range	[0.95, 1.05]	[0.95, 1.05]	[1.6, 1.8]
Baseline Value	1.0	1.0	1.7
Order of Interpolation	cubic	quadratic	quadratic

just re-weighting the events for each bremsstrahlung simulation and DOM efficiency reconstruction data set. The interpolation points are placed with an equidistant spacing between each other and span a grid of $9 \times 9 \times 9$ points in the fit parameter space for each bin, shown in Figure 6.11b.

To get an impression of how the energy loss bins change by varying the fit parameter and how the shape looks, one-dimensional interpolations are created. Thereby only one parameter is changed, while for the other two parameters, the default value is used. For the Bremsstrahlung multiplier, this is shown in Figure 6.10, and in section B.2 for the other settings. Compared to the DOM efficiency and spectral index, the effect of the bremsstrahlung multiplier is less significant. One reason is, that the bremsstrahlung datasets are independent of each other, while the other two interpolations are built on the same dataset. But the main reason for this is, that the Bremsstrahlung is just a smaller effect compared to the DOM efficiency and the spectral index, which are considered in every IceCube analysis. Also without smearing of the reconstructions, using the Monte-Carlo truths of the secondary spectrum directly to create these interpolations, the bremsstrahlung data points do fluctuate significantly more compared to the other parameters where the smearing of the reconstructions are included.

The used polynomials for each fit variable are also listed in Table 6.4. Thereby a trade-off is made between a small degree of freedom and a precise description while just interpolating the real physical changes and no fluctuation and do overfitting. For the DOM efficiency and the spectral index, the slight curvature can be well expressed with a quadratic polynomial. A cubic polynomial is used for the bremsstrahlung multiplier as it allows to describe more structures while still limiting overfitting.

Energy loss bins, which do not significantly change or have a slope, or where the interpolation does not describe the data points, due to large fluctuations, should

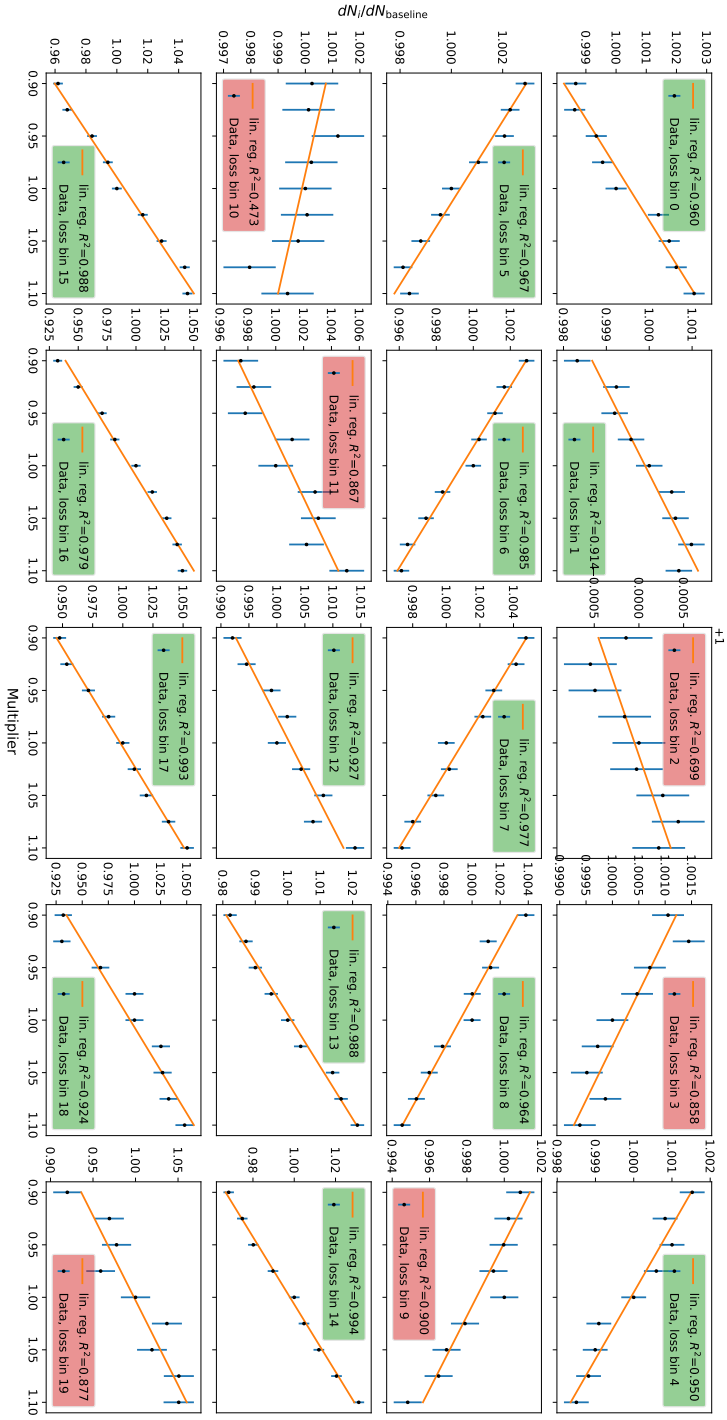

Figure 6.10: One dimensional interpolation of the differences between the energy loss histograms created with different bremsstrahlung multiplier. The baseline resolution is used and reconstructed muon energies between 10 TeV and 31.6 TeV using neural networks are selected. A coefficient of determination threshold of 0.9 is used to mark all energy loss bins (red colored legend box), which would not be included in a fit of the bremsstrahlung.

not be considered for this analysis. Therefore the coefficient of determination

$$R^2 = 1 - \frac{\sum(y - f(x))^2}{\sum(y - \bar{y})^2} \tag{6.2}$$

is calculated for each bin to be able to exclude bins with a bad interpolation or no significant changes. Thereby, y represents the difference between the energy loss bins and $f(x)$ the interpolation function.

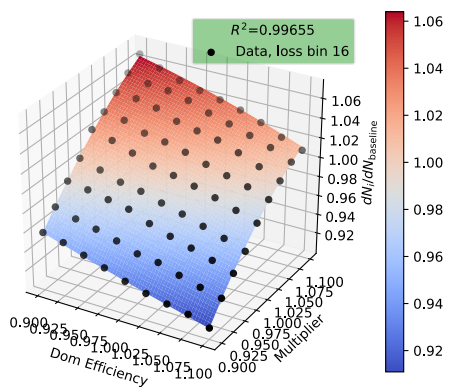

(a) 2D-Interpolation of the DOM efficiency and the bremsstrahlung multiplier.

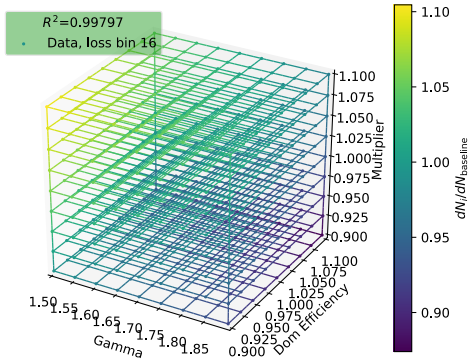

(b) 3D-Interpolation of the spectral index, DOM efficiency, and the bremsstrahlung multiplier.

Figure 6.11: The interpolation of the differences of the energy loss histogram for muons with reconstructed energies between 1 TeV and 31.6 TeV using neural networks for the energy reconstruction. The high resolution setting is considered, here. For the 2D-interpolation the color bar equals the z-axis, and is shown for a clearer understanding. In the 3D-interpolation only the color bar represents the bin difference. The coefficient of determination R is calculated.

Due to the correlations between the fit variables, one-dimensional interpolations do not take into account all these effects. This can be seen in Figure 6.11a in a 2D interpolation of the bremsstrahlung multiplier and the DOM efficiency. Although it is also possible to treat the spectral index rather independently of the other two processes in a 1D interpolation, assuming negligible correlation to the other parameters. In this analysis, a 3D-interpolation, shown in Figure 6.11b, is used with the function

$$\begin{aligned} f(x_{\text{brems}}, x_{\text{eff}}, x_{\text{gamma}}) = {} & a_0 + a_1 x_{\text{brems}} + a_2 x_{\text{brems}}^2 + a_3 x_{\text{brems}}^3 \\ & + a_4 x_{\text{gamma}} + a_6 x_{\text{gamma}}^2 + a_6 x_{\text{eff}} + a_7 x_{\text{eff}}^2 \\ & + a_8 x_{\text{brems}} \cdot x_{\text{gamma}} + a_9 x_{\text{brems}} \cdot x_{\text{eff}} + a_{10} x_{\text{gamma}} \cdot x_{\text{eff}}. \end{aligned} \tag{6.3}$$

The threshold for the coefficient of determination R^2 can be set for each resolution setting. For this study, the values are already listed in Table 6.1.

6.2.5 Performance of the Measurement

With these interpolations, a Poisson Likelihood is defined to describe the bin contents of the energy loss distributions. A Marcov-Chain-Monte-Carlo (MCMC) sampling is then applied to estimate the three parameters including their correlations, shown exemplarily in Figure 6.12.

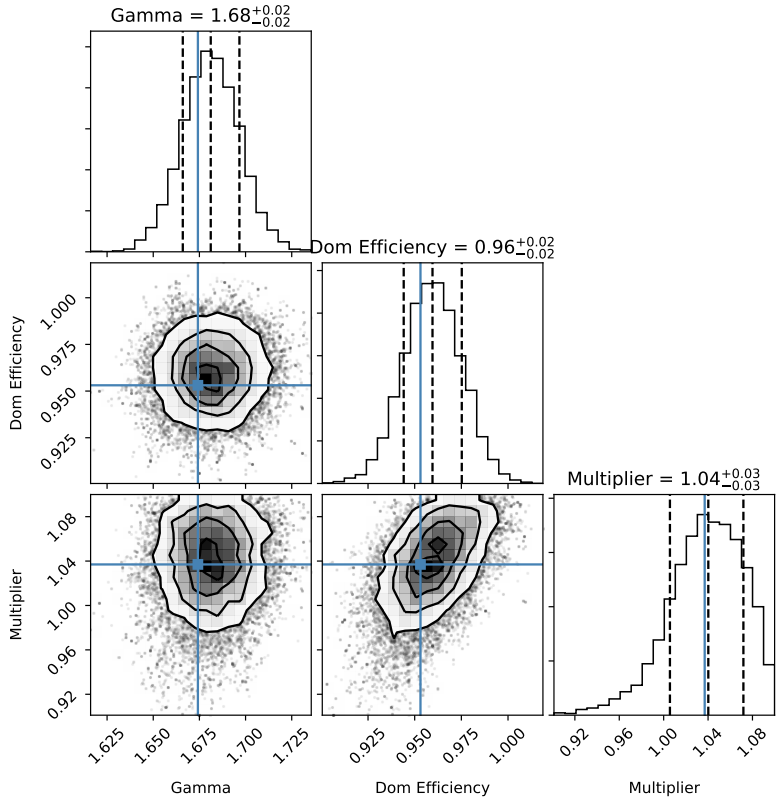

Figure 6.12: Sampling result of the MCMC estimation. The blue lines represent the true values.

To estimate the performance of the bremsstrahlung multiplier measurement for the different resolutions, Monte-Carlo simulation sets, each with random bremsstrahlung multipliers and fixed systematic parameters are produced propagating 10^6 muons.

The results for the baseline resolution setting are shown in Figure 6.13. Further results with different resolution settings or energy reconstruction methods are shown in section B.3. The values outside the fit range, defined in Table 6.4, are on the one site calculated to analyze the effect. But on the other side, these values are discarded from the performance estimation, due to boundaries effects biasing parameters at the edge of the ranges towards the center.

There is no notable difference in the performance between the truncated energy and the neural network approach to estimate the muon energy. For the high resolution, the bremsstrahlung multiplier can be estimated within $\pm 1\,\%$ and for the baseline resolution, this increases to $\pm 4\,\%$ (shown in Figure 6.14). For the low resolution, it is not feasible to estimate the bremsstrahlung multiplier, since the likelihood landscape for the 68 % central interval already exceeds the boundaries of the interpolated range (shown in Table 6.4). However, boundary effects can also be observed for higher resolutions, like in Figure 6.12.

The DOM efficiency can be measured with the highest precision and the spectral index with still high accuracy. The precision and the bremsstrahlung multiplier with the lowest accuracy, which is expected as the effect of the Bremsstrahlung on the energy loss distribution is already smaller and just significant at higher energy losses.

Concluding the results, it is possible to measure the bremsstrahlung multiplier with high resolutions similar to a cubic kilometer-sized DeepCore detector, in the percent level. Regarding resolution setting similar to IceCube, a measurement is still feasible, but with higher uncertainties of around 4 %. For a detector as sparsely instrumented as the IceCube-Gen2 detector or with similar resolutions, a measurement of the bremsstrahlung using the same techniques is not feasible. Thereby the amount of events surviving the cuts of a track length and in particular of the uncertainty of the energy estimation is reduced significantly with nearly no muons left to analyze. However, since Gen2 is designed to detect more muons at higher energies, the setup should be adapted to these energies and sizes.

The spectral index and the DOM efficiency can be measured in every setup, also for low resolutions. In this analysis, the spectral index is only taken into account as a nuisance parameter, as it describes only the spectrum of muons entering the detector, not relevant for other analyses. The DOM efficiency, however, is a systematic parameter relevant for every analysis. A measurement or reduction of the region, that needs to be considered for the DOM efficiency would directly increase the sensitivity for these analyses. But a more precise measurement of the DOM efficiency can be performed using a stopping muon sample with their minimal Ionizing muons. Further possible measurements of muon properties or systematics are described in the next section.

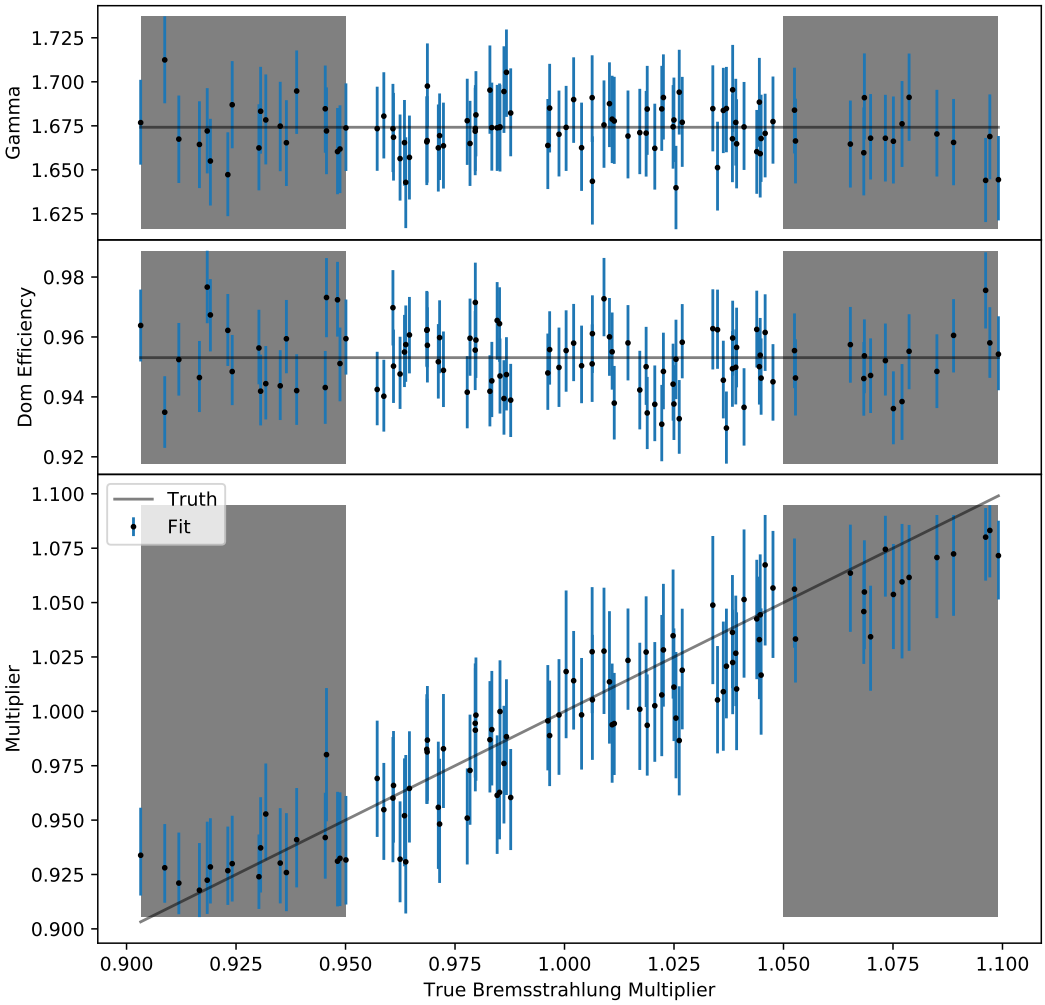

Figure 6.13: Correlation of the true values and the estimated results of the MCMC samplings with the baseline resolution settings for the spectral index, the DOM efficiency and the bremsstrahlung multiplier. The muon energy is reconstructed using the neural network. The region below 0.95 and above 1.05 is neglected for the performance to avoid boundary effects during the MCMC sampling at the edge of the allowed interpolation region. The error represents the 68 % central interval and the best fit value, the median.

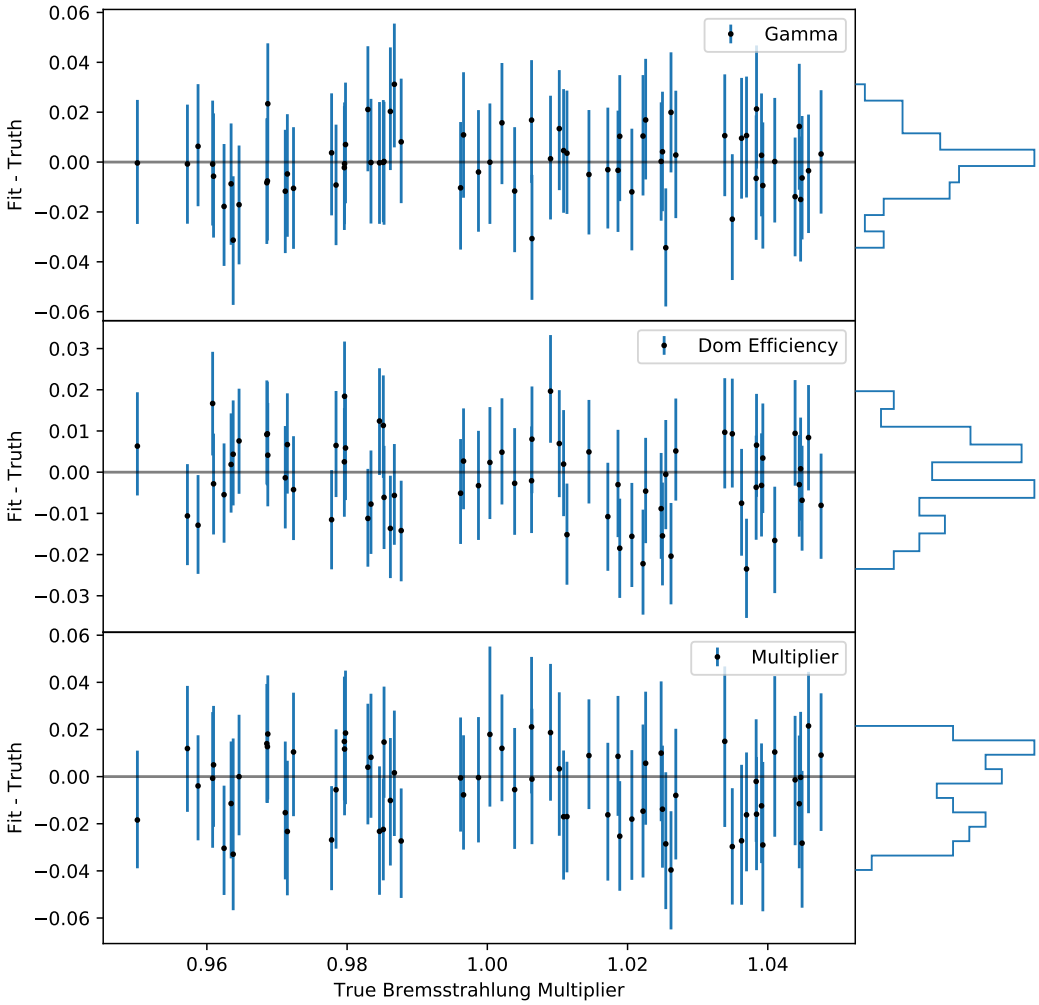

Figure 6.14: Pull distribution of the estimated results of the MCMC samplings with the baseline resolution settings for the spectral index, the DOM efficiency and the bremsstrahlung multiplier. The muon energy is reconstructed using the neural network. The region below 0.95 and above 1.05 is neglected for the performance to avoid boundary effects during the MCMC sampling at the edge of the allowed interpolation region. The error represents the 68 % central interval and the best fit value, the median.

6.3 Outlook of Measurements using Atmospheric Muons

The study described above using a neutrino-induced muon sample is one way to measure muon properties using large volume detectors like IceCube. To measure further parts of the muon cross-section, other approaches including atmospheric muon samples are required. The big benefit in using atmospheric muons is the increased sample size of several orders of magnitude, being able to make a more rigorous selection demanding a high reconstruction quality.

A dataset selecting stopping muons mainly consists of single muons [Hoi17; Nin19]. Usually, the last surviving muon is the highest energetic particle of the muon bundle produced in the air shower. Most of these muons are far below a TeV and with no stochastic loss and therefore not interesting for the study described in the previous section. However, at these energies, the ionization is dominating the energy loss with its nearly energy independent and constant energy loss probability. Either the DOM efficiency or the ionization cross-section can be measured while fixing the other parameter.

Next to the calibration advantages, this sample can also be used to measure the muon energy distribution at the surface. The range of these muons to the surface can be determined using their reconstructed direction for zenith angles below 80°, where the incoming muon flux is dominated by atmospheric muons and the neutrinos contribution is sub-dominant. Then, the energy distribution of the muons can be unfolded using the relation between the range and average energy loss, described in section 4.1. Furthermore, the differences between the muons traveling short distances through the ice and muons traveling long distances can be used to verify the muon cross-sections assuming both originate from the same distribution. Due to the relative comparison of the same sample, most systematic parameters cancel out.

Another approach is by using a leading muon sample selecting atmospheric muon bundles where a single muon contains most of the bundle energy. For bundles with an equal energy distribution between the muons, the event signature is a homogeneous bright track where all the stochastic losses by the different muon are 'washed' out. If a single muon contains most of the bundle energy, there is a higher fluctuation of the brightness along the track and more visible stochasticity. With this sample also higher energetic muons can be selected, but couldn't be used for the analysis above as it depends on the relation of high stochastic and low continuous energy losses. Fitting the Bremsstrahlung cross-section with this sample would therefore be a circle conclusion as just events with higher energy losses are selected. Due to the higher energy range, this dataset is used in an ongoing analysis to estimate the prompt atmospheric muon spectrum, similar to [Fuc16a; Fuc16b].

A goal would finally be to combine these three datasets low energetic stopping muons, muons and neutrino-induced single muons, and high energetic leading muons. Due to shared systematic parameters, a precise measurements of muon properties can be performed. Although large volume neutrino telescopes are not designed to measure muon properties, they provide the unique opportunity to analyze and verify muon physics at energies not feasible for accelerator detectors of the current and the next generation.

7 Summary and Outlook

In the context of the more precise measurements of underground experiments, where atmospheric muons are most-often the main source of background events, an accurate description of muon propagation in simulations is required. In this work, the systematic uncertainties of high energy muon simulation have been analyzed. Thereby, the theoretical models describing the main interactions, ionization, pair production, bremsstrahlung, and inelastic nuclear interaction, as well as rare processes were revised. Also, radiative corrections to the pair production cross-section were calculated.

Next to the theoretical work, the Leptonpropagator PROPOSAL was improved by implementing more accurate cross-section and decay calculations. Besides the improvements of the theoretical models, also propagation methods were revised and the runtime performance was improved by 10 % to 20 % depending on the energy of the propagation settings. The complete software was restructured from a simulation specialized for a single experiment, the IceCube detector, to a modular library used in multiple different applications and experiments ranging from neutrino astronomy to dark matter searches. A python interface was developed, which is used e.g. in the simulation framework nuRadioMC for experiments of radio neutrino astronomy, where the interface to PROPOSAL was implemented. Also, the restructured air shower simulation framework CORSIKA now uses PROPOSAL as a module providing electromagnetic interactions.

Besides larger experiments and simulation frameworks, also small scaled simulation studies can now be performed using PROPOSAL e.g. to analyze systematic uncertainties of the muon cross-sections and their effects on propagation parameters. The effects of more accurate cross-sections for pair production and bremsstrahlung on the muon range and energy distribution at certain distances were found to be negligible compared to the error introduced with an energy loss cut. However, regarding the produced secondaries for large calorimetric detectors, a significant change of the energy loss spectrum due to the new cross-sections was observed.

Therefore, a feasibility study was developed estimating the sensitivity for cubic kilometer-sized neutrino telescopes to measure the bremsstrahlung cross-section. The created toy Monte-Carlo framework propagates the muons with PROPOSAL and effectively simulates further detector components to produce smeared-out and

realistic energy losses along the muon track and reconstructing the muon energy out of these losses. Thereby, the energy reconstruction was found to be robust against variations of the bremsstrahlung cross-section of a few percent according to the theoretical uncertainty. With the energy loss profiles, the normalization of the bremsstrahlung has been estimated, considering also two further systematic parameters, the efficiency of the photo detectors and the spectral index of the muon flux. For a resolution similar to the IceCube experiment, and a single muons sample according to 10 years of neutrino-induced muons measured with IceCube, the bremsstrahlung cross-section can be measured with an uncertainty of $\pm 4\,\%$.

Regarding possible further works, the unique opportunities of cubic kilometer-sized calorimetric detectors to analyze muon properties have been discussed in the previous section 6.3. However, solving the muon puzzle will be the main task for the next years regarding muon physics. Thereby, the connection of PROPOSAL to CORSIKA is essential to provide a consistent treatment of the muons from the generation and propagation in the atmosphere to the detector, instead of propagating the muon inconsistent and independent of each other. Further possible works enhancing PROPOSAL as electromagnetic interaction module e.g. also for hadronic particles or by implementing muon pair production induced by a high energy photon are discussed in section 5. There is also still some amount of theoretical work required, e.g. to parametrize the radiative corrections to the pair production cross-section or to find a treatment of the LPM effect also in inhomogeneous media as discussed in section 4.

The simulation and the theoretical models of high energy muons have been improved in this thesis, but further work needs to be done, providing more accurate simulations thus increasing the sensitivity for experiments measuring high energy particles in the context of Multi-Messenger Astronomy.

A Appendix

A.1 Tables of the Photonuclear Interactions

Table A.1: Measured Photon-Nucleon cross-section $\sigma_{\gamma N}$ used in the photonuclear cross-section of the Rhode parametrization[Rho93], described in section 4.5.1. The the photon energies E_γ are equally distributed in $\log_{10}$ space.

E_γ/GeV	$\sigma_{\gamma N}/\mu$b	E_γ/GeV	$\sigma_{\gamma N}/\mu$b	E_γ/GeV	$\sigma_{\gamma N}/\mu$b
1.0000×10^{-1}	0.066 667	5.2481×10^{1}	114.37	2.7542×10^{4}	211.78
1.4454×10^{-1}	0.096 363	7.5858×10^{1}	114.79	3.9811×10^{4}	223.50
2.0893×10^{-1}	159.74	1.0965×10^{2}	115.86	5.7544×10^{4}	235.88
3.0200×10^{-1}	508.10	1.5849×10^{2}	117.61	8.3176×10^{4}	248.92
4.3652×10^{-1}	215.77	2.2909×10^{2}	120.01	1.2023×10^{5}	262.63
6.3096×10^{-1}	236.40	3.3113×10^{2}	123.08	1.7378×10^{5}	277.01
9.1201×10^{-1}	201.92	4.7863×10^{2}	126.81	2.5119×10^{5}	292.05
1.3183	151.38	6.9183×10^{2}	131.21	3.6308×10^{5}	307.75
1.9055	145.41	1.0000×10^{3}	136.28	5.2481×10^{5}	324.12
2.7542	132.10	1.4454×10^{3}	142.01	7.5858×10^{5}	341.16
3.9811	128.55	2.0893×10^{3}	148.40	1.0965×10^{6}	358.86
5.7544	125.05	3.0200×10^{3}	155.46	1.5849×10^{6}	377.22
8.3176	121.86	4.3652×10^{3}	163.19	2.2909×10^{6}	396.25
1.2023×10^{1}	119.16	6.3096×10^{3}	171.57	3.3113×10^{6}	415.95
1.7378×10^{1}	117.02	9.1201×10^{3}	180.63	4.7863×10^{6}	436.31
2.5119×10^{1}	115.50	1.3183×10^{4}	190.35	6.9183×10^{6}	457.33
3.6308×10^{1}	114.61	1.9055×10^{4}	200.73	1.0000×10^{7}	479.02

Table A.2: Fit values of the ALLM parametrization estimated in ALLM91[Abr+91], ALLM97 [AL97], and AbtFT[Abt+17], described in section 4.5.2.

Parameters	ALLM91	ALLM97	AbtFT17
$a_{1,R}$	0.604 08	0.584 00	0.882
$a_{2,R}$	0.173 53	0.378 88	0.082
$a_{3,R}$	1.618 12	2.6063	−8.5
$b_{1,R}$	1.260 66	0.011 47	0.339
$b_{2,R}$	1.836 24	3.7582	3.38
$b_{3,R}$	0.811 41	0.493 38	1.07
$c_{1,R}$	0.676 39	0.801 07	−0.636
$c_{2,R}$	0.490 27	0.973 07	3.37
$c_{3,R}$	2.662 75	3.4942	−0.660
$a_{1,P}$	−0.045 03	−0.0808	−0.075
$a_{2,P}$	−0.364 07	−0.448 12	−0.470
$a_{3,P}$	8.170 91	1.1709	9.2
$b_{1,P}$	0.492 22	0.362 92	−0.477
$b_{2,P}$	0.521 16	1.8917	54.0
$b_{3,P}$	3.551 15	1.8439	0.073
$c_{1,P}$	0.265 50	0.280 67	0.356
$c_{2,P}$	0.048 56	0.222 91	0.171
$c_{3,P}$	1.046 82	2.1979	18.6
m_γ^2 / GeV^2	0.305 08	0.319 85	0.388
m_R^2 / GeV^2	0.206 23	0.150 52	0.838
m_P^2 / GeV^2	10.675 64	49.457	50.8
Λ^2 / GeV^2	0.065 27	0.065 27	4.4×10^{-9}
$(Q_0^2 - \Lambda^2)$ / GeV^2	0.277 99	0.525 44	1.87×10^{-5}

A.2 Radiative Corrections to the Pair Production

In this section, radiative corrections of the pair production for the muon line are calculated, as described in section 4.4.6, considering only the e-diagrams, since they are the dominating process.

Before describing the calculation, the used dilogarithm is defined by

$$\mathrm{Li}_2(x) = -\mathrm{Re}\int_0^x \frac{\ln(1-t)}{t}\mathrm{d}t. \tag{A.1}$$

The tree-level cross-section of pair production and bremsstrahlung calculated by Bugaev [Bug77] are used as base to estimate radiative corrections. Due to the modular structure of the parametrization, dividing the cross-section into the muon line, the electron line, and the nuclear Interaction as three distinct tensors, each tensor can easily replaced introducing e.g. a correction to a fermion line. Furthermore, the bremsstrahlung cross-section is calculated in the same formalism allowing a combination of both processes due the their consistent treatment.

The differential cross section is given by

$$\frac{\mathrm{d}\sigma}{\mathrm{d}\omega\mathrm{d}\varepsilon_+\mathrm{d}k^2\mathrm{d}q^2\mathrm{d}\nu} = \frac{Z^2\alpha^4 m_e^2}{16\pi^2 p^2}\frac{1}{k^2q^2}(W_1(L_1M^{\mu\mu}_{\alpha\alpha} - L_2M_{44}\mu\mu) + W_2(L_2M^{44}_{44} - L_1M^{44}_{\alpha\alpha})), \tag{A.2}$$

where k^2 and q^2 are the squared momentum and $\omega and \nu$ the energies of the virtual photons connecting the electron with the muon line and the electron line with the nucleus respectively. The tensors of the nucleus W, the electron line M and the muon line L are already contracted. Instead of being differential in the asymmetry ρ, this cross section uses the energy of the positron ε_+.

To simplify the calculation, the same relativistic approximations as described in [Bug77] are applied, consisting of

- a high γ factor of the muon and the electron-positron pair ($E_\mu^2 \gg m_\mu^2$ and $\varepsilon_+^2 \gg m_e^2$)
- small momentum transfers ($k^2, q^2 \ll E_\mu^2$)
- not the smallest energy losses ($\omega^2 \gg m_\mu^2$)

Furthermore, the nucleus is assumed to be heavy and have no recoil, thus neglecting the energy transfered to the nucleus $\nu \approx 0$. Therefore, also the spatial components

of the electromagnetic structure functions are neglected $W_1 \approx 0$, while W_2 is defined by

$$W_2(q^2) = -((f_n - f_a)^2 + 1/Z * (f_{n,\text{in}} + f_{a,\text{in}})). \tag{A.3}$$

The form factors are taken from [Tsa74; ABB94]

$$f_n = (1 + a^2 q^2/12)^{-2}, \qquad f_a = (1 + b^2 q^2)^{-1}, \tag{A.4a}$$

$$f_{n,\text{in}} = 1 - f_n^2, \qquad f_{a,\text{in}} = \left(\frac{c^2 q^2}{1 + c^2 q^2}\right)^2, \tag{A.4b}$$

with

$$a = (0.58 + 0.82 A^{1/3}) \cdot 5.07/\text{GeV}, \tag{A.5a}$$

$$b = \frac{B_\text{el}}{\sqrt{e} m_e} Z^{-1/3}, \tag{A.5b}$$

$$c = \frac{B_\text{inel}}{\sqrt{e} m_e} Z^{-2/3}. \tag{A.5c}$$

For the tree-level process, the functions for the muon line $L_{1,2}$ can be described with eq. (44) of [Bug77] and tensors of the electron line M_{44}^{44} and $M_{\alpha\alpha}^{44}$ with eq. (36) of [Bug77]. Integrating the tree-level diagram over q^2, k^2, and ε_+ results in a similar differential cross-section in the energy loss, compared to the e-diagram of Kelner et al. (c.f. section 4.4.1), as shown in Figure A.1.

The overall correction due to the radiative corrections are in the percent level. However, regarding the differential cross-section, this correction can have larger effect, especially at higher energy losses. This is mainly driven by the hard bremsstrahlung with an energy loss spectrum similar to the μ-diagram. In future works, this only numerically integrated contribution needs to parameterized to be usable in simulations like PROPOSAL, as the correction is on the order as the μ-diagram.

In the following subsections, the calculation of the radiative correction is described.

A.2.1 Vacuum Polarization

Out of the tree-level cross-section, the vacuum polarization can simply be included with a correction factor before the integration over k^2, since it only depends on k^2. The correction factor to the tree process was calculated in [MO65] eq. (IV.2/3) and without setting the electron mass to 1 this results in

$$s_\text{vac}(k^2) = -\frac{2\alpha}{3\pi}\left[\frac{5}{3} - \zeta - \left(1 - \frac{\zeta}{2}\right)\sqrt{1+\zeta}\ln\left(\frac{k^2 + k^2\sqrt{1+\zeta}}{2m_e^2} + 1\right)\right] \tag{A.6}$$

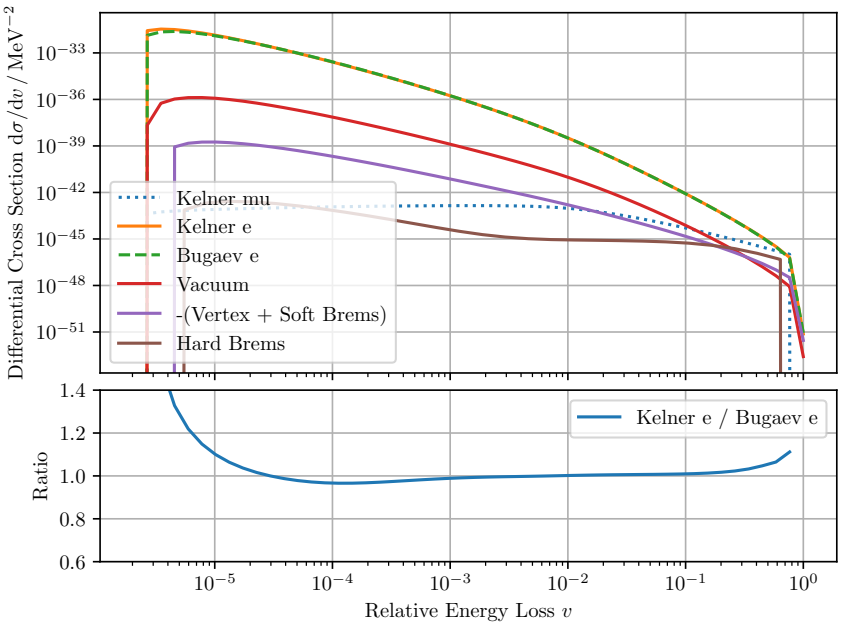

Figure A.1: Differential cross section of the pair production cross section including the tree-level of the e-diagram (Bugaev) and its radiative corrections along the muon line, vacuum polarization, vertex correction, and soft and hard bremsstrahlung. The e-diagram of the Kelner et al. parametrization is included and compared to the calculated e. Also the μ-diagram of Kelner et al. is included.

using

$$\zeta = \frac{4m_e^2}{k^2}. \tag{A.7}$$

Vertex Correction and Soft Bremsstrahlung

The Vertex correction to a fermion line for an outgoing space-like photon has been calculated in [AB81] in eq. (5.1.37) leading to the renormalized form

$$\Lambda_\mu = \frac{\alpha}{\pi}\left(\gamma_\mu \Lambda_1 + i\frac{\gamma_\mu \hat{k} - \hat{k}\gamma_\mu}{8M}\Lambda_2\right), \tag{A.8}$$

with the expressions

$$\Lambda_1 = \left(\ln\frac{M}{\lambda} - 1\right)\left(\frac{1+a^2}{2a}\ln b + 1\right) + \frac{\ln b}{4a}, \tag{A.9a}$$
$$- \frac{1+a^2}{4a}\left(-\frac{\pi^2}{6} + \frac{\ln^2 b}{2} - 2\ln b \ln(1+b) - 2\,\mathrm{Li}_2(-b)\right)$$
$$\Lambda_2 = \frac{a^2-1}{2a}\ln b, \tag{A.9b}$$

using abbreviations

$$a = \sqrt{1 + \frac{4M^2}{k^2}}, \qquad b = \frac{a-1}{a+1}. \tag{A.10}$$

The tensor of the muon line including the vertex correction can be written as

$$L_{\mu\nu} = \Lambda_\mu (i\hat{p}_1 - M)\gamma_\nu (i\hat{p}_2 - M). \tag{A.11}$$

To contract these tensors, and calculating the traces over the gamma matrices, the computer algebra program FORM [Ver00] was used resulting in

$$\delta^{\mu\nu} L_{\mu\nu} = L_{\mu\mu} = \left(\frac{k^2}{2} - M^2\right)\Lambda_1 - 3k^2\Lambda_2, \tag{A.12a}$$

$$\frac{1}{M^2} p^\mu p^\nu L_{\mu\nu} = L_{44} = \left(\frac{k^2}{4} - E_1 E_2\right)\Lambda_1 - k^{*2}\Lambda_2. \tag{A.12b}$$

Including (A.12) into the definition of $L_{1,2}$ in eq. (9) of [Bug77], eq. (44) of [Bug77] changes to

$$L_1 = \frac{2}{k^*} L_{\mu\mu} - \frac{k^2}{k^{*2}} L_{44}, \tag{A.13a}$$

$$L_2 = \frac{2k^2}{k^{*3}} L_{\mu\nu} - 3\frac{k^2}{k^{*2}} L_{44}. \tag{A.13b}$$

In (A.9) an effective photon mass λ was introduced to avoid the infrared divergence of this NLO process.

This unphysical photon mass get canceled out by including also a soft bremsstrahlung contribution using the same photon mass. For the soft bremsstrahlung, the correction calculated in [MO65] is used

$$\begin{aligned} I_{\text{soft}} = {} & 2(1 - 2y\coth(2y)\ln\frac{E_{\gamma,\text{max soft}}m_\mu}{\lambda\sqrt{E_1E_2}} \\ & + \frac{1}{2}\coth(2y)\left[2y\ln\frac{(1-\zeta^2)(\zeta^2\eta^2-1)}{4\zeta^2(\eta^2-1)} + \ln\frac{\eta+1}{\eta-1}\ln\frac{\zeta\eta+1}{\zeta\eta-1}\right. \\ & \quad + \text{Li}_2\left(\frac{(1+\zeta)(\zeta\eta+1)}{2\zeta(\eta+1)}\right) - \text{Li}_2\left(\frac{(1-\zeta)(\zeta\eta-1)}{2\zeta(\eta+1)}\right) \\ & \quad \left. + \text{Li}_2\left(\frac{(1+\zeta)(\zeta\eta-1)}{2\zeta(\eta-1)}\right) - \text{Li}_2\left(\frac{(1-\zeta)(\zeta\eta-1)}{2\zeta(\eta-1)}\right)\right], \end{aligned} \tag{A.14}$$

with

$$y = \text{arsinh}\sqrt{\frac{1}{4}\frac{k^2}{M^2}}, \qquad \zeta = \tanh y, \qquad \eta = \frac{E_1+E_2}{-E_1+E_2} \tag{A.15}$$

since it only valid for small photon energies, a maximum photon energy $E_{\gamma,\text{max soft}}$ is introduced.

A.2.2 Hard Bremsstrahlung

The bremsstrahlung cross-section can be derived from the μ-diagram by setting $k^2 = 0$. To include the hard bremsstrahlung into the e-diagram, the muon line of the e-diagram $L_{1,2}$ gets replace by the muon line of the bremsstrahlung $M^{44}_{\alpha\alpha}$ and $M^{\mu\mu}_{\alpha\alpha}$. Compared to described in eq. (49) of [Bug77], the substitutions $\omega \to \omega_{\text{brems}}$, $\nu \to -\omega$, and $q^2 \to k^2$ is necessary. Now, the differential cross section is additionally differential in the energy of the hard bremsstrahlung photon ω_{brems} with the lower integration limit defined by the maximum energy of the soft photon $E_{\gamma,\text{max soft}}$.

B Plots of the Feasibility Study

B.1 Energy Reconstruction Plots

B.1.1 Calibration of Truncated Energy

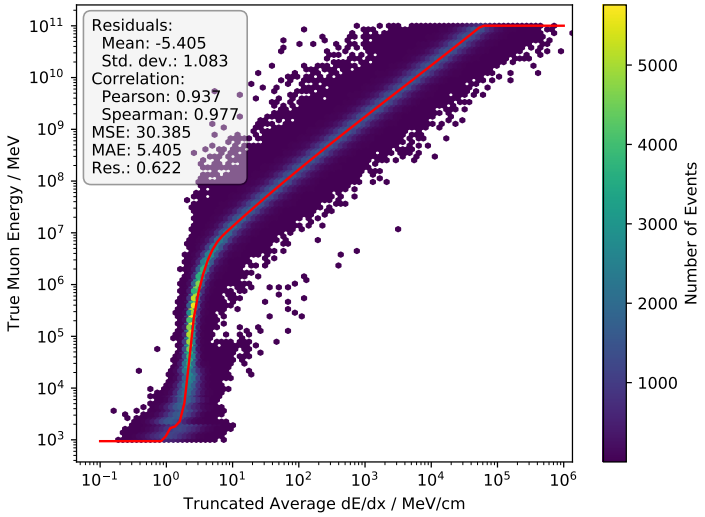

(a) High resolution.

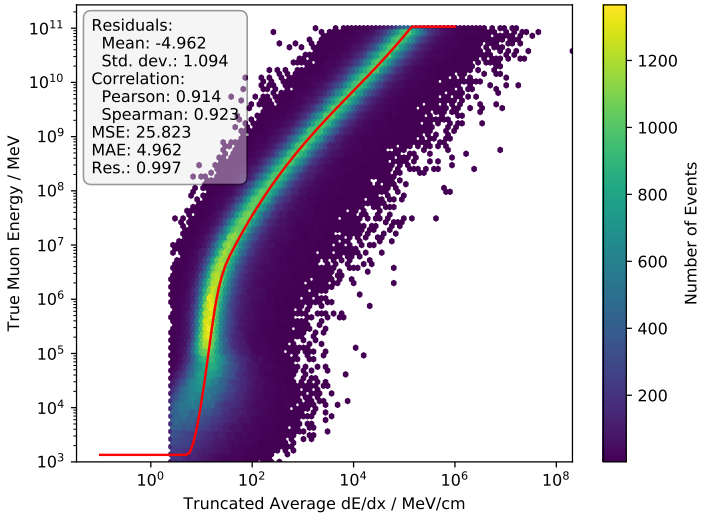

(b) Low resolution.

Figure B.1: The Calibration of truncated energy reconstruction by fitting a spline (red curve) through with the correlation between the average energy loss of the truncated track segments and the true muon energy.

B.1.2 Resolution of Energy Reconstruction

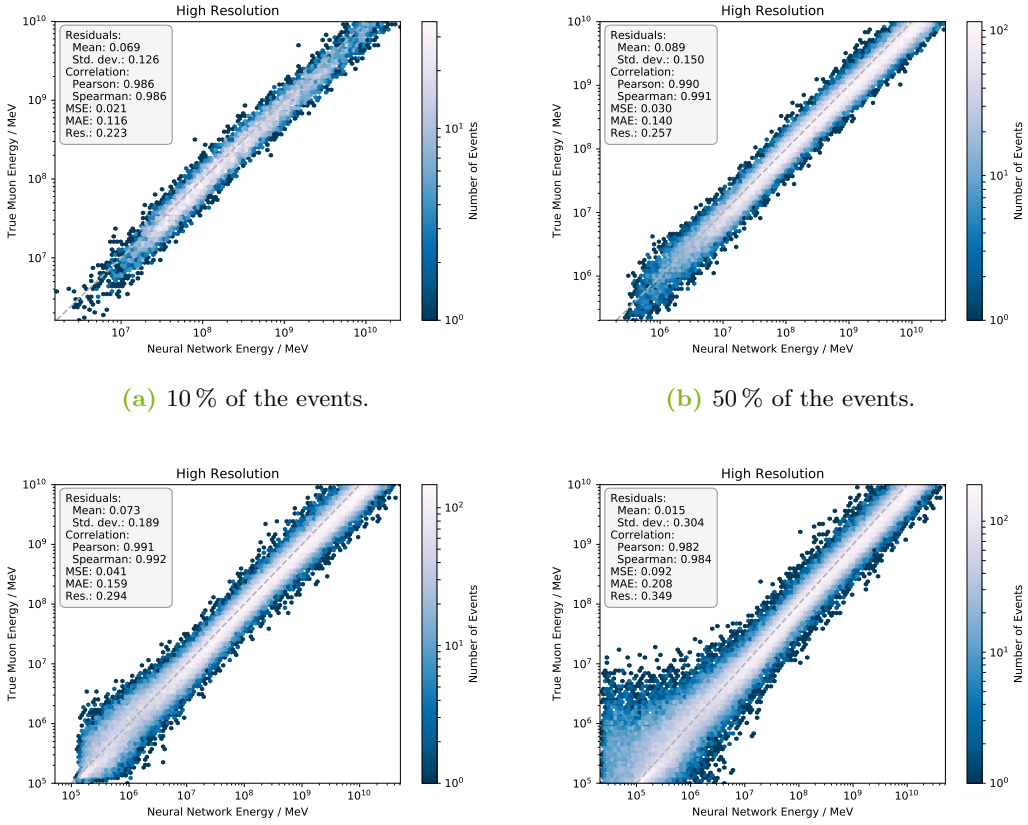

(a) 10 % of the events.

(b) 50 % of the events.

(c) 80 % of the events.

(d) All events.

Figure B.2: The performance of the neural network reconstruction of the muon energy for the high resolution. An uncertainty cut is applied filtering the best reconstructed events.

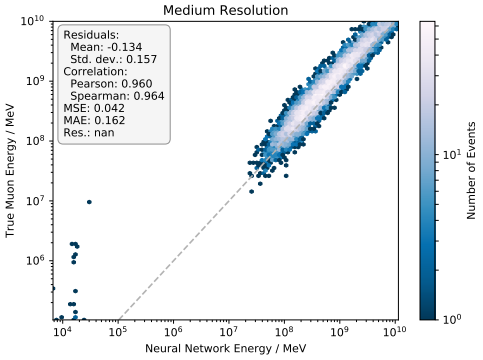

(a) 10 % of the events.

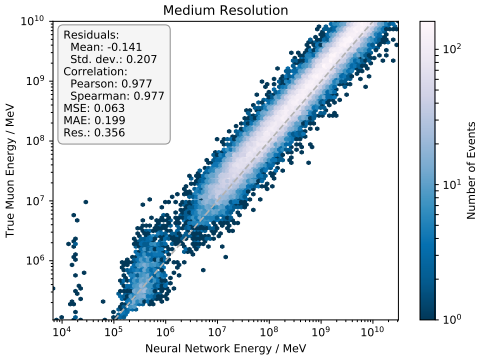

(b) 50 % of the events.

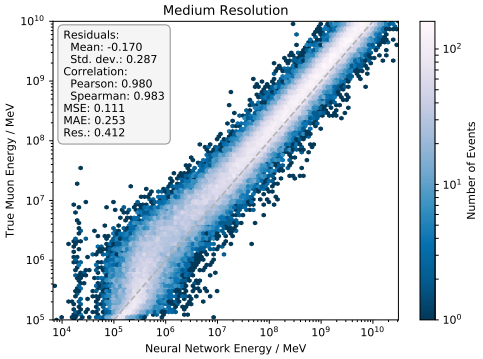

(c) 80 % of the events.

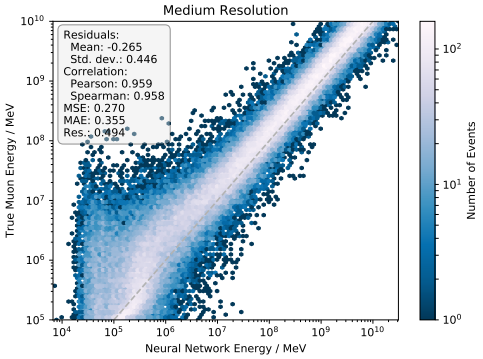

(d) All events.

Figure B.3: The performance of the neural network reconstruction of the muon energy for the baseline resolution. An uncertainty cut is applied filtering the best reconstructed events.

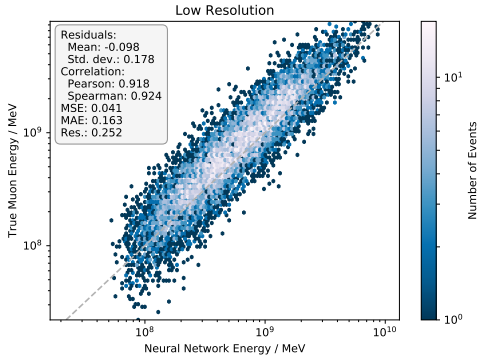

(a) 10 % of the events.

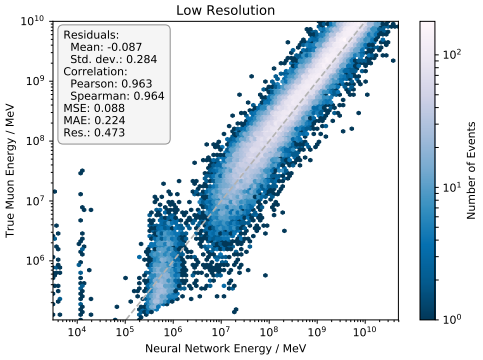

(b) 50 % of the events.

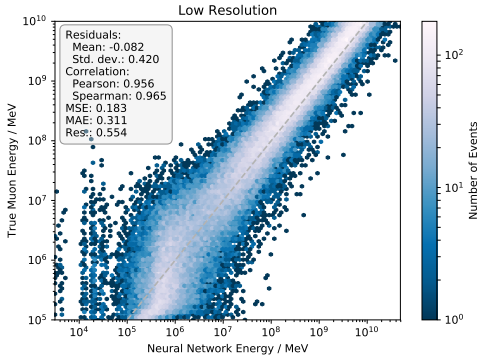

(c) 80 % of the events.

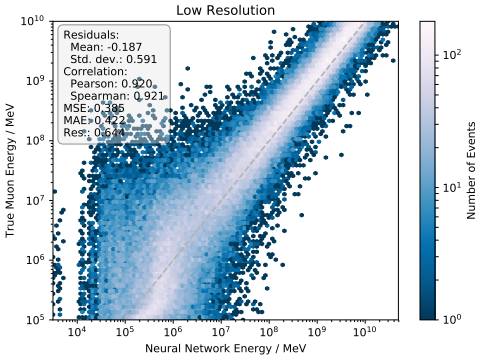

(d) All events.

Figure B.4: The performance of the neural network reconstruction of the muon energy for the low resolution. An uncertainty cut is applied filtering the best reconstructed events.

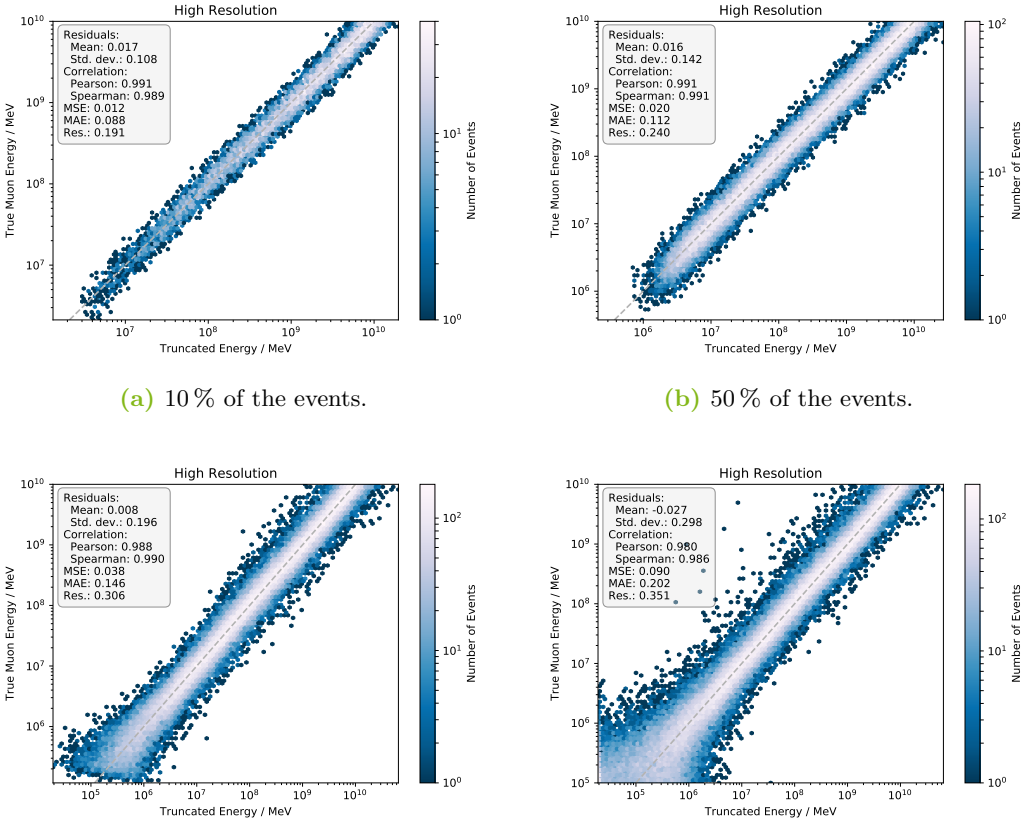

(a) 10 % of the events.

(b) 50 % of the events.

(c) 80 % of the events.

(d) All events.

Figure B.5: The performance of the truncated energy reconstruction of the muon energy for the high resolution. An uncertainty cut is applied filtering the best reconstructed events.

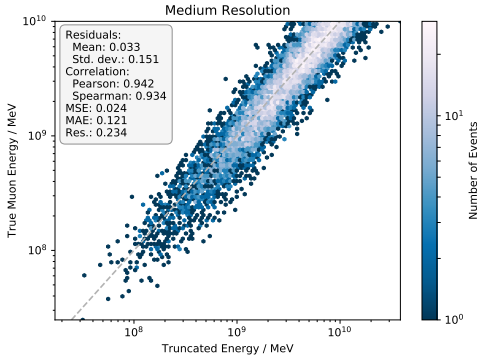

(a) 10 % of the events.

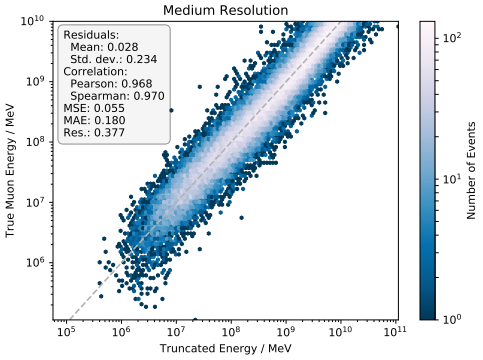

(b) 50 % of the events.

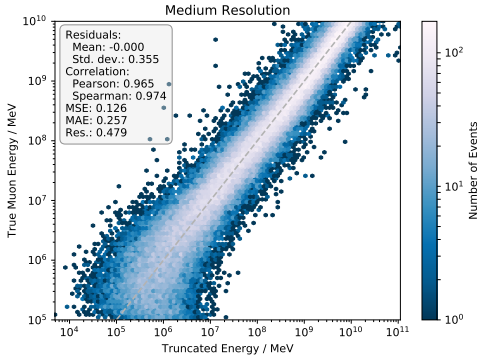

(c) 80 % of the events.

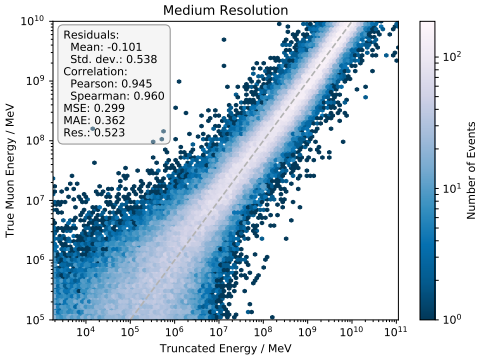

(d) All events.

Figure B.6: The performance of the truncated energy reconstruction of the muon energy for the baseline resolution. An uncertainty cut is applied filtering the best reconstructed events.

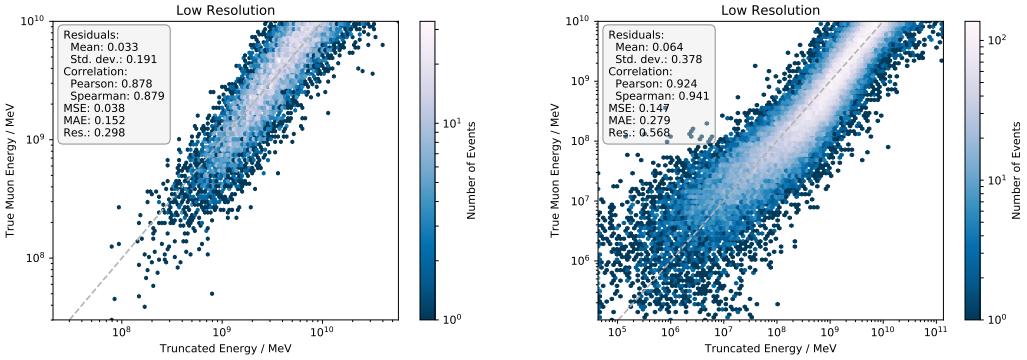

(a) 10 % of the events.

(b) 50 % of the events.

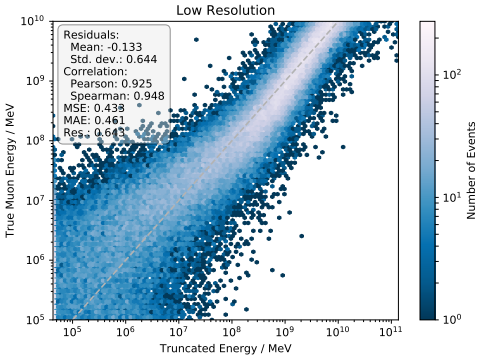

(c) 80 % of the events.

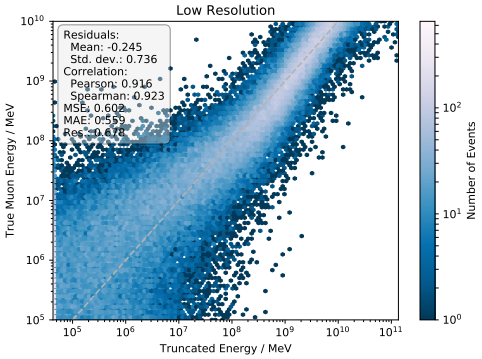

(d) All events.

Figure B.7: The performance of the truncated energy reconstruction of the muon energy for the low resolution. An uncertainty cut is applied filtering the best reconstructed events.

B.1.3 Sensitivity to Bremsstrahlung Multiplier

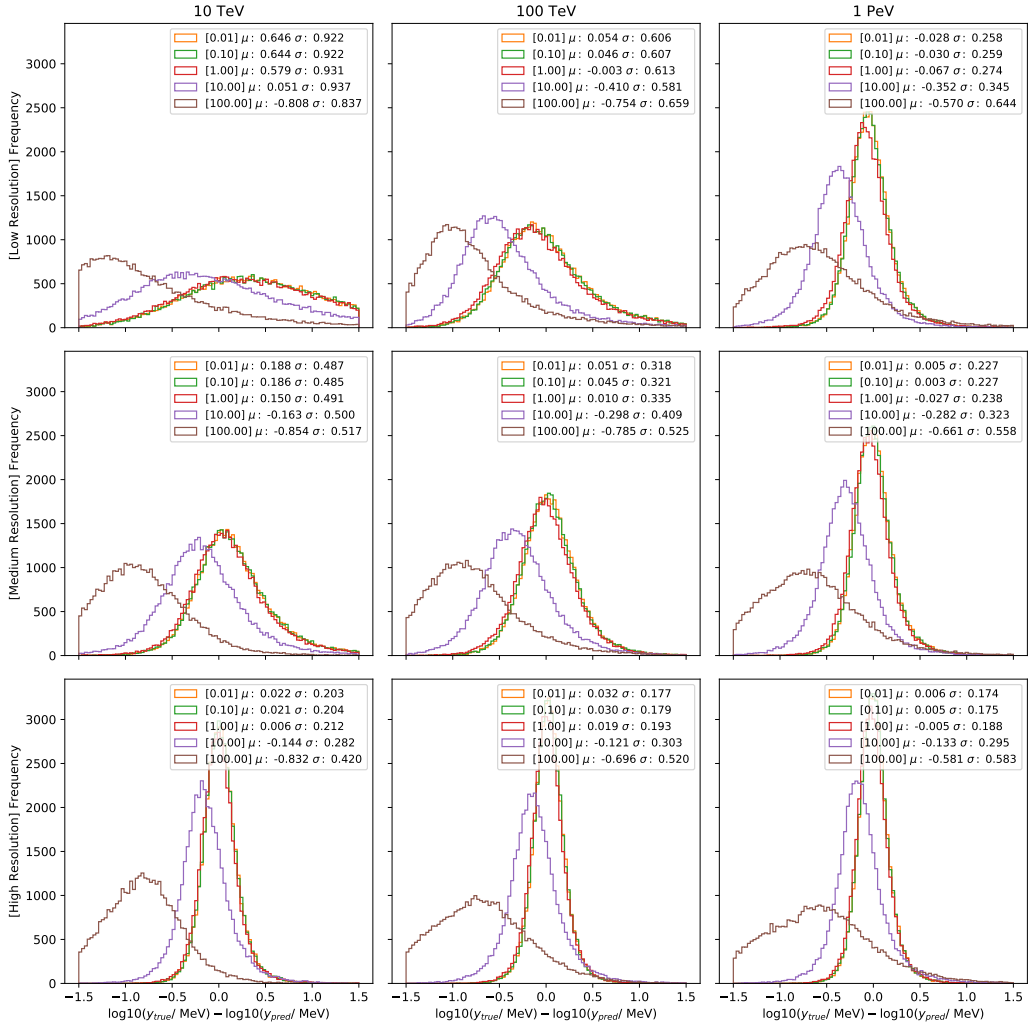

Figure B.8: The pull distribution of reconstructed energies using the truncated energy method for the three resolution settings and muon energies. The multiplier, scaling the bremsstrahlung cross-section is varied between 10^{-2} and 10^{2}, and the mean and standard deviation for each multiplier dataset is estimated.

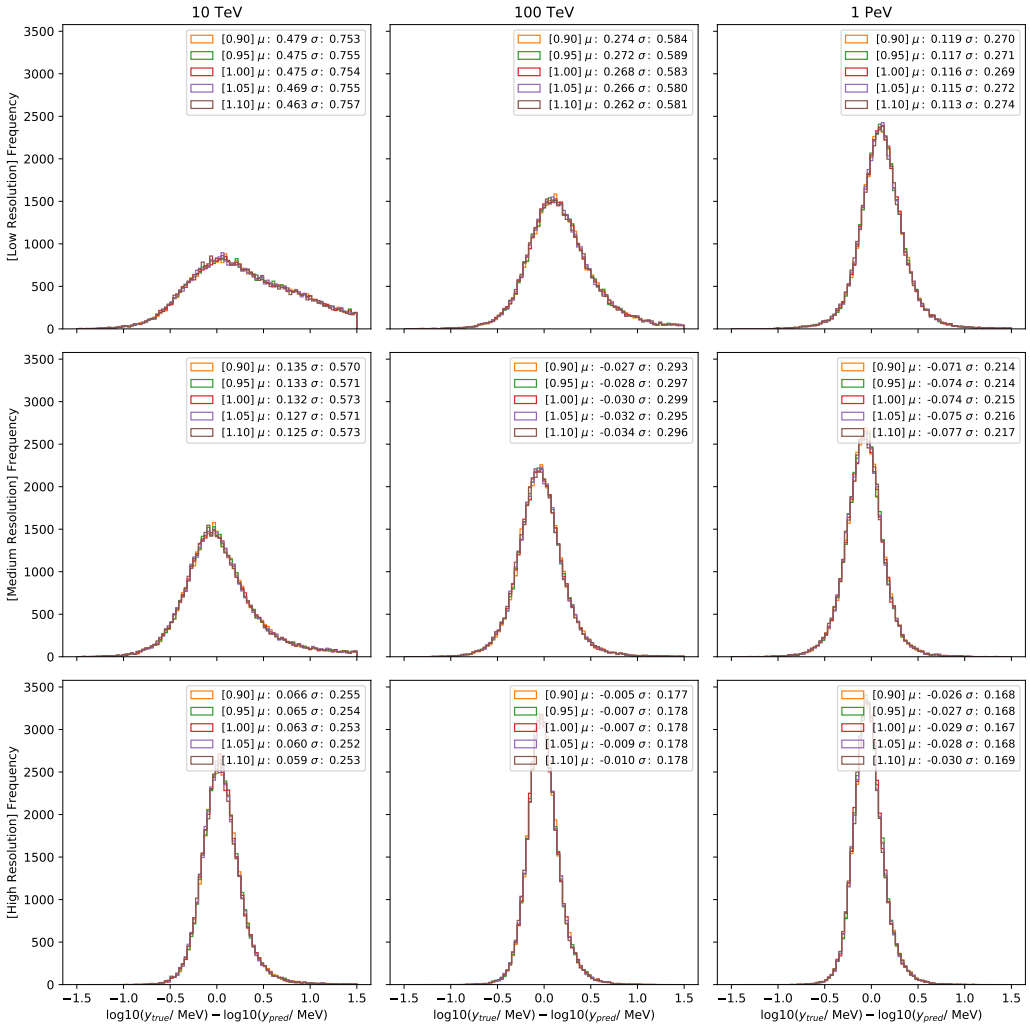

Figure B.9: The pull distribution of reconstructed energies using a neural network for the three resolution settings and muon energies. The multiplier, scaling the bremsstrahlung cross-section is varied between 0.9 and 1.1, and the mean and standard deviation for each multiplier dataset is estimated.

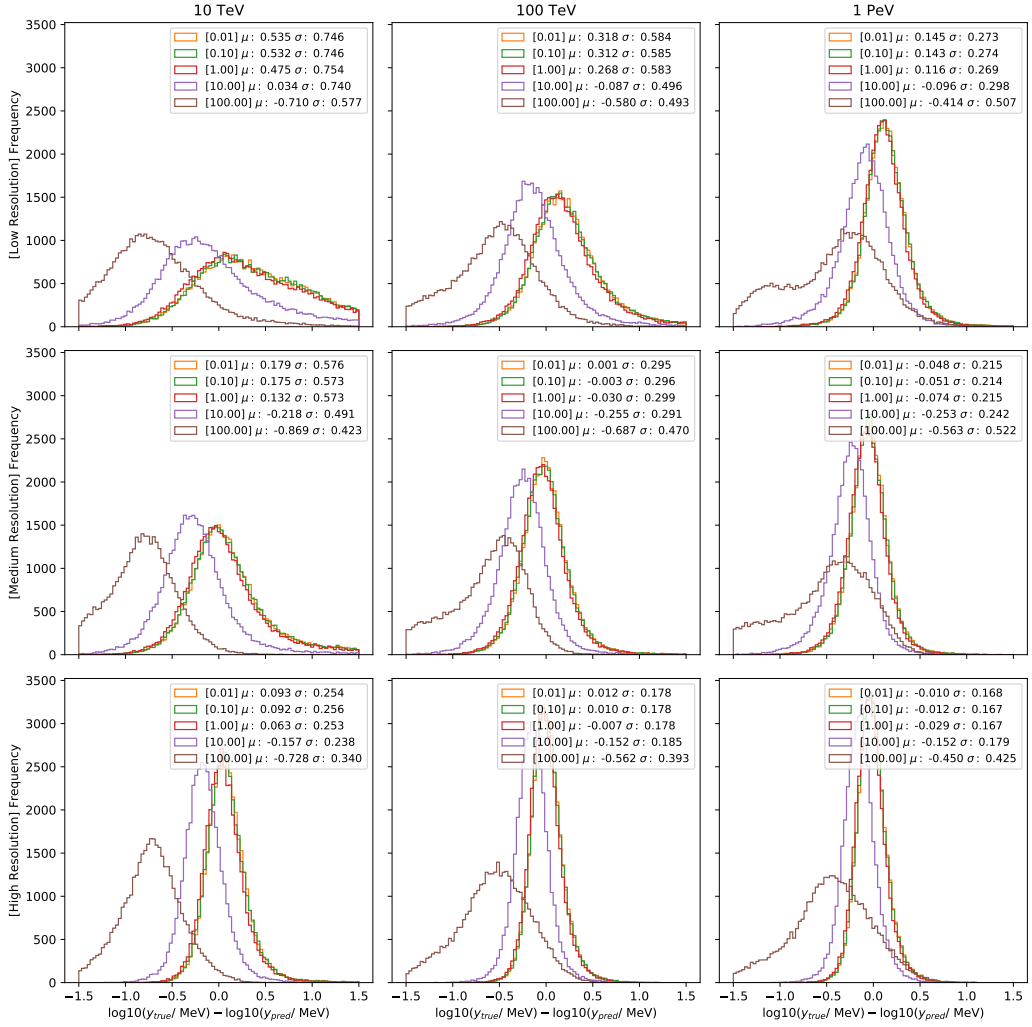

Figure B.10: The pull distribution of reconstructed energies using a neural network for the three resolution settings and muon energies. The multiplier, scaling the bremsstrahlung cross-section is varied between 10^{-2} and 10^{2}, and the mean and standard deviation for each multiplier dataset is estimated.

B.2 Parameterizing the Energy Loss Distribution

B.2.1 Interpolation of the Bremsstrahlung Multiplier using the Monte-Carlo Truth

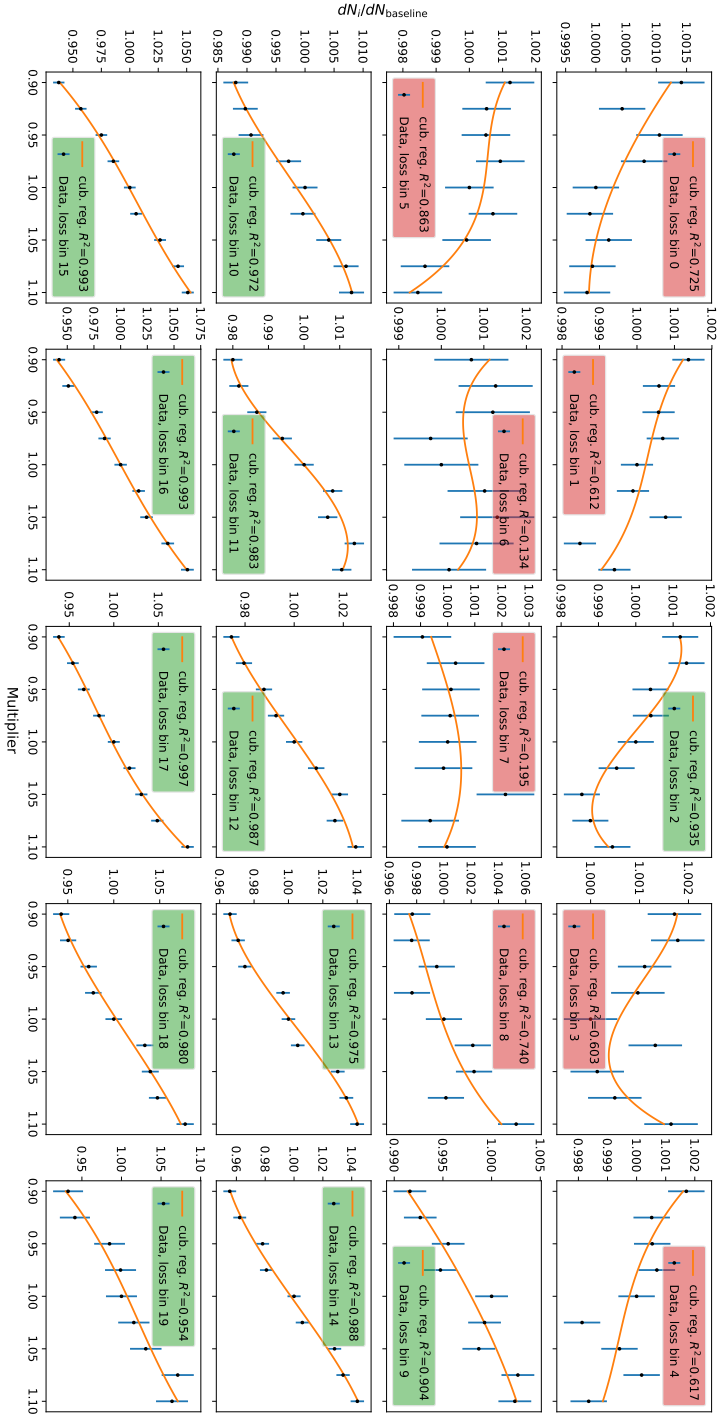

Figure B.11: One dimensional interpolation of the differences between the energy loss histograms created with different bremsstrahlung multiplier for the true muon energies from 1 TeV to 2.15 TeV. A coefficient of determination threshold of 0.9 is used to mark all energy loss bins (red colored legend box), which would not be included in the fit.

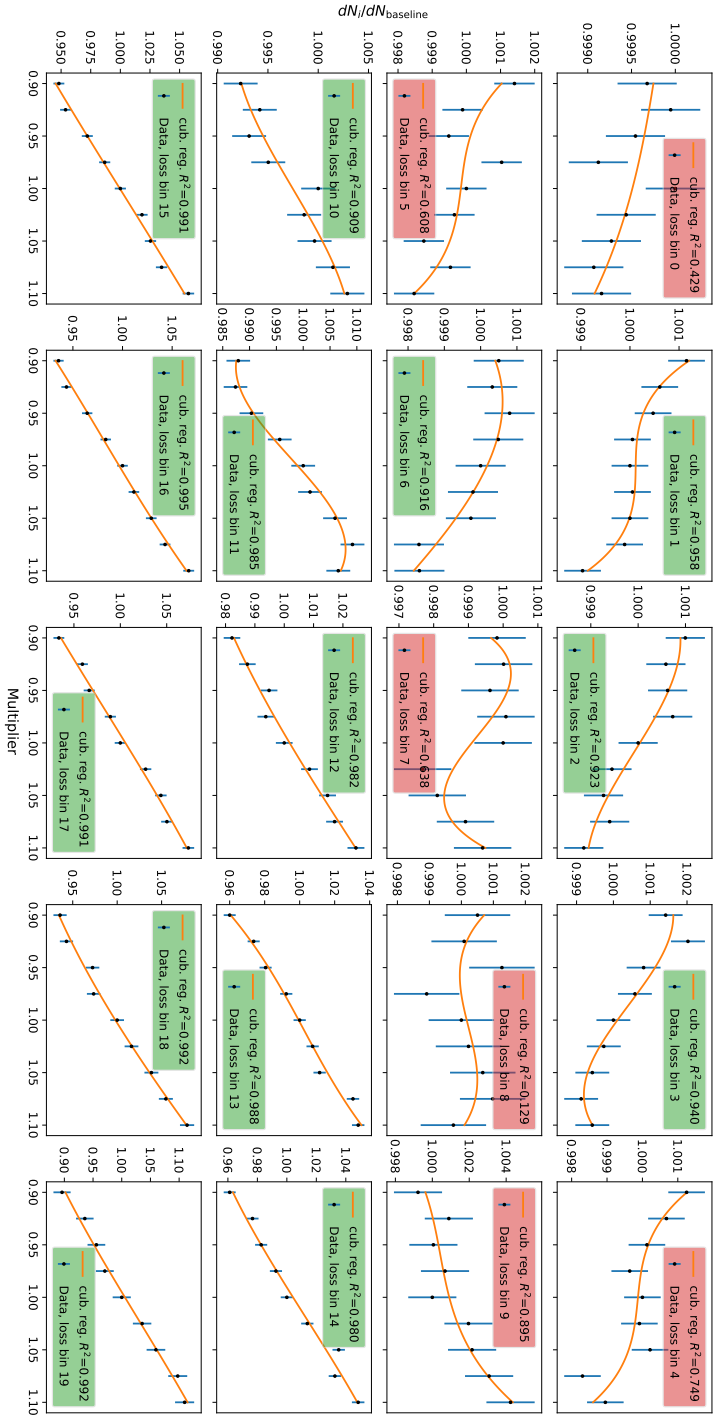

Figure B.12: One dimensional interpolation of the differences between the energy loss histograms created with different bremsstrahlung multiplier for the true muon energies from 2.15 TeV to 4.64 TeV. A coefficient of determination threshold of 0.9 is used to mark all energy loss bins (red colored legend box), which would not be included in the fit.

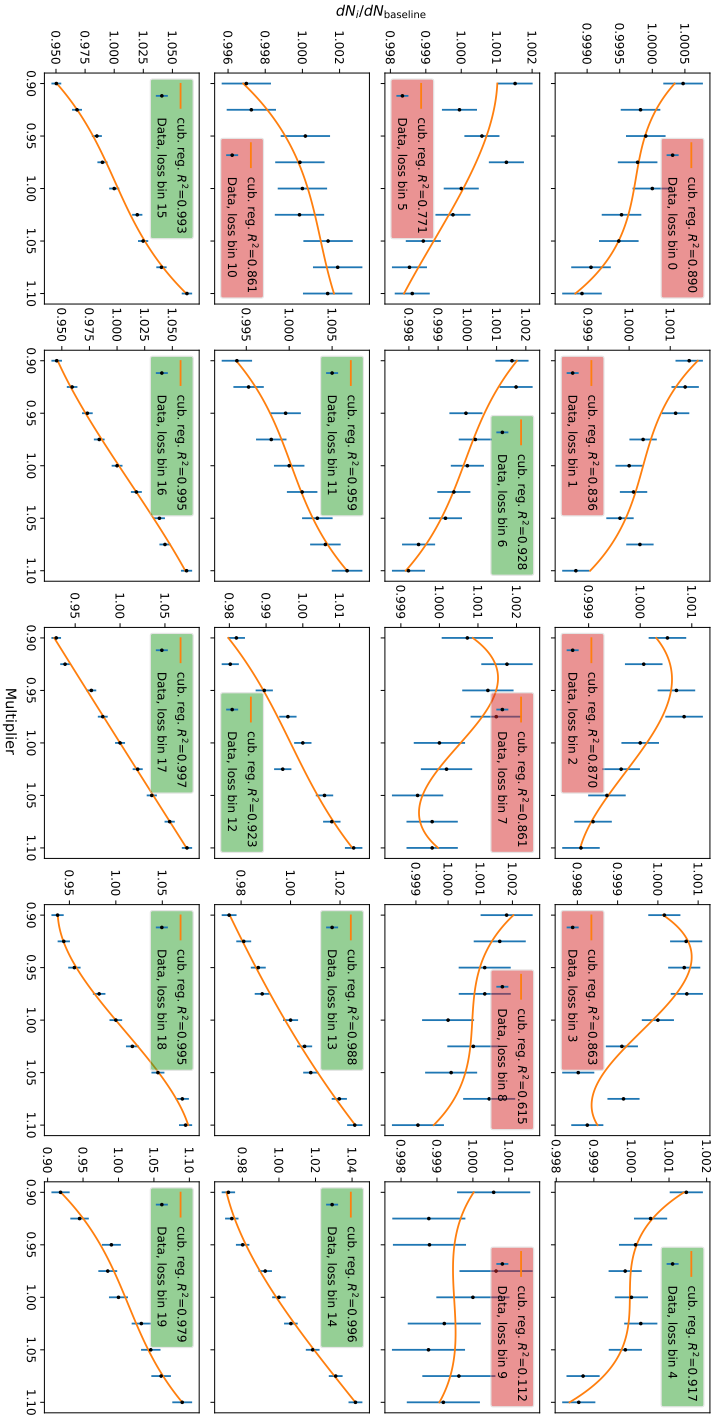

Figure B.13: One dimensional interpolation of the differences between the energy loss histograms created with different bremsstrahlung multiplier for the true muon energies from 4.64 10TeV. A coefficient of determination threshold of 0.9 is used to mark all energy loss bins (red colored legend box), which would not be included in the fit.

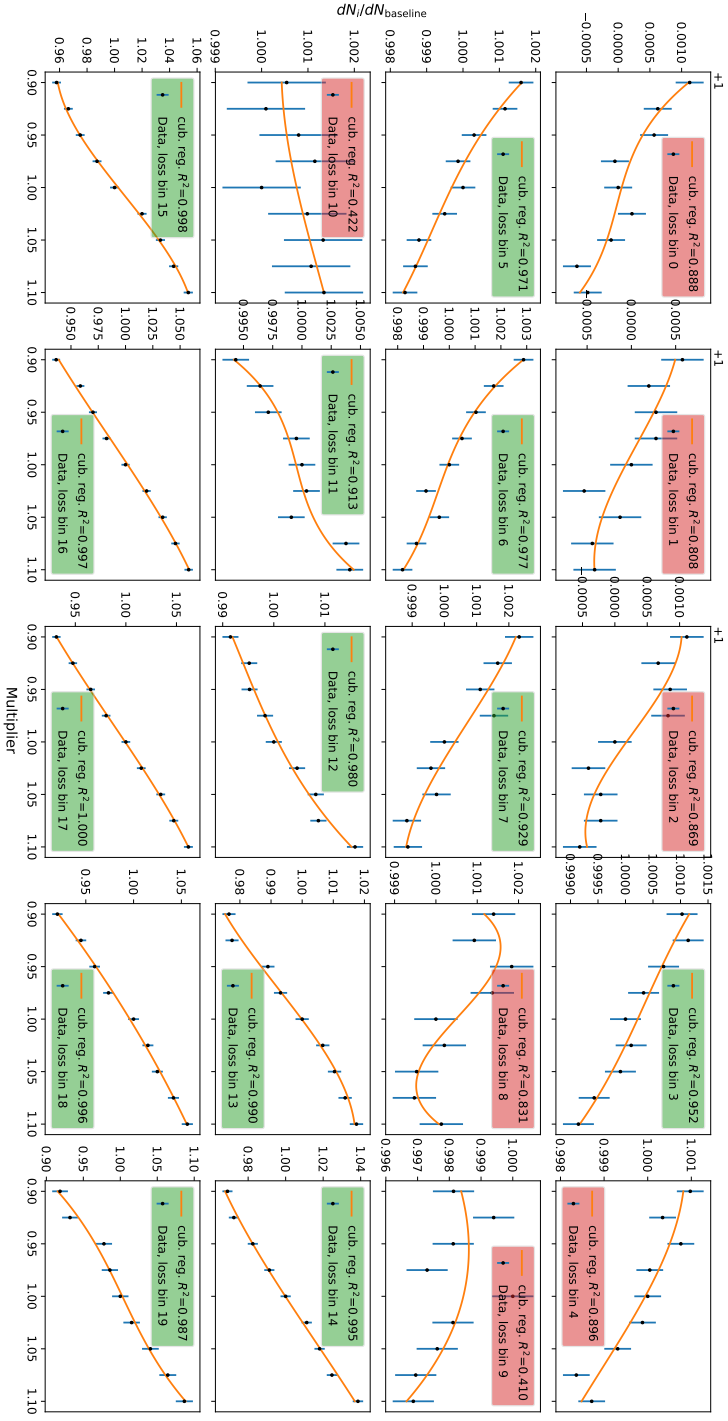

Figure B.14: One dimensional interpolation of the differences between the energy loss histograms created with different bremsstrahlung multiplier for the true muon energies from 10 31 6TeV. A coefficient of determination threshold of 0.9 is used to mark all energy loss bins (red colored legend box), which would not be included in the fit.

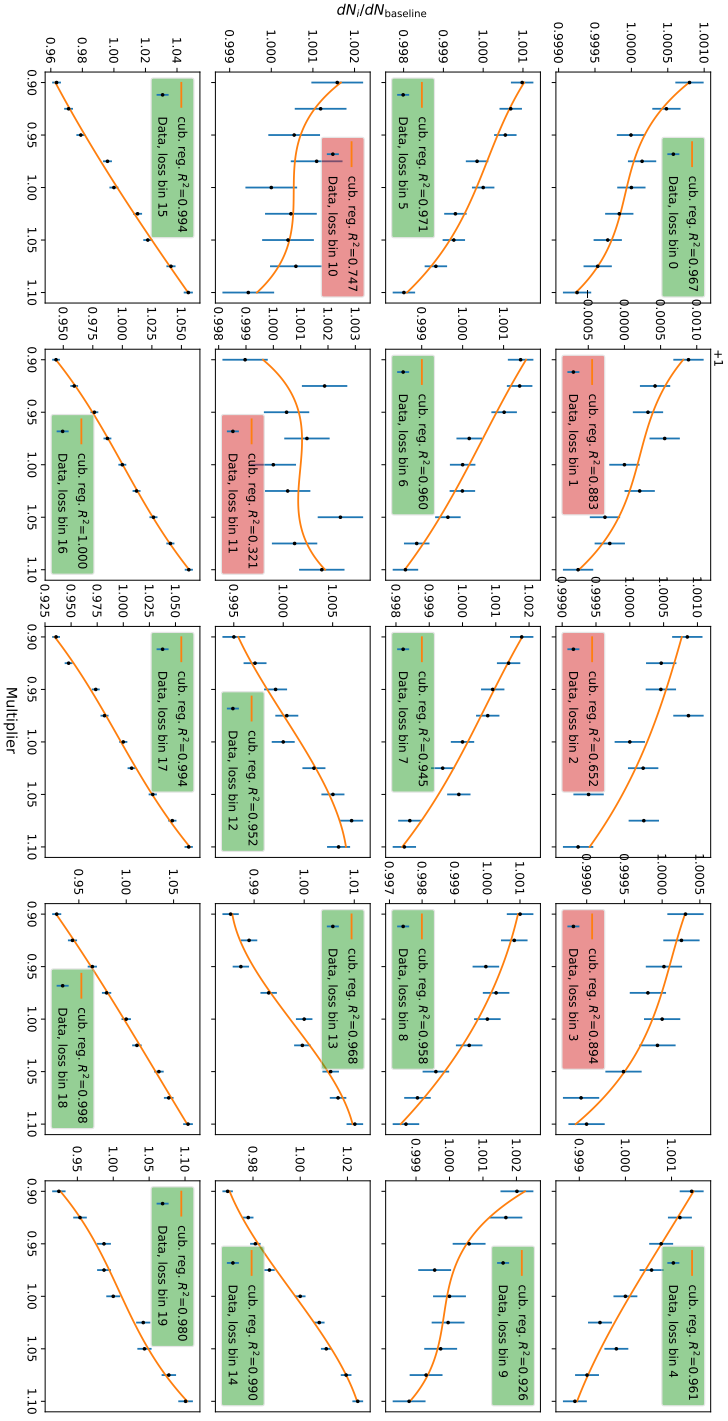

Figure B.15: One dimensional interpolation of the differences between the energy loss histograms created with different bremsstrahlung multiplier for the true muon energies from 31.6 100TeV. A coefficient of determination threshold of 0.9 is used to mark all energy loss bins (red colored legend box), which would not be included in the fit.

B.2.2 Interpolation of the Bremsstrahlung Multiplier using the Neural Network Energy Reconstruction and High Resolutions

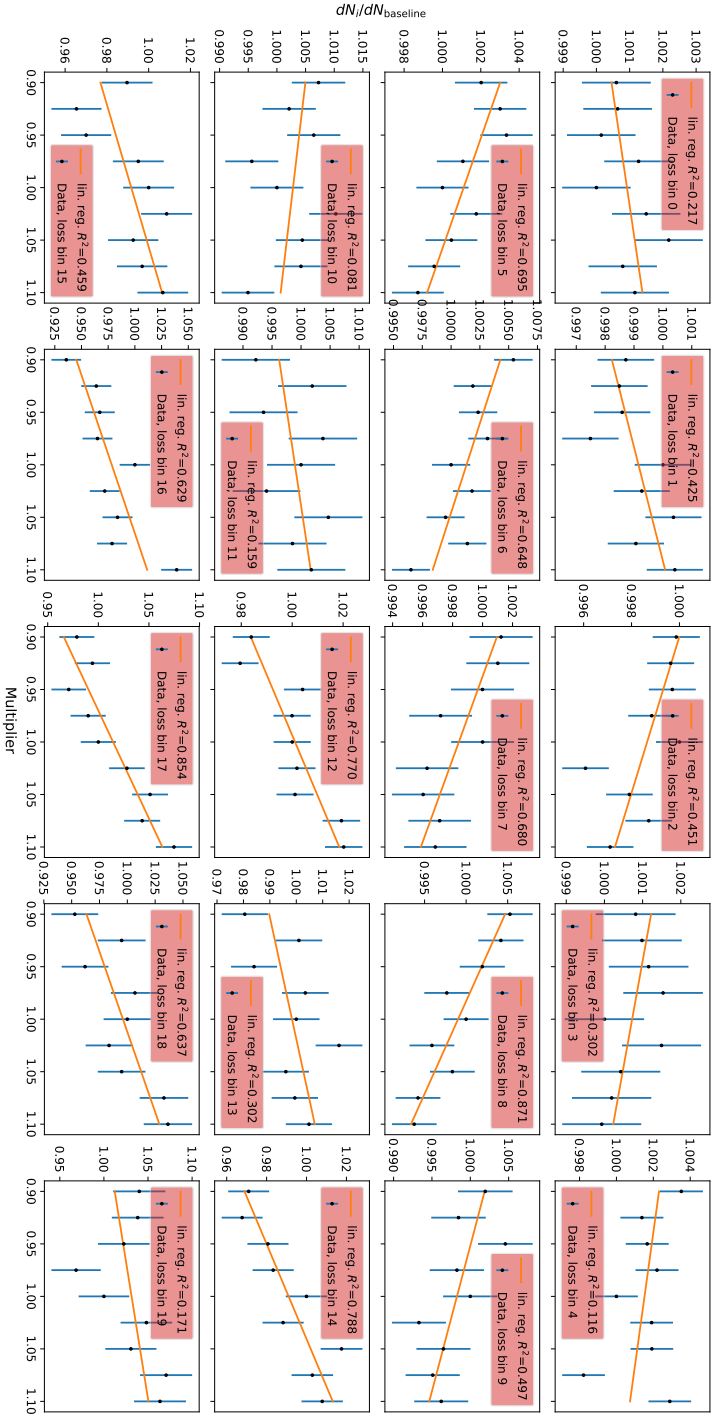

Figure B.16: One dimensional interpolation of the differences between the energy loss histograms created with different bremsstrahlung multiplier for reconstructed muon energies from 1 TeV to 2.15 TeV. A coefficient of determination threshold of 0.9 is used to mark all energy loss bins (red colored legend box), which would not be included in the fit.

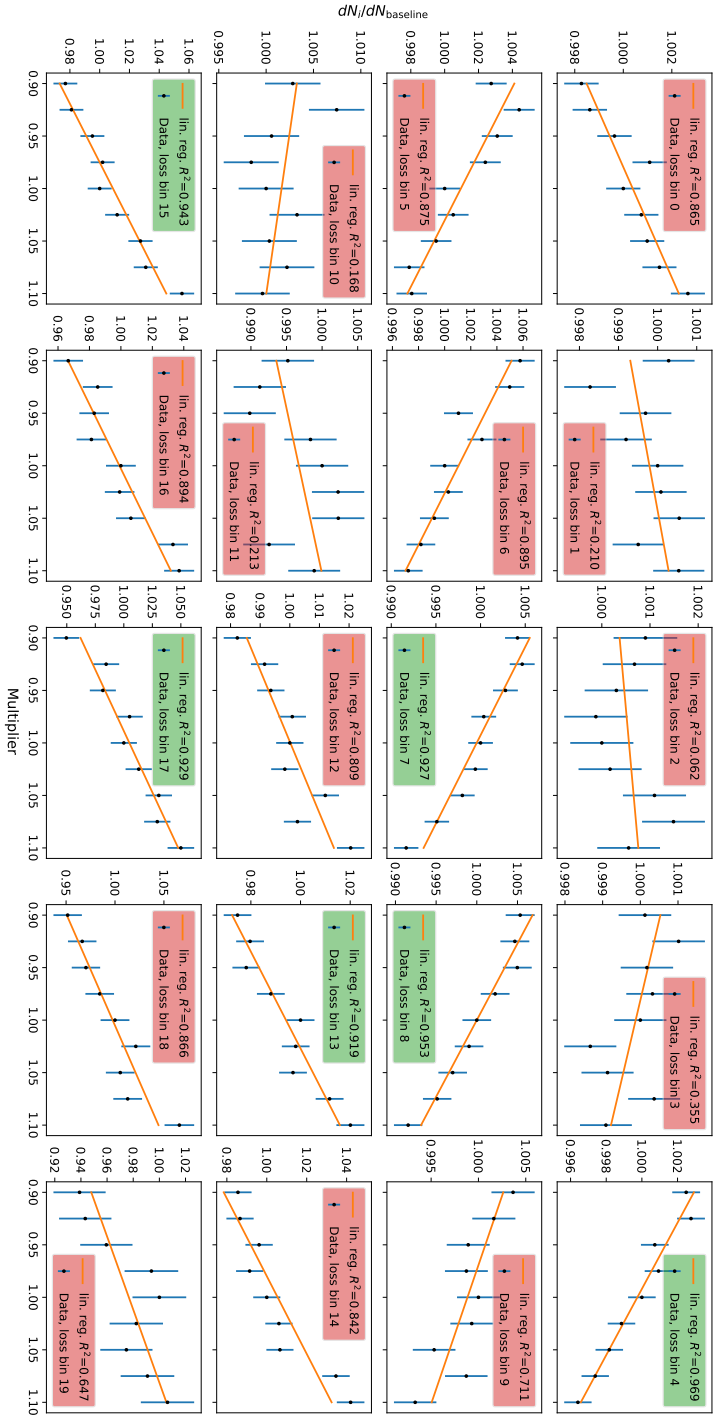

Figure B.17: One dimensional interpolation of the differences between the energy loss histograms created with different bremsstrahlung multiplier for reconstructed muon energies from 2.15 TeV to 4.64 TeV. A coefficient of determination threshold of 0.9 is used to mark all energy loss bins (red colored legend box), which would not be included in the fit.

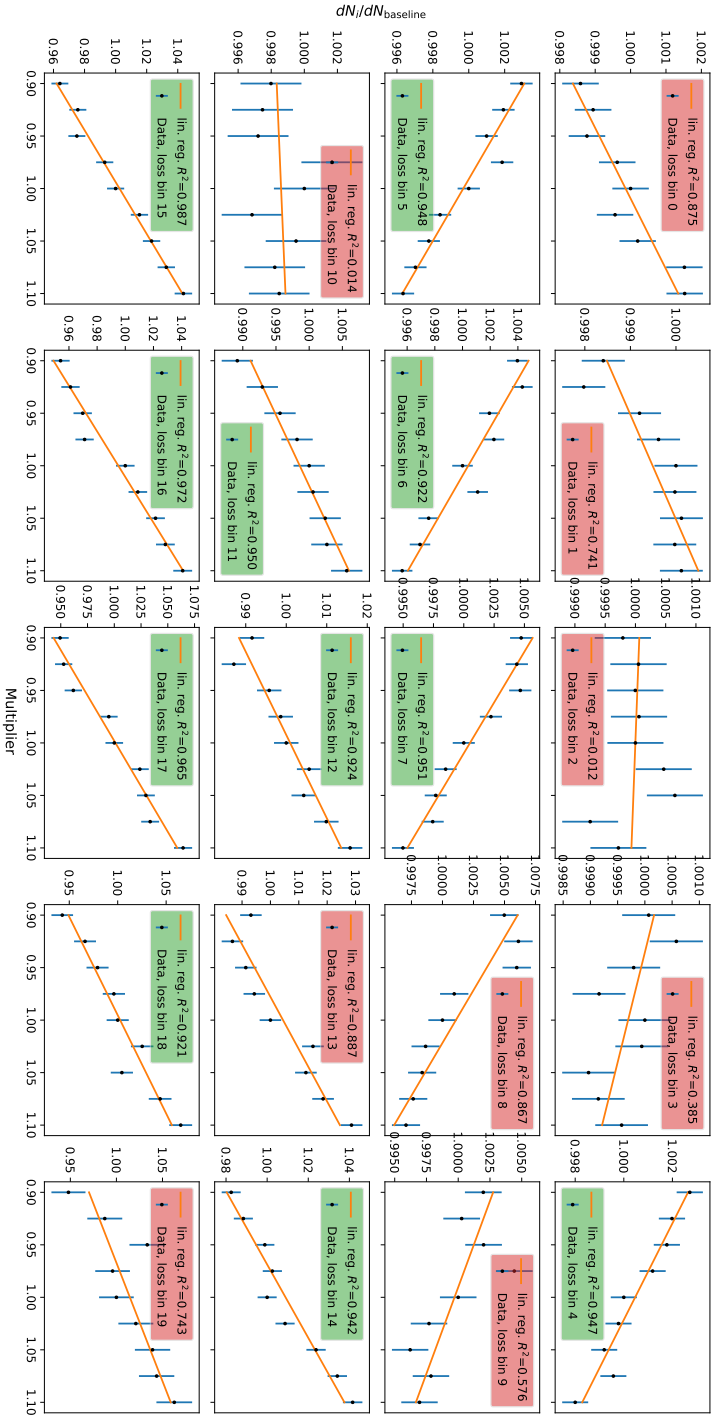

Figure B.18: One dimensional interpolation of the differences between the energy loss histograms created with different bremsstrahlung multiplier for reconstructed muon energies from 4.64 TeV to 10 TeV. A coefficient of determination threshold of 0.9 is used to mark all energy loss bins (red colored legend box), which would not be included in the fit.

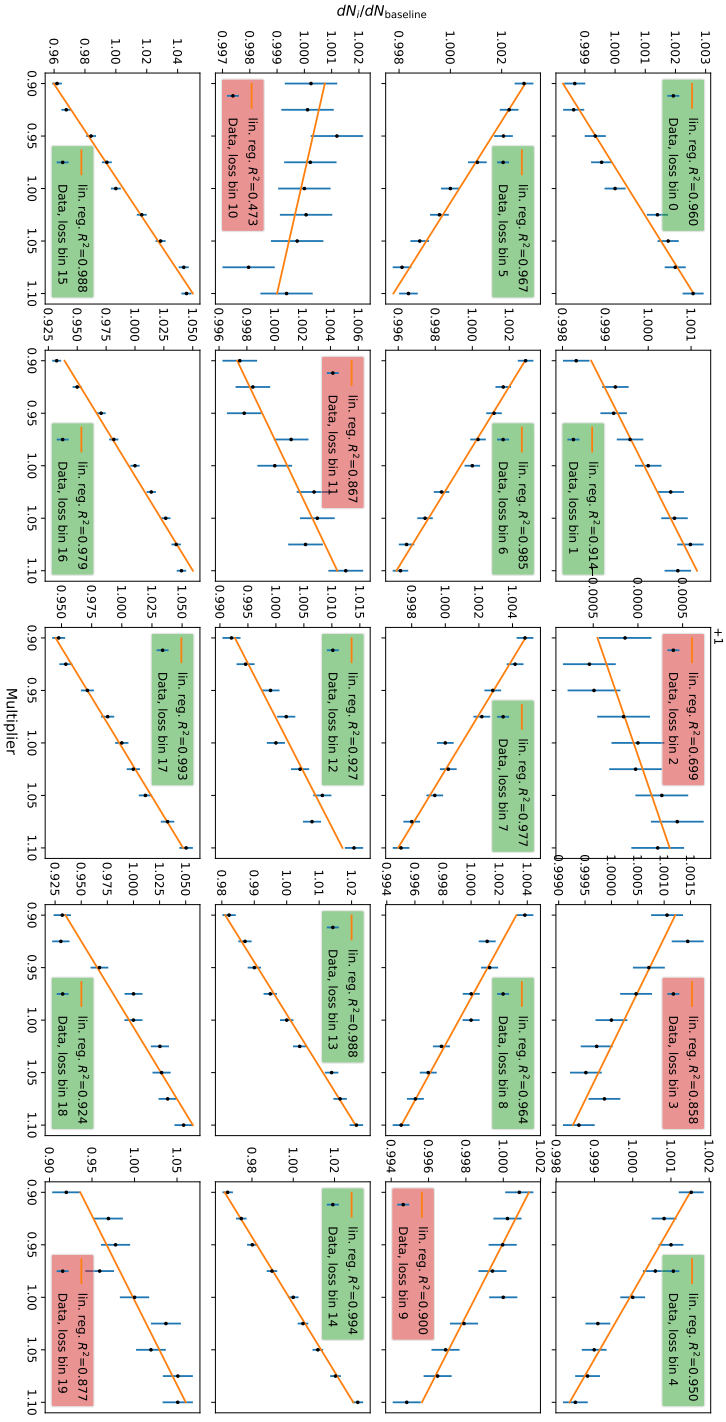

Figure B.19: One dimensional interpolation of the differences between the energy loss histograms created with different bremsstrahlung multiplier for reconstructed muon energies from 10 TeV to 31.6 TeV. A coefficient of determination threshold of 0.9 is used to mark all energy loss bins (red colored legend box), which would not be included in the fit.

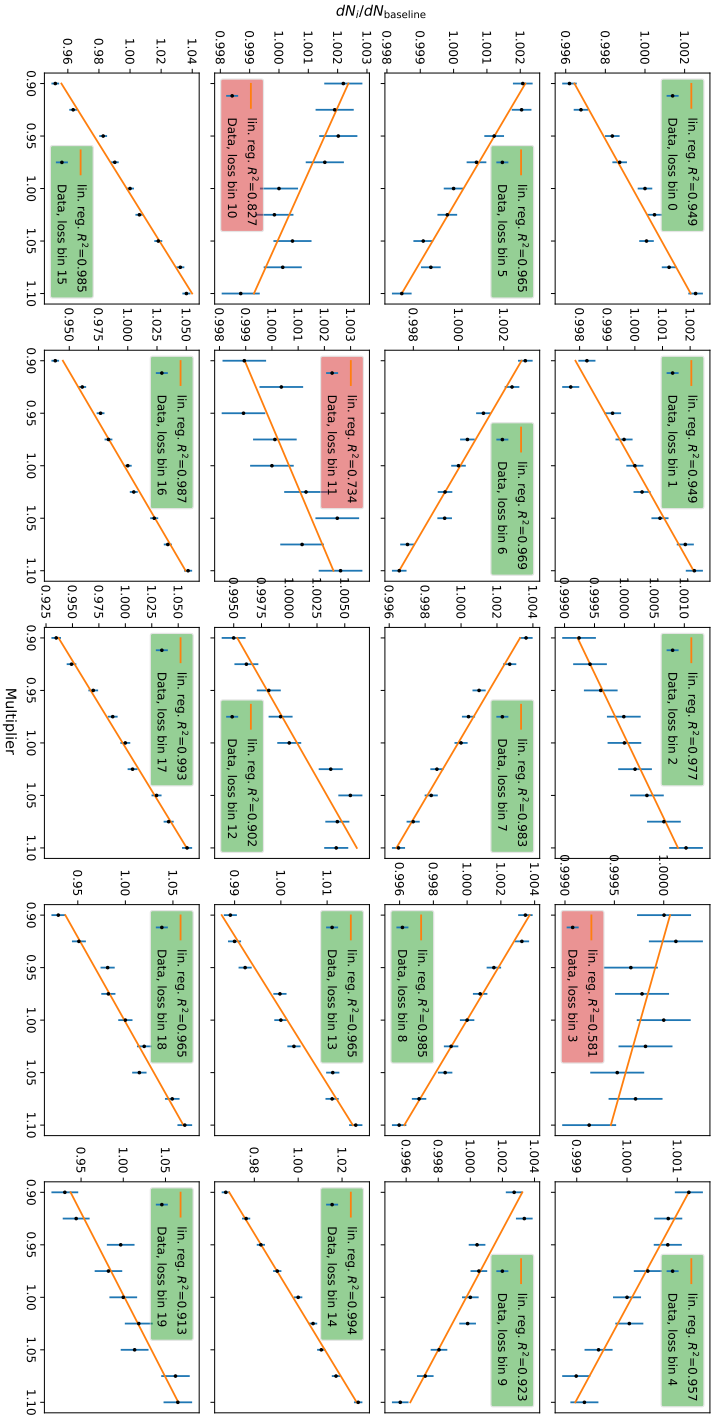

Figure B.20: One dimensional interpolation of the differences between the energy loss histograms created with different bremsstrahlung multiplier for reconstructed muon energies from 31.6 TeV to 100 TeV. A coefficient of determination threshold of 0.9 is used to mark all energy loss bins (red colored legend box), which would not be included in the fit.

B.2.3 Interpolation of the Bremsstrahlung Multiplier using the Neural Network Energy Reconstruction and Baseline Resolutions

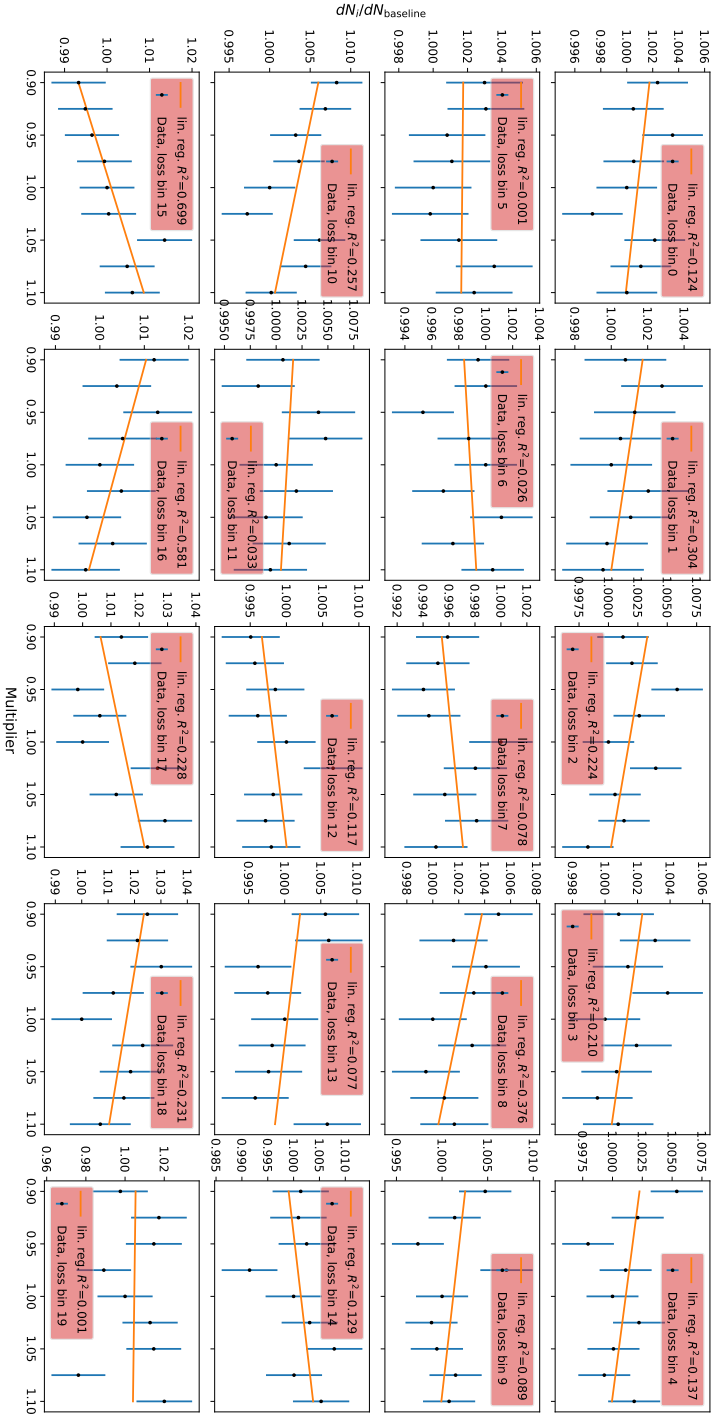

172 **Figure B.21:** One dimensional interpolation of the differences between the energy loss histograms created with different bremsstrahlung multiplier for reconstructed muon energies from 1 TeV to 2.15 TeV. A coefficient of determination threshold of 0.9 is used to mark all energy loss bins (red colored legend box), which would not be included in the fit.

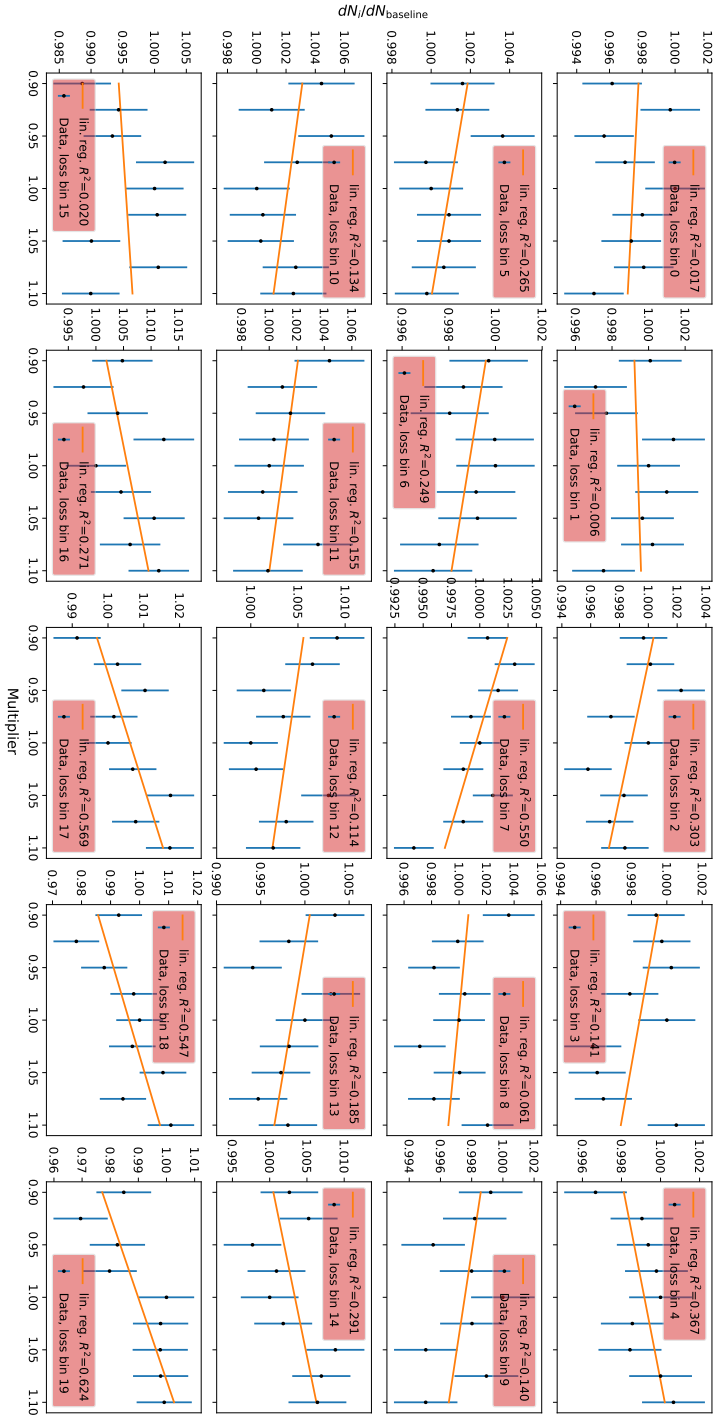

Figure B.22: One dimensional interpolation of the differences between the energy loss histograms created with different bremsstrahlung multiplier for reconstructed muon energies from 2.15 TeV to 4.64 TeV. A coefficient of determination threshold of 0.9 is used to mark all energy loss bins (red colored legend box), which would not be included in the fit.

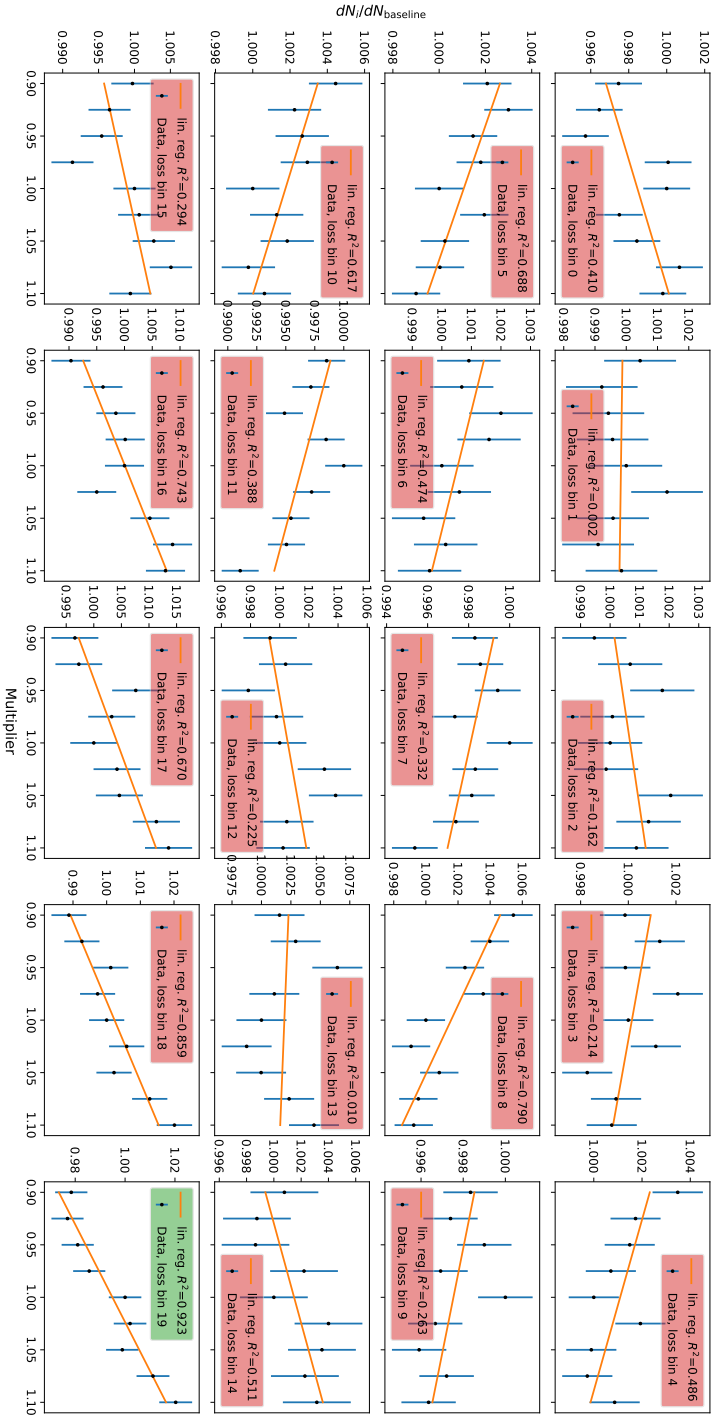

Figure B.23: One dimensional interpolation of the differences between the energy loss histograms created with different bremsstrahlung multiplier for reconstructed muon energies from 4.64 TeV to 10 TeV. A coefficient of determination threshold of 0.9 is used to mark all energy loss bins (red colored legend box), which would not be included in the fit.

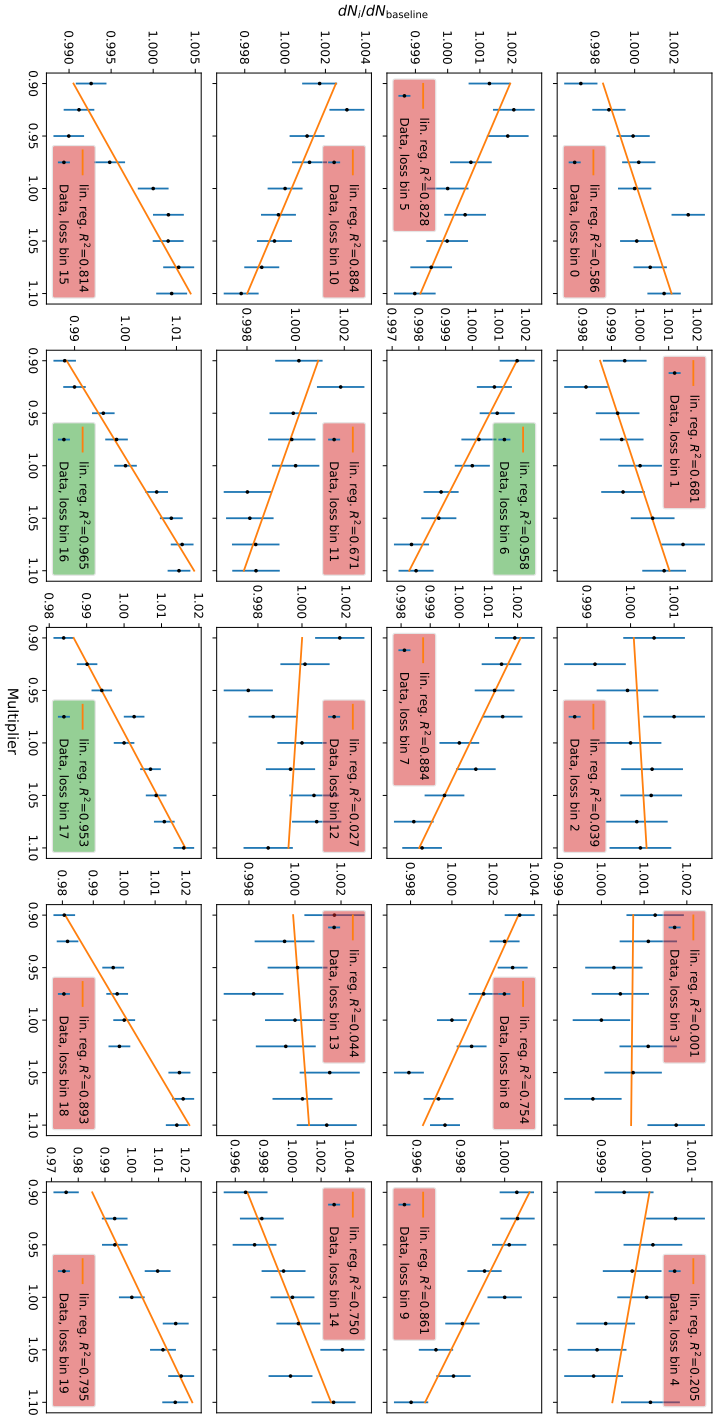

Figure B.24: One dimensional interpolation of the differences between the energy loss histograms created with different bremsstrahlung multiplier for reconstructed muon energies from 10 TeV to 31.6 TeV. A coefficient of determination threshold of 0.9 is used to mark all energy loss bins (red colored legend box), which would not be included in the fit.

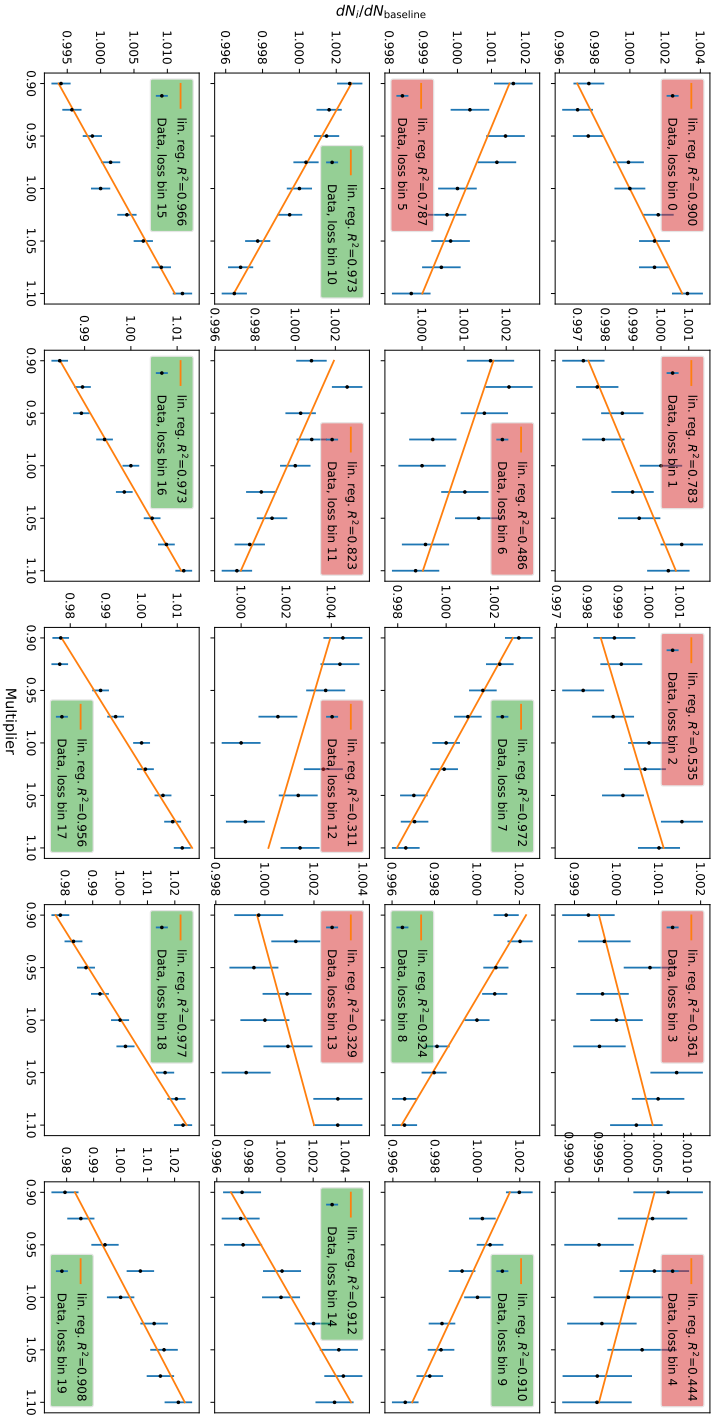

Figure B.25: One dimensional interpolation of the differences between the energy loss histograms created with different bremsstrahlung multiplier for reconstructed muon energies from 31.6 TeV to 100 TeV. A coefficient of determination threshold of 0.9 is used to mark all energy loss bins (red colored legend box), which would not be included in the fit.

B.2.4 Interpolation of the Bremsstrahlung Multiplier using the Neural Network Energy Reconstruction and Low Resolutions

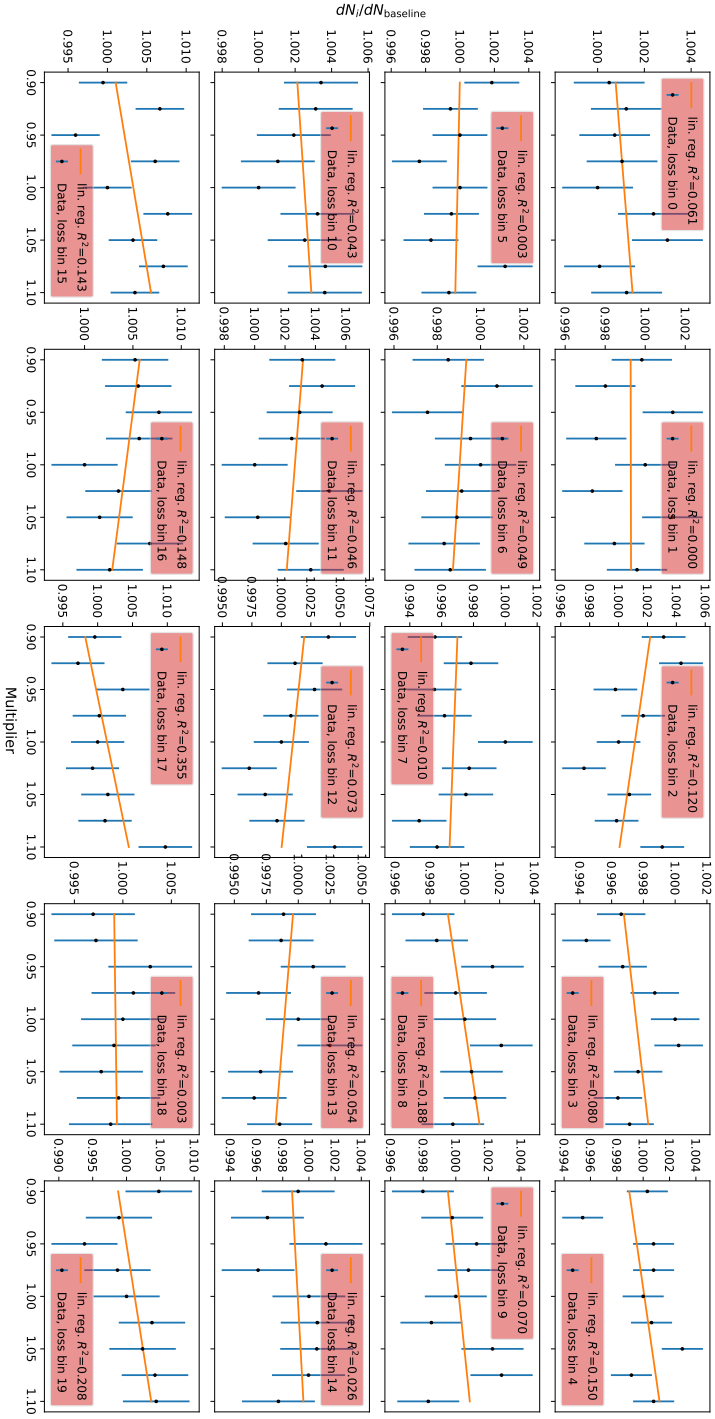

178 **Figure B.26:** One dimensional interpolation of the differences between the energy loss histograms created with different bremsstrahlung multiplier for reconstructed muon energies from 1 TeV to 2.15 TeV. A coefficient of determination threshold of 0.9 is used to mark all energy loss bins (red colored legend box), which would not be included in the fit.

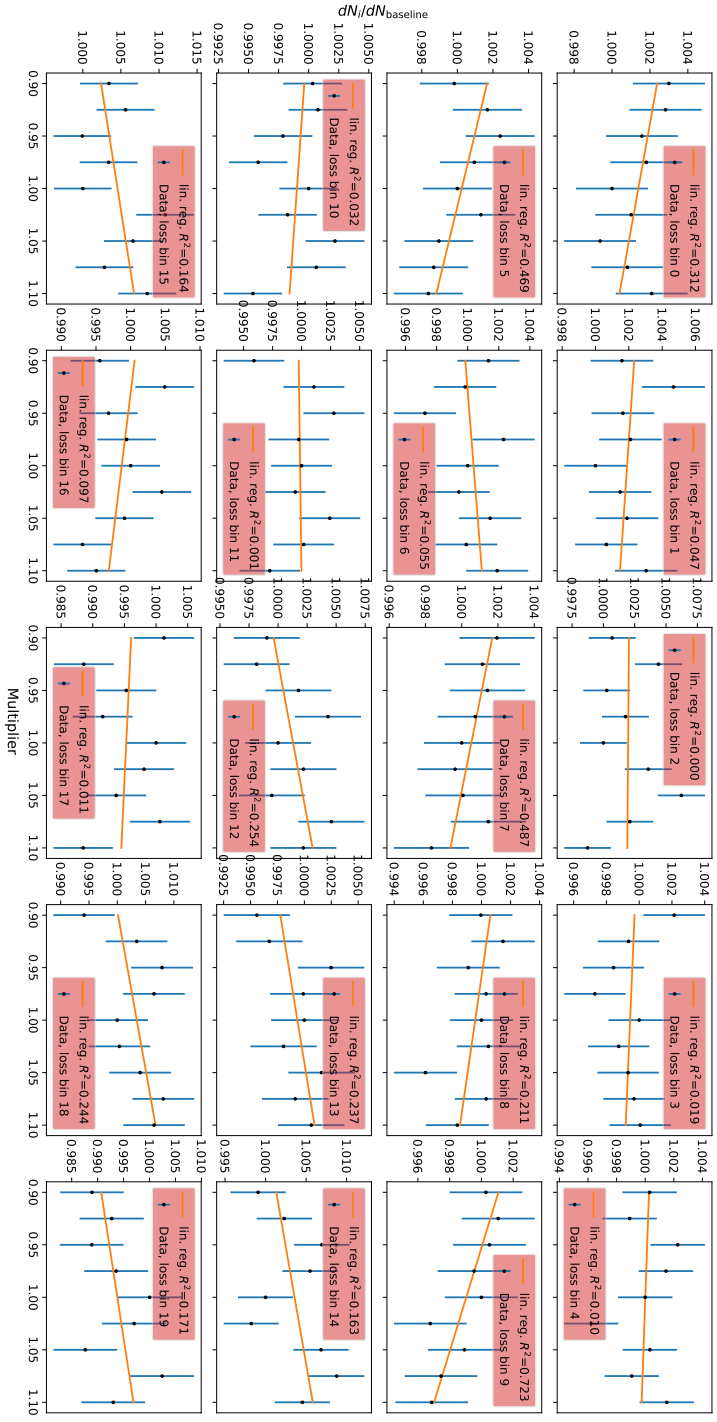

Figure B.27: One dimensional interpolation of the differences between the energy loss histograms created with different bremsstrahlung multiplier for reconstructed muon energies from 2.15 TeV to 4.64 TeV. A coefficient of determination threshold of 0.9 is used to mark all energy loss bins (red colored legend box), which would not be included in the fit.

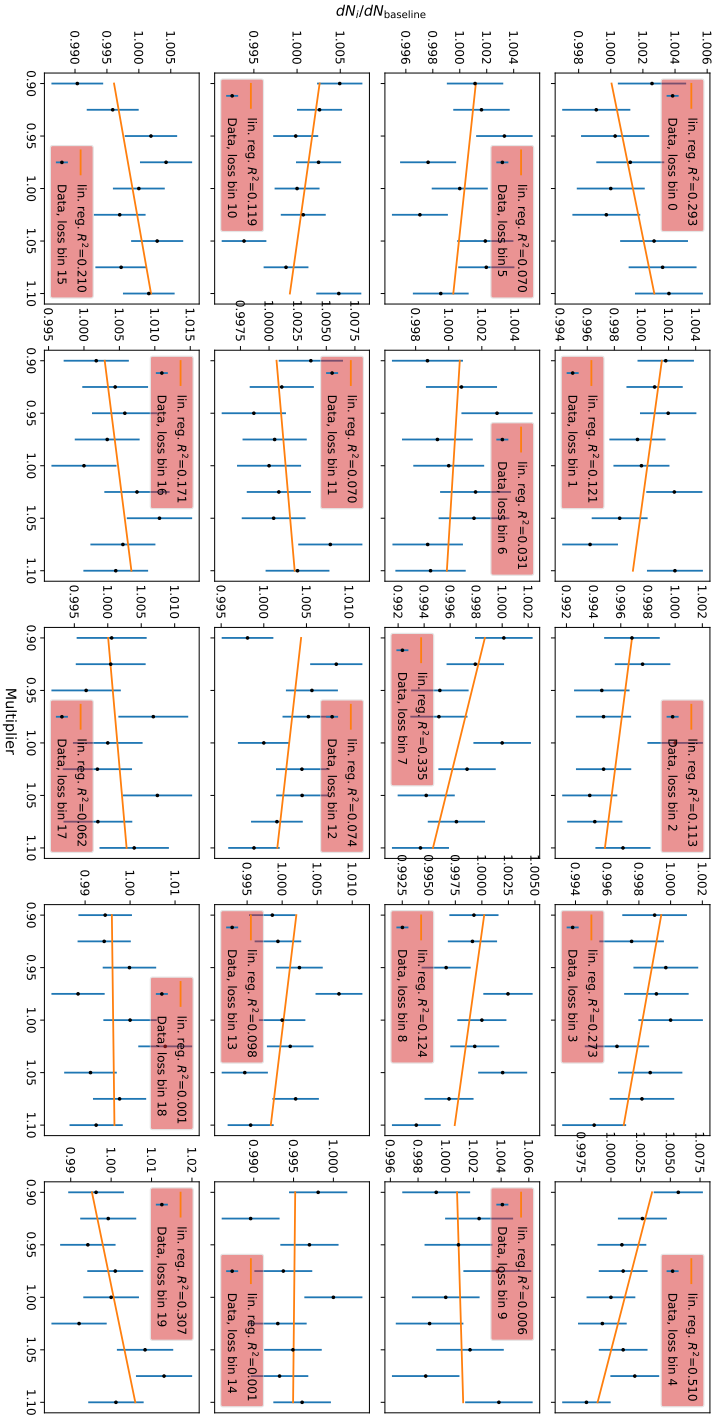

Figure B.28: One dimensional interpolation of the differences between the energy loss histograms created with different bremsstrahlung multiplier for reconstructed muon energies from 4.64 TeV to 10 TeV. A coefficient of determination threshold of 0.9 is used to mark all energy loss bins (red colored legend box), which would not be included in the fit.

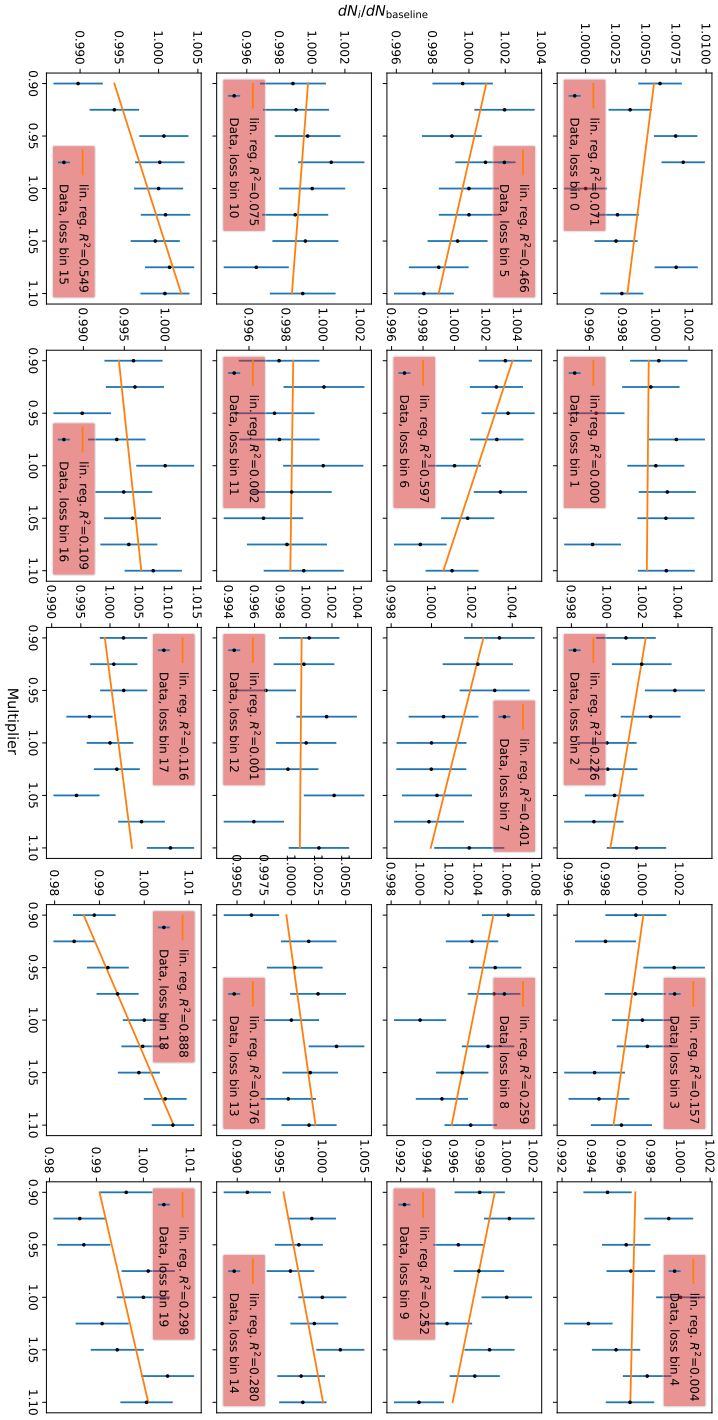

Figure B.29: One dimensional interpolation of the differences between the energy loss histograms created with different bremsstrahlung multiplier for reconstructed muon energies from 10 TeV to 31.6 TeV. A coefficient of determination threshold of 0.9 is used to mark all energy loss bins (red colored legend box), which would not be included in the fit.

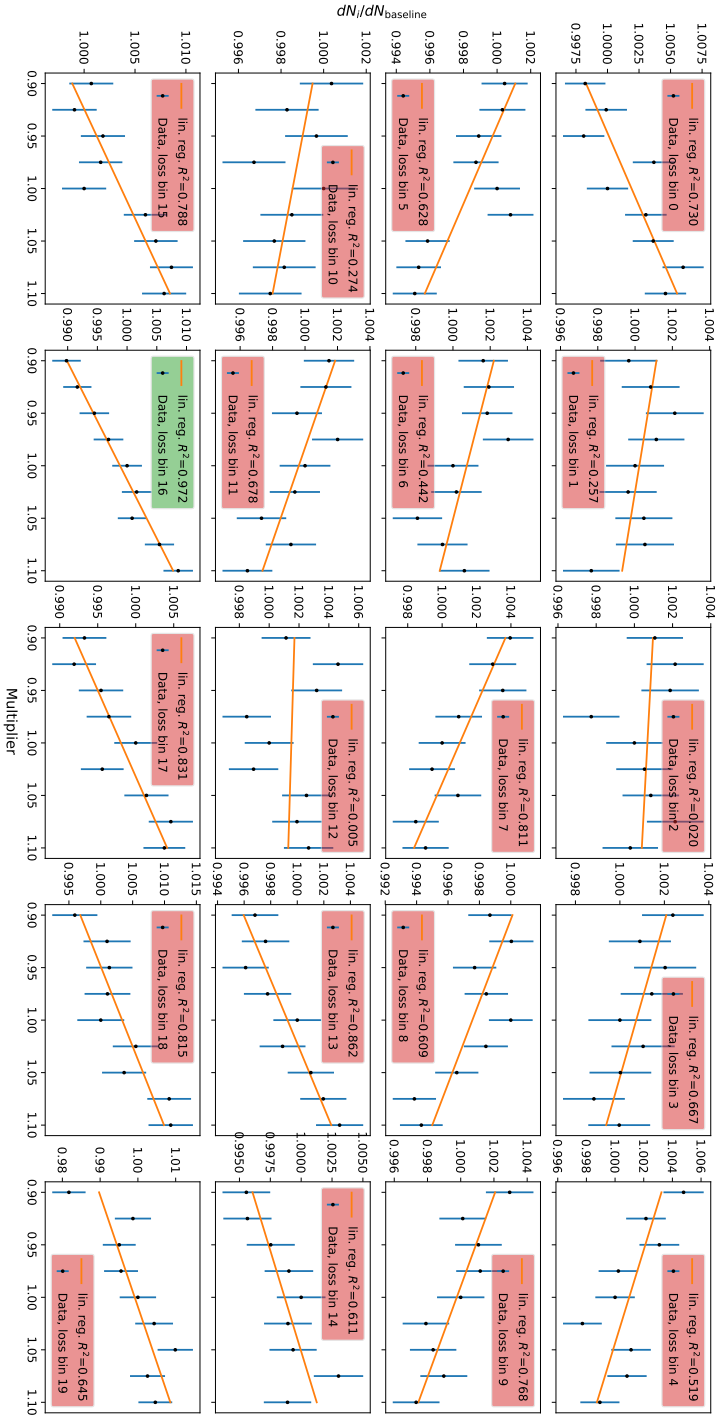

Figure B.30: One dimensional interpolation of the differences between the energy loss histograms created with different bremsstrahlung multiplier for reconstructed muon energies from 31.6 TeV to 100 TeV. A coefficient of determination threshold of 0.9 is used to mark all energy loss bins (red colored legend box), which would not be included in the fit.

B.2.5 Interpolation of the DOM Efficiency using the Neural Network Energy Reconstruction and High Resolutions

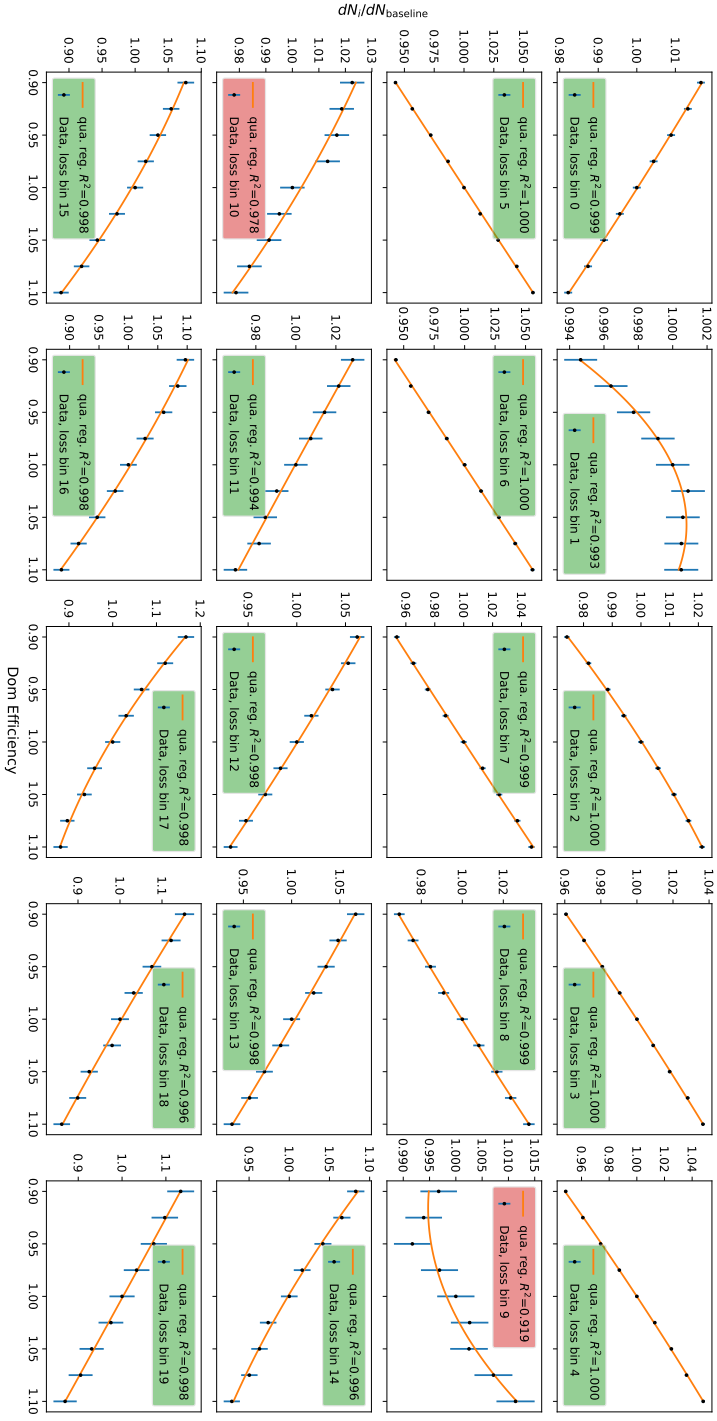

Figure B.31: One dimensional interpolation of the differences between the energy loss histograms created with different DOM efficiencies for reconstructed muon energies from 1 TeV to 2.15 TeV. A coefficient of determination threshold of 0.99 is used to mark all energy loss bins (red colored legend box), which would not be included in the fit.

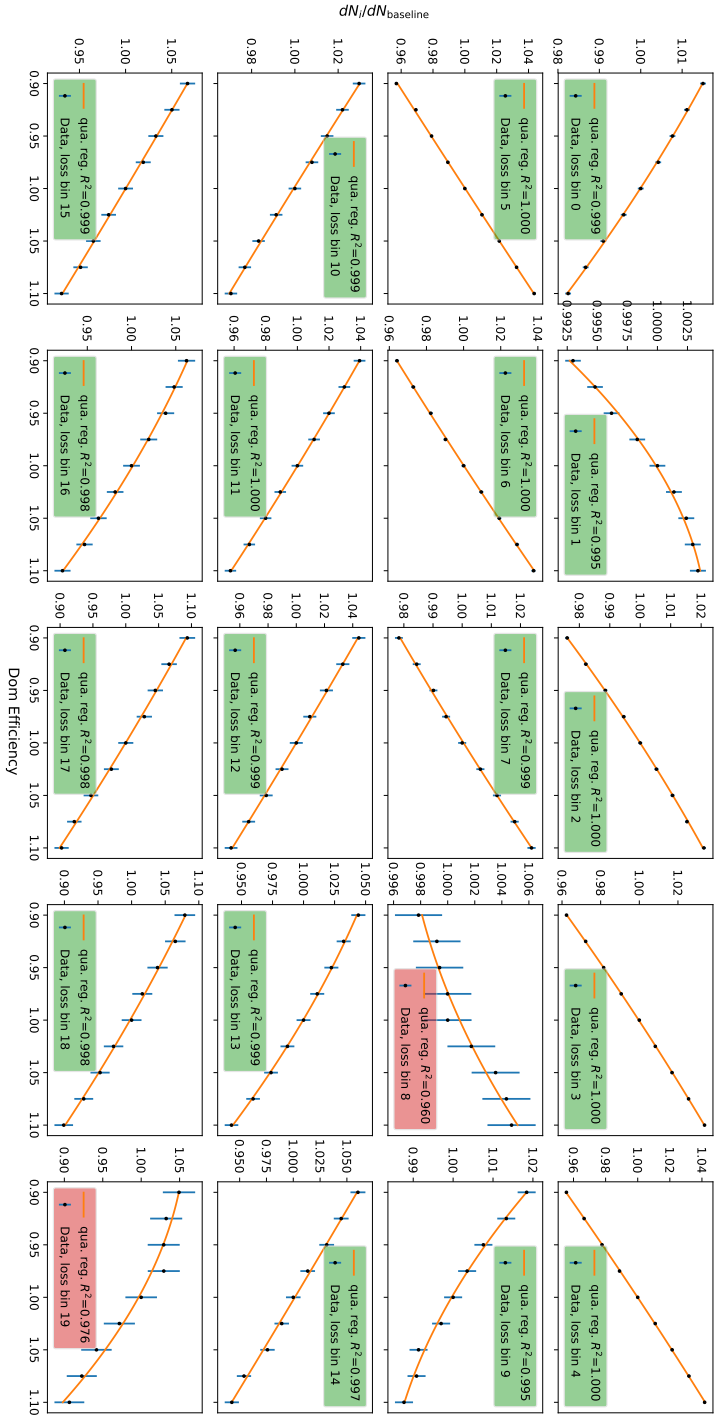

Figure B.32: One dimensional interpolation of the differences between the energy loss histograms created with different DOM efficiencies for reconstructed muon energies from 2.15 TeV to 4.64 TeV. A coefficient of determination threshold of 0.99 is used to mark all energy loss bins (red colored legend box), which would not be included in the fit.

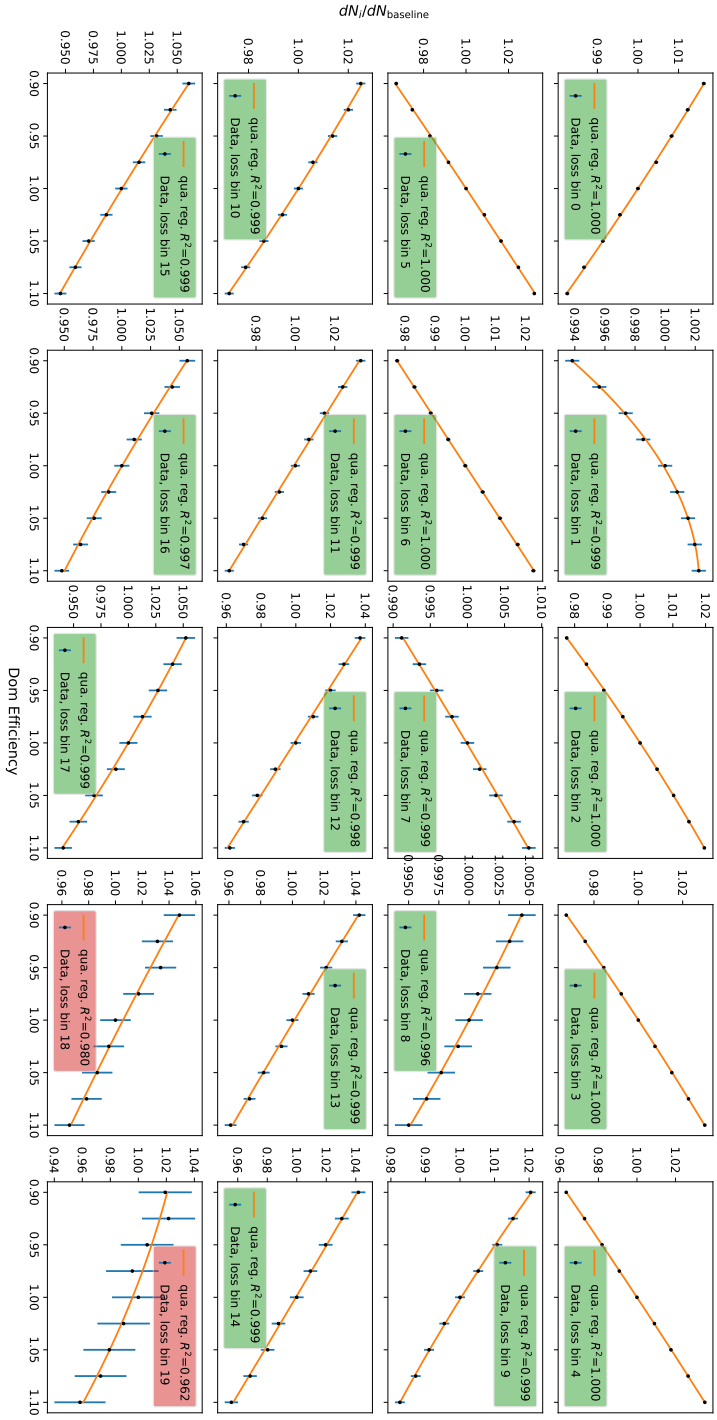

Figure B.33: One dimensional interpolation of the differences between the energy loss histograms created with different DOM efficiencies for reconstructed muon energies from 4.64 TeV to 10 TeV. A coefficient of determination threshold of 0.99 is used to mark all energy loss bins (red colored legend box), which would not be included in the fit.

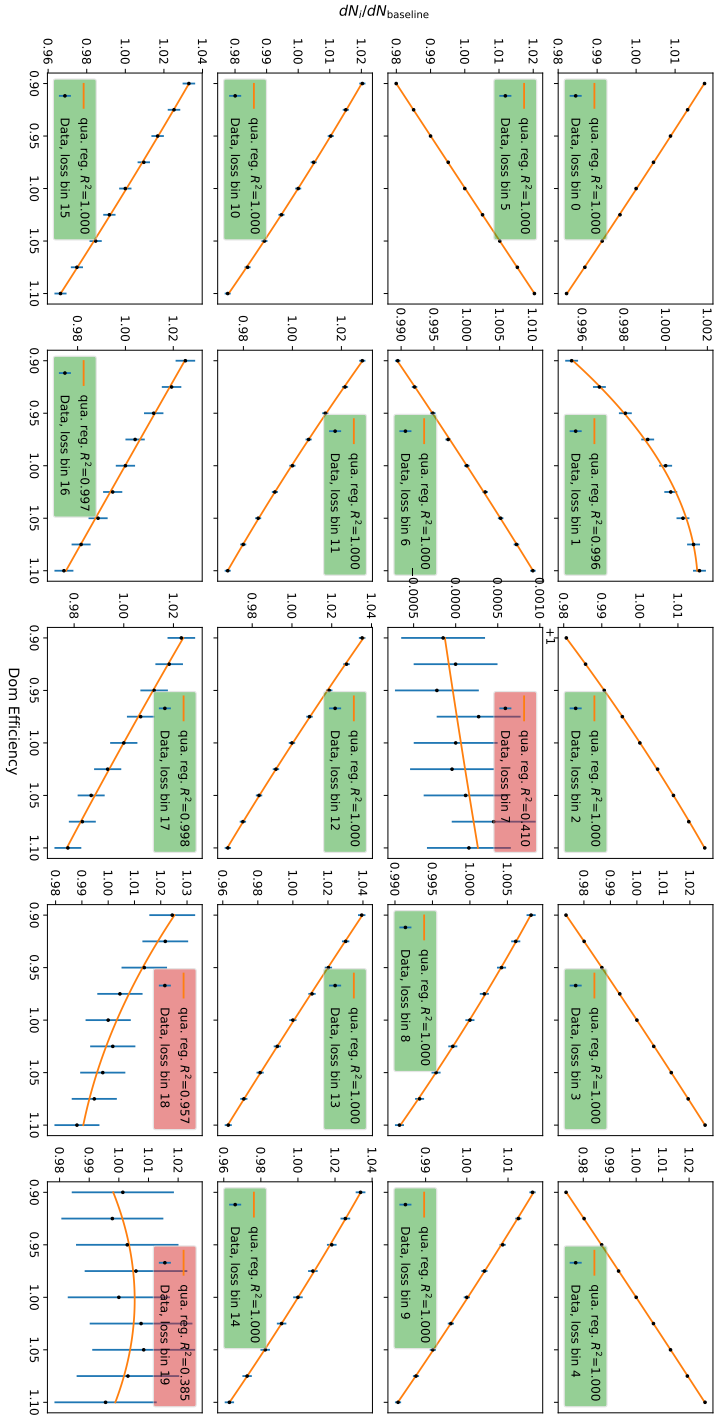

Figure B.34: One dimensional interpolation of the differences between the energy loss histograms created with different DOM efficiencies for reconstructed muon energies from 10 TeV to 31.6 TeV. A coefficient of determination threshold of 0.99 is used to mark all energy loss bins (red colored legend box), which would not be included in the fit.

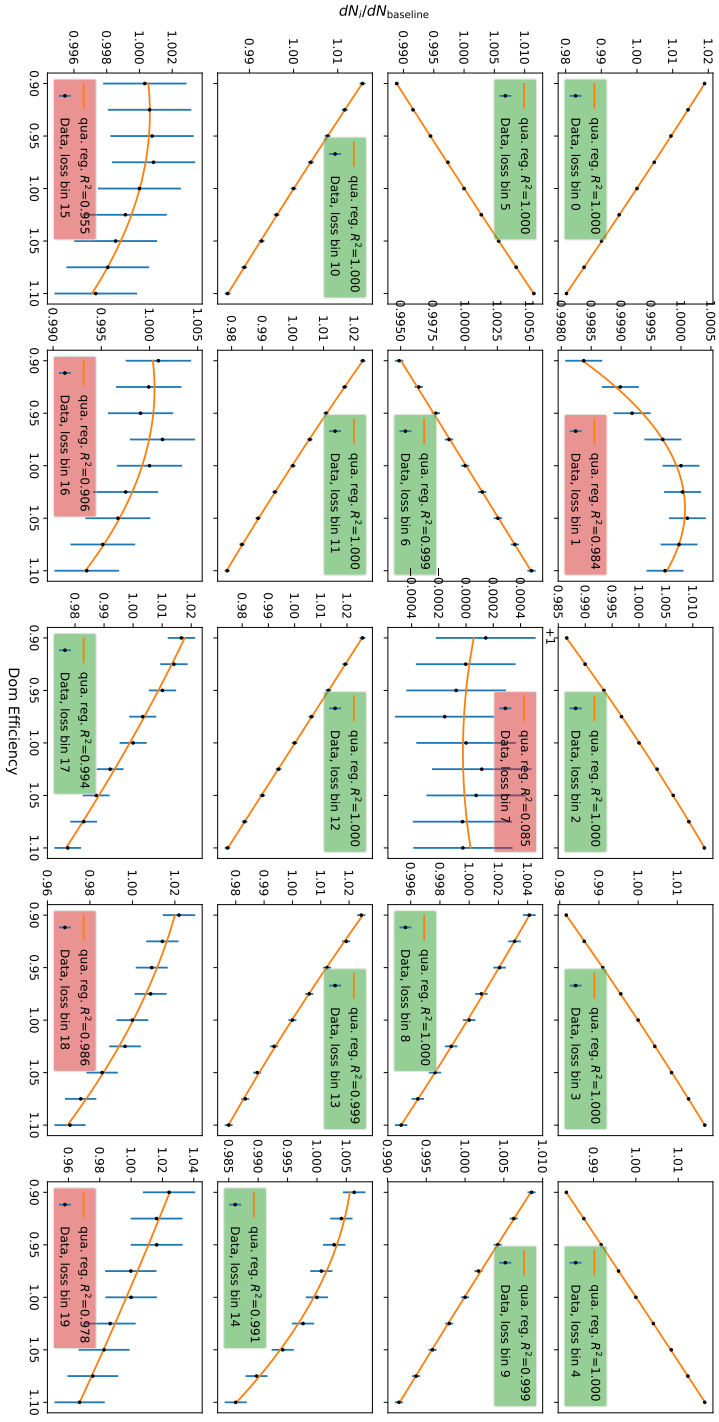

Figure B.35: One dimensional interpolation of the differences between the energy loss histograms created with different DOM efficiencies for reconstructed muon energies from 31.6 TeV to 100 TeV. A coefficient of determination threshold of 0.99 is used to mark all energy loss bins (red colored legend box), which would not be included in the fit.

B.2.6 Interpolation of the Spectral Index using the Neural Network Energy Reconstruction and High Resolutions

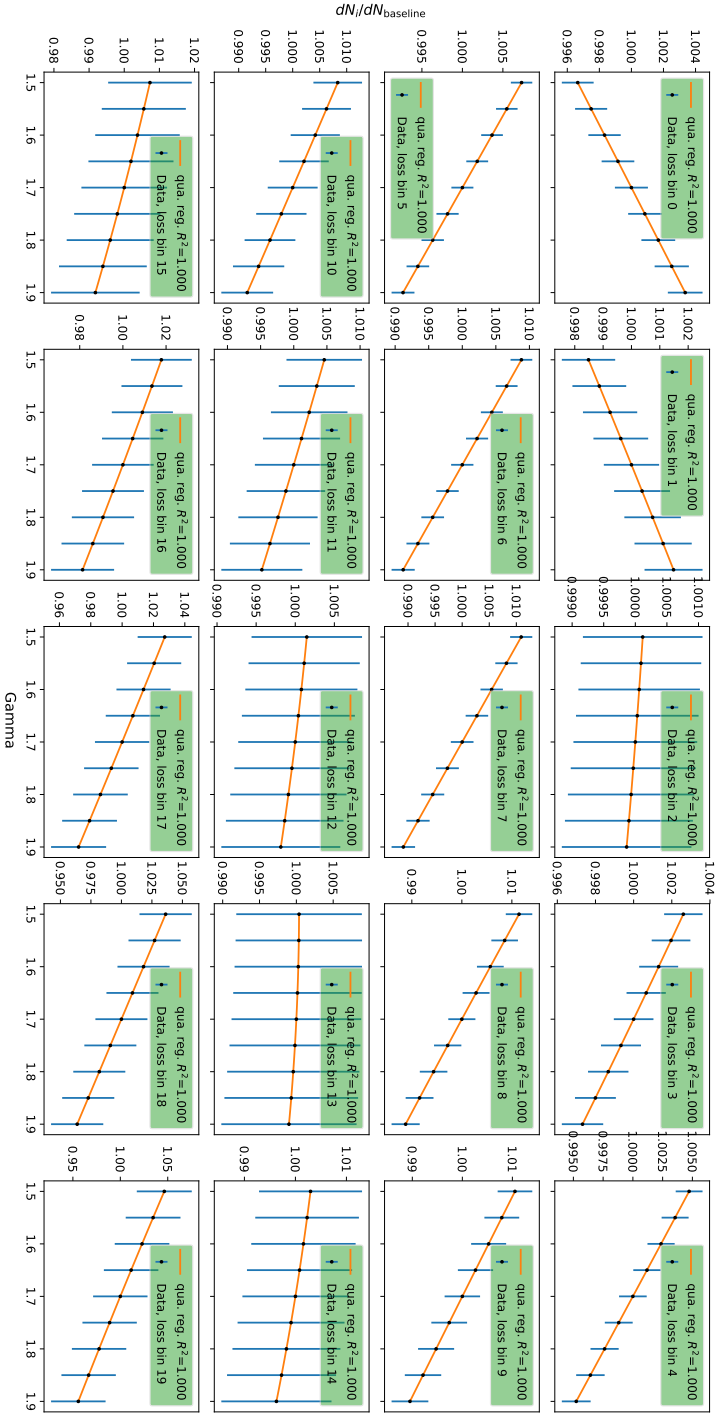

190 **Figure B.36:** One dimensional interpolation of the differences between the energy loss histograms created with different spectral indices for reconstructed muon energies from 1 TeV to 2.15 TeV. A coefficient of determination threshold of 0.99 is used to mark all energy loss bins (red colored legend box), which would not be included in the fit.

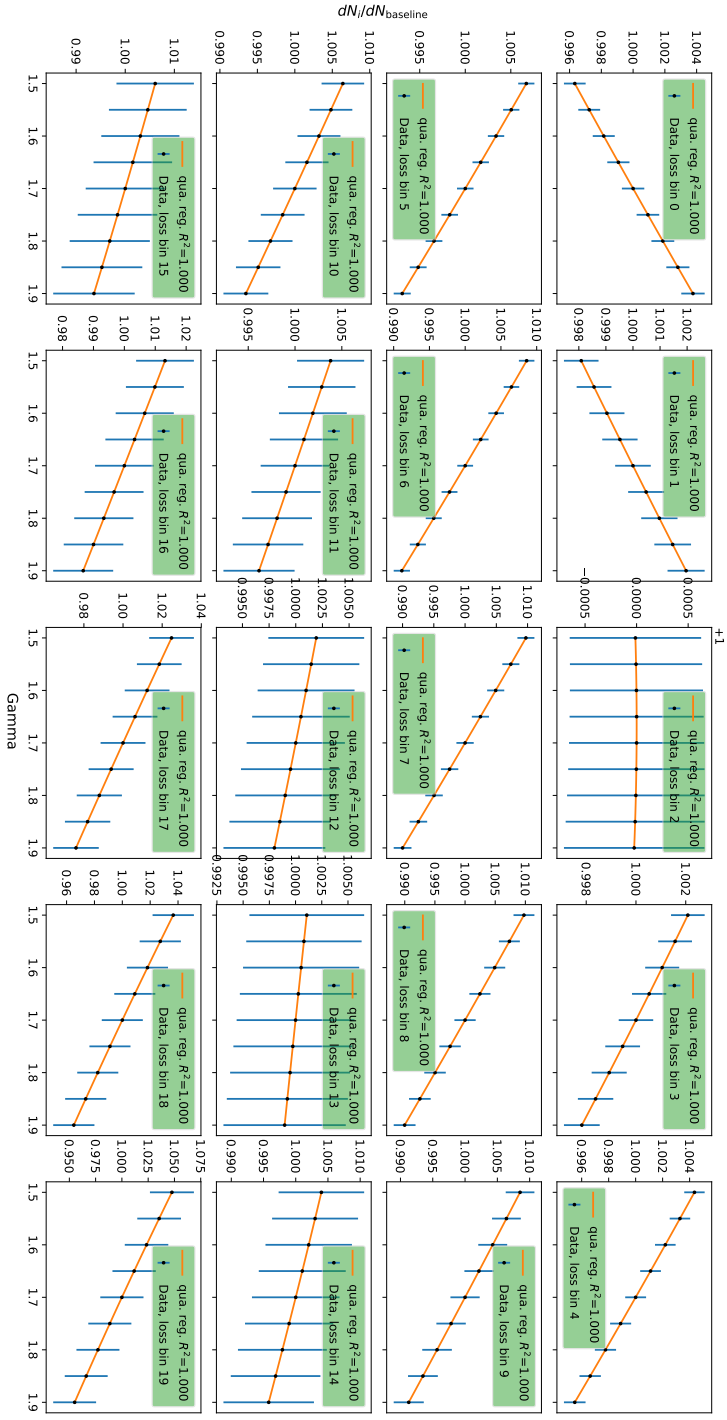

Figure B.37: One dimensional interpolation of the differences between the energy loss histograms created with different spectral indices for reconstructed muon energies from 2.15 TeV to 4.64 TeV. A coefficient of determination threshold of 0.99 is used to mark all energy loss bins (red colored legend box), which would not be included in the fit.

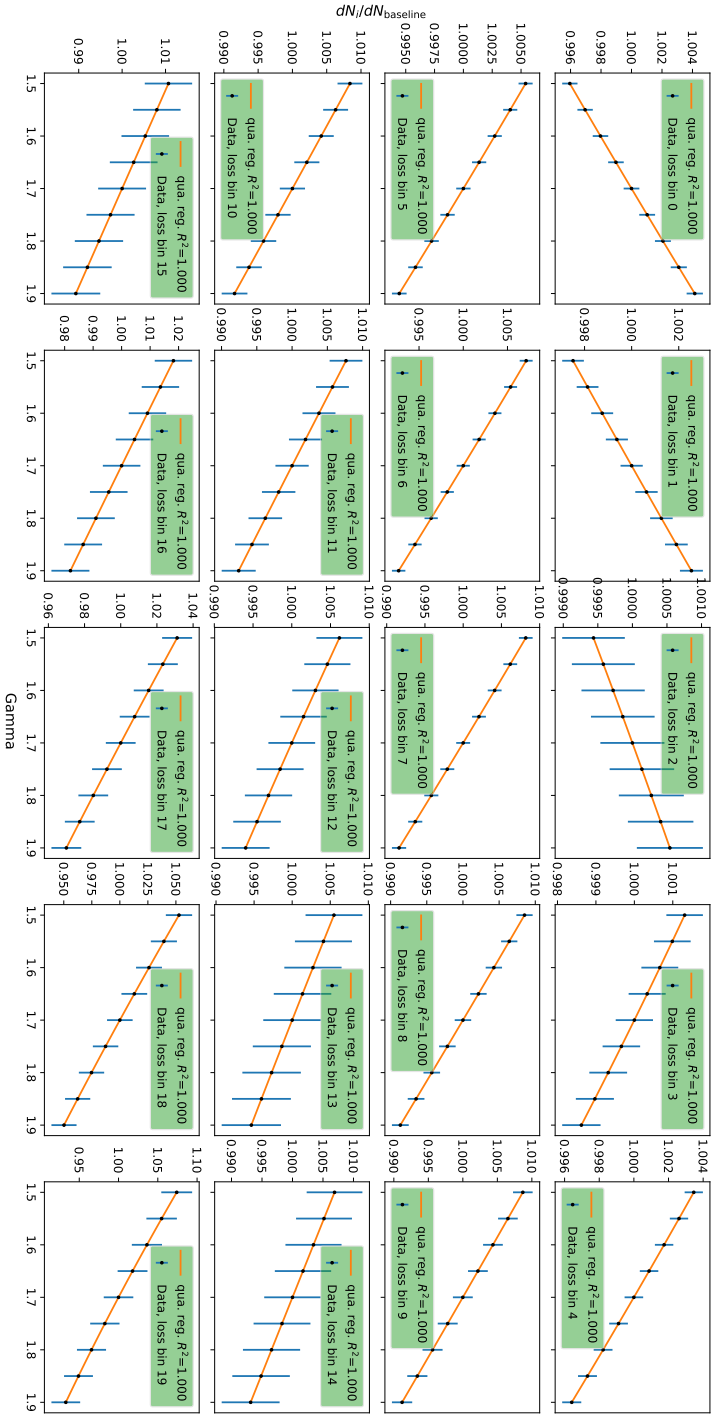

Figure B.38: One dimensional interpolation of the differences between the energy loss histograms created with different spectral indices for reconstructed muon energies from 4.64 TeV to 10 TeV. A coefficient of determination threshold of 0.99 is used to mark all energy loss bins (red colored legend box), which would not be included in the fit.

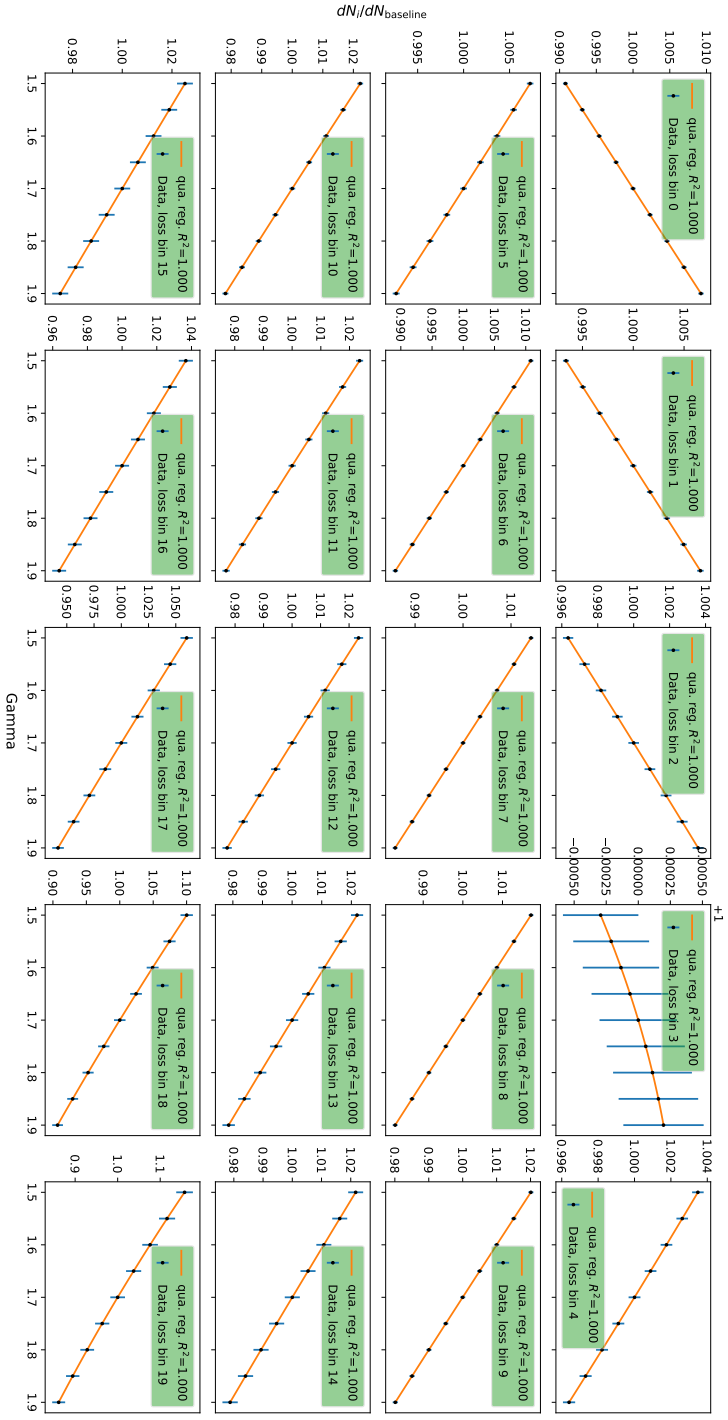

Figure B.39: One dimensional interpolation of the differences between the energy loss histograms created with different spectral indices for reconstructed muon energies from 10 TeV to 31.6 TeV. A coefficient of determination threshold of 0.99 is used to mark all energy loss bins (red colored legend box), which would not be included in the fit.

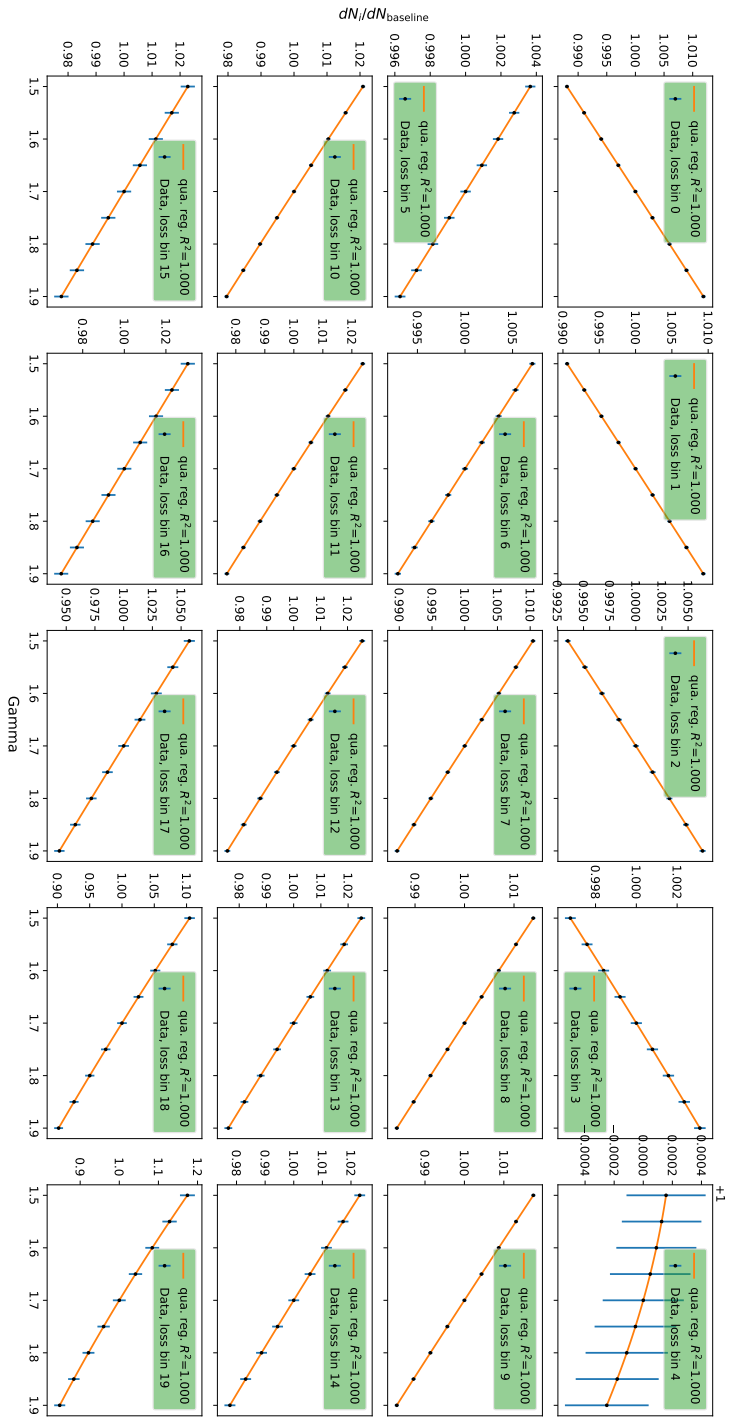

Figure B.40: One dimensional interpolation of the differences between the energy loss histograms created with different spectral indices for reconstructed muon energies from 31.6 TeV to 100 TeV. A coefficient of determination threshold of 0.99 is used to mark all energy loss bins (red colored legend box), which would not be included in the fit.

B.3 Performance of the Measurement

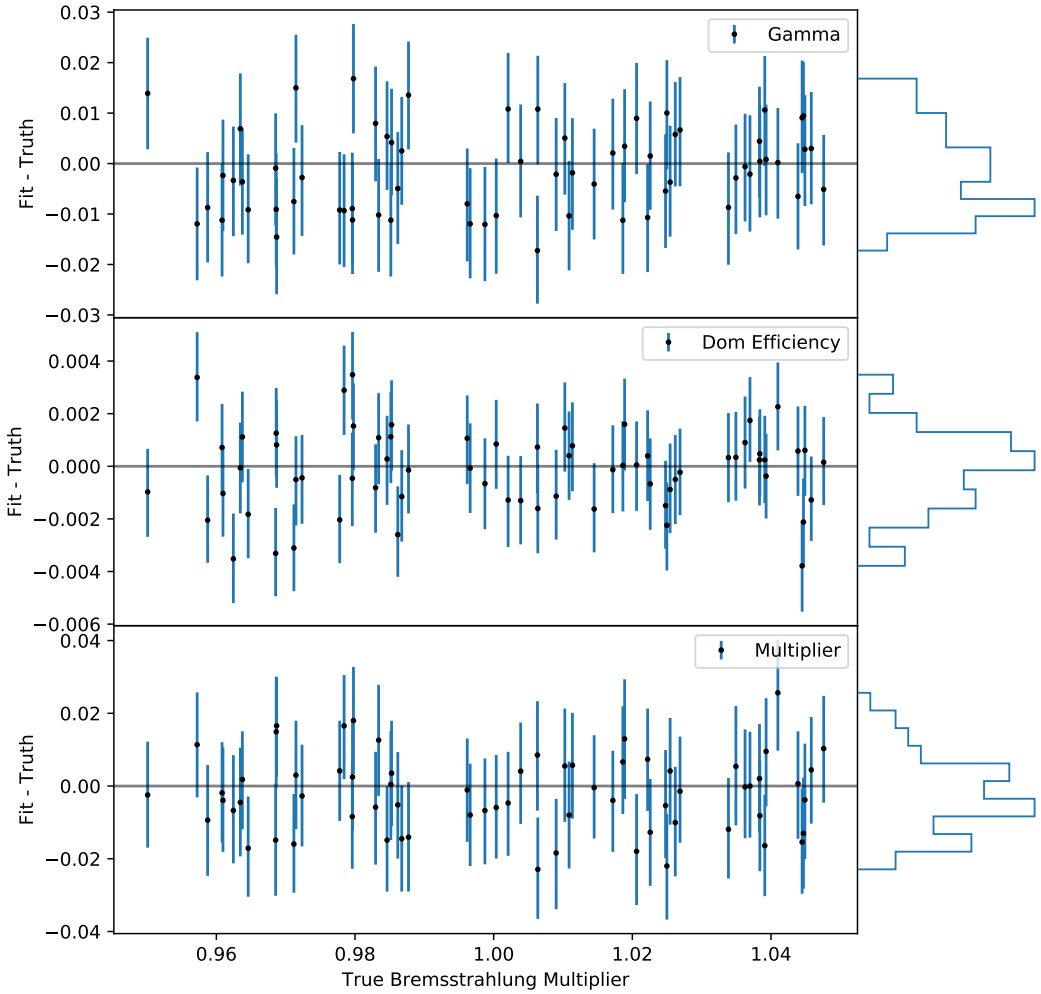

Figure B.41: Pull distribution of the estimated results of the MCMC samplings with the high resolution settings for the spectral index, the DOM efficiency and the bremsstrahlung multiplier. The muon energy is reconstructed using the neural network. The region below 0.95 and above 1.05 is neglected for the performance to avoid boundary effects during the MCMC sampling at the edge of the allowed interpolation region. The error represents the 68 % central interval and the best fit value, the median.

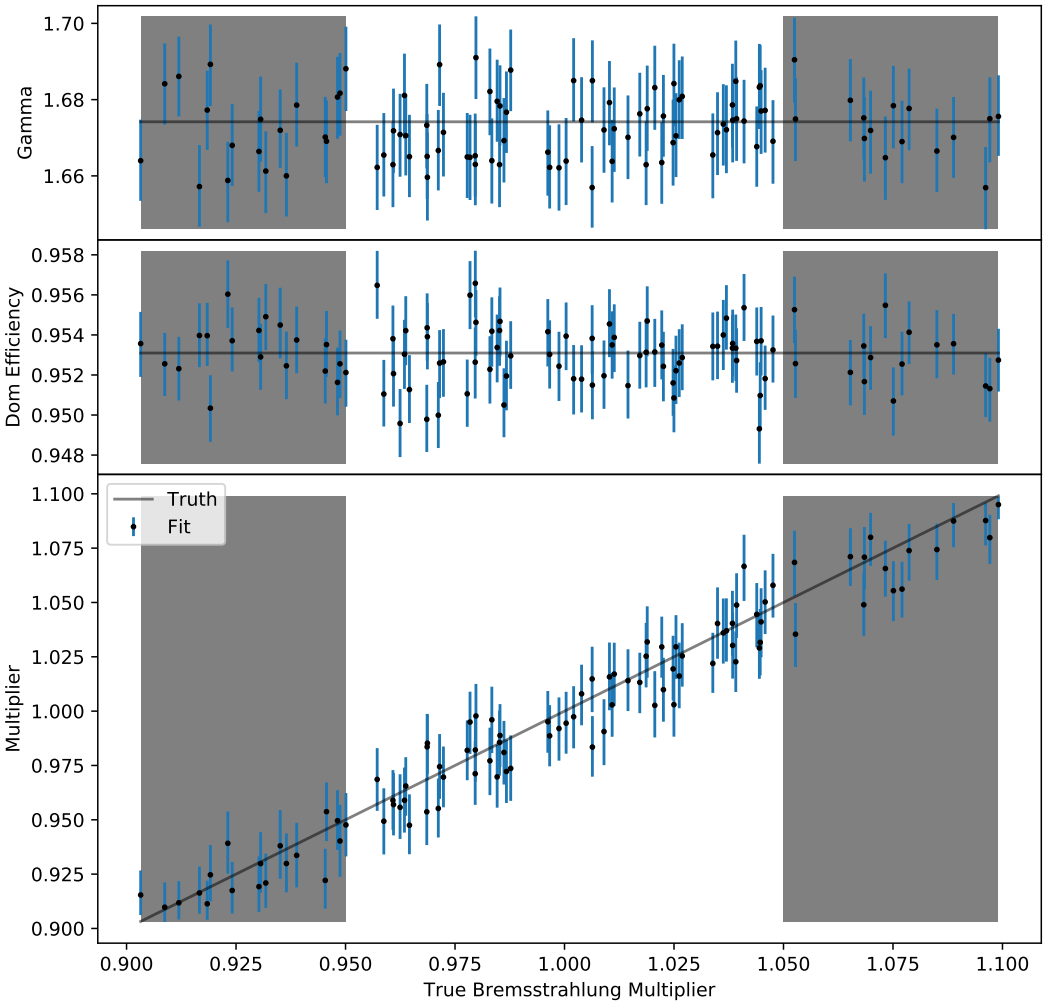

Figure B.42: Correlation of the true values and the estimated results of the MCMC samplings with the high resolution settings for the spectral index, the DOM efficiency and the bremsstrahlung multiplier. The muon energy is reconstructed using the neural network. The region below 0.95 and above 1.05 is neglected for the performance to avoid boundary effects during the MCMC sampling at the edge of the allowed interpolation region. The error represents the 68 % central interval and the best fit value, the median.

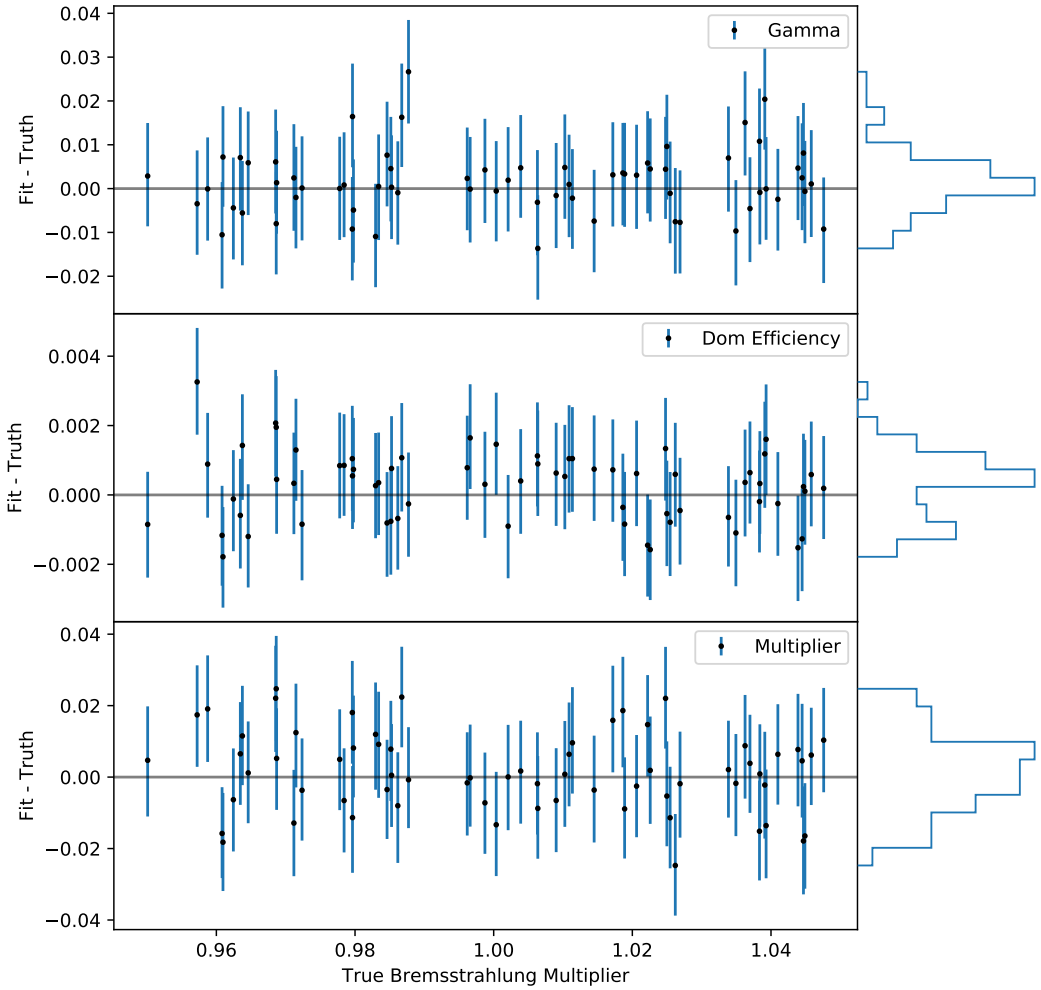

Figure B.43: Pull distribution of the estimated results of the MCMC samplings with the high resolution settings for the spectral index, the DOM efficiency and the bremsstrahlung multiplier. The muon energy is reconstructed using the truncated energy method. The region below 0.95 and above 1.05 is neglected for the performance to avoid boundary effects during the MCMC sampling at the edge of the allowed interpolation region. The error represents the 68 % central interval and the best fit value, the median.

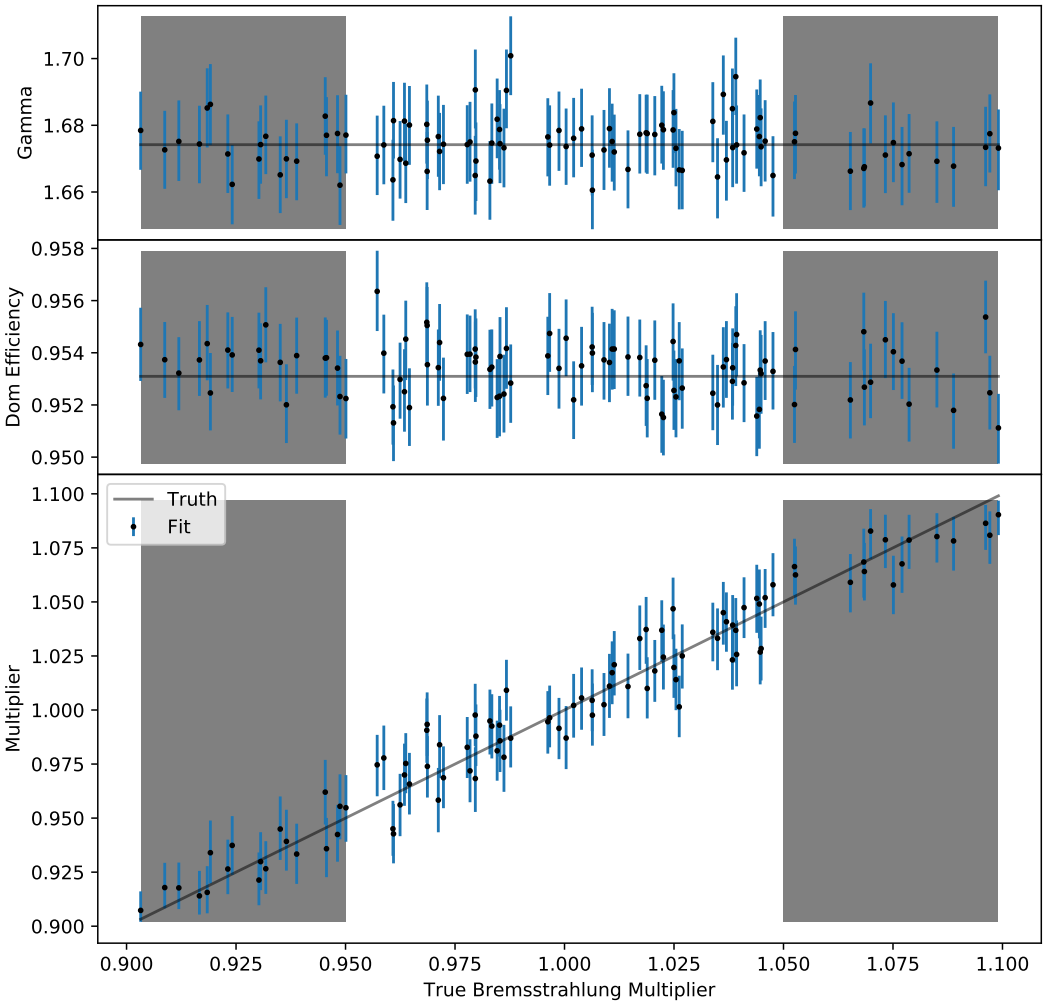

Figure B.44: Correlation of the true values and the estimated results of the MCMC samplings with the high resolution settings for the spectral index, the DOM efficiency and the bremsstrahlung multiplier. The muon energy is reconstructed using the truncated energy method. The region below 0.95 and above 1.05 is neglected for the performance to avoid boundary effects during the MCMC sampling at the edge of the allowed interpolation region. The error represents the 68 % central interval and the best fit value, the median.

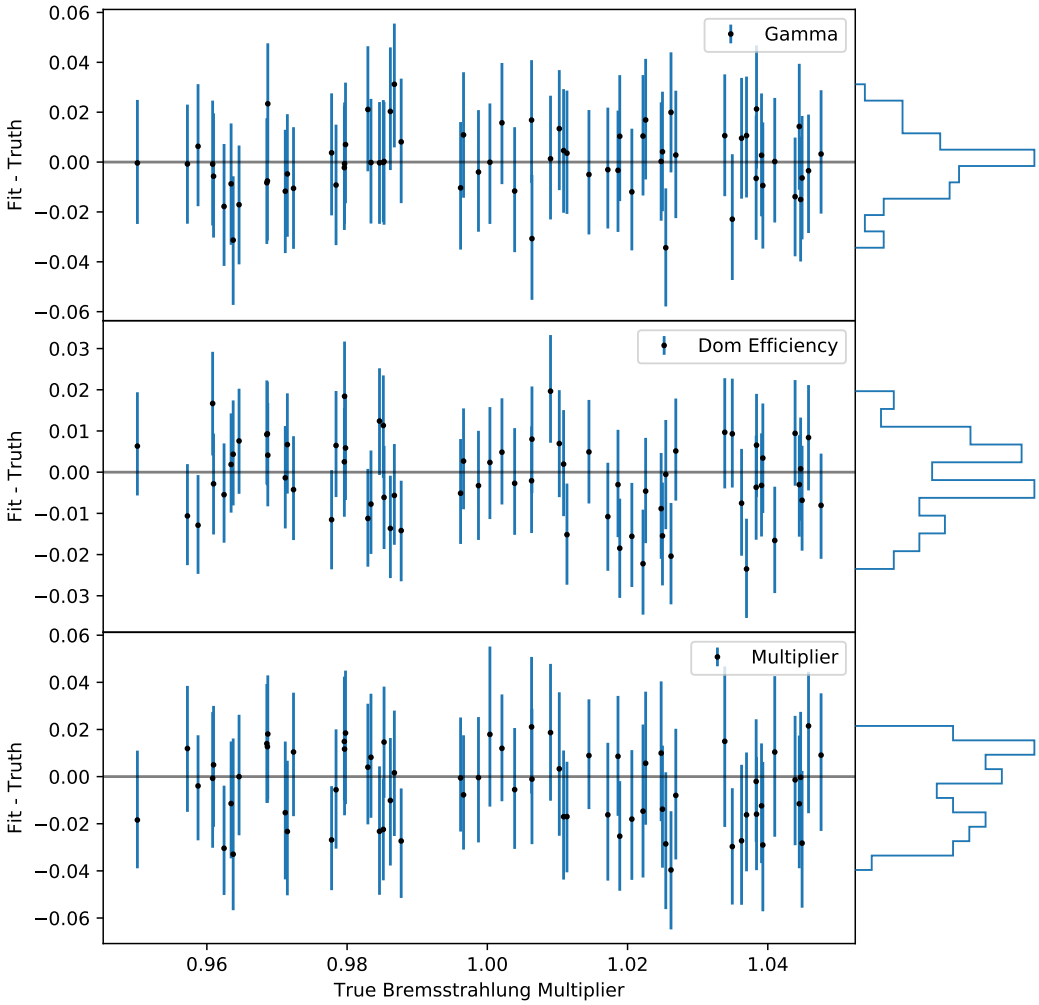

Figure B.45: Pull distribution of the estimated results of the MCMC samplings with the baseline resolution settings for the spectral index, the DOM efficiency and the bremsstrahlung multiplier. The muon energy is reconstructed using the neural network. The region below 0.95 and above 1.05 is neglected for the performance to avoid boundary effects during the MCMC sampling at the edge of the allowed interpolation region. The error represents the 68 % central interval and the best fit value, the median.

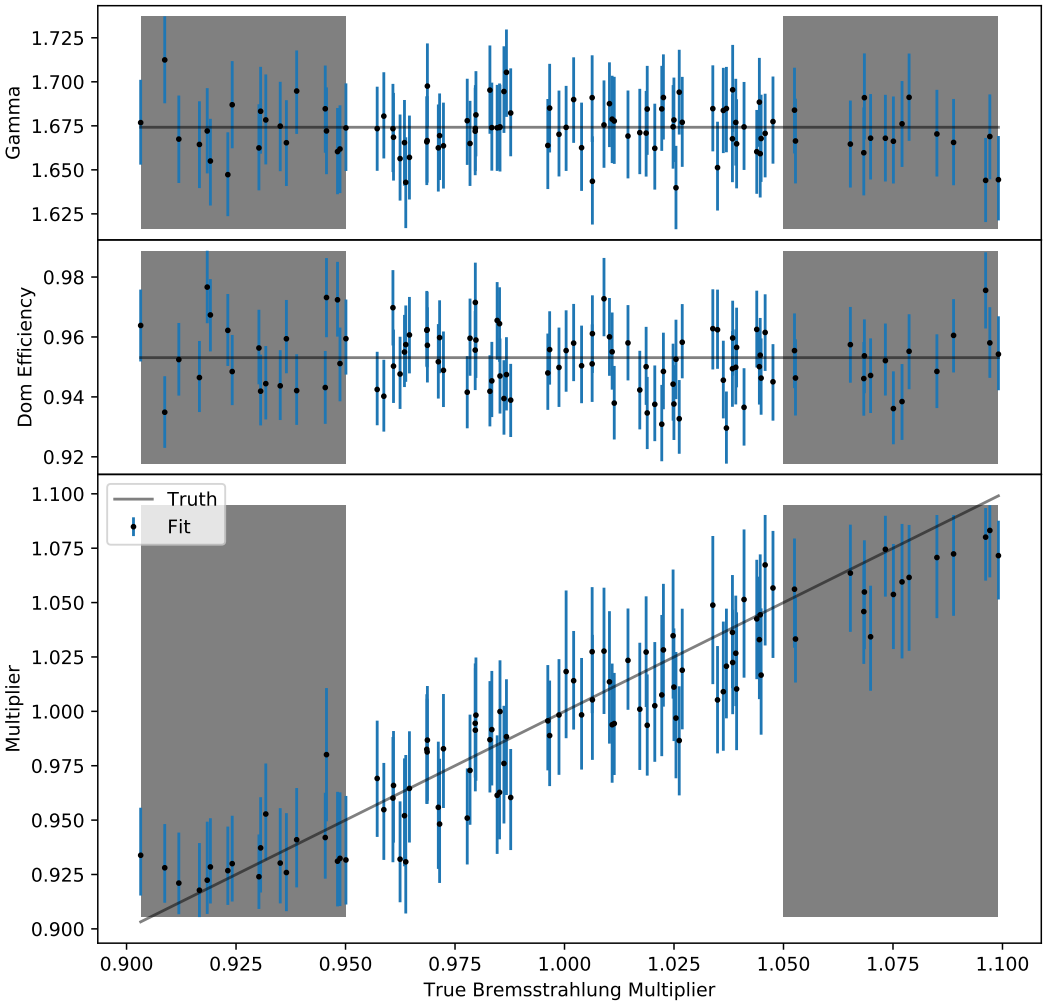

Figure B.46: Correlation of the true values and the estimated results of the MCMC samplings with the baseline resolution settings for the spectral index, the DOM efficiency and the bremsstrahlung multiplier. The muon energy is reconstructed using the neural network. The region below 0.95 and above 1.05 is neglected for the performance to avoid boundary effects during the MCMC sampling at the edge of the allowed interpolation region. The error represents the 68 % central interval and the best fit value, the median.

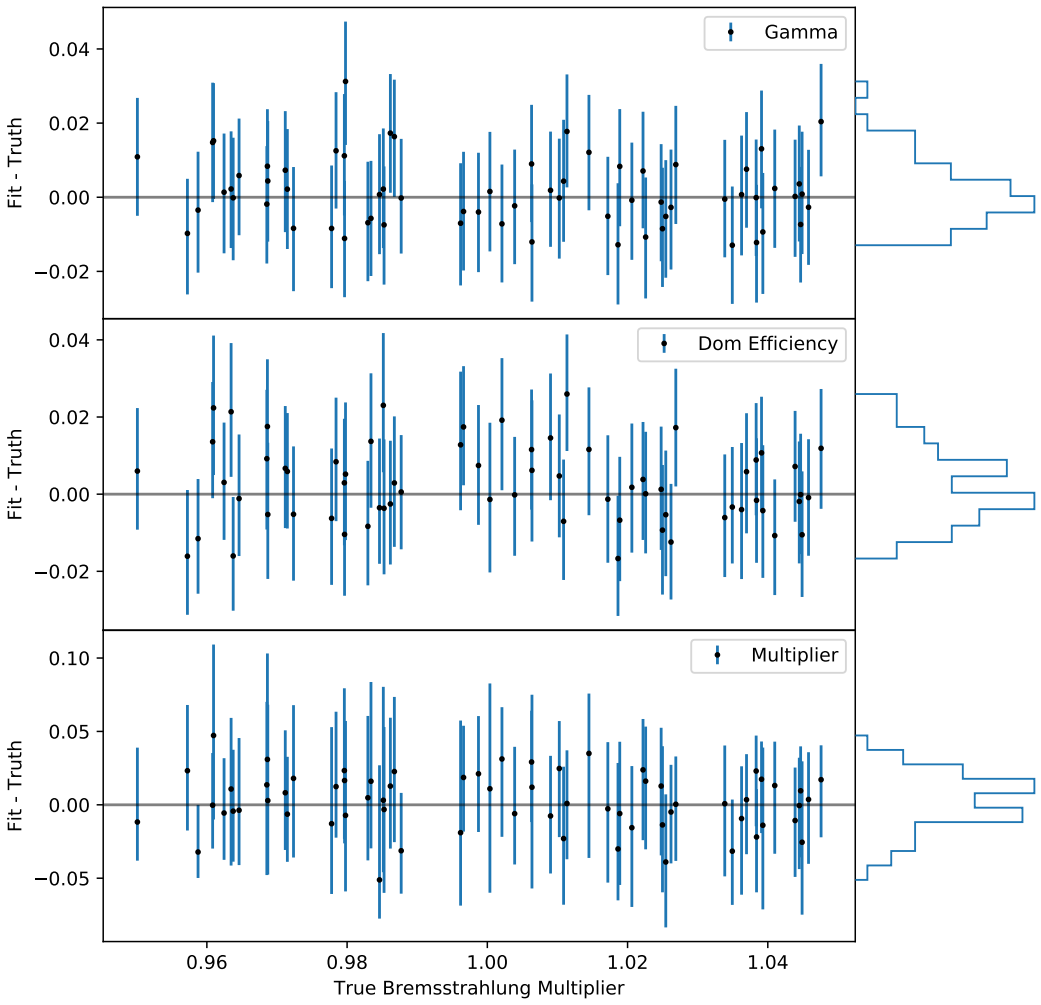

Figure B.47: Pull distribution of the estimated results of the MCMC samplings with the baseline resolution settings for the spectral index, the DOM efficiency and the bremsstrahlung multiplier. The muon energy is reconstructed using the truncated energy method. The region below 0.95 and above 1.05 is neglected for the performance to avoid boundary effects during the MCMC sampling at the edge of the allowed interpolation region. The error represents the 68 % central interval and the best fit value, the median.

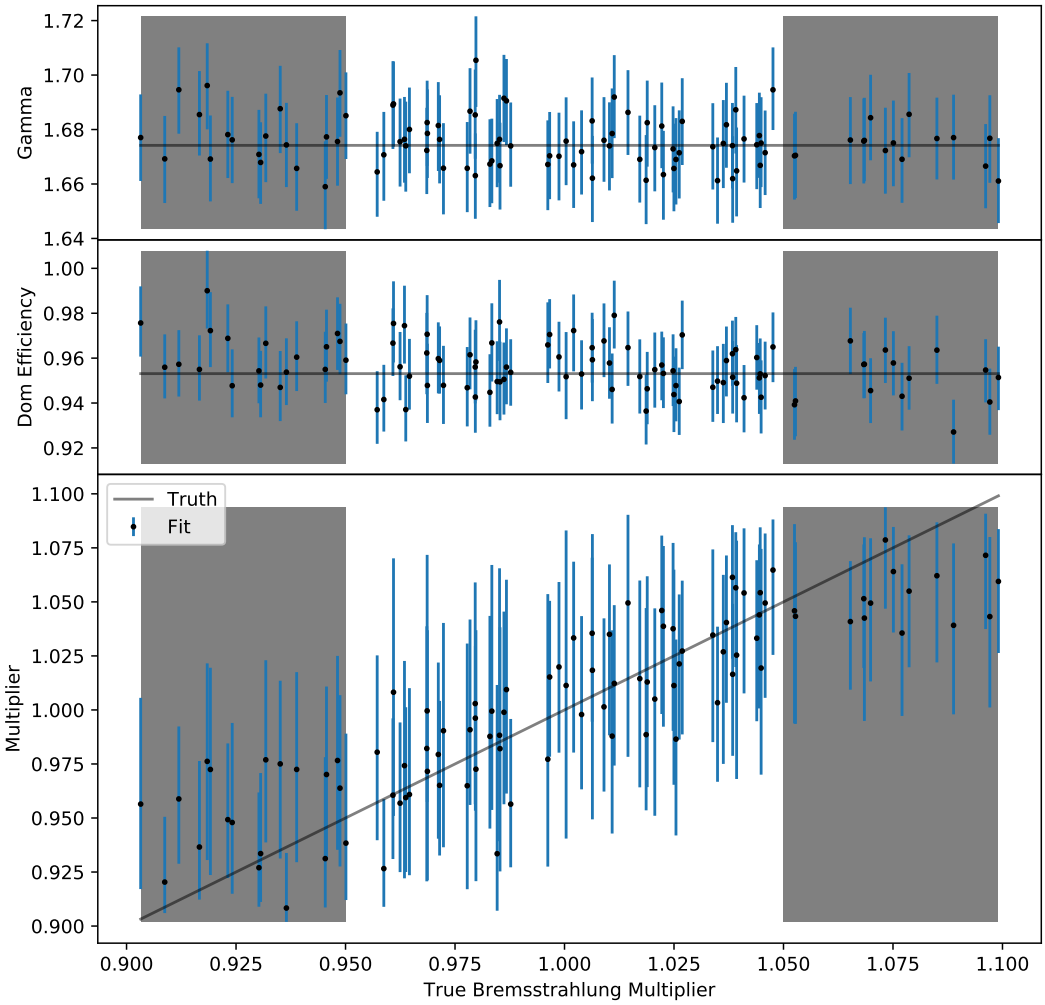

Figure B.48: Correlation of the true values and the estimated results of the MCMC samplings with the baseline resolution settings for the spectral index, the DOM efficiency and the bremsstrahlung multiplier. The muon energy is reconstructed using the truncated energy method. The region below 0.95 and above 1.05 is neglected for the performance to avoid boundary effects during the MCMC sampling at the edge of the allowed interpolation region. The error represents the 68 % central interval and the best fit value, the median.

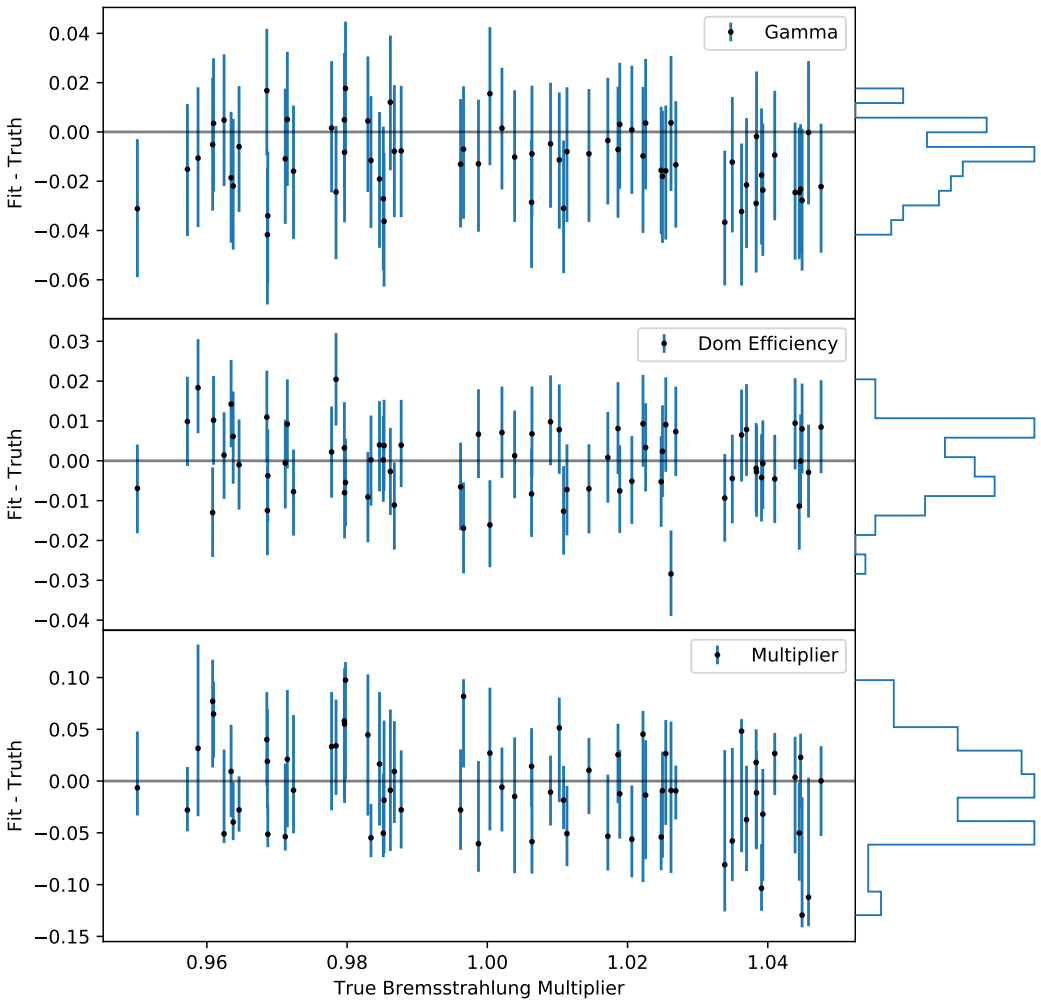

Figure B.49: Pull distribution of the estimated results of the MCMC samplings with the low resolution settings for the spectral index, the DOM efficiency and the bremsstrahlung multiplier. The muon energy is reconstructed using the neural network. The region below 0.95 and above 1.05 is neglected for the performance to avoid boundary effects during the MCMC sampling at the edge of the allowed interpolation region. The error represents the 68 % central interval and the best fit value, the median.

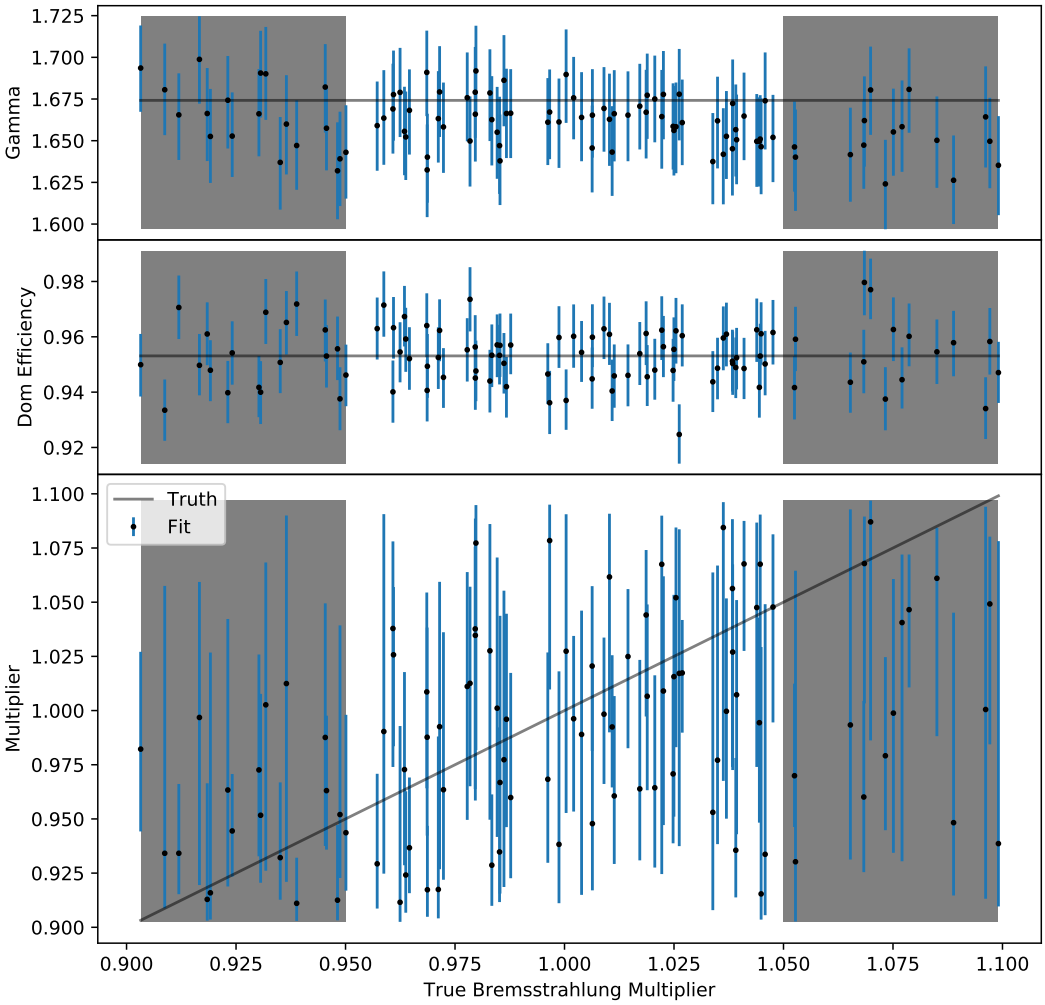

Figure B.50: Correlation of the true values and the estimated results of the MCMC samplings with the low resolution settings for the spectral index, the DOM efficiency and the bremsstrahlung multiplier. The muon energy is reconstructed using the neural network. The region below 0.95 and above 1.05 is neglected for the performance to avoid boundary effects during the MCMC sampling at the edge of the allowed interpolation region. The error represents the 68 % central interval and the best fit value, the median.

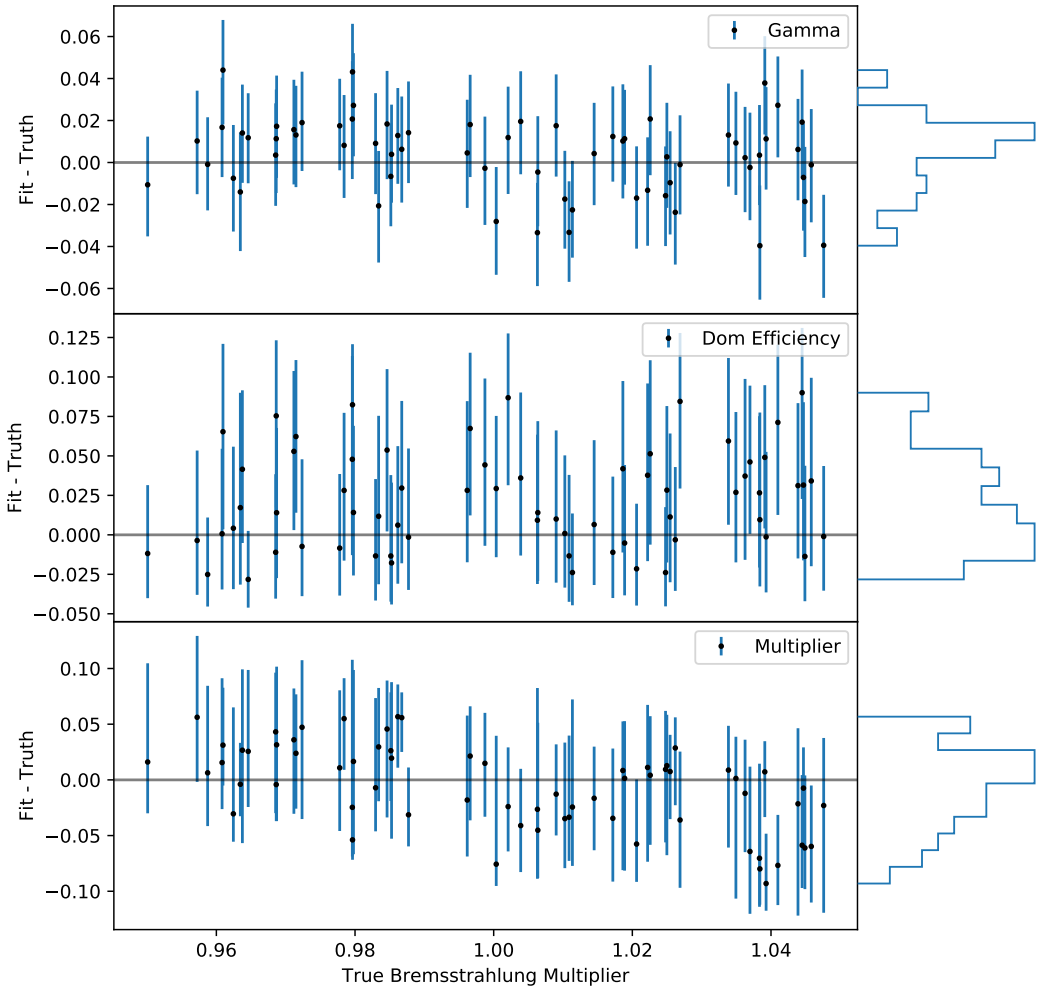

Figure B.51: Pull distribution of the estimated results of the MCMC samplings with the low resolution settings for the spectral index, the DOM efficiency and the bremsstrahlung multiplier. The muon energy is reconstructed using the truncated energy method. The region below 0.95 and above 1.05 is neglected for the performance to avoid boundary effects during the MCMC sampling at the edge of the allowed interpolation region. The error represents the 68 % central interval and the best fit value, the median.

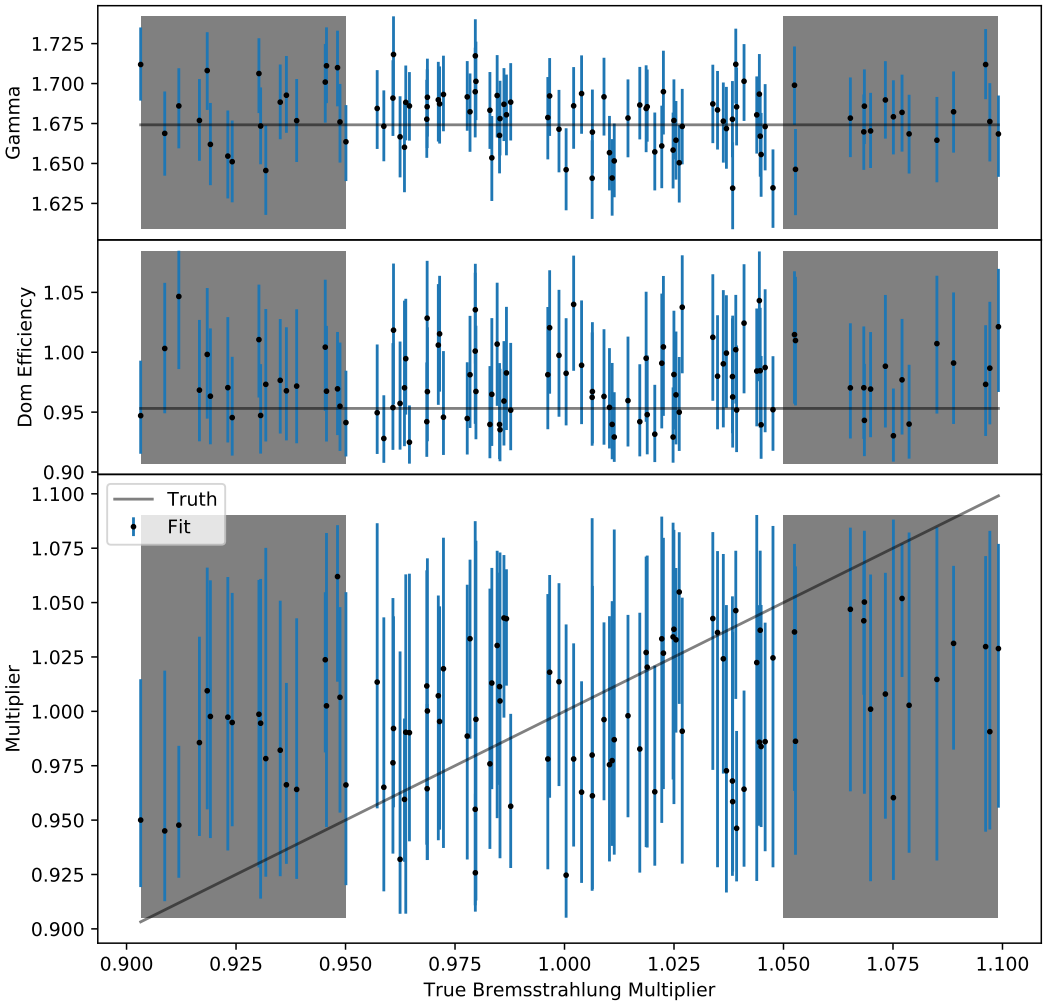

Figure B.52: Correlation of the true values and the estimated results of the MCMC samplings with the low resolution settings for the spectral index, the DOM efficiency and the bremsstrahlung multiplier. The muon energy is reconstructed using the truncated energy method. The region below 0.95 and above 1.05 is neglected for the performance to avoid boundary effects during the MCMC sampling at the edge of the allowed interpolation region. The error represents the 68 % central interval and the best fit value, the median.

C Used Software

The following open-source software packages were used in this thesis:

- cmake [MH07]
- python [VD09]
- FORM [Ver00]
- numpy [Har+20]
- scipy [Vir+20]
- matplotlib [Hun07]
- tqdm [Cos19]
- proposal [Ala+21b]
- jupyter [PG07]
- emcee [For+13]
- tensorflow [Mar+15]

Bibliography

[Aab+15] A. Aab et al., Pierre Auger Collaboration. "The Pierre Auger Cosmic Ray Observatory." In: *Nuclear Instruments and Methods in Physics Research Section A* 798 (2015), pp. 172–213. DOI: 10.1016/j.nima.2015.06.058. arXiv: 1502.01323.

[Aab+16] A. Aab et al., Pierre Auger Collaboration. *The Pierre Auger Observatory Upgrade - Preliminary Design Report*. 2016. arXiv: 1604.03637.

[Aar+10] F. D. Aaron et al., H1 and ZEUS Collaboration. "Combined Measurement and QCD Analysis of the Inclusive $e^{\pm}$p Scattering Cross Sections at HERA." In: *Journal of High Energy Physics* 01 (2010), p. 109. DOI: 10.1007/JHEP01(2010)109. arXiv: 0911.0884.

[Aar+13] M. G. Aartsen et al., IceCube Collaboration. "South Pole glacial climate reconstruction from multi-borehole laser particulate stratigraphy." In: *Journal of Glaciology* 59 (2013), pp. 1117–1128. DOI: 10.3189/2013JoG13J068.

[Aar+14] M. G. Aartsen et al., IceCube Collaboration. "Energy Reconstruction Methods in the IceCube Neutrino Telescope." In: *Journal of Instrumentation* 9 (2014), P03009. DOI: 10.1088/1748-0221/9/03/P03009. arXiv: 1311.4767.

[Aar+16] M. G. Aartsen et al., IceCube Collaboration. "Observation and Characterization of a Cosmic Muon Neutrino Flux from the Northern Hemisphere using six years of IceCube data." In: *Astrophysical Journal* 833 (2016), p. 3. DOI: 10.3847/0004-637X/833/1/3. arXiv: 1607.08006.

[Aar+17] M. G. Aartsen et al., IceCube Collaboration. "The contribution of Fermi-2LAC blazars to the diffuse TeV-PeV neutrino flux." In: *Astrophysical Journal* 835 (2017), p. 45. DOI: 10.3847/1538-4357/835/1/45. arXiv: 1611.03874.

[Aar+18a] M. G. Aartsen et al., IceCube, Fermi-LAT, MAGIC, AGILE, ASAS-SN, HAWC, H.E.S.S., INTEGRAL, Kanata, Kiso, Kapteyn, Liverpool Telescope, Subaru, Swift NuSTAR, VERITAS, VLA/17B-403 Collaborations. "Multi-messenger observations of a flaring blazar coincident with high-energy neutrino IceCube-170922A." In: *Science* 361 (2018), eaat1378. DOI: 10.1126/science.aat1378. arXiv: 1807.08816.

[Aar+18b] M. G. Aartsen et al., IceCube Collaboration. "Neutrino emission from the direction of the blazar TXS 0506+056 prior to the IceCube-170922A alert." In: *Science* 361 (2018), pp. 147–151. DOI: 10.1126/science.aat2890. arXiv: 1807.08794.

[Aar+18c] M. G. Aartsen et al., IceCube Collaboration. "Neutrinos and Cosmic Rays Observed by IceCube." In: *Advances in Space Research* 62 (2018), pp. 2902–2930. DOI: 10.1016/j.asr.2017.05.030. arXiv: 1701.03731.

[Aar+19] M. G. Aartsen et al., IceCube Collaboration. "Efficient propagation of systematic uncertainties from calibration to analysis with the SnowStorm method in IceCube." In: *Journal of Cosmology and Astroparticle Physics* 10 (2019), p. 048. DOI: 10.1088/1475-7516/2019/10/048. arXiv: 1909.01530.

[Aar+20a] M. G. Aartsen et al., IceCube Collaboration. "Characteristics of the diffuse astrophysical electron and tau neutrino flux with six years of IceCube high energy cascade data." In: *Physical Review Letters* 125 (2020), p. 121104. DOI: 10.1103/PhysRevLett.125.121104. arXiv: 2001.09520.

[Aar+20b] M. G. Aartsen et al., IceCube Collaboration. "Time-integrated Neutrino Source Searches with 10 years of IceCube Data." In: *Physical Review Letters* 124 (2020), p. 051103. DOI: 10.1103/PhysRevLett.124.051103. arXiv: 1910.08488.

[Aar+21] M. G. Aartsen et al., IceCube-Gen2 Collaboration. "IceCube-Gen2: The Window to the Extreme Universe." In: *Journal of Physics G: Nuclear and Particle Physics* 48 (2021), p. 060501. DOI: 10.1088/1361-6471/abbd48. arXiv: 2008.04323.

[AB81] A. I. Akhiezer and V. B. Berestezkii. *Quantum Electrodynamics*. 4th ed. in Russian. Moscow, 1981.

[AB97] Y. M. Andreev and E. V. Bugaev. "Muon bremsstrahlung on heavy atoms." In: *Physical Review D* 55 (1997), pp. 1233–1243. DOI: 10.1103/PhysRevD.55.1233.

[Abb+20a] R. Abbasi et al., IceCube Collaboration. *Measurement of Astrophysical Tau Neutrinos in IceCube's High-Energy Starting Events*. 2020. arXiv: 2011.03561.

[Abb+20b] R. Abbott et al., LIGO Scientific Collaboration. *Instrument Science White Paper 2020*. Tech. rep. LIGO-T2000407–v3. 2020.

[Abb+21a] R. Abbasi et al., IceCube Collaboration. *A Convolutional Neural Network based Cascade Reconstruction for the IceCube Neutrino Observatory*. 2021. arXiv: 2101.11589.

[Abb+21b] R. Abbasi et al., IceCube Collaboration. "LeptonInjector and LeptonWeighter: A neutrino event generator and weighter for neutrino observatories." In: *Computer Physics Communications* 266 (2021), p. 108018. DOI: 10.1016/j.cpc.2021.108018. arXiv: 2012.10449.

[ABB94] Y. Andreev, L. Bezrukov, and E. V. Bugaev. "Excitation of a Target in Muon Bremsstrahlung." In: *Physics of Atomic Nuclei* 57 (1994), pp. 2066–2074.

[Abe+17] A. U. Abeysekara et al., HAWC Collaboration. "Observation of the Crab Nebula with the HAWC Gamma-Ray Observatory." In: *Astrophysical Journal* 843 (2017), p. 39. DOI: 10.3847/1538-4357/aa7555. arXiv: 1701.01778.

[Abe+18] K. Abe et al., Hyper-Kamiokande Collaboration. *Hyper-Kamiokande Design Report*. 2018. arXiv: 1805.04163.

[Abe+99] K. Abe et al., SLAC E143 Collaboration. "Measurements of $R = \sigma_L/\sigma_T$ for $0.03 < x < 0.1$ and fit to world data." In: *Physics Letters B* 452 (1999), pp. 194–200. DOI: 10.1016/S0370-2693(99)00244-0. arXiv: hep-ex/9808028.

[Abr+91] H. Abramowicz et al. "A parametrization of $\sigma_T(\gamma^* p)$ above the resonance region for $Q^2 \geq 0$." In: *Physics Letters B* 269 (1991), pp. 465–476. DOI: 10.1016/0370-2693(91)90202-2.

[Abt+17] I. Abt et al. "Investigation into the limits of perturbation theory at low Q^2 using HERA deep inelastic scattering data." In: *Physical Review D* 96 (2017), p. 014001. DOI: 10.1103/PhysRevD.96.014001. arXiv: 1704.03187.

[Abu+13] T. Abu-Zayyad et al., Telescope Array Collaboration. "The surface detector array of the Telescope Array experiment." In: *Nuclear Instruments and Methods in Physics Research Section A* 689 (2013), pp. 87–97. DOI: 10.1016/j.nima.2012.05.079. arXiv: 1201.4964.

[Ach+19] B. S. Acharya et al., CTA Consortium. *Science with the Cherenkov Telescope Array*. World Scientific, 2019. ISBN: 978-981-3270-08-4. DOI: 10.1142/10986. arXiv: 1709.07997.

[Ack+06] M. Ackermann et al., AMANDA Collaboration. "Optical properties of deep glacial ice at the South Pole." In: *Journal of Geophysical Research* 111 (2006), p. D13203. DOI: 10.1029/2005JD006687.

[Adr+16] S. Adrián-Martínez et al., KM3Net Collaboration. "Letter of intent for KM3NeT 2.0." In: *Journal of Physics G: Nuclear and Particle Physics* 43 (2016), p. 084001. DOI: 10.1088/0954-3899/43/8/084001. arXiv: 1601.07459.

[Age+11] M. Ageron et al., ANTARES Collaboration. "ANTARES: The first undersea neutrino telescope." In: *Nuclear Instruments and Methods in Physics Research Section A* 656 (2011), pp. 11–38. DOI: 10.1016/j.nima.2011.06.103. arXiv: 1104.1607.

[Ago+03] S. Agostinelli et al. "Geant4 - A simulation toolkit." In: *Nuclear Instruments and Methods in Physics Research* 506 (2003), pp. 250–303. DOI: 10.1016/S0168-9002(03)01368-8.

[Ago+20] M. Agostini et al., P-ONE Collaboration. "The Pacific Ocean Neutrino Experiment." In: *Nature Astronomy* 4 (2020), pp. 913–915. DOI: 10.1038/s41550-020-1182-4. arXiv: 2005.09493.

[Agu+20] J. A. Aguilar et al., RNO-G Collaboration. "Design and Sensitivity of the Radio Neutrino Observatory in Greenland (RNO-G)." In: *Journal of Instrumentation* 16 (2020), P03025. DOI: 10.1088/1748-0221/16/03/P03025. arXiv: 2010.12279.

[Ahm+01] Q. R. Ahmad et al., SNO Collaboration. "Measurement of the rate of $\nu_e + d \rightarrow p + p + e^-$ interactions produced by ^8B solar neutrinos at the Sudbury Neutrino Observatory." In: *Physical Review Letters* 87 (2001), p. 071301. DOI: 10.1103/PhysRevLett.87.071301. arXiv: nucl-ex/0106015.

[Ahr+04] J. Ahrens et al., AMANDA Collaboration. "Muon Track Reconstruction and Data Selection Techniques in AMANDA." In: *Nuclear Instruments and Methods in Physics Research Section A* 524 (2004), pp. 169–194. DOI: 10.1016/j.nima.2004.01.065. arXiv: astro-ph/0407044.

[Aie+20] S. Aiello et al., KM3NeT Collaboration. "gSeaGen: The KM3NeT GENIE-based code for neutrino telescopes." In: *Computer Physics Communications* 256 (2020), p. 107477. DOI: 10.1016/j.cpc.2020.107477. arXiv: 2003.14040.

[AKM21] C. A. Argüelles Delgado, K. J. Kelly, and V. M. Muñoz-Albornoz. *Millicharged Particles from the Heavens: Single- and Multiple-Scattering Signatures*. FERMILAB-PUB-21-214-T. 2021. arXiv: 2104.13924.

[AL97] H. Abramowicz and A. Levy. *The ALLM Parametrization of $\sigma_{\text{tot}}(\gamma^* p)$ - An Update*. 1997. arXiv: hep-ph/9712415.

[Ala+20] J.-M. Alameddine et al. "PROPOSAL: A library to propagate leptons and high energy photons." In: *Journal of Physics: Conference Series* 1690 (2020): *Proceedings of the 5th International Conference on Particle Physics and Astrophysics (ICPPA 2020), Moscow*, p. 012021. DOI: 10.1088/1742-6596/1690/1/012021.

[Ala+21a] J.-M. Alameddine et al. "Electromagnetic Shower Simulation for CORSIKA 8." In: Proceedings of the 37th International Conference on Cosmic Rays (ICRC 2021). 102281. Berlin, Germany, 2021.

[Ala+21b] J.-M. Alameddine et al. *tudo-astroparticlephysics/PROPOSAL: Zenodo*. 2021. DOI: 10.5281/zenodo.1484180.

[Ala20] J.-M. Alameddine. "Simulation of rare processes and electromagnetic shower components within the Monte Carlo propagation library PROPOSAL." Master's thesis. TU Dortmund, 2020.

[Alb+21] J. Albrecht et al. *The Muon Puzzle in cosmic-ray induced air showers and its connection to the Large Hadron Collider*. 2021. arXiv: 2105.06148.

[Ale+16] J. Aleksić et al., MAGIC Collaboration. "The major upgrade of the MAGIC telescopes, Part II: A performance study using observations of the Crab Nebula." In: *Astroparticle Physics* 72 (2016), pp. 76–94. DOI: 10.1016/j.astropartphys.2015.02.005. arXiv: 1409.5594.

[Alf+17] R. Alfaro et al., HAWC Collaboration. "All-particle cosmic ray energy spectrum measured by the HAWC experiment from 10 to 500 TeV." In: *Physical Review D* 96 (2017), p. 122001. DOI: 10.1103/PhysRevD.96.122001. arXiv: 1710.00890.

[Ali+09] G. Alimonti et al., BOREXINO Collaboration. "The Borexino detector at the Laboratori Nazionali del Gran Sasso." In: *Nuclear Instruments and Methods in Physics Research Section A* 600 (2009), pp. 568–593. DOI: 10.1016/j.nima.2008.11.076. arXiv: 0806.2400.

[All+06] J. Allison et al. "Geant4 developments and applications." In: *IEEE Transactions on Nuclear Science* 53 (2006), pp. 270–278. DOI: 10.1109/TNS.2006.869826.

[All+16] J. Allison et al. "Recent developments in Geant4." In: *Nuclear Instruments and Methods in Physics Research* 835 (2016), pp. 186–225. DOI: 10.1016/j.nima.2016.06.125.

[Ama+01] P. Amaral et al., ATLAS TileCal Collaboration. "A precise measurement of 180 GeV muon energy losses in iron." In: *European Physical Journal C* 20 (2001), pp. 487–495. DOI: 10.1007/s100520100645.

[Amo+19] C. Amole et al., PICO Collaboration. "Dark Matter Search Results from the Complete Exposure of the PICO-60 C_3F_8 Bubble Chamber." In: *Physical Review D* 100 (2019), p. 022001. DOI: 10.1103/PhysRevD.100.022001. arXiv: 1902.04031.

[AN36] C. D. Anderson and S. H. Neddermeyer. "Cloud Chamber Observations of Cosmic Rays at 4300 Meters Elevation and Near Sea-Level." In: *Physical Review* 50 (1936), pp. 263–271. DOI: 10.1103/PhysRev.50.263.

[And+10] C. V. Andreopoulos et al. "The GENIE neutrino Monte Carlo generator." In: *Nuclear Instruments and Methods in Physics Research Section A* 614 (2010), pp. 87–104. DOI: 10.1016/j.nima.2009.12.009. arXiv: 0905.2517.

[And+21] M. R. Anderson et al., SNO+ Collaboration. "Development, characterisation, and deployment of the SNO+ liquid scintillator." In: *Journal of Instrumentation* 16 (2021), P05009. DOI: 10.1088/1748-0221/16/05/P05009. arXiv: 2011.12924.

[Ant+97] P. Antonioli et al. "A three-dimensional code for muon propagation through the rock: MUSIC." In: *Astroparticle Physics* 7 (1997), pp. 357–368. DOI: 10.1016/S0927-6505(97)00035-2. arXiv: hep-ph/9705408.

[Ash+20] T. Ashton et al., HESS Collaboration. "A NECTAr-based upgrade for the Cherenkov cameras of the H.E.S.S. 12-meter telescopes." In: *Astroparticle Physics* 118 (2020), p. 102425. DOI: 10.1016/j.astropartphys.2019.102425. arXiv: 2001.04510.

[Ask57] G. A. Askar'yan. "Hydrodynamic radiation from the tracks of ionizing particles in stable liquids." In: *The Soviet Journal of Atomic Energy* 3 (1957), pp. 921–923. DOI: 10.1007/BF01480076.

[Ask62] G. A. Askar'yan. "Excess Negative Charge of an Electron-Photon Shower and its Coherent Radio Emission." In: *Journal of Experimental and Theoretical Physics* 14 (1962), pp. 441–443.

[Avr+19] A. D. Avrorin et al., Baikal-GVD Collaboration. "Neutrino Telescope in Lake Baikal: Present and Future." In: *Proceedings of Science* 358.1011 (2019): *Proceedings of the 36th International Cosmic Ray Conference (ICRC 2019), Madison*. DOI: 10.22323/1.358.1011. arXiv: 1908.05427.

[Bai+19] X. Bai et al., LHAASO Collaboration. *The Large High Altitude Air Shower Observatory (LHAASO) Science White Paper*. 2019. arXiv: 1905.02773.

[Bar+06] G. D. Barr et al. "Uncertainties in Atmospheric Neutrino Fluxes." In: *Physical Review D* 74 (2006), p. 094009. DOI: 10.1103/PhysRevD.74.094009. arXiv: astro-ph/0611266.

[Bar+14] V. Barger et al. "Glashow resonance as a window into cosmic neutrino sources." In: *Physical Review D* 90 (2014), p. 121301. DOI: 10.1103/PhysRevD.90.121301. arXiv: 1407.3255.

[BB80] L. B. Bezrukov and E. V. Bugaev. "Inelastic muon-nucleon scattering in the diffraction region." In: *Soviet Journal of Nuclear Physics* 32 (1980), pp. 847–852.

[BB81] L. B. Bezrukov and E. V. Bugaev. "Nucleon shadowing effects in photonuclear interactions." In: *Soviet Journal of Nuclear Physics* 33 (1981), pp. 635–641.

[BDG20] L. Bonechi, R. D'Alessandro, and A. Giammanco. "Atmospheric muons as an imaging tool." In: *Reviews in Physics* 5 (2020), p. 100038. DOI: 10.1016/j.revip.2020.100038. arXiv: 1906.03934.

[BDH14] M. M. Block, L. Durand, and P. Ha. "Connection of the virtual $\gamma^* p$ cross section of ep deep inelastic scattering to real γp scattering, and the implications for νN and ep total cross sections." In: *Physical Review D* 89 (2014), p. 094027. DOI: 10.1103/PhysRevD.89.094027. arXiv: 1404.4530.

[Bec+06] Y. Becherini et al. "A Parameterisation of single and multiple muons in the deep water or ice." In: *Astroparticle Physics* 25 (2006), pp. 1–13. DOI: 10.1016/j.astropartphys.2005.10.005. arXiv: hep-ph/0507228.

[Bel+97] I. A. Belolaptikov et al., BAIKAL Collaboration. "The Baikal underwater neutrino telescope: Design, performance, and first results." In: *Astroparticle Physics* 7 (1997), pp. 263–282. DOI: 10.1016/S0927-6505(97)00022-4.

[Ber+07] T. Bergmann et al. "One-dimensional Hybrid Approach to Extensive Air Shower Simulation." In: *Astroparticle Physics* 26 (2007), pp. 420–432. DOI: 10.1016/j.astropartphys.2006.08.005. arXiv: astro-ph/0606564.

[Ber+93] M. J. Berger et al. "ICRU Report 49: Stopping Powers and Ranges for Protons and Alpha Particles." In: *Journal of the International Commission on Radiation Units and Measurements* os-25.2 (1993). DOI: 10.1093/jicru_os25.2.1.

[Bet30] H. A. Bethe. "Zur Theorie des Durchgangs schneller Korpuskularstrahlen durch Materie." In: *Annalen der Physik* 397 (1930), pp. 325–400. DOI: 10.1002/andp.19303970303.

[Bet34] H. A. Bethe. "The influence of screening on the creation and stopping of electrons." In: *Mathematical Proceedings of the Cambridge Philosophical Society* 30.4 (1934), pp. 524–539. DOI: 10.1017/S0305004100012779.

[BF52] L. M. Brown and R. P. Feynman. "Radiative Corrections to Compton Scattering." In: *Physical Review* 85 (1952), pp. 231–244. DOI: 10.1103/PhysRev.85.231.

[BH34a] H. A. Bethe and W. H. Heitler. "On the Stopping of Fast Particles and on the Creation of Positive Electrons." In: *Proceedings of the Royal Society of London A* 146.856 (1934), pp. 83–112. DOI: 10.1098/rspa.1934.0140.

[BH34b] H. A. Bethe and W. H. Heitler. "On the Stopping of Fast Particles and on the Creation of Positive Electrons." In: *Proceedings of the Royal Society of London A* 146.856 (1934), pp. 83–112. DOI: 10.1098/rspa.1934.0140.

[Bha36] H. J. Bhabha. "The scattering of positrons by electrons with exchange on Dirac's theory of the positron." In: *Proceedings of the Royal Sociaty A* 154 (1936), pp. 195–206. DOI: 10.1098/rspa.1936.0046.

[Bie+17] D. Biehl et al. "Astrophysical Neutrino Production Diagnostics with the Glashow Resonance." In: *Journal of Cosmology and Astroparticle Physics* 1701 (2017), p. 033. DOI: 10.1088/1475-7516/2017/01/033. arXiv: 1611.07983.

[Bie+94] A. F. Bielajew et al. *History, overview and recent improvements of EGS4*. Tech. rep. SLAC-PUB-6944, KEK-Report-94-4. Stanford Linear Accelerator Center, 1994.

[BM02] A. V. Butkevich and S. P. Mikheyev. "Cross Section of the Muon-Nuclear Inelastic Interaction." In: *Journal of Experimental and Theoretical Physics* 95 (2002), pp. 11–25. DOI: 10.1134/1.1499897. arXiv: hep-ph/0109060.

[BM54] H. A. Bethe and L. C. Maximon. "Theory of Bremsstrahlung and Pair Production. I. Differential Cross Section." In: *Physical Review* 93 (1954), pp. 768–784. DOI: 10.1103/PhysRev.93.768.

[Bog18] A. G. Bogdanov, NEVOD Collaboration. "Investigation of very high energy cosmic rays by means of inclined muon bundles." In: *Astrophysical Physics* 98 (2018), pp. 13–20. DOI: 10.1016/j.astropartphys.2018.01.003.

[Bol21] L. Bollmann. "Validation of simulated electromagnetic air showers in CORSIKA 8." Bachelor thesis. TU Dortmund, 2021.

[Bor+03] K. N. Borozdin et al. "Radiographic imaging with cosmic-ray muons." In: *Nature* 422 (2003), p. 277. DOI: 10.1038/422277a.

[Bot16] O. Bottner. *Neutrino Astronomy*. Presented at the 2nd MERCUR Winter School on Plasma-Astroparticle Physics. Bad Honnef, Germany, 2016.

[BP75] V. V. Borog and A. A. Petrukhin. "The cross-section of the nuclear interaction of high energy muons." In: *Proceedings of the 14th International Conference on Cosmic Rays* 6 (1975), pp. 1949–1954.

[Bre+99] J. Breitweg et al., ZEUS Collaboration. "ZEUS results on the measurement and phenomenology of F_2 at low x and low Q^2." In: *The European Physical Journal C* 7 (1999), pp. 609–630. DOI: 10.1007/s100529901084.

[BS03] E. V. Bugaev and Y. V. Shlepin. "Photonuclear interaction of high energy muons and tau leptons." In: *Physical Review D* 67 (2003), p. 034027. DOI: 10.1103/PhysRevD.67.034027. arXiv: hep-ph/0203096. E. V. Bugaev et al. "Propagation of τ-neutrinos and τ-leptons through the Earth and their detection in underwater/ice neutrino telescopes." In: *Astroparticle Physics* 21 (2004), pp. 491–509. DOI: 10.1016/j.astropartphys.2004.03.002. arXiv: hep-ph/0312295.

[BS64] M. J. Berger and S. Seltzer. *Tables of energy losses and ranges of electrons and positrons*. Tech. rep. NASA Special Publication 3012. National Aeronautics and Space Administration, 1964. URL: https://ntrs.nasa.gov/citations/19650002905.

[BSK00] E. V. Bugaev, I. A. Sokalski, and S. I. Klimushinm. *Simulation accuracy of long range muon propagation in medium: analysis of error sources.* 2000. arXiv: hep-ph/0010323.

[Bug+04] E. V. Bugaev et al. "Propagation of τ-neutrinos and τ-leptons through the Earth and their detection in underwater/ice neutrino telescopes." In: *Astroparticle Physics* 21 (2004), pp. 491–509. DOI: 10.1016/j.astropartphys.2004.03.002. arXiv: hep-ph/0312295.

[Bug77] E. V. Bugaev. "Effect of target recoil and excitation in bremsstrahlung and pair production processes." In: *Soviet Physics - Journal of Experimental and Theoretical Physics* 45 (1977), pp. 12–16.

[Cal+79] D. O. Caldwell et al. "Measurement of Shadowing in Photon-Nucleus Total Cross Sections from 20 to 185 GeV." In: *Physical Review Letters* 42 (1979), pp. 553–556. DOI: 10.1103/PhysRevLett.42.553.

[Cao+19] D.-W. Cao et al., JUNO Collaboration. "Light Absorption Properties of the High Quality Linear Alkylbenzene for the JUNO Experiment." In: *Nuclear Instruments and Methods in Physics Research Section A* 927 (2019), pp. 230–235. DOI: 10.1016/j.nima.2019.01.077. arXiv: 1801.08363.

[Cas19] A. Castellina, Pierre Auger Collaboration. "AugerPrime: the Pierre Auger Observatory Upgrade." In: *EPJ Web of Conferences* 210 (2019): *Proceedings of the 5th international symposium on Ultra High Energy Cosmic Rays (UHECR 2018) , Paris*, p. 06002. DOI: 10.1051/epjconf/201921006002. arXiv: 1905.04472.

[Che34] P. A. Cherenkov. "Visible emission of clean liquids by action of γ radiation." In: *Doklady Akademii Nauk SSSR* 2 (1934). in Russian, pp. 451–454.

[Chi03] D. A. Chirkin. "Cosmic Ray Energy Spectrum Measurement with the Antarctic Muon and Neutrino Detector Array (AMANDA)." PhD thesis. University of California at Berkeley, 2003.

[Chr+18] M. Chrzaszcz et al. "TAUOLA of tau lepton decays - framework for hadronic currents, matrix elements and anomalous decays." In: *Computer Physics Communications* 232 (2018), pp. 220–236. DOI: 10.1016/j.cpc.2018.05.017. arXiv: 1609.04617.

[CMS09] G. Carminati, A. Margiotta, and M. Spurio. "MUons from PArametric formulas: A fast GEnerator of atmospheric muonbundles for neutrino telescopes (MUPAGE)." In: *Nuclear Instruments and Methods in Physics Research Section A* 602 (2009), pp. 95–97. DOI: 10.1016/j.nima.2008.12.026.

[CMS11] A. Cooper-Sarkar, P. Mertsch, and S. Sarkar. "The high energy neutrino cross-section in the Standard Model and its uncertainty." In: *Journal of High Energy Physics* 08 (2011), p. 042. DOI: 10.1007/JHEP08(2011)042. arXiv: 1106.3723.

[Coo10] A. Cooper-Sarkar, H1 and ZEUS Collaboration. "Proton Structure from HERA to LHC." In: Proceedings, 40th International Symposium on Multiparticle Dynamics (ISMD 2010). Antwerp, Belgium, 2010, pp. 277–284. arXiv: 1012.1438. URL: https://www.desy.de/h1zeus/combined_results/herapdftable/.

[Cos19] C. O. da Costa-Luis. "'tqdm': A Fast, Extensible Progress Meter for Python and CLI." In: *Journal of Open Source Software* 4 (2019), p. 1277. DOI: 10.21105/joss.01277.

[CR04] D. A. Chirkin and W. Rhode. *Propagating leptons through matter with Muon Monte Carlo (MMC)*. 2004. arXiv: hep-ph/0407075.

[Dau+95] K. Daum et al., Fréjus Collaboration. "Determination of the atmospheric neutrino spectra with the Fréjus detector." In: *Zeitschrift für Physik C* 66 (1995), pp. 417–428. DOI: 10.1007/BF01556368.

[Dav+12] N. Davidson et al. "Universal interface of TAUOLA: Technical and physics documentation." In: *Computer Physics Communications* 183 (2012), pp. 821–843. DOI: 10.1016/j.cpc.2011.12.009. arXiv: 1002.0543.

[DBM54] H. Davis, H. A. Bethe, and L. C. Maximon. "Theory of Bremsstrahlung and Pair Production. II. Integral Cross Section for Pair Production." In: *Physical Review* 93 (1954), pp. 788–795. DOI: 10.1103/PhysRev.93.788.

[Dem+18] H. P. Dembinski et al. "Data-driven model of the cosmic-ray flux and mass composition from 10 GeV to 10^{11} GeV." In: *Proceedings of Science* 301.533 (2018): *Proceedings of the 35th International Cosmic Ray Conference (ICRC 2017), Busan*. DOI: 10.22323/1.301.0533. arXiv: 1711.11432.

[Dem+19] H. P. Dembinski et al. "Report on Tests and Measurements of Hadronic Interaction Properties with Air Showers." In: *EPJ Web of Conferences* 210 (2019): *Proceedings of the 5th Conference on Ultra High Energy Cosmic Rays (UHECR 2018), Paris*, p. 02004. DOI: 10.1051/epjconf/201921002004. arXiv: 1902.08124.

[Des06] P. Desiati, IceCube Collaboration. "IceCube: Toward a km^3 Neutrino Telescope." In: Proceedings of the 20th European Cosmic Ray Symposium (ECRS 2006), Lisbon. 2006. arXiv: astro-ph/0611603.

[DGR13] A. De Angelis, G. Galanti, and M. Roncadelli. "Transparency of the Universe to gamma rays." In: *Monthly Notices of the Royal Astronomical Society* 432 (2013), pp. 3245–3249. DOI: 10.1093/mnras/stt684. arXiv: 1302.6460.

[DR01] P. Desiati and W. Rhode. "Analysis of atmospheric muons with AMANDA." In: Proceedings of the 27th International Conference on Cosmic Rays (ICRC 2001). Vol. 3. Hamburg, Germany, 2001, pp. 985–988.

[Dun+19] M. Dunsch et al. "Recent improvements for the lepton propagator PROPOSAL." In: *Computer Physics Communication* 242 (2019), pp. 132–144. DOI: 10.1016/j.cpc.2019.03.021. arXiv: 1809.07740.

[Dun18] M. Dunsch. "Make PROPOSAL great again." Master's thesis. TU Dortmund, 2018.

[Dut+01] S. I. Dutta et al. "Propagation of Muons and Taus at High Energies." In: *Physical Review D* 63 (2001), p. 094020. DOI: 10.1103/PhysRevD.63.094020. arXiv: hep-ph/0012350.

[EHP11] R. Engel, D. Heck, and T. Pierog. "Extensive Air Showers and Hadronic Interactions at High Energy." In: *Annual Review of Nuclear and Particle Science* 61 (2011), pp. 467–489. DOI: 10.1146/annurev.nucl.012809.104544.

[Eng+19] R. Engel et al. "Towards A Next Generation of CORSIKA: A Framework for the Simulation of Particle Cascades in Astroparticle Physics." In: *Computing and Software for Big Science* 3 (2019), pp. 1–12. DOI: 10.1007/s41781-018-0013-0.

[Fed+15] A. Fedynitch et al. "Calculation of conventional and prompt lepton fluxes at very high energy." In: *EPJ Web of Conferences* 99 (2015): *Proceedings of the 18th International Symposium on Very High Energy Cosmic Ray Interactions (ISVHECRI 2014), Geneva*, p. 08001. DOI: 10.1051/epjconf/20159908001. arXiv: 1503.00544.

[For+13] D. Foreman-Mackey et al. "emcee: The MCMC Hammer." In: *Publications of the Astronomical Society of the Pacific* 125 (2013), pp. 306–312. DOI: 10.1086/670067. arXiv: 1202.3665.

[Fra11] K. Frantzen. "Wirkungsquerschnitte in PROPOSAL - Beschreibung alter und Implementierung neuer Parametrisierungen." Diploma thesis. TU Dortmund, 2011.

[Fra20] Y. N. Franz. "Untersuchung der Tauregeneration mit der Simulationsbibliothek PROPOSAL." Bachelor thesis. TU Dortmund, 2020.

[FT37] I. M. Frank and I. Y. Tamm. "Coherent Visible Radiation of Fast Electrons Passing through Matter." In: *Doklady Akademii Nauk SSSR* 14 (1937), pp. 107–113.

[Fuc12] T. Fuchs. "Leptonpropagation mit PROPOSAL unter Verwendung von Grafikprozessoren." Master's thesis. TU Dortmund, 2012.

[Fuc16a] T. Fuchs. "Charmante Myonen im Eis." PhD thesis. TU Dortmund, 2016. DOI: 10.17877/DE290R-17241.

[Fuc16b] T. Fuchs, IceCube Collaboration. "Development of a Machine Learning Based Analysis Chain for the Measurement of Atmospheric Muon Spectra with IceCube." In: Proceedings of the 25th European Cosmic Ray Symposium (ECRS 2016). Vol. 4. Turin, Italy, 2016. arXiv: 1701.04067.

[Fuk+98] Y. Fukuda et al., Super-Kamiokande Collaboration. "Evidence for oscillation of atmospheric neutrinos." In: *Physical Review Letters* 81 (1998), pp. 1562–1567. DOI: 10.1103/PhysRevLett.81.1562. arXiv: hep-ex/9807003.

[FWP21] A. Fedynitch, W. Woodley, and M.-C. Piro. *On the Accuracy of Underground Muon Intensity Calculations*. 2021. arXiv: 2109.11559.

[Gai16] T. K. Gaisser. "Cosmic-Ray Showers Reveal Muon Mystery." In: *Physics* 9 (2016), p. 125. DOI: 10.1103/Physics.9.125.

[GEA19] GEANT4, GEANT4 Collaboration. *GEANT4 Physics Reference Manual*. 10.6. 2019.

[Gei13] M. Geisel-Brinck. "Revision of the multiple scattering algorithms in PROPOSAL." Bachelor thesis. TU Dortmund, 2013.

[GER16] T. K. Gaisser, R. Engel, and E. Resconi. *Cosmic Rays and Particle Physics*. 2nd ed. Cambridge University Press, 2016. ISBN: 978-0-521-01646-9.

[GK05] A. Z. Gazizov and M. P. Kowalski. "ANIS: High energy neutrino generator for neutrino telescopes." In: *Computer Physics Communications* 172 (2005), pp. 203–213. DOI: 10.1016/j.cpc.2005.03.113. arXiv: astro-ph/0406439.

[Gla+20] C. Glaser et al. "NuRadioMC: Simulating the radio emission of neutrinos from interaction to detector." In: *European Physical Journal C* 80 (2020), p. 77. DOI: 10.1140/epjc/s10052-020-7612-8. arXiv: 1906.01670.

[Gla60] S. L. Glashow. "Resonant Scattering of Antineutrinos." In: *Physical Review* 118 (1960), pp. 316–317. DOI: 10.1103/PhysRev.118.316.

[GMS01] D. E. Groom, N. V. Mokhov, and S. I. Striganov. "Muon stopping power and range tables 10 MeV-100 TeV." In: *Atomic Data and Nuclear Tables* 78 (2001), pp. 183–356. DOI: 10.1006/adnd.2001.0861. URL: https://pdg.lbl.gov/AtomicNuclearProperties/.

[GNG20] D. García-Fernández, A. Nelles, and C. Glaser. "Signatures of secondary leptons in radio-neutrino detectors in ice." In: *Physical Review D* 102 (2020), p. 083011. DOI: 10.1103/PhysRevD.102.083011. arXiv: 2003.13442.

[Gre66] K. I. Greisen. "End to the Cosmic-Ray Spectrum?" In: *Physical Review Letters* 16 (1966), pp. 748–750. DOI: 10.1103/PhysRevLett.16.748.

[Gut21] P. T. Gutjahr. "Study of muon deflection angles in the TeV energy range with IceCube." Master's thesis. TU Dortmund, 2021.

[Har+20] C. R. Harris et al. "Array programming with NumPy." In: *Nature* 585 (2020), pp. 357–362. DOI: 10.1038/s41586-020-2649-2.

[Hec+98] D. Heck et al. *CORSIKA: A Monte Carlo Code to Simulate Extensive Air Showers*. Tech. rep. 6019. Forschungszentrum Karlsruhe, 1998.

[Hei54] W. Heitler. *The Quantum Theory of Radiation*. Dover Books on Physics and Chemistry. Dover Publications, 1954. ISBN: 9780486645582.

[Hes12] V. F. Hess. "Über Beobachtungen der durchdringenden Strahlung bei sieben Freiballonfahrten." In: *Physikalische Zeitschrift* 13 (1912), pp. 1084–1091.

[Hig75] V. L. Highland. "Some practical remarks on multiple scattering." In: *Nuclear Instruments and Methods* 129 (1975), pp. 497–499. DOI: 10.1016/0029-554X(75)90743-0. "Erratum - Some practical remarks on multiple scattering." In: *Nuclear Instruments and Methods* 161 (1979), p. 171. DOI: 10.1016/0029-554X(79)90379-3.

[Hir+05] H. Hirayama et al. *The EGS5 code system*. Tech. rep. SLAC-Report-730, KEK-Report-2005-8. Stanford Linear Accelerator Center, 2005. DOI: 10.2172/877459.

[HMS18] R. Hill, K. W. Masui, and D. Scott. "The Spectrum of the Universe." In: *Applied Spectroscopy* 72 (2018), pp. 663–688. DOI: 10.1177/0003702818767133. arXiv: 1802.03694.

[Hoi17] T. Hoinka. "Extraction and Analysis of Stopping Muons in IceCube Using Machine Learning." Master thesis. TU Dortmund, 2017.

[Hue17a] M. Huennefeld, IceCube Collaboration. "Deep Learning in Physics exemplified by the Reconstruction of Muon-Neutrino Events in IceCube." In: *Proceedings of Science* 301.1057 (2017): *Proceedings of the 35th International Cosmic Ray Conference (ICRC 2017), Busan*. DOI: 10.22323/1.301.1057.

[Hue17b] M. Huennefeld. "Online Reconstruction of Muon-Neutrino Events in IceCube using Deep Learning Techniques." Master thesis. TU Dortmund, 2017.

[Hue18] M. Huennefeld, IceCube Collaboration. "Reconstruction Techniques in IceCube using Convolutional and Generative Neural Networks." In: *EPJ Web of Conferences* 207.05005 (2018): *Proceedings of the 8th Very Large Volume Neutrino Telescop Workshop (VLVnT 2018), Dubna*. DOI: 10.1051/epjconf/201920705005.

[Hun07] J. D. Hunter. "Matplotlib: A 2D graphics environment." In: *Computing in Science & Engineering* 9 (2007), pp. 90–95. DOI: 10.1109/MCSE.2007.55.

[Ice20] IceCube, IceCube Collaboration/NSF. *IceCube Gallery*. 2020. URL: https://gallery.icecube.wisc.edu/.

[Iva+98a] D. Y. Ivanov et al. "Lepton pair production by high energy photon in a strong electromagnetic field." In: *Physical Review D* 57 (1998), pp. 4025–4034. DOI: 10.1103/PhysRevD.57.4025.

[Iva+98b] D. Y. Ivanov et al. "Production of e^+e^- pairs to all orders in Z for collisions of high-energy muons with heavy nuclei." In: *Physics Letters B* 442 (1998), pp. 453–458. DOI: 10.1016/S0370-2693(98)01278-7. arXiv: hep-ph/9807311.

[Jad+93] S. Jadach et al. "The τ decay library TAUOLA, version 2.4." In: *Computer Physics Communications* 76 (1993), pp. 361–380. DOI: 10.1016/0010-4655(93)90061-G.

[JKW91] S. Jadach, J. H. Kühn, and Z. Wa s. "TAUOLA - a library of Monte Carlo programs to simulate decays of polarized τ leptons." In: *Computer Physics Communications* 64 (1991), pp. 275–299. DOI: 10.1016/0010-4655(91)90038-M.

[Kei+13] B. Keilhauer et al. "Nitrogen fluorescence in air for observing extensive air showers." In: *EPJ Web of Conferences* 53 (2013): *Proceedings of the 2nd International Symposium on Future Directions in UHECR Physics (UHECR 2012), Geneva*, p. 01010. DOI: 10.1051/epjconf/20135301010. arXiv: 1210.1319.

[Kel67] S. R. Kelner. "Pair Production in Collisions Between a Fast Particle and a Nucleus." In: *Soviet Journal of Nuclear Physics* 5 (1967), pp. 778–783.

[Kel98] S. R. Kelner. "Pair Production in Collisions between Muons and Atomic Electrons." In: *Physics of Atomic Nuclei* 61 (1998), pp. 448–456.

[KF99] S. R. Kelner and A. Fedotov. "Diffractive Corrections to Bremsstrahlung from Muons." In: *Physics of Atomic Nuclei* 62 (1999), pp. 272–280.

[KK68] S. R. Kelner and Y. . Kotov. "Muon energy loss to pair production." In: 7 (1968), pp. 237–240. "Pair production by muons in the field of nuclei." In: *Canadian Journal of Physics* 46 (1968), pp. 387–390.

[KKP00] S. R. Kelner, R. P. Kokoulin, and A. A. Petrukhin. "Direct Production of Muon Pairs by High-Energy Muons." In: *Physics of Atomic Nuclei* 63 (2000), pp. 1603–1611. DOI: 10.1134/1.1312894.

[KKP95] S. R. Kelner, R. P. Kokoulin, and A. A. Petrukhin. "About cross section for high-energy muon bremsstrahlung." In: *Moscow:Preprint/MEPhI* 024-95 (1995).

[KKP97] S. R. Kelner, R. P. Kokoulin, and A. A. Petrukhin. "Bremsstrahlung from muons scattered by atomic electrons." In: *Physics of Atomic Nuclei* 60 (1997), pp. 576–583.

[KKP99] S. R. Kelner, R. P. Kokoulin, and A. A. Petrukhin. "Radiation logarithm in the Hartree-Fock model." In: *Physics of Atomic Nuclei* 62 (1999), pp. 1894–1898.

[KKS99] V. Kudryavtseva, E. Korolkovab, and N. Spoonera. "Narrow muon bundles from muon pair production in rock." In: *Physics Letters B* 471 (1999), pp. 251–256. DOI: 10.1016/S0370-2693(99)01378-7. arXiv: hep-ph/9911493.

[Kle99] S. Klein. "Suppression of Bremsstrahlung and Pair Production due to Environmental Factors." In: *Reviews of Modern Physics* 71 (1999), pp. 1501–1538. DOI: 10.1103/RevModPhys.71.1501.

[Köh+13] J.-H. Köhne et al. "PROPOSAL: A tool for propagation of charged leptons." In: *Computer Physics Communication* 184 (2013), pp. 2070–2090. DOI: 10.1016/j.cpc.2013.04.001.

[Köh13] J.-H. Köhne. "Der Leptonpropagator PROPOSAL." PhD thesis. TU Dortmund, 2013. DOI: 10.17877/DE290R-13191.

[Kok99] R. P. Kokoulin. "Uncertainties in underground muon flux calculations." In: *Nuclear Physics B (Proc. Suppl.)* 70 (1999), pp. 475–479. DOI: 10.1016/S0920-5632(98)00475-7.

[KP69] R. P. Kokoulin and A. A. Petrukhin. "Analysis of the cross-section of direct pair production by fast muons." In: Proceedings of the 11th International Conference on Cosmic Rays (ICCR 1969). Vol. 4. Budapest, Hungary, 1969, pp. 277–284.

[KP71] R. P. Kokoulin and A. A. Petrukhin. "Influence of the Nuclear Formfactor on the Cross-Section of Electron Pair Production by High Energy Muons." In: Proceedings of the 12th International Conference on Cosmic Rays (ICCR 1971). Vol. 4. Hobart, Australia, 1971, pp. 2436–2444.

[KP97] R. P. Kokoulin and A. A. Petrukhin. "Muon interactions and consequences in underground physics." In: *Frontier Objects in Astrophysics and Particle Physics* 57 (1997): *Proceedings of the 6th Vulcano Workshop (1996), Bologna*, pp. 379–393.

[Kra15] M. Krause. "High energy astroparticle physics for high school students." In: *Proceedings of Science* 236.304 (2015): *Proceedings of the 34th International Cosmic Ray Conference (ICRC 2015), Den Haag*. DOI: 10.22323/1.236.0304.

[KS12] U. F. Katz and C. Spiering. "High-energy neutrino astrophysics: Status and perspectives." In: *Progress in Particle and Nuclear Physics* 67 (2012), pp. 651–701. DOI: 10.1016/j.ppnp.2011.12.001. arXiv: 1111.0507.

[Kud09] V. Kudryavtsev. "Muon simulation codes MUSIC and MUSUN for underground physics." In: *Computer Physics Communications* 180 (2009), pp. 339–346. DOI: 10.1016/j.cpc.2008.10.013. arXiv: 0810.4635.

[Lah17] R. Lahmann. "Acoustic detection of high energy neutrinos in sea water: status and prospects." In: *EPJ Web of Conferences* 135.06001 (2017): *Proceedings of the 7th International Workshop on Acoustic and Radio EeV Neutrino Detection Activities (ARENA 2016), Groningen*. DOI: 10.1051/epjconf/201713506001.

[LD91] G. R. Lynch and O. I. Dahl. "Approximations to multiple Coulomb scattering." In: *Nuclear Instruments and Methods in Physics Research Section B* 58 (1991), pp. 6–10. DOI: 10.1016/0168-583X(91)95671-Y.

[LKV85] W. Lohmann, R. Kopp, and R. Voss. "Energy loss of muons in the energy range 1-10000 GeV." In: *CERN Yellow Reports* 85.3 (1985). DOI: 10.5170/CERN-1985-003.

[LP04] A. Lahiri and P. B. Pal. *A First Book of Quantum Field Theory*. 2nd ed. Narosa Publishing House, 2004.

[LP53a] L. D. Landau and I. J. Pomeranchuk. "Electron cascade process at very high-energies." In: *Doklady Akademii Nauk SSSR* 92 (1953). in Russian, pp. 735–738.

[LP53b] L. D. Landau and I. J. Pomeranchuk. "Limits of applicability of the theory of bremsstrahlung electrons and pair production at high-energies." In: *Doklady Akademii Nauk SSSR* 92 (1953). in Russian, pp. 535–536.

[LS91] P. Lipari and T. Stanev. "Propagation of multi-Tev muons." In: *Physical Review D* 44 (1991), pp. 3543–3554. DOI: 10.1103/PhysRevD.44.3543.

[Mar+15] Martín Abadi et al. *TensorFlow: Large-Scale Machine Learning on Heterogeneous Systems*. Software available from tensorflow.org. 2015.

[MDP19] A. M. Mitchell, H. P. Dembinski, and R. D. Parsons. "Potential for measuring the longitudinal and lateral profile of muons in TeV air showers with IACTs." In: *Astrophysical Journal* 111 (2019), pp. 23–34. DOI: 10.1016/j.astropartphys.2019.03.005. arXiv: 1903.12040.

[Mea01] D. F. Measday. "The nuclear physics of muon capture." In: *Physics Reports* 453 (2001), pp. 243–409. DOI: 10.1016/S0370-1573(01)00012-6.

[Men14] T. Menne. "Berechnung eines neuen Wirkungsquerschnitts für Myon-Proton-Bremsstrahlung." Master's thesis. TU Dortmund, 2014.

[MFH19] S. Meighen-Berger, A. Fedynitch, and M. Huber. *EmCa - Electromagnetic-Cascades Simulation Package*. To get access to the currently private repository ask the main author Stephan Meighen-Berger. 2019. arXiv: 1907.06924. URL: https://gitlab.com/stephan.meighenberger/emca.

[MH07] K. Martin and B. Hoffman. "An Open Source Approach to Developing Software in a Small Organization." In: *IEEE Software* 24 (2007), pp. 46–53. DOI: 10.1109/MS.2007.5.

[Mig56] A. B. Migdal. "Bremsstrahlung and Pair Production in Condensed Media at High Energies." In: *Physical Review* 103 (1956), pp. 1811–1820. DOI: 10.1103/PhysRev.103.1811.

[Mig57] A. B. Migdal. "Bremsstrahlung and Pair Production at High Energies in Condensed Media." In: *Soviet Physics - Journal of Experimental and Theoretical Physics* 5 (1957), pp. 527–536.

[ML19] S. Meighen-Berger and M. Li. "Atmospheric muons from electromagnetic cascades." In: *Proceedings of Science* 358.961 (2019): *Proceedings of the 36th International Cosmic Ray Conference (ICRC 2019), Madison*. DOI: 10.22323/1.358.0961. arXiv: 1910.05984.

[MO65] K. J. Mork and H. Olsen. "Radiative Corrections. I. High-Energy Bermsstahlung and Pair Production." In: *Physical Review* 140 (1965), B1661–B1674. DOI: 10.1103/PhysRev.140.B1661.

[Møl32] C. Møller. "Zur Theorie des Durchgangs schneller Elektronen durch Materie." In: *Annalen der Physik* 406 (1932), pp. 531–585. DOI: 10.1002/andp.19324060506.

[Mol47] G. Moliere. "Theorie der Streuung schneller geladener Teilchen I - Einzelstreuung am abgeschirmten Coulomb-Feld." In: *Zeitschrift für Naturforschung A* 2 (1947), pp. 133–145.

[Mol48] G. Moliere. "Theorie der Streuung schneller geladener Teilchen II - Mehrfach- und Vielfachstreuung." In: *Zeitschrift für Naturforschung A* 3 (1948), pp. 78–97.

[Mor+17] K. Morishima et al. "Discovery of a big void in Khufu's Pyramid by observation of cosmic-ray muons." In: *Nature* 552 (2017), pp. 386–390. DOI: 10.1038/nature24647. arXiv: 1711.01576.

[MRS99] A. D. Martin, M. G. Ryskin, and A. M. Stasto. "The Description of F_2 at low Q^2." In: *European Physics Journal C* 7 (1999), pp. 643–654. DOI: 10.1007/s100529801035. arXiv: hep-ph/9806212.

[MS19] M. Meier and J. Soedingrekso, IceCube Collaboration. "Search for Astrophysical Tau Neutrinos with an Improved Double Pulse Method." In: *Proceedings of Science* 358.960 (2019): *Proceedings of the 36th International Cosmic Ray Conference (ICRC 2019), Madison*. DOI: 10.22323/1.358.0960. arXiv: 1909.05127.

[MS85] S. P. Mikheyev and A. Y. Smirnov. "Resonance enhancement of oscillations in matter and solar neutrino spectroscopy." In: *Soviet Journal of Nuclear Physics* 42 (1985), pp. 913–917.

[Nel+94] W. R. Nelson et al. *EGS4 in 94 - A Decade of Enhancements*. Tech. rep. SLAC-Report-6625. Stanford Linear Accelerator Center, 1994.

[Nie+18] V. Niess et al. "Backward Monte-Carlo applied to muon transport." In: *Computer Physics Communications* 229 (2018), pp. 54–67. DOI: 10.1016/j.cpc.2018.04.001. arXiv: 1705.05636.

[Nin19] S. Ninfa. "Reconstruction of the cosmic-ray spectrum based on stopping muons in IceCube." Master thesis. TU Dortmund, 2019.

[Ost11] S. Ostapchenko. "Monte Carlo treatment of hadronic interactions in enhanced Pomeron scheme: I. QGSJET-II model." In: *Physical Review D* 83 (2011), p. 014018. DOI: 10.1103/PhysRevD.83.014018. arXiv: 1010.1869.

[Pan+09] S. Panknin et al. "Muon Production of Hadronic Particle Showers in Ice and Water." In: Proceedings of the 31st International Cosmic Ray Conference. Łódź, Poland, 2009.

[Pas19] B. Pastirčák. "CORSIKA Based Simulations of Background in Baikal Experiment." In: *EPJ Web of Conferences* 226 (2019): *Proceedings of the 12th International Conference Mathematical Modeling and Computational Physics (MMCP 2019), Stara Lesna, Slovakia*, p. 03015. DOI: 10.1051/epjconf/202022603015.

[Pet15] A. A. Petrukhin, NEVOD Collaboration. "Cherenkov water detector NEVOD." In: *Physics-Uspekhi* 58 (2015), pp. 486–494. DOI: 10.3367/UFNe.0185.201505i.0521.

[PG07] F. Pérez and B. E. Granger. "IPython: a System for Interactive Scientific Computing." In: *Computing in Science and Engineering* 9 (2007), pp. 21–29. DOI: 10.1109/MCSE.2007.53.

[Ple+20] R. Plestid et al. "New Constraints on Millicharged Particles from Cosmic-ray Production." In: *Physical Review D* 102 (2020), p. 115032. DOI: 10.1103/PhysRevD.102.115032. arXiv: 2002.11732.

[Pol+01] S. Polityko et al. "The bremsstrahlung of muons at extremely high energies with LPM and dielectric suppression effect." In: *Nuclear Instruments and Methods in Physics Research Section B* 173 (2001), pp. 30–36. DOI: 10.1016/S0168-583X(00)00114-2. arXiv: hep-ph/9911330.

[Pol+02] S. Polityko et al. "Muon Cross-Section with both the LPM Effect and the Ter-Mikayelyan Effekt at Extremely High Energies." In: *Journal of Physics G: Nuclear and Particle Physics* 28 (2002), pp. 427–449. DOI: 10.1088/0954-3899/28/3/306.

[PP19] A. Pollmann and S. Pieper, IceCube Collaboration. "Enabling a new detection channel for beyond standard model physics with in-situ measurements of ice luminescence." In: *Proceedings of Science* 358.983 (2019): *Proceedings of the 36th International Cosmic Ray Conference (ICRC 2019), Madison*. DOI: 10.22323/1.358.0983. arXiv: 1908.07231.

[PS68] A. A. Petrukhin and V. V. Shestakov. "The influence of nuclear and atomic form factors on the muon bremsstrahlung cross section." In: *Canadian Journal of Physics* 46 (1968), pp. 377–380.

[Rho93] W. Rhode. "Untersuchung der Energiespektren hochenergetischer Muonen im Frejusdetektor." PhD thesis. Bergische Universität Wuppertal, 1993.

[Rie+20] F. Riehn et al. "Hadronic interaction model Sibyll 2.3d and extensive air showers." In: *Physical Review D* 102 (2020), p. 063002. DOI: 10.1103/PhysRevD.102.063002. arXiv: 1912.03300.

[Ron19] M. Rongen. "Calibration of the IceCube Neutrino Observatory." PhD thesis. RWTH Aachen, 2019. DOI: 10.18154/RWTH-2019-09941. arXiv: 1911.02016.

[Ros52] B. B. Rossi. *High Energy Particles*. Prentice-Hall, Inc., 1952. ISBN: 978-0133873245.

[Sac21] M. Sackel. "First electromagnetic interaction model in CORSIKA8 using the Monte Carlo simulation tool PROPOSAL." Master's thesis. TU Dortmund, 2021.

[Sak+92] W. K. Sakumoto et al. "A Measurement of TeV muon energy loss in iron." In: *Physical Review D* 45 (1992), p. 3042. DOI: 10.1103/PhysRevD.45.3042.

[San14] A. Sandrock. "Einschleifenkorrekturen zur Bremsstrahlung von Myonen im Feld eines Atomkerns." Master's thesis. TU Dortmund, 2014.

[San18] A. Sandrock. "Higher-order corrections to the energy loss cross sections of high-energy muons." PhD thesis. TU Dortmund, 2018. DOI: 10.17877/DE290R-19810.

[SBK01] I. A. Sokalski, E. V. Bugaev, and S. I. Klimushinm. "MUM: Flexible precise Monte Carlo algorithm for muon propagation through thick layers of matter." In: *Physical Review D* 64 (2001), p. 074015. DOI: 10.1103/PhysRevD.64.074015. arXiv: hep-ph/0010322.

[Sch+21] A. Schneider et al. *Closing the Neutrino "BSM Gap": Physics Potential of Atmospheric Through-Going Muons at DUNE*. 2021. arXiv: 2106.01508.

[Sch11] M. Schmitz. "Präzisionsbetrachtung, Test und Erweiterungen für das auf Monte-Carlo Methoden basierende Leptonpropagationsprogramm PROPOSAL." Diploma thesis. TU Dortmund, 2011.

[Sch19] H. Schoorlemmer, SWGO Collaboration. "A next-generation ground-based wide field-of-view gamma-ray observatory in the southern hemisphere." In: *Proceedings of Science* 358.785 (2019): *Proceedings of the 36th International Cosmic Ray Conference (ICRC 2019), Madison*. DOI: 10.22323/1.358.0785. arXiv: 1908.08858.

[Sci19] S. J. Sciutto. *AIRES - A system for air shower simulations*. Version 19.04.00. 2019. DOI: 10.13140/RG.2.2.12566.40002. arXiv: astro-ph/9911331.

[SKP20] A. Sandrock, R. P. Kokoulin, and A. A. Petrukhin. "Theoretical uncertainties of muon transport calculations for very large volume neutrino telescopes." In: *Journal of Physics: Conference Series* 1690 (2020): *Proceedings of the 5th International Conference on Particle Physics and Astrophysics (ICPPA 2020), Moscow*, p. 012005. DOI: 10.1088/1742-6596/1690/1/012005.

[SKR18] A. Sandrock, S. R. Kelner, and W. Rhode. "Radiative corrections to the average bremsstrahlung energy loss of high-energy muons." In: *Physics Letters B* 776 (2018), pp. 350–354. DOI: 10.1016/j.physletb.2017.11.047. arXiv: 1706.07242.

[Soe+20] J. Soedingrekso et al. "Feasibility study to measure the muon bremsstrahlung cross section with the energy loss profile using neutrino telescopes." In: *Journal of Physics: Conference Series* 1690 (2020): *Proceedings of the 5th International Conference on Particle Physics and Astrophysics (ICPPA 2020), Moscow*, p. 012020. DOI: 10.1088/1742-6596/1690/1/012020.

[Soe16] J. Soedingrekso. "Korrekturen zum Paarproduktions-Wirkungsquerschnitt." Master's thesis. TU Dortmund, 2016.

[SR18] A. Sandrock and W. Rhode. *Coulomb corrections to the bremsstrahlung and electron pair production cross section of high-energy muons on extended nuclei*. 2018. arXiv: 1807.08475.

[SSR19] J. Soedingrekso, A. Sandrock, and W. Rhode. "The effect of improved high-energy muon cross-sections." In: *Proceedings of Science* 358.429 (2019): *Proceedings of the 36th International Cosmic Ray Conference (ICRC 2019), Madison*. DOI: 10.22323/1.358.0429. arXiv: 1910.07050.

[Sta+16] D. Staszak et al., VERITAS Collaboration. "Science Highlights from VERITAS." In: *Proceedings of Science* 236.868 (2016): *Proceedings of the 34th International Cosmic Ray Conference (ICRC 2015), The Hague*. DOI: 10.22323/1.236.0868. arXiv: 1510.01269.

[Sta+82] T. Stanev et al. "Development of ultrahigh-energy electromagnetic cascades in water and lead including the Landau-Pomeranchuk-Migdal effect." In: *Physical Review D* 25 (1982), pp. 1291–1304. DOI: 10.1103/PhysRevD.25.1291.

[Ste17] A. K. Steuer, IceCube Collaboration. "Delayed light emission to distinguish astrophysical neutrino flavors in IceCube." In: *Proceedings of Science* 301.1008 (2017): *Proceedings of the 35th International Cosmic Ray Conference (ICRC 2017), Busan*. DOI: 10.22323/1.301.1008.

[Ste19] J. Stettner, IceCube Collaboration. "Measurement of the diffuse astrophysical muon-neutrino spectrum with ten years of IceCube data." In: *Proceedings of Science* 358.1017 (2019): *Proceedings of the 36th International Cosmic Ray Conference (ICRC 2019), Madison*. DOI: 10.22323/1.358.1017. arXiv: 1908.09551.

[Ste52] R. M. Sternheimer. "The Density Effect for the Ionization Loss in Various Materials." In: *Physical Review* 88 (1952), pp. 851–859. DOI: 10.1103/PhysRev.88.851. "Erratum: The Density Effect for the Ionization Loss in Various Materials." In: *Physical Review* 89 (1953), p. 1309. DOI: 10.1103/PhysRev.89.1309.2.

[Tan+09] H. K. M. Tanaka et al. "Detecting a mass change inside a volcano by cosmic-ray muon radiography (muography): First results from measurements at Asama volcano, Japan." In: *Geophysical Research Letters* 36 (2009), p. L17302. DOI: 10.1029/2009GL039448.

[Ter54] M. L. Ter-Mikaelian. In: *Doklady Akademii Nauk SSSR* 94 (1954), p. 1033. Discussed in English in *High-energy electromagnetic processes in condensed media*. John Wiley & Sons, Inc., 1972. ISBN: 978-0471851905.

[Ter60] F. F. Ternovskii. "Effect of Multiple Scattering on Pair Production by High-Energy Particles in a Medium." In: *Journal of Experimental and Theoretical Physics* 10 (1960), pp. 718–722.

[Tok+12] H. Tokuno et al., Telescope Array Collaboration. "New air fluorescence detectors employed in the Telescope Array experiment." In: *Nuclear Instruments and Methods in Physics Research Section A* 676 (2012), pp. 54–65. DOI: 10.1016/j.nima.2012.02.044. arXiv: 1201.0002.

[Tsa74] Y.-S. Tsai. "Pair production and bremsstrahlung of charged leptons." In: *Review of Modern Physics* 46 (1974), pp. 815–851. DOI: 10.1103/RevModPhys.46.815. "Erratum: Pair production and bremsstrahlung of charged leptons." In: *Review of Modern Physics* 49 (1977), pp. 421–423. DOI: 10.1103/RevModPhys.49.421.

[Usm+15] S. M. Usman et al. "AGM2015: Antineutrino Global Map 2015." In: *Nature Scientific Reports* 5 (2015), p. 13945. DOI: 10.1038/srep13945. arXiv: 1509.03898.

[Van86] A. Van Ginneken. "Energy loss and angular characteristics of high energy electromagnetic processes." In: *Nuclear Instruments and Methods in Physics Research Section A* 152 (1986), pp. 21–39. DOI: 10.1016/0168-9002(86)91146-0.

[VD09] G. Van Rossum and F. L. Drake. *Python 3 Reference Manual*. Scotts Valley, CA: CreateSpace, 2009. ISBN: 1441412697.

[Ver00] J. A. M. Vermaseren. *New features of FORM*. 2000. arXiv: `math-ph/0010025`.

[Vir+20] P. Virtanen et al. "SciPy 1.0: Fundamental Algorithms for Scientific Computing in Python." In: *Nature Methods* 17 (2020), pp. 261–272. DOI: `10.1038/s41592-019-0686-2`.

[VTR20] E. Vitagliano, I. Tamborra, and G. Raffelt. "Grand Unified Neutrino Spectrum at Earth: Sources and Spectral Components." In: *Reviews of Modern Physics* 92 (2020), p. 045006. DOI: `10.1103/RevModPhys.92.045006`. arXiv: `1910.11878`.

[Wer17] J. Werthebach. "Analyse hochenergetischer atmosphärischer Myonen mit IC86-II Daten des IceCube-Detektors." Master thesis. TU Dortmund, 2017.

[Wol78] L. Wolfenstein. "Neutrino oscillations in matter." In: *Physical Review D* 17 (1978), pp. 2369–2374. DOI: `10.1103/PhysRevD.17.2369`.

[ZHS92] E. Zas, F. Halzen, and T. Stanev. "Electromagnetic pulses from high-energy showers: Implications for neutrino detection." In: *Physical Review D* 45 (1992), pp. 362–376. DOI: `10.1103/PhysRevD.45.362`.

[ZK66] G. T. Zatsepin and V. A. Kuz'min. "Upper Limit of the Spectrum of Cosmic Rays." In: *Journal of Experimental and Theoretical Physics Letters* 4 (1966), pp. 78–80.

[Zyl+20] P. A. Zyla et al., Particle Data Group. "Review of Particle Physics." In: *Progress of Theoretical and Experimental Physics* (2020), p. 083C01. DOI: `10.1093/ptep/ptaa104`.

Acknowledgments

At first, I want to thank my advisor Prof. Rhode from whom I have learned many things since I started my Bachelor thesis at his chair in 2014. He gave me the opportunity to do this work and invested a lot of time advising me and discussing problems. Thank You for your support. Furthermore, I want to thank Prof Spaan, who agreed to be the second assessor of this thesis.

I also want to thank the chair of Prof. Rhode, who welcomed me warmly when I started as a Bachelor, and ever since I experienced a supporting and kind atmosphere towards me. Especially I want to thank Alexander Sandrockwith my deepest gratitude, who invested a lot of time in me and thereby had a lot of patience. But we had a good collaboration and I still appreciate working together with you. Furthermore, I want to thank my office, Thorben Menne, Maximilian Meier, and Mario Dunsch for the good working atmosphere. I appreciate it, especially in the context of writing this acknowledgment after more than one year of the pandemic. I want to highlight Mirco Hünnefeld and Mathis Börner and thank you for the numerous discussions. To the PROPOSAL development squad, including Mario Dunsch, Jean-Marco Alameddine, and Maximilian Sackel, Alexander Sandrock, Maximilian Meier, and Thorben Menne I just want to say, that you are the best. Special thanks thereby to Maximilian Nöthe for his special help. Finally, I want to thank the heart of this chair, thank you, Andrea Teichmann.

I acknowledge the DFG for funding this muon project, the Wilhelm and Else Heraeus Foundation for funding the DPG conferences, and the DAAD for the 3-month scholarship. Thereby, I want to thank Prof. Claudio Kooper and the whole IceCube group at the Michigan State University for the interesting discussions and insights I could get. Huge thanks also to the complete IceCube collaboration for the fruitful discussions. I gained a lot of experience and it was an honor to work in one of the most exciting experiments on earth. I also want to thank the CORSIKA collaboration for their support, their ideas, and just the very good collaboration.

Finally, I thank my family. No words can describe how much you have always supported me and how I can trust in you, which gives me strength. Thank You

Eidesstattliche Versicherung

Ich versichere hiermit an Eides statt, dass ich die vorliegende Abschlussarbeit mit dem Titel “Systematic Uncertainties of High Energy Muon Propagation using the Leptonpropagator PROPOSAL” selbstständig und ohne unzulässige fremde Hilfe erbracht habe. Ich habe keine anderen als die angegebenen Quellen und Hilfsmittel benutzt, sowie wörtliche und sinngemäße Zitate kenntlich gemacht. Die Arbeit hat in gleicher oder ähnlicher Form noch keiner Prüfungsbehörde vorgelegen.

Ort, Datum | Unterschrift

Belehrung

Wer vorsätzlich gegen eine die Täuschung über Prüfungsleistungen betreffende Regelung einer Hochschulprüfungsordnung verstößt, handelt ordnungswidrig. Die Ordnungswidrigkeit kann mit einer Geldbuße von bis zu 50 000 € geahndet werden. Zuständige Verwaltungsbehörde für die Verfolgung und Ahndung von Ordnungswidrigkeiten ist der Kanzler/die Kanzlerin der Technischen Universität Dortmund. Im Falle eines mehrfachen oder sonstigen schwerwiegenden Täuschungsversuches kann der Prüfling zudem exmatrikuliert werden (§ 63 Abs. 5 Hochschulgesetz –HG–).

Die Abgabe einer falschen Versicherung an Eides statt wird mit Freiheitsstrafe bis zu 3 Jahren oder mit Geldstrafe bestraft.

Die Technische Universität Dortmund wird ggf. elektronische Vergleichswerkzeuge (wie z. B. die Software “turnitin”) zur Überprüfung von Ordnungswidrigkeiten in Prüfungsverfahren nutzen.

Die oben stehende Belehrung habe ich zur Kenntnis genommen.

Ort, Datum | Unterschrift